UNIVERSITÀ DEGLI STUDI DI MILANO

DOTTORATO DI RICERCA IN SCIENZE DELLA TERRA

Ciclo XXXIV

DIPARTIMENTO DI SCIENZE DELLA TERRA "A. DESIO"

Sedimentology and stratigraphy of turbidite systems with contrasting architectures: examples from the Tertiary Piedmont Basin (NW Italy) and the Taza-Guercif Basin (NE Morocco)

GEO/02 - Geologia stratigrafica e sedimentologica

Simone Reguzzi

Matricola R12189

Tutor
Dr. Mattia Marini

Co- Tutor
Prof. Fabrizio Felletti
Dr. Massimo Rossi

Coordinator
Prof. Fernando Camara
Prof. Maria Iole Spalla

Academic Year

2020-2021

Intentionally blank page

A quelle persone fondamentali nella mia vita

che hanno contribuito a farmi diventare la persona che sono…

Ai miei genitori e a mia sorella…

A quelle persone che oggi non ci sono più…

"Happiness can be found even in the darkerst of times,
if one only remembers to turn on the light"

Harry Potter and the Prisoner of Azkaban,
J. K: Rowling (novelist)

"In One Dimensions, did not a moving Point produce a Line with two terminal points?
In two Dimensions, did not a moving Line produce a Square with four terminal points?
In Three Dimensions, did not a moving Square produce - did not the eyes of mine behold it - that blessed being, a Cube, with eight terminal points?
And in Four Dimensions, shall not a moving Cube - alas, for Analogy, and alas for the Progress of Truth if it be not so - shall not, I say the motion of a divine Cube result in a still more divine organization with sixteen terminal points?"

Flatland: A romance of Many Dimensions
Edwin A. Abbott (novelist)

"The Earth is what we have in common"
Wendell Berry (poet and novelist)

The research reported in this Thesis was carried out at the
Department of Earth Science “A. Desio”
Università degli Studi di Milano
Via Luigi Mangialli, 34
20133 Milano
Italy

Financial support was provided by the Ministero dell’Università e della Ricerca

Acknowledgements

During the last three years and half, I could not have had a better chance to work with such kind people.

First of all, I would like to warmly thank Mattia Marini, my supervisor, mentor, and friend, for his constant presence and support during this PhD. Even though sometimes we argued about many “geological stuff” because of our different ideas, he provided me an invaluable scientific help and geological knowledge. Thank you Mattia for having shared with me the logic behind writing a scientific paper, and I will never forget our strong discussion about what is really important in a paper and what is “trash”.

Many many thanks to Fabrizio Felletti for having introduced me into the world of sedimentology (actually, you had already done it during the MSc thesis), and for the chance you gave me to work both in the Tertiary Piedmont Basin (your “geological baby”) and in Morocco. However, I know that sometimes I stressed you with my “scarse-inspiration mood”, but I would like to thank you for the help and the support that you always provided me like a friend.

A special thanks to Riccardo Bersezio, who officially replaced Mattia during the “supervisor’s vacancy period”. Above all, I would like to warmly thank Riccardo because it is because of the enthusiasm for geology that he shared with students during the first year of the Bachelor’s degree if I have arrived until the end of the PhD.

A great thanks to Massimo Rossi, who shared with me his passion for the Tertiary Piedmont Basin and thanks to whom I had the chance to work on inedit seismic data in collaboration with Eni S.p.A. (which I officially thank as well).

A warm thank to Prof. Hassan Tabyaoui and the local Authorities of Douar Tachrift and Ras El Ksar, for their support during the field works.

I would like to thank you Prof. Maria Rose Petrizzo as well for the help provided during the biostratigraphic review.

A generous thanks to Andrea Di Giulio e Antonio Langone who taught me a lot about sandstones petrography and zircons analyses during my internship at University of Pavia. Thank to Chiara Amadori as well, who gave me the opportunity to work on the thermochronology of the Tertiary Piedmont Basin.

Obviously, I cannot forget to acknowledge all my adventure fellows, starting from “La Zuffa” (i.e., Chiara Zuffetti, for those who don’t know), Imad and Nicolò, with whom I shared unforgettable adventures in Morocco, eating tajine until blowing up and logging from the sunrise to the sunset. Furthermore, I would warmly thank the “Hachimi Family” for the hospitality and help during the stay in Morocco, you made me feel like at home!

A special thanks to all my “PhD classmates” of the XXXIV cycle. I want remember Sara, Liyenne, Gabriele and Greta with whom I shared time of “bureaucratic panic” and endless lunches chatting about how hard, but cool, the PhD-life can be.

An extra huge warm-hearted thank to Luca Forti, who randomly arrived in MY office and randomly became one of my best and closest friends. Thanks, Lu, for being enough crazy to staying in OUR office (yes, now I can share it with you), for all the pints of beer and for the stupid, even though philosophic, speeches.

I’ve certainly forgetten to thank someone else, but I cannot forget to thank Mattia Nembrini, Matteo Maron (Magneto!) and Mario De Matteis, my old office mates with whom I started this PhD adventure.

A warm thank to Stefano Longinotti, Bepi Cadel, Michele Zucali and Claudio Chesi to have followed the “crazy geological ideas” of this crazy man (who’s me!).

I also wanna thank all the students that I had supervised during my tutoring activities. Thanks to you all, if I have improved my skills of human being, teacher, and geologist it is also ‘cause of what you have shared with me.

At last, not for importance, many thanks to my family, who supported me during all these years of study and who gave me always the possibility to try to get what I wanted in life. Thank you for the values that you taught me mom, dad, and Giada. I love you all.

I also wanna thank my friend Stefi, who opened my mind to a new world by expanding my horizons beyond the limit that I had prefixed to myself. I will never forget you!

And finally, the greatest and most important thank to you, Katya, my love, for your constant support, your kindness, and your love.

Table of Contents

Abstract

Architectures of submarine fans and turbidite systems are endowed by a high grade of complexity, inherited by the large variability of depositional flows characterising them. This complexity is reflected upon the superimposition of depositional elements (e.g., channels, levées, splays, etc.) giving rise to contrasting sedimentary facies and geometries at different scales. Thus, the understanding and prediction of their heterogeneity over space is essential to obtain reliable depositional models, which can be applied in the field of natural resources exploration.

Despite heterogeneities of facies and architectures in turbidite deposits are largely studied, several questions regarding evolutionary controls still remain open due to the intricate interplay between autocyclic and allocyclic factors and the lack of roboust chronostratigraphic (i.e., time-related) constraints to be applied to turbidite systems evolution.

This doctoral work focuses on two turbidite units, different for facies, architectures, age, and depositional setting. The work pursues the goal of complementing sedimentological data (collected with cm-scale resolution) with bio-chronostratigraphic data (both novel and collected from the literature) in order to provide a trustworthy estimation of the geological time in turbidite systems depositional models.

In the first two chapters an overview on sediment gravity flows and their evolutionary models is provided, emphasising classical facies and depositional geometries.

In chapter three, the sedimentary architecture and the controls on the evolution of a channel-levée complex from the Tachrift Turbidite System (Upper Miocene, Melloulou Fm., TazaGuercif Basin, NE Morocco) is addressed. The studied complex is spectacularly well exposed and then suitable for detailed sedimentological logging with cm-scale resolution.

Results show a tripartite stratigraphic organisation of the complex, including: (i) a lowermost mud-prone interval with relatively small (a few hundred of metres across and metre-thick) and vertically stacked channels fills, (ii) a middle interval (ca. 4 m-thick and >1 km-wide) made of dominantly amalgamated sandstones with eastward-directed lateral accretion packages (LAPs), and (iii) an uppermost interval made of vertically aggraded channel fills with variously directed LAPs and well-developed levées. This organisation suggests that, after a relatively short phase of inception

(lowermost interval), the channel underwent a prolonged lateral migration, prior to become aggradational (uppermost interval). Proportions of turbidite vs. hemipelagic deposits suggest that the migrational and aggradational phases straddle a lapse of reduced turbidite input to the studied section of the slope. It is suggested that the observed architectural style turnaround reflects the feedback of channel morphodynamics, sediment input, and along-dip channel depth profile.

In chapter four, the Rupelian Monastero Fm. turbidite system (Tertiary Piedmont Basin, NW Italy) is addressed. This 1100 m-thick turbidite system was deposited adjacent to a coeval and heteropic fan delta system (i.e., the Savignone Conglomerates), upon a south-eastward dipping clastic ramp, and consists of an apparently monotonous succession of thin-bedded sandstone-mudstone couplets intercalated by erosive-based amalgamated bedsets made of sandstones and conglomerates. The unit was studied along the best exposed and most continuous section (Val di Grue-San Gaudenzio section) by cm-scale resolution sedimentological logging. Thesedimentological data were subsequently complemented with bio-magnetostratigraphic data (novel and from the literature) to refine the depositional model. In addition, seismic lines interpretation (in professional partnership with Eni S.p.A.) was used to constrain the Monastero Fm. depositional setting in the host basin.

Results provide information about facies and architecture of the Monastero Fm. and insights for analogue systems: (i) the investigated stratigraphy is dominated for the 60% of section thickness by a muddy heterolithic background (with a density of 3 beds/m on average) alternated with conglomeratic channel fills and sandy lobes, (ii) the 65% of the studied section is composed of sedimentary bed repetitions interpreted as hyperpycnites, (iii) these repetitions cohexist with ‘classical’ turbidite facies indicating that the latter may represent the transformation of the former, (iv) bio-magnetostratigraphic data suggest an average accumulation rate of 400 m/Ma for the Monastero Fm., with an estimated return period of sedimentary gravity flows lower than a few thousand years, (v) seismic interpretations confirm the confined nature of the Monastero Fm. turbidite system.

In conclusion, the new results of this doctoral work suggest that the use of magneto-biochronology can provide useful constraints for depositional age models, thus contributing to enhance our understanding of the time-scale and control factors of changes in sediment delivery to deep-water.

Intentionally blank page

Aim and rationale

Submarine fan and turbidite systems are important targets for hydrocarbon exploration (e.g., Weimer, 2000; McCaffrey & Kneller, 2001; Pettingill & Weimer, 2002; Weimer & Pettingill, 2007; Morley *et al.*, 2011). They represent the product of deposition by a variety of submarine sediment-laden flows (sediment gravity flows hereafter), initiated either by submarine failures or river floods in seas and lakes, which have contrasting fluid-dynamics (see Section 1 for a review) and can transform one into another along path as a result of water ingestion and sediment entrainment (Shanmugam, 2000; Baas *et al.*, 2009, 2011; Kane & Pontén, 2012; Terlaky & Arnott, 2014).

The deposits of sediment gravity flows are generally referred to collectively as turbidites, albeit various facies scheme have been proposed to differentiate the products of different flow types (see Section 2 for a review).

Whether one sediment gravity flow type or another will dominate and deposit at given location is a complex function of several control factors (e.g., initial flow type, substrate characteristics, along-dip profile of the system, etc.), most of which are non-stationary due to external controls (e.g., tectonics, sediment input, and eustasy; Mutti, 1985; Shanmugam *et al.*, 1997; Kneller, 2003; Kane & Hodgson, 2009; Hodgson *et al.*, 2011; Catuneanu, 2020).

As a result, the architecture of submarine fan and turbidite systems is inherently complex (see Section 2 for a review), as it reflects the superimposition of depositional elements (e.g., channels, associated levées, levée crevasses, frontal splays, and mass transport complexes; see Section 2.1.1 for a review) with contrasting sedimentary facies composition and geometry.

Understanding and predicting sedimentary heterogeneity of submarine fans and buried turbidite systems heavily rely on outcrop study of depositional analogues. To study turbidites at outcrop has been particularly popular in the last few decades (e.g., Mutti & Normark, 1991; Mutti *et al.*, 2003, 2002; Navarro *et al.*, 2007; Deptuck *et al.*, 2007; Bersezio *et al.*, 2009; Marini *et al.*, 2016b; a; Cunha *et al.*, 2017; Fonnesu & Felletti, 2019; Patacci *et al.*, 2020; Arnott *et al.*, 2021) as it is cost-effective, allows collecting sedimentological data down to the scale of pores and can be pursued with (benefiting from) a multidisciplinary approach (e.g., Krijgsman *et al.*, 1999; Oms *et al.*, 2003; Payros

& Martínez-Braceras, 2014; Hopkins *et al.*, 2020; Marini *et al.*, 2020). Yet, there are many open research questions on deep-water systems, especially regarding the role of autocyclic (system morphodynamics and self-organisation) vs. allocyclic (sediment input variations, tectonics, etc) factors in controlling sedimentary architecture. Tackling some of these questions is made difficult by the fact that deep-water clastic successions are generally not adequately constrained for chronostratigraphy, partly due to biostratigraphic reworking (e.g., Garrett *et al.*, 2000) and lack of materials suitable for geochronology (e.g., Carey & Sigurdsson, 1980; Hopkins *et al.*, 2020), or simply because the stratigraphic scale of investigation is often too small. However, there are examples where a combined use of different stratigraphic techniques (biostratigraphy, magnetostratigraphy, geochronology) has been successfully applied to dating turbidite systems (e.g., Oms *et al.*, 2003; Marini *et al.*, 2020), which can contribute to better understand the time duration and meaning of their component elements.

This doctoral work focuses of two turbidite units with contrasting depositional architectures and sedimentary facies. These are 1) Complex 4, one of the nine channel-levée complexes of the Tachrift Turbidite System (Tortonian, Taza-Guercif Basin, NE Morocco; Gelati *et al.*, 2000; Felletti *et al.*, 2020; see Section 3) and 2) the Monastero Formation (Rupelian, Tertiary Piedmont Basin, NW Italy; Gelati, 1977; see Section 4). Although very different, these two systems were chosen because they represents two turbidite systems which are proximal to the relative feeding systems, promoting a better record of the sedimentary input. This is a necessary condition to assess the sedimentation rate of these systems.

Furthermore, both the turbidite systems were already dated by bio-magnetostratigraphic analyses and then suitable for the integration with more detailed sedimentological data.

In this work classical sedimentological approach to outcrop study of deep-water clastics (see methods in Sections 0 and 4.3) and analysis and integration of biostratigraphic and magnetostratigraphic data from the literature (see Sections 4.3.2 and 4.4.4) are combined in order to:

1) detail sedimentary facies and architectural elements of the studied turbidite units, with a special reference to their process sedimentology meaning.

2) assess internal facies variability, dimensional parameters, and shape of architectural elements, useful to aid recognition and characterization of depositional analogues both at outcrop and in the subsurface.
3) devise depositional models that embed geological time from available biostratigraphy and magnetostratigraphy data, thereby contributing to better understanding of key controls on the architecture of analogue deep-water systems.

These key points are fundamental to contribute in the understanding of turbidite systems heterogeneity in terms of their features distribution over space and time.

Intentionally blank page

CHAPTER I

Introduction to gravity flow deposits

Intentionally blank page

1. Introduction to gravity flow deposits

This chapter provides background information on deep-water sediment gravity flows and their deposits, giving a general overview of the main facies and depositional environments. Firstly, a general historical overview of sedimentary gravity flows and their associated deposits is provided. Subsequently, different types of sediment gravity flows and their general flow structures are explained for completeness, giving emphasis to their deposits, even though just the turbidity flows will be the subject of this study in chapters 3 and 4.

1.1. Gravity flows and their deposits

The comprehension of deep-water sea floor environments has been challenging since the first studies dated back to the 1850s (Studer, 1847; Maury, 1860; Bertrand, 1897; Hsü, 1970; Mutti, 1992; Sumner *et al.*, 2008; Reading, 2009), giving several different interpretation of their deposits and architectures. Only with the first exploration of submarine canyons and the sequential breaking of submarine pipelines and telegraph cables was prompted the hypothesis that oceanic sea floors were probably the site of submarine currents (Heezen & Ewing, 1952; Piper *et al.*, 1999a). In this direction, the hypothesis that submarine canyons were the result of submarine erosion by means of sediment-laden density currents was advanced (Daly, 1936). These deep-water currents were the responsible of downslope developing of natural depression on the sea floor.

Even though it was firstly introduced by Johnson (1939), the term *turbidity current* was better defined during the first half of the 20th century, after outcrop descriptions and laboratory experiments carried out by Migliorini (1943) and Kuenen (1937, 1948). By means of these works, erosion and deposition by gravity flows was defined as the result of flows that are driven by the weight of their suspended sediments. The term *turbidity current* (Kuenen & Migliorini 1950) was used to refer to graded bedded sandstones in which individual graded beds were interpreted as the deposition of a discrete flow. Afterwards, the definition was amended by Arnold H. Bouma, based on field studies of the Annot Sandstones (SE France), defining five typical facies intervals (Fig. 1) (Bouma, 1962, 1964): T_a- graded structureless interval; T_b- horizontal parallel lamination; T_c- current-ripple lamination; T_d- fine grained horizontal parallel lamination; T_e- a mud dominated interval.

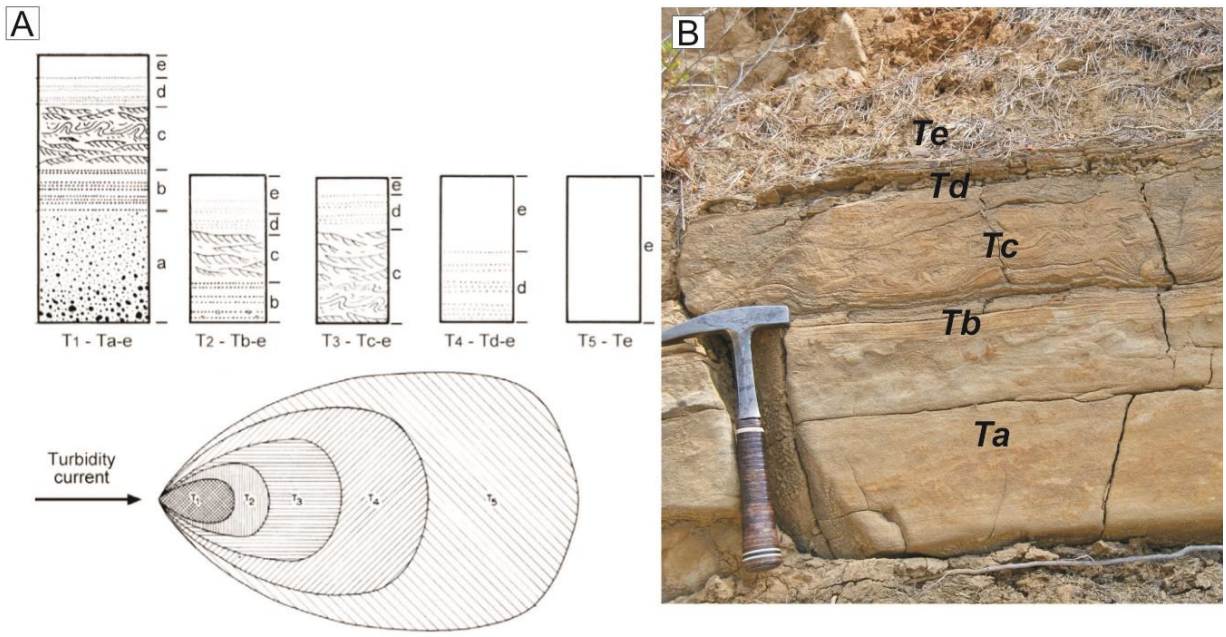

Fig. 1. (A) 'Bouma sequence' and the depositional cone showing its downcurrent evolution (Bouma, 1962). (B) Example of complete Bouma's sequence from the Cilento Flysch (Lago Marina Bay, Castellabate, Italy); the T_c ripple laminated interval is here convoluted due to syndepositional water escape (geological hammer for scale) (Fonnesu, 2016).

Following Bouma's classification, the head of the turbidity current transports coarse-grained sediments and the tail transports finer-grained sediments leading to the formation of an overall vertical fining-upward trend in these deposits. The different intervals are explained as to be due to decreasing flow energy and lateral segregation of the grain-sizes. Therefore, the interpretation depicts a turbidity current as a non-uniform flow, which is characterised by decreasing velocity and competence moving downslope toward the basin plain (i.e., generating fining-upward trends basinward), as well as an unsteady flow with decreasing velocities and competence over time (i.e., generating graded beds). In the 1960s, Walker (1967) introduced the distinction between relatively "proximal" and "distal" turbidite deposits (see Section 2 for further details).

Following the aforementioned classifications, turbidite deposits were identified in a variety of ancient depositional settings. However, even though Bouma's classification was more or less always applicable, the analysis of deep-water proximal successions (i.e., canyons, channels, proximal lobes) points out some discrepancies and differences in coarser-grained deposits that do not fit with Bouma's facies model. More recent studies (Mutti & Ricci Lucchi, 1972; Lowe, 1982; Mutti, 1992; Kneller, 1995a; Kneller & Buckee, 2000; Kneller & McCaffrey, 2003; Sumner *et al.*,

2008; McHargue *et al.*, 2011a; b; Cunha *et al.*, 2017; Stow & Smillie, 2020; Meirovitz *et al.*, 2021) described these coarser-grained facies (i.e., conglomeratic to coarse-grained sandstones) forming sedimentary features such as traction carpets (*sensu* Sohn, 1997), dunes, and inverse grading, as the result of fully-turbulent, pulsate and bypass flows. Furthermore, only recently studies pointed out a major complexity in turbidite deposits represented by hybrid-beds (Haughton *et al.*, 2009; Hodgson, 2009; Fonnesu *et al.*, 2015, 2018; Mueller *et al.*, 2017; Carnevale *et al.*, 2018; Fonnesu & Felletti, 2019; Patacci *et al.*, 2020b), which can be classified as gravity flows showing evidence of abrupt and/or progressive changes in flow behaviour, with transformation from poorly cohesive and essentially turbulent flows to increasingly cohesive deposition with suppressed turbulence. Therefore, these studies pointed out how the flow rheology represents an important factor to fully understand the complexity of deep-water gravity flows over space and time.

1.1.1. Physics and dynamics of gravity flows

Since the experiments performed by Kuenen (1937, 1948), the understanding of turbidite gravity flows physics and dynamics has increased over the last eight decades. In such a view, Middleton & Hampton (1973) distinguished a four-folded classification of gravity flows on the basis of their support mechanism (Fig. 2): 1) *turbidity currents*, such as those flows in which particles are supported by flow turbulence, 2) *fluidized flows*, such as those flows in which particles are supported by upward movement of pore fluid, 3) *grain flows*, such as those flows in which particles are supported by dispersive pressure, and 4) *debris flows*, such as those flows in which particles are supported by matrix strength and density. Furthermore, all these flow types can be grouped in two wider categories, i.e. *plastic* or *fluidal*, on the basis of their rheological features. This distinction influenced Mulder & Alexander (2001), who distinguished gravity flows between two categories, i.e. *cohesive* and *frictional*. *Cohesive flows* are characterised by both plastic and chiefly laminar behaviour, with the particle support that is mostly exerted by the matrix strengths. This rheological behaviour is due to the presence of a sufficient amount of cohesive material, such as mud, which is able to exercise a cohesive strength on particles. These kind of flows are mainly represented by debris-flows, which are able to carry large quantities of coarse-grained material, up to decametres-sized (Johnson, 1970; Reading, 2009; Talling *et al.*, 2010), to smaller clasts or chips enveloped by

a clay-rich matrix. Debris-flows travel as driven by laminar flows overlying a basal shear zone and final deposit en-mass, once the yield-strength is no longer greater than the shear stress so as to freeze the flow (i.e., cohesive freezing in Mulder & Alexander, 2001).

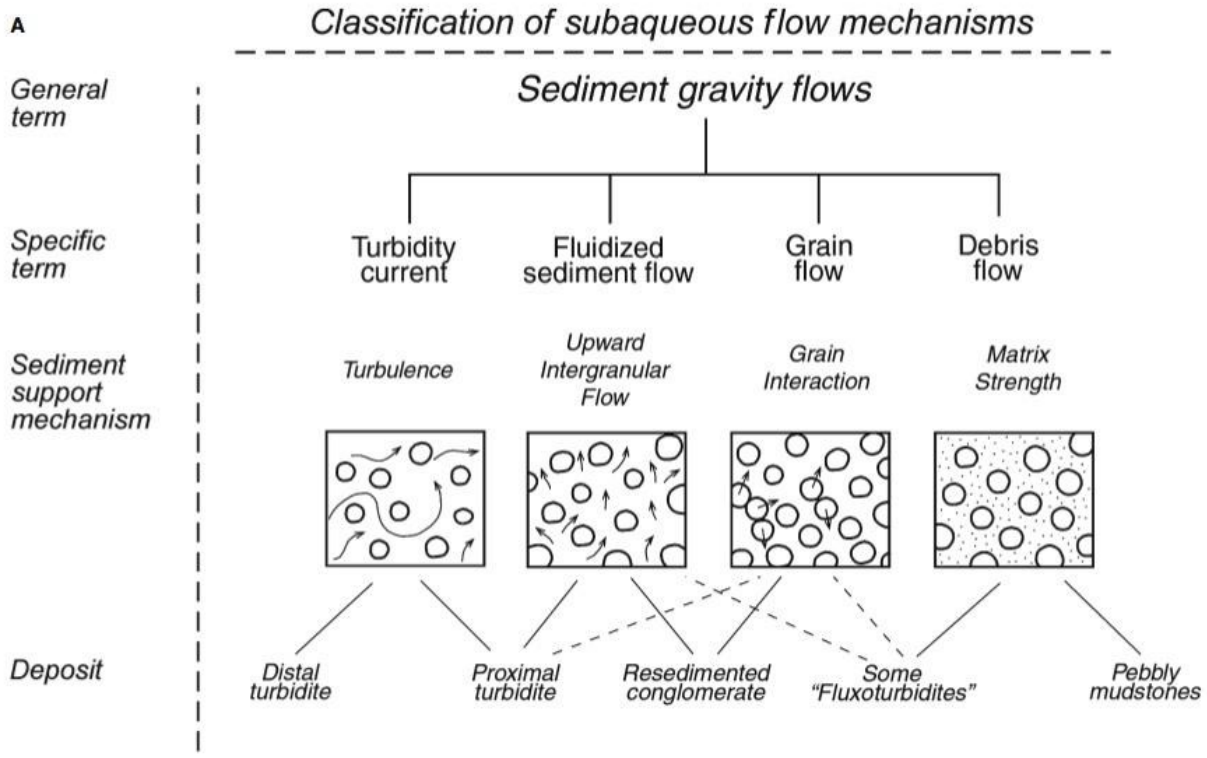

Fig. 2. Classification of subaqueous sediment gravity flows and their associated sedimentary deposits (Middleton & Hampton, 1973; modified after Mutti et al., 2009). Those flow types represent part of a continuum of flow behaviour and a single event can exhibit more than one flow type.

On the other hand, *frictional flows* derive from the gravity force activity upon a fluidal mixture of fluid and suspended sediment, because of the density gradient between the mixture and surrounding ambient fluid (Kneller & Buckee, 2000). In this view, Mulder & Alexander, (2001) distinguished two different types of frictional flows on the basis of sediment concentration. When the concentration does not exceed 9% by volume, sediments are supported via the upward component of the turbulence (Bagnold, 1962). At higher concentrations, the combination of fluidal turbulence, buoyant lift and dispersive pressure can operate during final sediment transportation phase. These two states of concentration represent end-members of a continuous range of flows, particularly difficult to split in different sub-states (Mulder & Alexander, 2001). As so, the terminologies *High-density* and *Low-density turbidity currents* are used as descriptive terms for these states, following classification by Lowe (1982). In the case very high concentrations are

reached (over 25% of volume), flows are defined as *hyperconcentrated* (Mutti, 1992; Mulder & Alexander, 2001), as they can move like laminar flows, but they lack significant cohesion (i.e., pseudo-plastic fluid, Barnes *et al.*, 1989). According to Mulder & Alexander (2001), grain-flows, in which grain-to-grain collisions govern the flow mechanism, are considered as a sub-category of hyperconcentrated flows even though they require a steeper slope gradient to be activated and travel for a shorter distance than hyperconcentrated flows, without depositing a large amount of sediments (Mutti, 1992; Nichols, 2009 and references therein).

Despite these classifications seem to provide a well-established definition of different rheological states for gravity flows, taking into account the subtle nature of such rheological limits, the term *turbidity current* is used in the literature in its broadest meaning, which coincides with that of Middleton & Hampton (1973), who referred it to *Newtonian flows* in which the turbulence is the main support mechanism.

1.1.1.1. Bi-partite flows

As previously mentioned, most of knowledge about physical features of turbidity currents derives from laboratory experiments and theoretical mathematical models, which act like good analogues of the flow rheology conditions. The application of new technological techniques allowed to improve understanding in flow velocity, concentration of structures (Kneller & Buckee, 2000), and the effect of flow interaction with relict topography (Kneller, 1995; Al Ja'Aidi *et al.*, 2004; Patacci *et al.*, 2014, 2015). Particularly, the analysis of velocity distribution in turbidity currents (Middleton, 1966; Kneller *et al.*, 1997; Kneller & Buckee, 2000) brought to attention the distinction between two main regions featured by opposite velocity gradients (Fig. 3). An inner region characterised by upward increase in flow velocity and an outer region characterised by upward decrease of flow velocity. These two regions are likely separated by an ideal surface joining up all points moving with the highest velocity (i.e., Umax in Fig. 3) within a given flow. As shown by experimental data (Middleton, 1966; Kneller *et al.*, 1997; Kneller & Buckee, 2000), the position of this boundary surface is controlled by the ratio between inertial drag-forces depending on the interaction with depositional surfaces and ambient water, and is located at a height of 0.2-0.3 times of the height of the entire turbidity current.

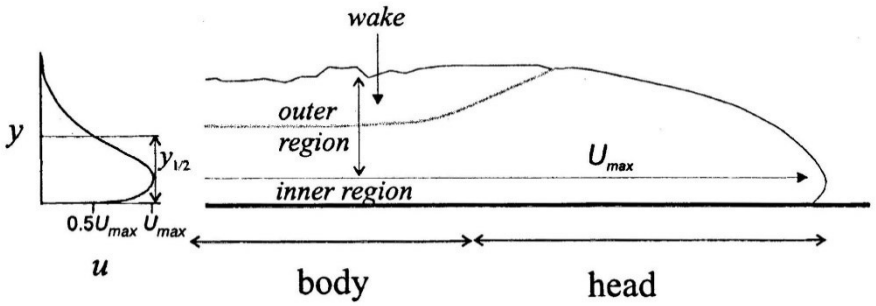

Fig. 3. Sketch showing the anatomy of a turbidity currents and it velocity vertical structure (Kneller & Buckee, 2000).

Therefore, turbidity currents can be defined as density stratified flows (Middleton, 1966, 1993; Simpson & Britter, 1979) in which sediment concentration varies internally as function of the flow type (See Section 1.1.1), internal distribution of velocity and inertial forces at flow boundaries (Garcia, 1989; García, 1993; Garcia & Hull, 1994; Altinakar *et al.*, 1996). As a consequence of these characters, coarse-grained particles concentrate at the base of the flow, whilst fine-grained particles are dispersed rather homogenously throughout the flow.

The anatomy of a turbidity current can be further described as composed of a head, a body and a tail, and each one is characterised by typical sediment concentrations, grain sizes and dynamics (Middleton, 1966; Kneller & Buckee, 2000).

The head of the turbidity current has a typical erosional behaviour and plays an important role in controlling the bulk volume of the flow by entraining sediments along the downstream path of the current (Allen, 1971; Simpson & Britter, 1979; Middleton, 1993; Kneller *et al.*, 1997). The head of the turbidity current is thicker compared to its body and is characterised by having eddies (Kelvin-Helmholtz billows *sensu* Kneller & Buckee, 2000) in its uppermost part, striking orthogonally to flow direction. The head of the current is turbulent and expanded due to the resistance encountered by the flow front as it tries to penetrate the ambient fluid.

The head shape is peculiar and has an over-hanging front (Allen, 1971) and planform with lobes and clefts which are formed in response to drag-forces and collapse of Kelvin-Helmholtz billows (Fig. 4). The collapse of billows chiefly depends on the turbulence degree and represents an important part of the turbidity current process because it exerts control on flow mixing and dilution (Parsons & García, 1998; Parsons *et al.*, 2007).

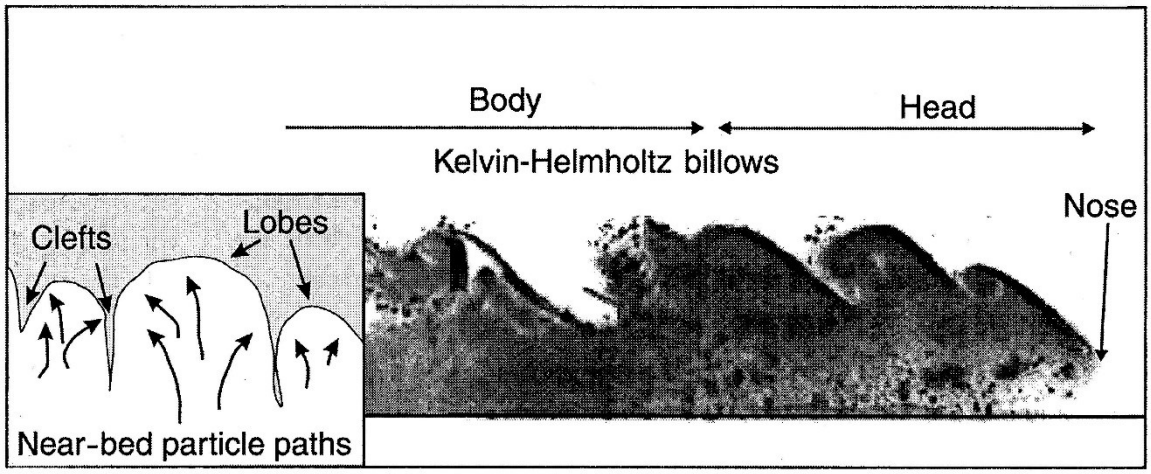

Fig. 4. Quasi two-dimensional image of thee head and body of an experimental saline gravity current illustrating well-developed Kelvin-Helmhotz billows. The small cartoon on the left shows a schematic view of lobes and clefts seen from below (Kneller & Buckee, 2000).

Compared to the head of the turbidity current, its body is more homogeneous, thinner and it presents an irregular succession of large eddies in its upper boundary which depend on mixing with ambient fluid. Furthermore, it is characterised by velocity flow variations depending on the slope gradient on which the current runs. These variation leads to a downcurrent acceleration of the turbidity current body which can run faster than the head protruding into it and determining its thickening (Middleton, 1966).

Finally, the tail of the turbidity current is thinner than both the head and the body and is typically represented by a very dilute cloud of sediments carrying the finest-grained fraction of the flow.

Nevertheless, the structure of turbidity flows can be more complicate. As suggested by Kneller (1995), spatial and temporal accelerations of the flow can occur as a function of the slope gradient and evolution of the total discharge over time. The Author defined the so-called acceleration matrix (Fig. 5) consisting of nine fields describing as many possible flow behaviours as possible along with five likely deposits typologies. These are defined for *accumulative* (i.e., accelerating flows), *uniform* (i.e., neither accelerating nor decelerating flows) and *depletive* flows (i.e., uniform or accelerating flows).

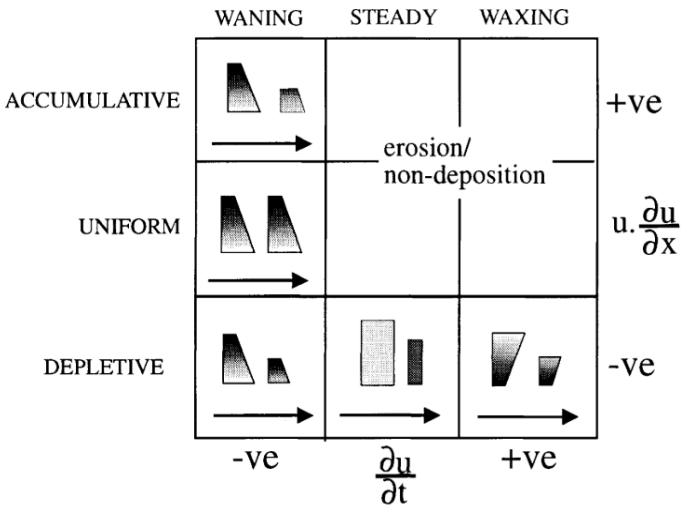

Fig. 5. Acceleration matrix, with illustrative bed sequences for each field showing downstream and vertical changes in relative grain size of the deposits of each field; arrows point downstream. The five represented depositional profiles differ one from another for both vertical and downstream relative grain-size variation. From Kneller (1995).

A further distinction was proposed by Mulder & Alexander (2001), characterising three types of turbidity currents based on their duration.

Surge turbidity currents are short-lived (i.e., up to some tens of hours) and non-uniform flows likely generated by almost instantaneous events on a slope (e.g., those generated by submarine slope collapses). The body of these turbidity currents accelerate pushing forward the head of the flow. Typically, the body is not well developed and the head represents the most important and voluminous part of the turbidity current.

Surge-like turbidity currents are short-lived even though they differ from surges because of their well-developed body and greater uniformity through the flow. They can be formed by collapsing of sediment suspensions (Wilson & Roberts, 1995), multiple submarine failures occurring in front of mouth bars (Van Den Berg *et al.*, 2002), flow transformations of hyper-concentrated, concentrated, and cohesive flows, such as slumps and debris flows (Van der Knaap & Eijpe, 1968; Van Andel & Komar, 1969; Allen, 1971; Komar, 1971; Hampton, 1972; Weirich, 1988; Weaver *et al.*, 1992; Garcia & Hull, 1994; Mulder & Alexander, 2001).

Finally, *quasi-steady turbidity currents* (*cf.* with 'sustained flows' in Kneller & Branney, 1995) can be produced at river mouths by hyperpycnal flows entering a lake (Gihm & Hwang, 2016; Lewis *et al.*, 2017) or sea (Kneller & Buckee, 2000; Mulder *et al.*, 2003; Plink-Björlrklund & Steel, 2004; Warrick *et al.*, 2008; Piper & Normark, 2009) as well as by breach failures (Van Den Berg *et al.*,

2002). They are long-lived turbidity currents which can last for many days up to some weeks, involving a large volume of sediments. In such flows the body represents the best developed part, showing a high degree of stationarity in terms of velocity and sediments concentration.

Additionally, the role of basin size and morphology in controlling deposition by turbidity currents has been explored by several experimental studies (Kneller, 1995b; Kneller & Branney, 1995; Al Ja'Aidi *et al.*, 2004; Amy *et al.*, 2004; Patacci *et al.*, 2015) and documented by a number of outcrop studies (Sinclair, 1994; Amy *et al.*, 2000, 2004; Haughton, 2000; Felletti & Bersezio, 2010; Kane *et al.*, 2012; Marini *et al.*, 2016b; Tek *et al.*, 2021).

The effects of the turbidity current interaction with obstacles depend on the relative size and geometry of the obstruction and mainly consist of generation of internal bores and changes in flow velocity and rheological structure and deflection of the flow path. The main effect is the decrease of turbidity currents velocity which leads to deposition in proximity of the obstruction. The same effect can be generated by interaction of turbidity currents with basin topography in such settings as confined basins. This effect is reflected on facies, depositional geometries, and overall architectures of deposits.

1.1.1.2. Hyper-, Homo-, Hypopycnal flows

Turbulent flows can also form by continuation of river discharge at sea. Sediments can bypass the coastal area during both normal and flood regimes, allowing to transfer a quantity of sediments up to hundreds of kilometres off-shoreward (Bates, 1953; Nemec, 1995; Mulder & Syvitski, 1995; Mulder *et al.*, 1997, 1998, 2001a; b; c, 2003; Bryn, 1998; Plink-Bjölrklund & Steel, 2004; Lamb & Mohrig, 2009; Zavala & Pan, 2018; Shanmugam, 2019).

When the river flow enters the sea water, the density contrast between the inflow and the ambient fluid can form different types of flows (Fig. 6 and Fig**. 7**).

Hypopycnal flows (Fig. 6A) are those characterised by a density lower than the one of ambient fluid (i.e., sea water). These flows creates a buoyant plume of sediments spreading off-shoreward (Zavala *et al.*, 2011a; Mutti, 2019).

On the contrary, hyperpycnal flows (Fig. 6B) are those characterised by a density higher than the one of the sea water. In this case, the fluvial outflow sinks below the sea-water body,

continuing to travel off-shoreward as a quasi-steady underflow (Mulder *et al.*, 2003; Zavala *et al.*, 2011a).

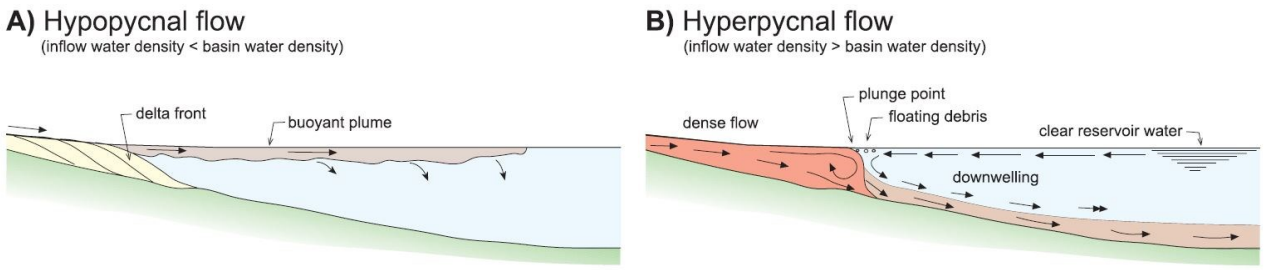

Fig. 6. Comparison between hypopycnal (A, inflow density < sea-water density) and hyperpycnal (B, inflow density > sea-water density) flows (original concept by Bates, 1953). From Zavala et al. (2011).

A further category is represented by inflows of river water having the same density of the sea water, i.e. homopycnal flows (Allaby, 2008). The entrance of these flows results in intense local mixing of waters with considerable sedimentation (Mulder & Syvitski, 1995).

However, the actual distinction in natural environments is more complicated than what is represented by these three categories due to the dynamic evolution of flows.

According to Mulder & Syvitski (1995), ignition of hyperpycnal flows requires a critical sediment concentration of the turbid water entering the sea water at river mouths of 36-44 kg/m^3. However, oceanographic observations and experimental data highlighted that lower concentrations are sufficient to initiate an hyperpycnal flow and suggested that their importance in the geological record may have been larger than expected (Mulder *et al.*, 2003; Plink-Björlrklund & Steel, 2004).

As summarised by Mulder *et al.* (2003) and discussed by Lamb & Mohrig (2009), the hypothesis that hyperpycnal flows, along with associate deposits, record the time evolution of flooding rivers is real but not all the river produces hyper-homo-hypopycnal flows. In this hypothesis, hyperpycnal flows show an initial acceleration due to the river flood peak, followed by a deceleration due to the energy loss of the river flood peak. Thus, hyperpycnal flows occurrence should follow the flood hydrograph of the feeding river in terms of frequency and flow energy.

Flow discharges generated at the river mouth as related to fluvial discharge consist of three distinct parts: the plunge region, the main body, and the leading head (Kassem & Imram, 2001). Each one of these parts has peculiar features, and plays a different role in the hydrodynamic of

the flow, depending on the interaction with the surrounding sea water (Kassem & Imram, 2001; Mulder *et al.*, 2003).

Based on Kassem & Imram (2001) experimental model, as the sediment-laden flow enters the sea water, its dynamic force pushes forward the ambient fluid and a separation surface between the two fluids becomes pronounced. As soon as the pressure force at the bottom increases significantly, the flow undergoes acceleration at a rate higher than the movement at the top. As the pressure forces continue to grow, the flow plunges to the bottom and begins to move as an underflow. At the top the velocity is still significant to move the plunging point forward. When the equilibrium between forces at the bottom and forces at the top is reached, the velocity at the top disappears and a stable plunge point is formed (i.e., turbidity current. See Section 1.1.1.1).

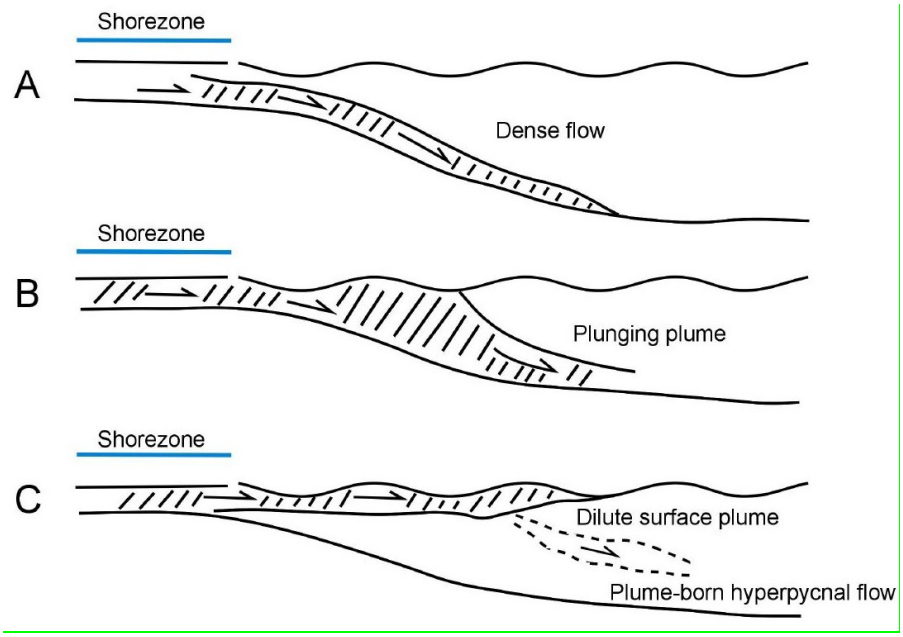

Fig. 7. Main types of fluvial discharges entering sea water. (A) Dense flow transferring coarse-grained sediments. (B) Plunging plume transferring fine-grained sediments. (C) Buoyant plume evolving into hyperpycnal flow. From Mutti (2019).

The current continues to move forward with a bulge-shaped head and an elongated body. In this view, hyperpycnal flows are considered as the mere product of plunging plumes formed at the river mouths and loaded with fine-grained sediments transported as suspended load (Fig. 7B). However, as observed in many case studies dealing with ancient (Mutti *et al.*, 1996, 2003; Plink-Björlrklund & Steel, 2004; Petter & Steel, 2006) and recent (Warrick & Milliman, 2003; Yoshida *et al.*, 2009; Warrick *et al.*, 2013; Gao *et al.*, 2016) fluvio-deltaic systems, a substantial amount of

coarse-grained sediments are directly transferred to the sea by dense gravelly and sandy flows (see Section 1.1.1) moving as “bedload” (Plink-Bjölrklund & Steel, 2004; Zavala *et al.*, 2006a, 2011a; Zavala, 2008). These inflows propagate downcurrent as highly concentrated hyperpycnal flows with a turbulent behaviour (Fig. 7A) (Mutti *et al.*, 2003; Zavala *et al.*, 2006b, 2011a). Furthermore, hypopycnal buoyant plumes propagating off-shoreward can eventually die out either after losing their load due to sediment settling or after convection processes (Fig. 7C) (Sparks *et al.*, 1993; Hesse *et al.*, 2004; Zavala *et al.*, 2011a). When convection processes occur affecting a large volume of the plume characterised by high sediment concentration, they can lead part of this plume to sink through the sea water, because of an increased state of density, generating a plum-born hyperpycnal flow (Mutti, 2019).

Assuming a direct transition of the river outflow to sea water, an ideal individual flow, containing all the grain-size populations and being accelerated in a high-gradient system, may split in three parts. A dense coarse-grained basal flow moving along bed downcurrent, a finer-grained dense to turbulent flow mainly evolving into a plunging plume, and a dilute hypopycnal flow floating on seawater and propagating as long as it is fed by the fluvial discharge (Fig. 8).

The great variability of flow types is reflected upon the complexity of their deposits, which include multiple stacked inverse and normal graded units, in some cases, derived by a single-peaked hydrograph.

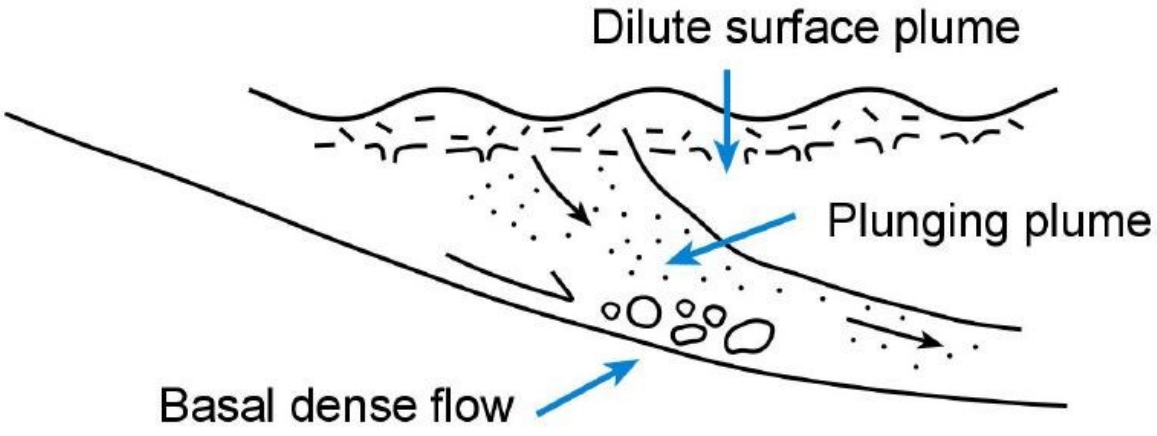

Fig. 8. Tripartition of a composite fluvial outflow into a hyperpycnal turbidity current and associated surface plume assuming direct transition of river outflow to deep-water. Modified after Mutti (2019).

1.1.2. Facies models

The attempt to define a generalised and always valid facies model for turbidity currents deposits has been pursued by several Authors (e.g., Bouma, 1962; Piper, 1978; Lowe, 1982; Mutti, 1992; see Shanmugam, 2000 and Stow & Smillie, 2020 for a review of facies models) since 1950s. These schemes are based on either flow behaviour (Middleton & Hampton, 1973; Nardin *et al.*, 1979; Mulder & Alexander, 2001), the systematic description of ancient deposits (Ghibaudo, 1992), or the interpretation of flow behaviour from ancient deposits (Lowe, 1982; Pickering *et al.*, 1989; Mutti, 1992; Mutti *et al.*, 1999, 2003; Sumner *et al.*, 2012).

However, a generalised facies model valid in every case study has never been obtained.

As stressed by Shanmugam (2000), the applicability of a facies model is a direct function of its generalisation. The more general a facies model is, the more applicable the model is. On the contrary, the more precise a facies model is and the less applicable is.

In this paragraph three main classifications useful to synthesise all the composite characteristics of classical turbidity current deposits will be succinctly shown.

1.1.2.1. Bouma (1962), Stow and Shanmugam (1980) and Lowe (1982) facies models

Bouma (1962) proposed the first vertical facies model for turbidite deposits consisting of five divisions (Fig. 9), referred to as the Bouma Sequence (see Section 1.1.1). Subsequent amendments to this classifications distinguished another interval consisting of pelagic deposits, namely T_f (Fig. 9), which overlays the T_e interval. However, the T_f is not easily distinguishable from the T_e in fine-grained silty to sandy deposits at outcrop scale, but it can be often recognised in core samples.

Later workers realized that the muddy division of the Bouma Sequence was not sufficiently adequate to represent all the distinction occurring in the mud-rich turbidites. Stow & Shanmugam (1980) proposed a new vertical facies model just for the fine-grained turbidites consisting of nine different divisions, from T_0 to T_8 (Fig. 10).

Subsequently, Lowe (1982) proposed a new vertical facies model for coarse-grained turbidite deposits of high-density turbidity currents consisting of 6 division capped atop by a finer-grained division, namely T (Fig. 11).

These three proposed sequences are event deposits, chosen for convenience, representing the transition from coarser-grained to finer-grained sediments deposited by a turbidity flow. In natural environments turbidity currents are Newtonian flows (see Section 1.1.1) which always behave with the same hydrodynamic (i.e., sediments are suspended by fluid turbulence) regardless of the grain size of sediments that are transported. Therefore, a hypothetic turbidity current which transports sediment with grain size from gravel to mud should deposit a continuum of Lowe-Bouma-Stow's divisions, from R1 to T_8 (Fig. 12). There is no fluid dynamic reason determining that such turbidity current cannot deposit all these divisions. In this composite model an ideal turbidity current comprises a total of sixteen divisions eliminating four overlapping divisions (Shanmugam, 2000).

However, all these sequences are rarely complete in turbidite deposits (i.e., <10%, for examples in megaturbidites, Stow & Smillie, 2020). Conversely, partial sequences are more common and preserve the same order of divisions even though incomplete (Fig. 9, Fig. 10, and Fig. 11).

In each sequence the lower divisions are associated to higher-energy currents and the upper divisions are associated to lower-energy currents. For a single turbidity current, this energy regime can be achieved from more proximal to more distal downslope-ward, respectively, and also from channel axis to overbank settings (Fig. 13).

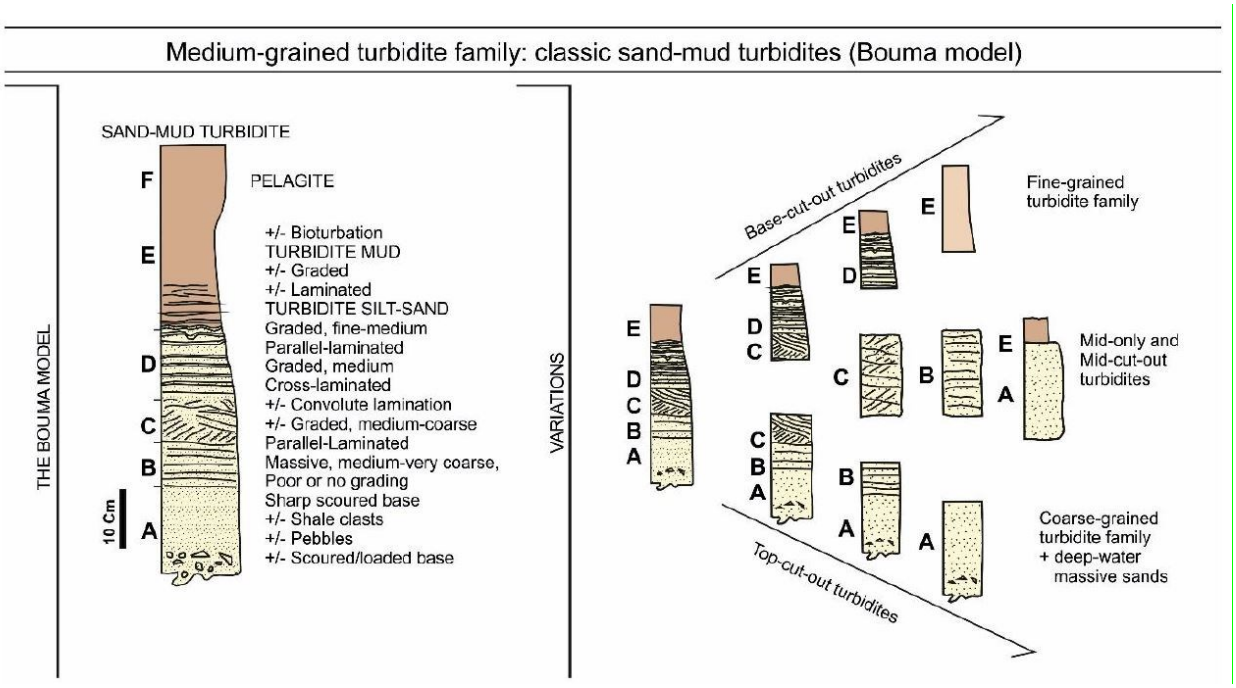

Fig. 9. The ideal Bouma's facies model showing the complete sequence of divisions A-E (Bouma, 1962), and typical partial sequences found commonly in nature, is given. F is now commonly used for pelagites above a turbidite.

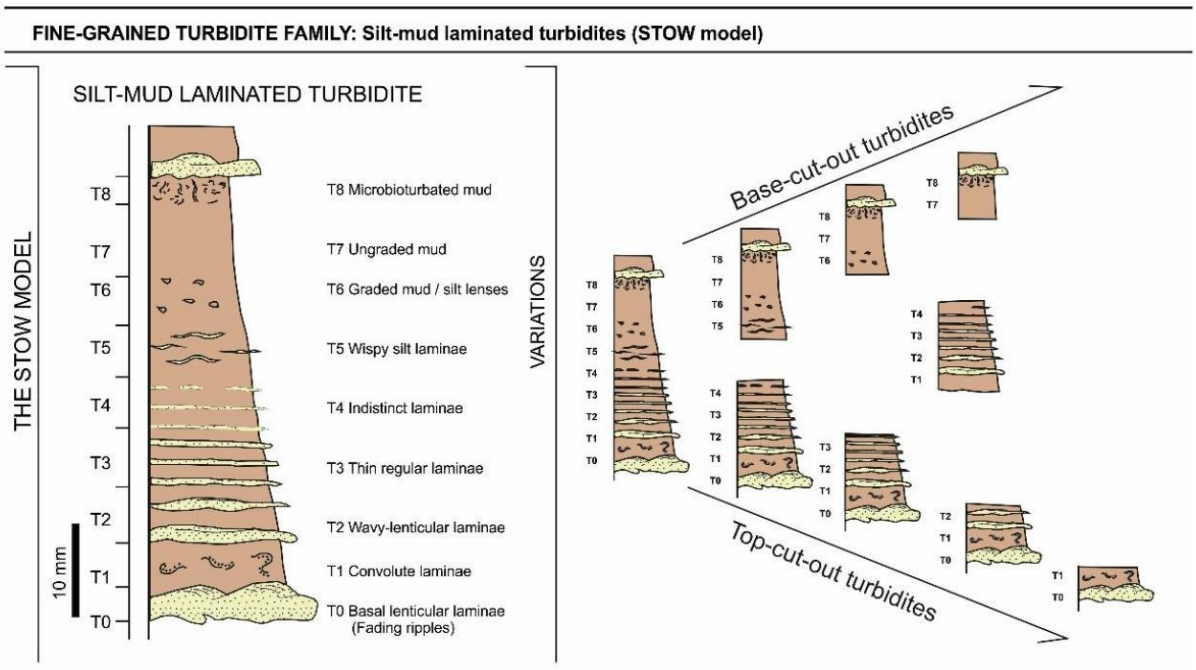

Fig. 10. The ideal Stow's facies model showing the complete sequence of divisions T_0-T_9 (Stow & Shanmugam, 1980), and typical partial sequences found commonly in nature, is given.

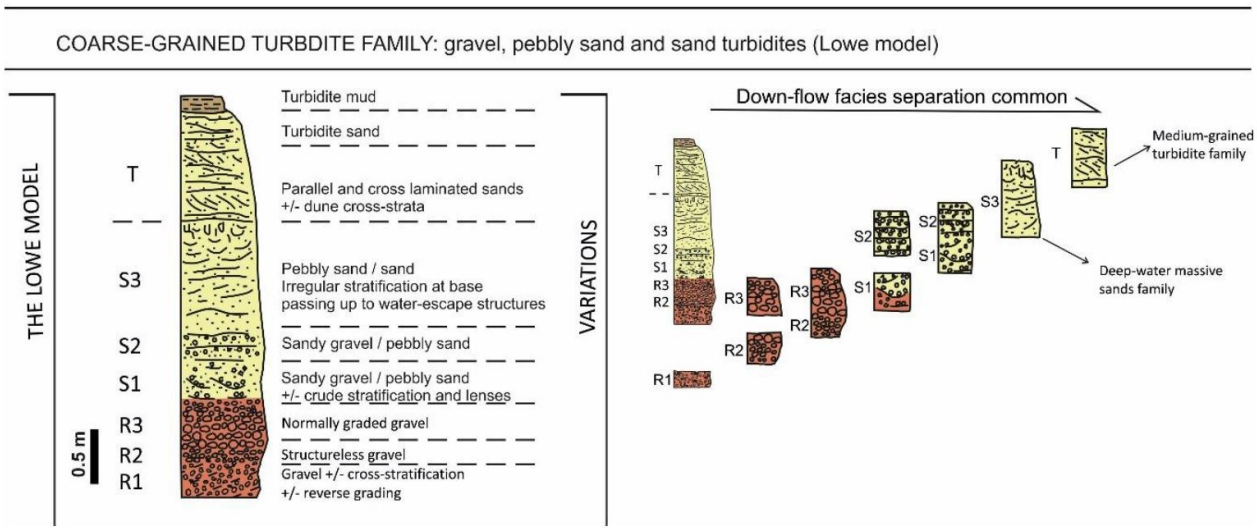

Fig. 11. The ideal Lowe's facies model showing the complete sequence of divisions R_1-S_3 covered atop by the finer-grained T interval (Lowe, 1982), and typical partial sequences found commonly in nature, is given.

In a variety of environments, such as ponded basins (Blanpied & Stanley, 1981; McCave & Jones, 1988; Tripsanas *et al.*, 2004; Marini *et al.*, 2016b), channel fill successions (Elliott, 2000; Navarro *et al.*, 2007; Felletti *et al.*, 2020), open slope and base of slope (Stow & Tabrez, 1998), and distal fan lobes (Stow *et al.*, 1990), gravel and sand beds are more abundant than silt beds and commonly occur as turbidites.

Conversely, in distal turbidite environments and channel levée overbank settings, silt beds prevail occurring as thin or medium-bedded turbidites (see Reading, 2009 and Stow & Smillie, 2020 for more details). For natural turbidite deposits, there are several variations from the standard sequences from the above-described model. These depend on flow transformations (see Section 1.1.1.1) and the actual process and rate of deposition during a single turbidity current event (Stow & Smillie, 2020).

These facies models were developed for siliciclastic systems but can be applied equally to calcareous and volcaniclastic turbidites, even though some differences were documented (e.g., Scholle, 1971; Stow *et al.*, 1984; Eberli, 1991; Schneider *et al.*, 2001).

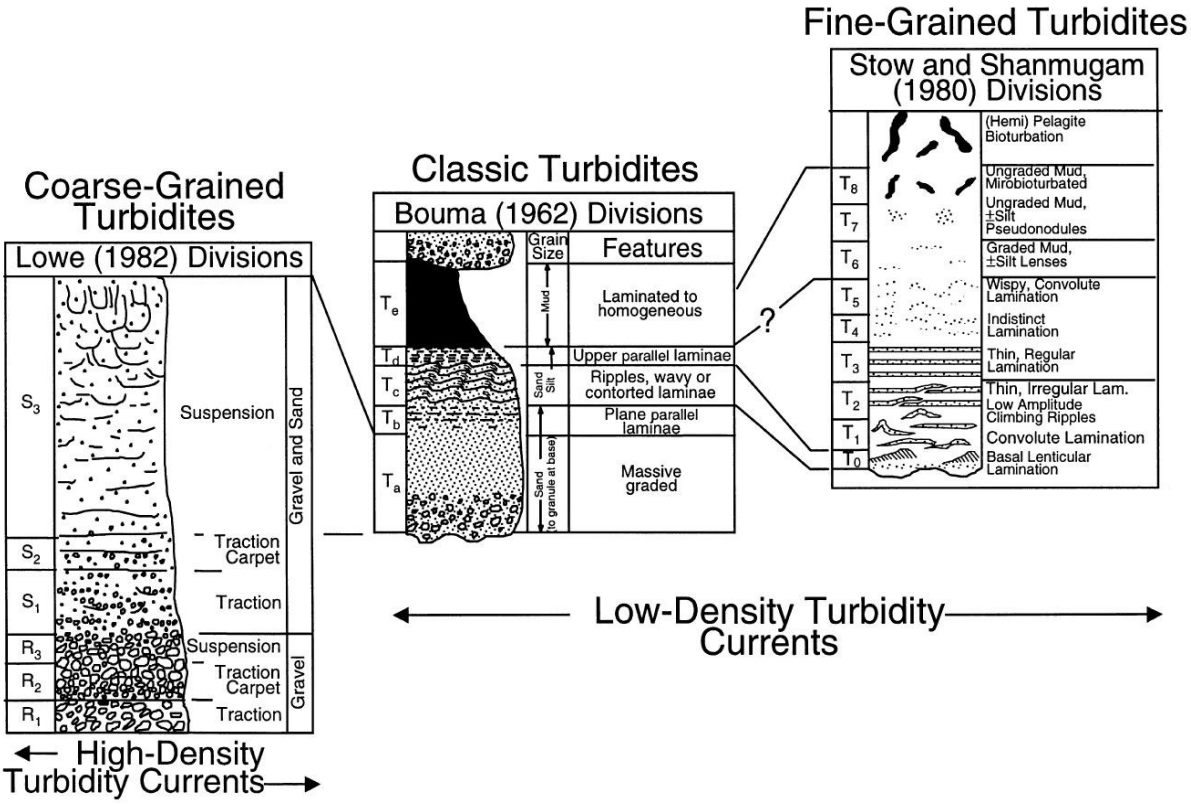

Fig. 12. Existing vertical facies models of Lowe (1982), Bouma (1962), and Stow & Shanmugam (1980). Correlation of S3 division of coarse-grained turbidites with the Ta division of the Bouma Sequence is after Lowe (1982). Correlation of various divisions between Bouma Sequence and Stow and Shanmugam sequence is after Pickering et al. (1989).

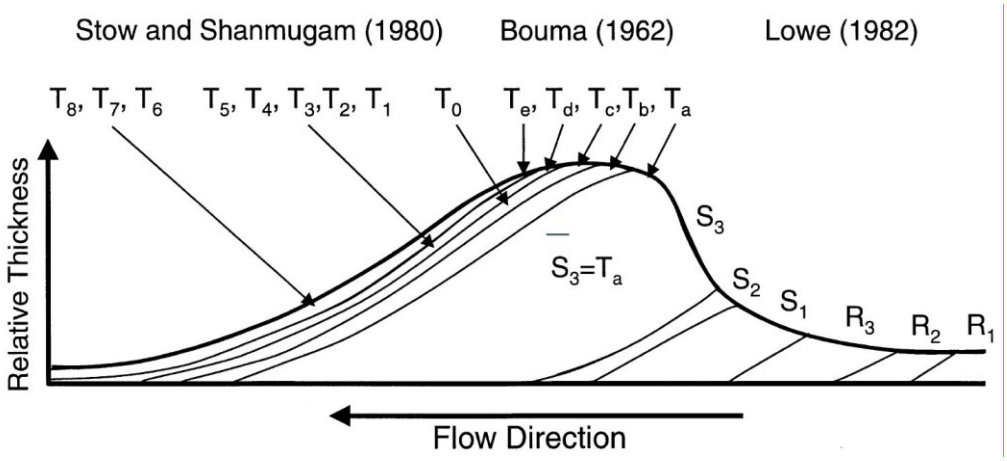

Fig. 13. A schematic diagram showing downslope changes in turbidite division from coarse-grained turbidites (Lowe, 1982), through classical turbidites (Bouma, 1962), to fine-grained turbidites (Stow & Shanmugam, 1980). A total of 16 divisions is expected from an ideal turbidite bed even though a complete sequence has never been documented. From Shanmugam (2000).

1.1.2.2. Hyper-, homo-, hypopycnal facies models

River flow discharges (conventionally hyperpycnal flows hereafter) represent one of the most direct, and abundant, way of connection with marine depositional basins (Mulder & Syvitski, 1995; Mulder *et al.*, 2003; Mutti *et al.*, 2003; Lamb & Mohrig, 2009; Zavala & Pan, 2018). Because of few direct observations available and a complex flow dynamics (see Section 1.1.1.2), hyperpycnal flow-related deposits (namely hyperpycnites) are not easily recognisable in the sedimentary record (e.g., Mulder *et al.*, 2001a; Plink-Björlrklund & Steel, 2004; Myrow *et al.*, 2008; Soyinka & Slatt, 2008; Zavala *et al.*, 2011a; Zavala & Pan, 2018).

Being related to river floods (see Section 1.1.1.2), hyperpycnal flows are characterised by an increase in energy during the waxing discharge period at the river mouth and a decrease in energy during the waning discharge period at the river mouth. This variation of flow energy develops hyperpycnites depositional units (Fig. 14). During the waxing and waning phases (*sensu* McHargue *et al.*, 2011a), a coarsening-upward basal unit (Ha in Fig. 14) and a fining-upward top unit (Hb in Fig. 14) are respectively deposited (Mulder *et al.*, 2001a, 2003). The transition between these two units occurs in correspondence of the maximum peak of the river flood (Mulder *et al.*, 2003; Plink-Björlrklund & Steel, 2004). Being this the period of maximum discharge of the river flow, the generated hyperpycnal flows have a higher energy leading to develop an erosional base for the top unit (hydrograph number 4, Fig. 14), eroding almost completely the basal unit. Based on the river discharge magnitude and time duration of the flow, this depositional pattern can be different (e.g., Zavala *et al.*, 2011), especially if they are related to catastrophic flood events following either artificial or natural dam breakings, erosion of natural dams, jökulhaups or lahar transformation (Mulder *et al.*, 2003; Plink-Björlrklund & Steel, 2004).

Typical hyperpycnal deposits are clearly sorted (Zavala *et al.*, 2011a), with the diameter of suspended clastic particles ranging from silt to very fine sand (i.e., 0.004-0.25; Wentworth, 1922) and characterised by sedimentary structures, such are ripple-cross lamination, climbing ripple-cross lamination, thin parallel laminae in the muddier part, and high content of organic matter. The presence of both sedimentary structures and sand with clear sorting indicates that flows are low-concentrated and the particle deposition is larger than the particle transport (Mulder *et al.*,

2003). The thin parallel laminae represents hydrodynamic fluctuation in the bottom boundary layer of a single flow (Hesse & Chough, 1980). The occurrence of generally high contents of organic matter, such as plant and wood fragments and pollens, indicates the close connection of this deposits to an emerged continental source area (Mulder & Syvitski, 1995; Mulder *et al.*, 2003; Zavala *et al.*, 2012).

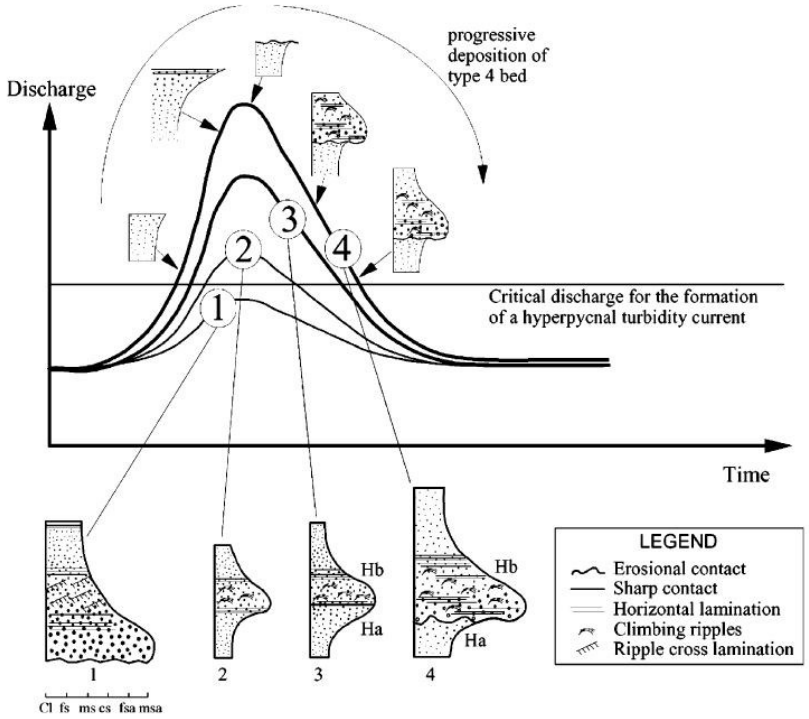

Fig. 14. Facies and sequences deposited as a function of the magnitude of the flood at the river mouth. (1) Low-magnitude flood. The maximum discharge is less than the critical discharge to produce a hyperpycnal turbidity current. Failure-induced turbidity currents are generated. (2) Low-magnitude flood. The maximum discharge is more than the critical discharge to produce a hyperpycnal turbidity current. Hyperpycnal turbidity currents are produced. A complete sequence with a transitional boundary between inversely graded unit Ha and normally graded unit Hb is deposited. (3) Mid-magnitude sequence. Identical to 2 but grain size can be coarse and sequence thicker. Sharp contact between Ha and Hb. (4) High-magnitude flood. Same as 3 but particles deposited are coarser. Erosional surface exists between Ha and Hb. Ha may have been completely eroded during the peak flood period. Cl= clay; fs= fine silt; ms= medium silt; cs= coarse silt; fsa= fine sand; msa= medium sand. From Mulder *et al.* (2003).

A further complexity for hyperpycnal deposits is represented by lower scale waxing-waning phases during a flood discharge period (e.g., McHargue *et al.*, 2011a). Many orders of waxing-waning cycles generate pulses of the flow which are reflected into hyperpycnal deposits as minor variable vertical stackings. These stackings are characterised by an erosive base overlain by coarser- and finer-grained laminae couplets, or lenses, associated to numerous intrasequential

erosional contacts (Mutti *et al.*, 2002a, 2003; Mulder *et al.*, 2003). A synthetic summary of criteria of hyperpycnal deposits in comparison with Bouma's turbidite deposits are reported in Tab. 1.

	Turbidite sequence (Bouma-like)	**Hyperpycnal sequence**
Flow type	Turbulent surge	Turbidity current
Flow behaviour	Unsteady. Mainly waning flow	Mainly steady. Waxing then waning
Flow regime	Turbulent	Turbulent
Flow duration	Minutes to days	Hours to weeks, up to months
Base contact	Erosive to sharp	Gradational
Top contact	Gradational	Gradational
Intrabed contact	Infrequent between facies	Erosive to sharp
Grading	Clear, normal	Clear, inverse then normal
Structures	Well-developed parallel- and cross-bedding, convolutes	Well-developed parallel- and cross-bedding. Climbing frequent
Fauna/flora	Allochtonous mainly marine	Allochtonous mainly continental. Frequent plant and wood fragments

Tab. 1. Recognition criteria of turbidites (surge-like deposits) and hyperpycnites. Modified after Mulder *et al.* (2003) and (Zavala & Pan, 2018).

Zavala *et al.* (2011) and Zavala & Pan (2018) proposed a facies classification for hyperpycnal deposits based on a genetic approach in order to obtain a conceptual facies tract and to predict the expected facies types in every case study (Fig. 15). Three main groups of facies related to the three main processes characteristic for all sustained hyperpycnal flows can be distinsuished: 1) facies related to bed-load processes (i.e., Facies B); 2) facies related to collapse of suspended load (i.e., Facies S); 3) facies related to flow lofting (i.e., Facies L) (Fig. 15B and C).

A *Sedimentary processes and facies*

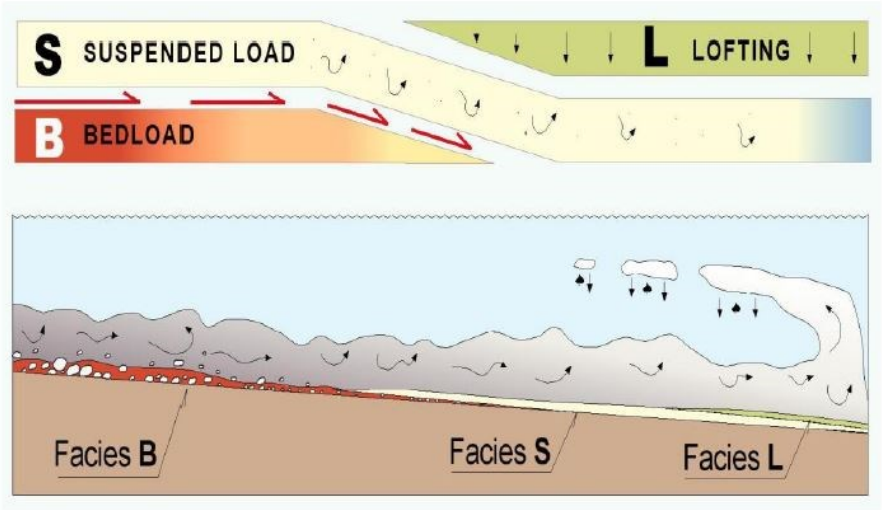

B *Longitudinal facies changes*

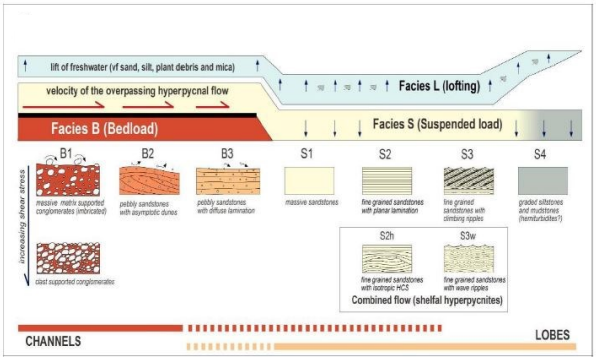

C *Lateral facies changes*

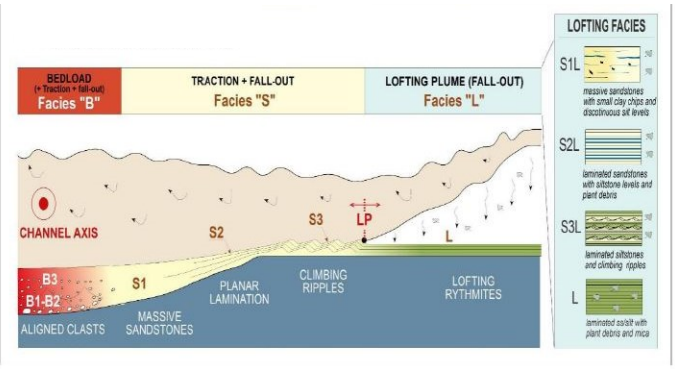

Fig. 15. Sedimentary processes and genetic facies tracts of sustained hyperpycnal flows. (A) Main sedimentary processes and related facies during hyperpycnal discharge with associated bedload. (B) Facies association along the depositional system. (C) Lateral facies changes towards flow margins. Modified after Zavala & Pan (2018).

Facies B

It includes a large specturum of corase-grained deposits representing the bedload of hyperpycnal flows (Fig. 15). The accummulation of these sediments depends on shear/drag forces exerted by the overpassing long-lived turbulent hyperpycnal flow and the partial fall-out of finer-grained suspended load trapping at the rising flow bottom (Zavala *et al.*, 2011a; Zavala & Pan, 2018). The resulting deposit has a bimodal texture due to the join coarser and finer grain-sizes, consisting of a well-sorted sand-grained background with scattered oversized clasts in the range of gravel-bulder. Coarse-grained lags may show imbrication of clasts, which can be extrabasinal (e.g., well-rounded pebbles and gravels), intra- or extra-basinal (mud-chips and clay clasts

respectively), intrabasinal (e.g., shell fragments or marine fossils), or a mixture of thereof. The finer-grained part of this facies association might be also constituted by a silty-clayly matrix. As the content of gravel-grained clasts decreases, the occurrence of large-scale climbing dunes, or anti-dunes, increases (Zavala *et al.*, 2011a).

Three main categories of facies were distinguished for this association (Fig. 16), B1, B2, and B3, from the more proximal to the more distal. The downcurrent transition from B1 to B3 is characterised by a decrese in grain-size.

Flow dynamic: coarser-grained clasts are deposited by the progressive loss of competence of the flow, which becomes unable to trasport larger clasts by saltation, sliding and rolling. Rolling can give imbrication of clasts since non spherical clasts tend to rest in stable position. Furthermore, imbrication suggests that large clasts were free to move by rotation at the base of an overpassing non-cohesive turbulent flow, indicating that the flow was fluid (Zavala *et al.*, 2011a). The occurrence of extrabasinal coarse-grained clast components suggests that badload was probably inherited from the original riverine discharge (Zavala & Pan, 2018).

Conversely, the finer-grained clasts would correspond to suspended material trapped in the low-velocity and relatively high-concentrated part of the turbulent hyperpycnal flow (Fig. 16).

Large-scale bedforms indicates that flows are in a high regime state (McCracken, 1969; Pickering *et al.*, 1986; Reading, 2009).

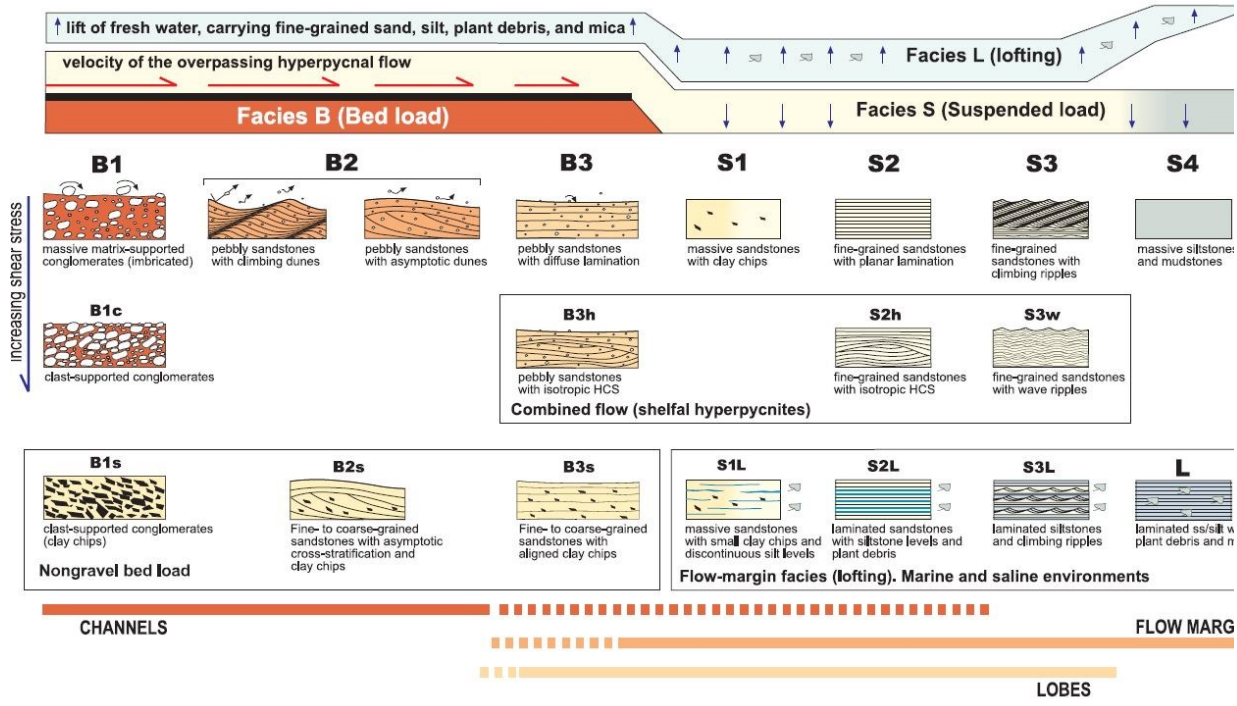

Fig. 16. A detail of Fig. 15B. Conceptual scheme for the genetic classification of clastic facies for turbulent hyperpycnal flow deposits. Facies B: it relates to bedload processes at the base of an overpassing long-lived turbulent flow. Facies S: it originates from the gravitative collapse of sand-size suspended materials carried in the turbulent flow. Facies L: it is composed of very fine-grained sandstones interbedded with laminated silts with abundant plant debris and micas, accumulated by fall-out from lofting plumes. HCS= hummocky cross-stratification; ss/silt= sandstone/silt. From Zavala *et al.* (2011a).

Facies S

It mostly consists of fine-grained sediments, from sand to silt, forming thick and internally complex tabular beds that can be either massive with subtle grain-size variations or characterised by traction plus fall-out sedimentary structures, such as plane parallel- and ripple-cross laminations, sometimes also convoluted (Zavala *et al.*, 2011a). Particularly, the silty part can display an erosional basal boundary, characterised by flames and cyclic grain-size changes (Zavala & Pan, 2018). This facies association is typically rich in carbonaceous remains, charcoal and woody fragments, often displaying fully-preserved leaves (Plink-Björlrklund & Steel, 2004; Zavala *et al.*, 2012). Some intervals are characterised by ichnotaxa, such as Ophiomorpha and Thalassinoides (Buatois *et al.*, 2011). Four facies were distinguished for this facies association: S1, S2, S3, and S4 (Fig. 16). The downcurrent transition from facies S1 to facies S4 is characterised by a decrease in size of both sediments and organic remnants, and likely represent

a transition from a Bouma-like T_a to T_d (see Section 1.1.2.1). These facies are ofter superimposed on each other giving a cyclic alternance (Zavala & Pan, 2018).

Flow dynamic: sediments are transported as suspended load (Fig. 16) within a sustained turbulent hyperpycnal flow and accumulated by gradual gravitational collpase as the flow wanes losing transport capability (Zavala *et al.*, 2011a; Zavala & Pan, 2018). The origin of this facies association is related to the progressive aggradation from the bottom by means of long-living flows characterised by a high suspended load (Sanders, 1965; Kneller & Branney, 1995; Camacho *et al.*, 2002), such as the hyperpycnal flows. This process inhibits the formation of sedimentary structures and leads to high rates of fall-out tapping organic remains and plant debris in a massive deposit (i.e., S1 in Fig. 16).

The parallel-laminated part (i.e., S2 in Fig. 16) of this facies association is the result of traction plus fall-out processes (Sanders, 1965; Simons *et al.*, 1965; Sumner *et al.*, 2008). On the other hand, the transition to the rippled part (i.e., S3 in Fig. 16) represents a decrease in flow velocity leading to a subsequent increase in the fall-out rate (Sumner *et al.*, 2008 and references therein). Because of the pulsating nature of hyperpycnal flows (see Section 1.1.1.2), the increase in fall-out rate is cyclic producing the above-mentioned alternation of these facies. Finally, the silty part (i.e., S4 in Fig. 16) of this facies association, characterised by an erosional base and flame structures, is the result of deposition by fluid flows capable of eroding the not-yet consolidated substrate. Furthermore, grain-size breakes are indicators of the pulsating character of these flows (Zavala *et al.*, 2011a; Zavala & Pan, 2018).

Facies L

It consists of centimetre- to decimetre-thick, normal graded, thin-bedded sandstone-siltstone couplets, with grain sizes ranging beteween fine/very fine-grained sand and fine-grained silt, typically rich in plant debris and micas forming bounding surfaces layers (Petter & Steel, 2006; Zavala *et al.*, 2012). Sometimes load cast structures occur commonly associated to syneresis cracks and siderite nodules (Zavala *et al.*, 2011a; Zavala & Pan, 2018). Ichnotaxa are rare and mostly limited to some *Palaeophycus* (Buatois *et al.*, 2011).

This type of bedsets are known as *rhytmites* in literature (e.g., Zavala, 2008 and references therein).

Flow dynamic: the absence of tractive structures in the sandy part suggests an accumulation by normal settling from a suspension load cloud in the water column (Fig. 16). The vertical alternation of couplets suggests that they are the result of several pulsating hyperpycnal flows producing the relative pulsating lofting clouds (Zavala *et al.*, 2011a).

Intentionally blank page

CHAPTER II

Introduction to turbidite systems

Intentioanlly blank page

2. Introduction to turbidite systems

This chapter provides background information on turbidite systems, both for shallow water and deep-water depositional environments, and their component architectural elements.

A general overview of the main classifications of the different components of turbidite systems is reported. Firstly, a general overview of the different type of turbidite systems and their component architectures is provided by following an historical perspective. Subsequently the different types of turbidite systems and their depositional elements are explained, with particular regards to submarine channel belts and hyperpycnal systems, which represent the main topics of this work.

2.1. Turbidite system models

From 1950s onwards, both outcrop and seismic studies of ancient turbidite deposits and marine geomorphological observations of modern turbidite accummulations have been conducted in order to infer depositional processes and dynamics. Different evolutionary models arose by pursuing these research lines (Normark, 1970; Mutti & Ghibaudo, 1972; Mutti & Ricci Lucchi, 1974; Mutti & Ricci Lucchi, 1975; Mutti & Normark, 1987, 1991; Posamentier & Vail, 1988; Normark *et al.*, 1993; Mutti *et al.*, 2003; Sprague *et al.*, 2005; Flint *et al.*, 2008; Sumner *et al.*, 2012; Pickering & Cantalejo, 2015; Talling *et al.*, 2015; Cullis *et al.*, 2018; Catuneanu, 2020) for both ancient and modern turbidite accummulations. These models are constantly updated to include all the possible controlling depositional processes and architectures.

According to the above-mentioned models, different types of depositional elements and characteristic facies associations were distinguished for turbidite accumulations. These include: 1) major erosive features (slump-scar) and feeder canyons; 2) channels; 3) overbank deposits; 4) channel-lobe transition deposits; 5) lobes, and 6) basin plain deposits. Furthermore, a large volume of turbidite accumulations is represented by exceptional events related to instability phenomena of the slope, such as 7) megaturbidites and 8) mass-transport deposits (MTDs hereafter). These depositional elements are included withinin a sediment transfer zone and in a sediment depositional zone (Fig. 17).

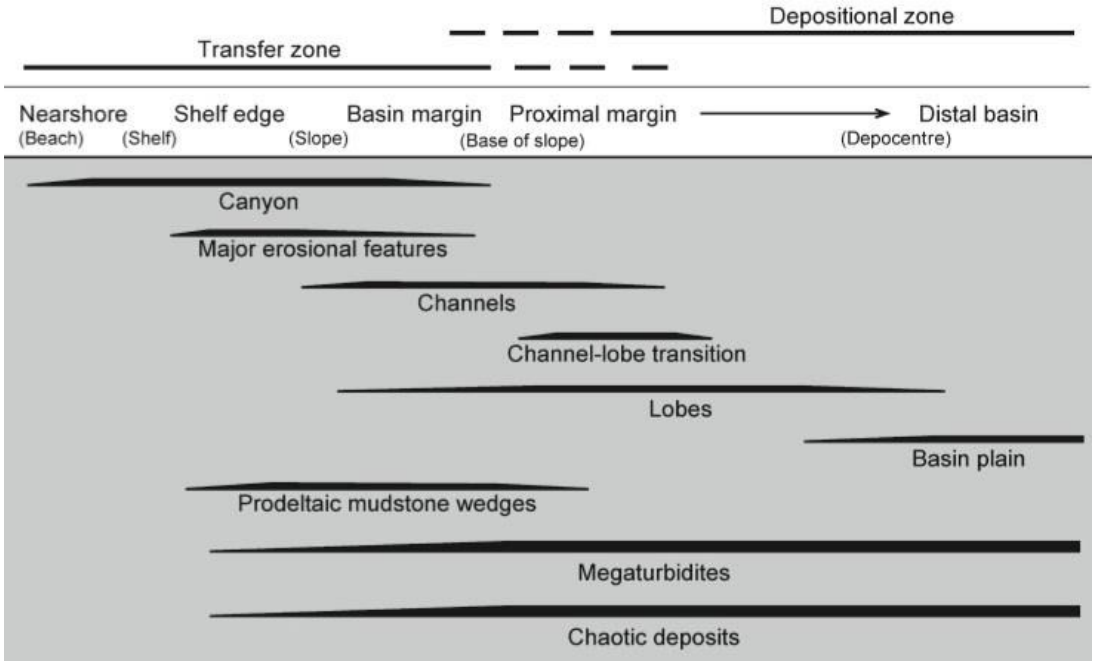

Fig. 17. Main depositional elements of turbidite systems and their distribution with respect to the transfer and depositional zones (Mutti *et al.*, 2009).

The extension and shape of a turbidite system, as well as the type of facies and geometires of depositional elements, are strongly dependent on the type of system and the geodynamic context in which they develop (Mutti & Lucchi, 1975; Mutti, 1992; Reading, 2009).

According to Normark (1970) and Mutti & Ricci Lucchi (1972), a deep-water turbidite system can be subdivided in theree different regions: the inner fan, the mid-fan, and the outer fan. The inner fan represents the most proximal, i.e. up-dip, part of the system and is composed of the main transfer conduit. The mid-fan represents an intermediate sector chiefly hosting distributary channels and associated levées (*cf*. suprafan in Normark, 1970). The outer fan hosts depositional lobes and is characterised by a rather flat geometry.

Furthermore, Mutti (1979) proposed two different types of submarine turbidite fan systems, distinguished on the basis of the ability of flows to travel downstream and efficiently segregate grain sizes in space (i.e., flows efficiency). The term ‘highly efficient’ is used to refer to mud-rich turbidite fans, which are characterised by distributary channels in the innermost sector and detached depositional lobes in their outermost sector. These channels progressively disappear downstream into basin plain turbidite deposits. On the other hand, the term ‘poorly efficient’ is used to refer to

sand-rich turbidite fans, which are typically characterised by a suprafan, which is physically linked to the main feeding conduit.

Shanmugam & Moiola (1985, 1988) proposed a classification for modern submarine fans consisting of two end-members: 1) fine-grained delta-fed elongated turbidite fans and 2) radial fans receiving coarse-grained sediments from poorly efficient flows. However, it is recognised by these Authors that the geodynamic setting of the sedimentary basin plays a major role in controlling fans physiography and relative architectures, leading to increase the variability of this exemplary classification. In fact, as demonstrated also by Reading & Richards (1994) and Richards *et al.* (1998), the physiography of submarine fans and depositional architecture depend on the interplay among different factors, such as the feeding system, size and features of the catchment area, and grain sizes of sediments.

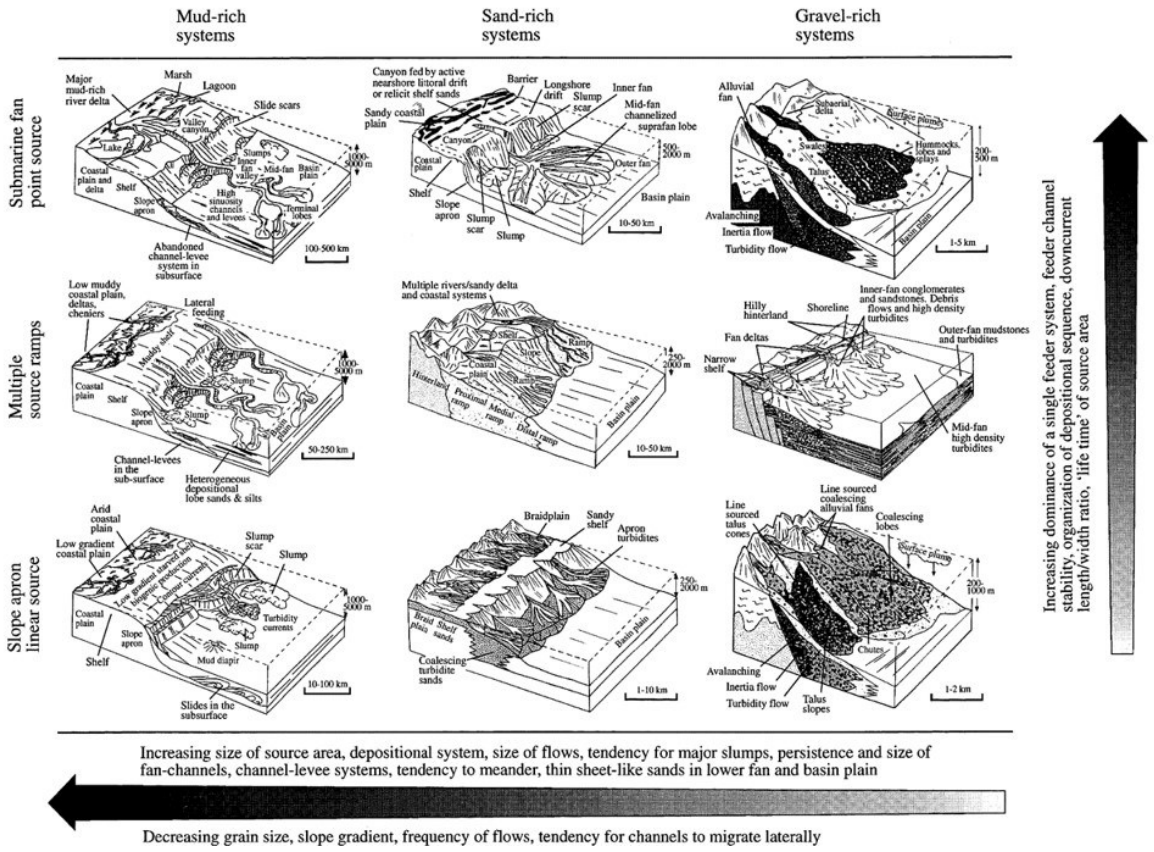

Fig. 18. Summary environmental models for submarine fans, ramps and slope-apron systems, classified on the basis of volume and grain size of available sediment and nature of the supply system (i.e., number of input points) (from Stow & Mayall, 2000)

Based on the type of feeding system and grain size of sediments, three main categories of deep-water systems were defined (Reading & Richards, 1994; Richards *et al.*, 1998): 1) single point

source submarine fan; 2) multiple-source submarine ramps; and 3) linear-source slope aprons (Fig. 18). Other fundamental synthesis of the many concepts were provided by Reading & Richards (1994), Richards *et al.* (1998), and Bouma & Stone (2000), who stressed how grain size, size and relief of the catchment area inland of deep-sea clastic systems, and the geodynamic context are the main controls on physiography and depositional architectures of submarine fan systems.

It follows that on the basis of the sediment load transported and deposited by turbidite gravity flows, three types of submarine systems are categorised (Richards *et al.*, 1998): 1) coarse-grained sand-rich systems; 2) fine-grained mud-rich systems; and 3) sand/mud-rich systems (Fig. 19). The coarse-grained systems are generally located along active margins with narrow shelves, typically deeply incised by canyons and fed by low-efficiency flows. These flows tend to deposit their load at the base of the slope (Fig. 19A). On the contrary, fine-grained systems typically occur on passive margins characterised by broad shelves and are fed by high-efficiency flows originating in front of deltaic systems (Fig. 19C). Finally, the sand/mud-grained systems represent the intermediate category between the above-described ones (Fig. 19B).

Also in this classification (Richards *et al.*, 1998), upper, middle, and outer fan sectors are distinguished with few amendments compared to Normark (1970). The upper fan hosts a feeding channel branching downstream into a more complex channel network. The middle fan is charcterised by channels with their correlative levées and intervening overbank deposits. Finally, the outer fan hosts sheet sand deposits or depositional lobes.

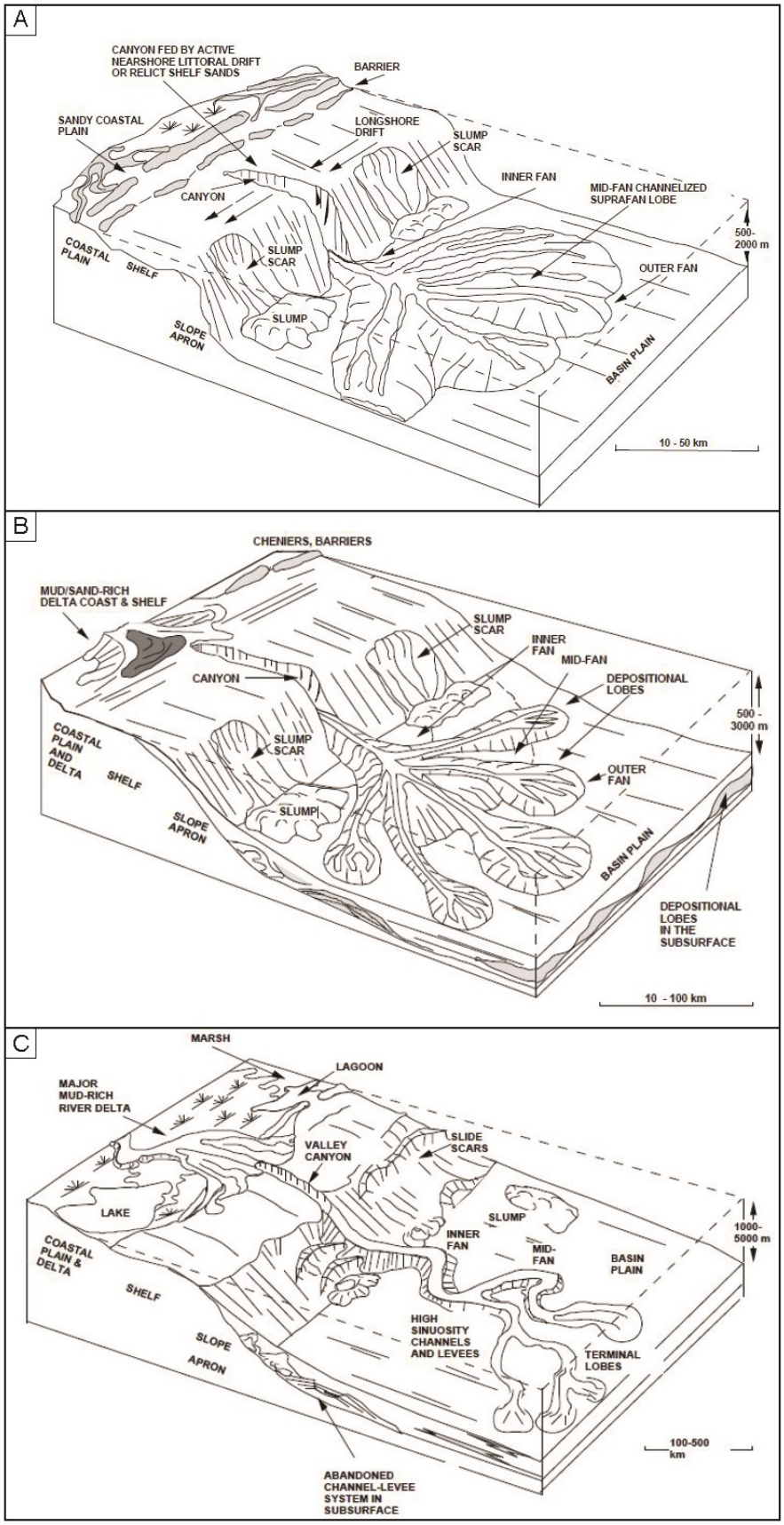

Fig. 19. Summary of depositional models for submarine fans based on the different types of source terrains. (A) Depositional model for a point-source sand-rich submarine fan; (B) Depositional model for a point-source mud/sand-rich submarine fan; (C) Depositional model for a point-source mud-rich submarine fan. From Reading & Richards (1994).

2.1.1. Turbidite systems and their depositional elements

In order to distinguish between ancient and recent systems, the term ‘Turbidite System’ was introduced by Bouma and co-authors in 1985 (Bouma *et al.*, 2012).

The gap between the description of ancient and recent turbidite systems dwells in the nature and geometrichal-temporal scale of observations. The description of modern turbidite systems is fundamentally based on their current morphologies at large scale without taking into great account data about their facies, which remain scarsely represented. Conversely, outcrop examples allow to look in detail within turbidity system deposits and their facies (down to the scale of a single lamina), resulting into a good control on sedimentation evolutionary processes.

However, due to their not always excellent preservations, outcrops do not represent suitable cases to study large scale and 3D geometrical architectures in the most of cases.

In order to fill the gap between these two analytical scales, the integration of seismic data with outcrop data, and *viceversa*, is fundamental for capturing the complex interplay of control factors on sediment gravity flow depositional processes.

Aiming at categorising and assigning order to otherwise complex turbidite systems, characterised by variable spatial and temporal evolution, several classifications schemes have been proposed through time (see Cullis *et al.*, 2018 for a review).

Among these schemes, Mutti (1985) introduced a first classification (Fig. 20) consisting of three types of turbidite systems, which distinction is based on the *locus* of sand bulk deposition as function of grain size and volume of sediment supply for passive margin turbidite basins.

The Type I (Fig. 20) corresponds to the ‘high-efficiency’ submarine fans described in Section 2. Turbidite fans are characterised by thick-bedded sandstones lobes passing downcurrent to thin-bedded sandstones and mudstones lobe fringes. Typically depositional lobes are deposited downcurrent of a large-scale erosional form (i.e., canyons) and a well-developed channel belt transfer zone completely lacks. As reported in the literature (e.g., Mutti, 1979, 1985, 1992; Reading & Richards, 1994), this type of turbidite systems are common in correspondence of passive margins or in large foreland system basins, in which they are part of elongated and laterally extensive turbidite accumulations.

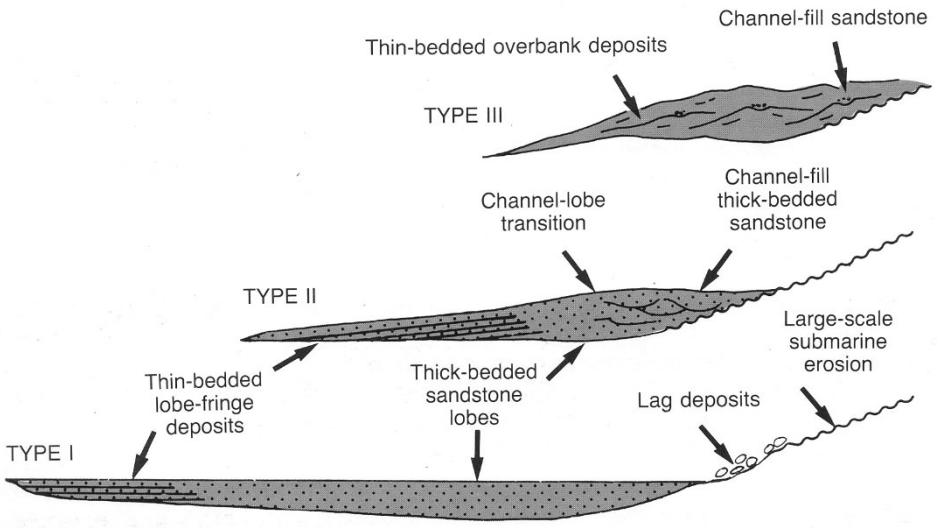

Fig. 20. Main types of turbidite systems. From Mutti (1992).

The Type II (Fig. 20) corresponds to the 'poorly-efficiency' submarine fans described in Section 2. Turbidite fans are characterised by a back-filled channel belt characterised by thick-bedded sandstones passing downcurrent to coarse-grained channel-lobe transition deposits in their proximal sector. These turbidite fans terminate by fringing downcurrent into poorly-developed depositional lobes.

Finally, the Type III (Fig. 20) is represented by fine-grained thin-bedded turbidites deposited in the proximal reach of channels, between channels as overbank or on muddy slopes, and would develop close to the slope. The feeding of this type of turbidite fans would be directly linked to fine-grained deltaic systems (e.g., Heller & Dickinson, 1985; Mutti *et al.*, 1994, 1996, 2003; Plink-Björlrklund & Steel, 2004; Gobo, 2014; Gobo *et al.*, 2015; Chen *et al.*, 2016).

These three types of submarine fan systems can be vertically stacked (i.e., from Type I to III) in response to relative sea-level changes. The transition from voluminous lobe accumulations (i.e., Type I) to consistent overbank deposition (i.e., Type III) would record the change from lowstand deposition on the basin floor to gradually finer-grained and less voluminous sedimentation in base-of-slope and slope environments depending on a relative sea-level-rise (Posamentier & Allen, 1999; Catuneanu, 2020).

Despite this classification is functional for turbidite systems developed along passive margins, it has to be applied with caution in foreland turbidite basins because of the interplay between tectonic subsidence (or uplift) and eustasy, which influences relative sea-level changes (Posamentier &

Allen, 1999; Catuneanu, 2020). Furthermore, also major depocentre shifts related to thrusts propagation and structurally-related topographic lows/highs (e.g., Artoni *et al.*, 2000; Tinterri & Muzzi Magalhaes, 2011; Tinterri & Tagliaferri, 2015; Tinterri & Piazza, 2019), halokinesis (e.g., Tripsanas *et al.*, 2004; Alves *et al.*, 2009; Kane *et al.*, 2012), and mass-wasting deposition due to tectonic instability (e.g., Alves *et al.*, 2014; Bull *et al.*, 2020; Tek *et al.*, 2020, 2021) may control along dip deposition of turbidite systems affecting their degree of confinement and preventing the full deposition of their architectural elements.

Therefore, studying turbidite systems implies the recognition and correlation of both erosional and depositional architectural elements which are composed of peculiar facies associations. On the basis of the facies pattern, and depositional and erosional features, three main sectors of a turbidite system can be distinguished: 1) channels; 2) channel-lobe transition; and 3) lobes (Mutti & Normark, 1987; García *et al.*, 2015). The transition from the first sector to the third sector along the turbidite system is by nature accompanied with a decrease in grain-size and thickness of event beds.

Particularly, the channels sector is characterised by both canyons and channel elements, or channel fill deposits, with correlative levées and overbank areas, that traverse slopes and basin floors conveying sediments, organic matter, and pollutants transported by gravity flows. Deposits are typically coarser-grained and characterised by erosional features (Mutti & Lucchi, 1975; Mutti, 1992; Peakall & Sumner, 2015; Kane & Clare, 2019).

The lobe zone is composed of non-channelised bodies representing the outboard of a stable fan valley and accumulating typically lobate-shaped, thin-bedded and finer-grained, deposits (Mutti & Ghibaudo, 1972; Mutti & Lucchi, 1975; Mutti, 1992; Prélat *et al.*, 2009; Prélat & Hodgson, 2013; Bell *et al.*, 2018).

Consequently, the channel-lobe transition is defined as a region separating well-defined channel elements, or channel fill deposits, from well-defined lobes, or lobe facies, exhibiting some characteristics of both channels and lobes (Mutti & Lucchi, 1975; Mutti, 1992; Reading, 2009).

The lateral extension of these zones, along with their facies types, is a function of both the grain-size of sediment load and sedimentary input rates (Mutti & Ghibaudo, 1972; Mutti & Lucchi, 1975; Mutti, 1992; Reading, 2009; McHargue *et al.*, 2011a; b).

Looking at the meaning of architectural elements, canyons and channels are defined as long-lived sediment fairways which are traversed by gravity flows from the source to the sink. They have a typical irregular shape and represent the main erosive features of the turbidite system.

Canyons have steep sidewalls, cutting into the underlaying bedrock or relatively recent sediments, and are characterised by several processes through time, such as regressive erosion and sidewall failures (e.g., Gillet *et al.*, 2013; Petit *et al.*, 2015; Sulli *et al.*, 2021). In recent depositional systems they are either frequently linked to rivers, deltas and fan-deltas or directly fed by long-shore currents (e.g., Burke, 1972; Heller & Dickinson, 1985; Collinson, 1986; Neuberger, 1987; Plink-Björlrklund & Steel, 2004; Wan *et al.*, 2020).

Channels architecture and depositional processes broadly vary, especially in modern systems. They can occur as freestanding elements or give rise to either braided-like channel belts of relatively short-lived channels or meander-like channel belts as function of gradient and grain size carried by flows. Overall, channel belts can be dominantly erosional, depositional, or can be a combination of thereof (Janocko *et al.*, 2013).

Given their relevance to the subject of this work, channel belts and their features in terms of facies and architectures will be described in Section 2.1.2.

Opposite to canyons and channels, levées and overbank areas, as well as mounds and lobes or sheets, represent the main depositional architectural elements in the turbidite system (e.g., Reading, 2009 and references therein; García *et al.*, 2015; Piazza & Tinterri, 2020; Zhang & Li, 2020; Fryer *et al.*, 2021). These are related to overbank deposition (Peakall *et al.*, 2000) in both modern and ancient turbidite systems, and they are typically constituted by thin-bedded and fine-grained sandstone-mudstones couplets and/or monotonous pattern of graded mudstones where slumps are relatively common (e.g., Morris & Busby-Spera, 1990; Cronin *et al.*, 2000; Palozzi *et al.*, 2018). Well-structured levées are common in large modern mud-rich fans and appear to be less common in ancient turbidite systems, either because they can be mistaken in some cases for

distal turbidite deposits (Mutti & Normark, 1991) or because of their low preservation potential (Reading, 2009).

Depositional mounds and sheets occur in either proximal or distal sectors of both modern and ancient turbidite systems, showing a more irregular geometry compared to levées .

Mounds have irregular shape and are deposited by accumulation of slides, slumps and debris flow masses in the lower slope or proximal sector of turbidite systems. They display a typical chaotic facies association, both in outcrop and in seismic imaging (Reading, 2009 and references therein). Among the depositional mounds in modern systems, elongate drifts are built up by long-term currents showing a more regular mounded relief. Such deposits are found along passive margins swept by strong geostrophic currents and are rarely described, often controversially, from ancient turbidite systems (Reading, 2009).

Differently from mounds, sheets are smaller, wider than thicker, in volume and mainly represented by interbedded fine-grained turbidites and hemipelagites occurring in the interchannel areas, open slopes and basin plain systems (Booth *et al.*, 2000; Sullivan *et al.*, 2005; Dailly *et al.*, 2013; Mayall & Kneller, 2021).

Finally, the transition from channels to depositional lobes can be seen as the hinge point between a sector where erosion and deposition alternate in time and a mostly depositional sector. Such transition corresponds with a major gradient break along the depositional profile system, constituting the turning point from an erosive waxing flow to a waning flow, which loses competence moving downcurrent. Depositional lobes are composed of an association of both non-channelised and channelised sandstone facies building up lobate shape geometries (Mutti & Ghibaudo, 1972; Mutti & Lucchi, 1975; Mutti, 1979). The 3D geometry and internal architectures of turbidite depositional lobes mostly depends upon the dynamic of flow evolution downstream of channel mouths (Kneller, 1995) and on basin size and seafloor morphology (Deptuck & Sylvester, 2018). Lobe deposits typically consist of sandstones and mudstones organised in thickening-upward trends, which are interpreted as the result of compensation cycles of progressive smoothing of depositional bulges (i.e., such those associated to sand lobes themselves) (Mutti & Sonnino, 1981).

2.1.2. Submarine channel belts

A submarine channel is defined as a conduit formed by and conveying sediment gravity flows. These channelised flows typically deposit both inside and outside the conduit, which may migrate. The resulting channel body is referred to broadly as *channel belt* (Fig. 21; *cf*. with Bridge, 2003). Different types of channel belts were distinguished in the literature (Kane & Hodgson, 2011; Janocko *et al.*, 2013) based on their planform, cross-sectional geometry and range of architectural elements: 1) *erosional channel belts* (Fig. 21A); 2) *meandering channel belts* (Fig. 21B); 3) *levéed channel belts* (Fig. 21C); and 4) *hybrid channel belts*.

Erosional channel belts are those resulting by the simple downcutting and vertical aggradation of their deposits. Meandering channel belts are those showing significant lateral accretion and conduit sideway migrations. Levéed channel belts are those characterised by detectable levées confining a relatively stable channel conduit. Finally, hybrid channel belts represent a mixed type composed of a combination of the three above-mentioned channel belts and for such reason they will not be addressed in the following subparagraphs.

Within a channel belt, the deepest axial zone of the channel is referred to as the *channel thalweg* (*cf*. with Bridge, 2003). This does not correspond to the planar view geometrical axis, or centreline, of the channel (Fig. 21D). Properly, channels have also a sinuosity index, which can be referred to either the entire channel or an its particular segment. The sinuosity index is defined as the ratio of the centreline length to the corresponding straight-line distance (Bridge, 2003). If the *sinuosity index* is higher than 1.05, then a channel is considered sinuous (Reimchen *et al.*, 2016). Other geometrichal parametres useful to describe channel morphologies are the 1) *channel width* (Fig. 21D), considered to be the maximum local distance between the channel banks; 2) *channel depth*, measured as the vertical relief from the channel base in axial zone to the bank or levée crest; 3) *channel bend amplitude* (i.e., radius of curvature), defined as the maximum departure of channel centreline from a straight-line path through the centreline inflection points (Fig. 21D); 4) *channel bend half-wavelenght*, defined as the distance between centreline inflection points measured along the channel centreline (Fig. 21D).

The channel belt can be either contained within a submarine incised valley (*sensu* Prather *et al.*, 2000; Prather, 2003), representing a submerged conduit deeper than the channel belt and cut into the underlying slope deposits by means of erosive gravity flows, or not. The incised valleys containing the channel belts are bordered by levées, named *external levées*. Instead, levées that flank the channel belt, or a single channel, are named *internal levées* (Kane & Hodgson, 2011; Janocko *et al.*, 2013; Mayall & Kneller, 2021).

In such a case, being contained within an incised valley, a channel belt is defined as *erosionally confined* (Fig. 21A). Differently, a channel belt confined laterally by the external levées is defined as *levée confined* (Fig. 21C and F) (Kane & Hodgson, 2011; Janocko *et al.*, 2013). If the channel belt does not show any lateral confinement, neither by levées nor by valley flanks, it is defined as an *unconfined channel belt* (Janocko *et al.*, 2013).

Moreover, different types of channel belts can be vertically associated showing a stacking upon one another, with or without significant offsets, recording a multiphase evolution of the turbidite system through time. These associated channel belts constitute the *channel belt complex* (Janocko *et al.*, 2013), which can be either confined within an incised valley (i.e., valley-fill complex, Fig. 21E) or unconfined (i.e., *unconfined channel belt complex*, Fig. 21G). If more channel belt complexes are stacked, even though they are either confined within an incised valley or unconfined, they defines a *channel belt complex set* (*cf*. with Sprague *et al.*, 2005; Janocko *et al.*, 2013). A channel belt complex set confined within an incised valley is named as *valley-fill complex set* (Fig. 21H). On the other hand, a channel belt complex set not confined within an incised valley is named as *unconfined complex set*.

In the following paragraphs, the different types of channel belts will be described with particular regards on meandering channel belts, which represent the topic of this work.

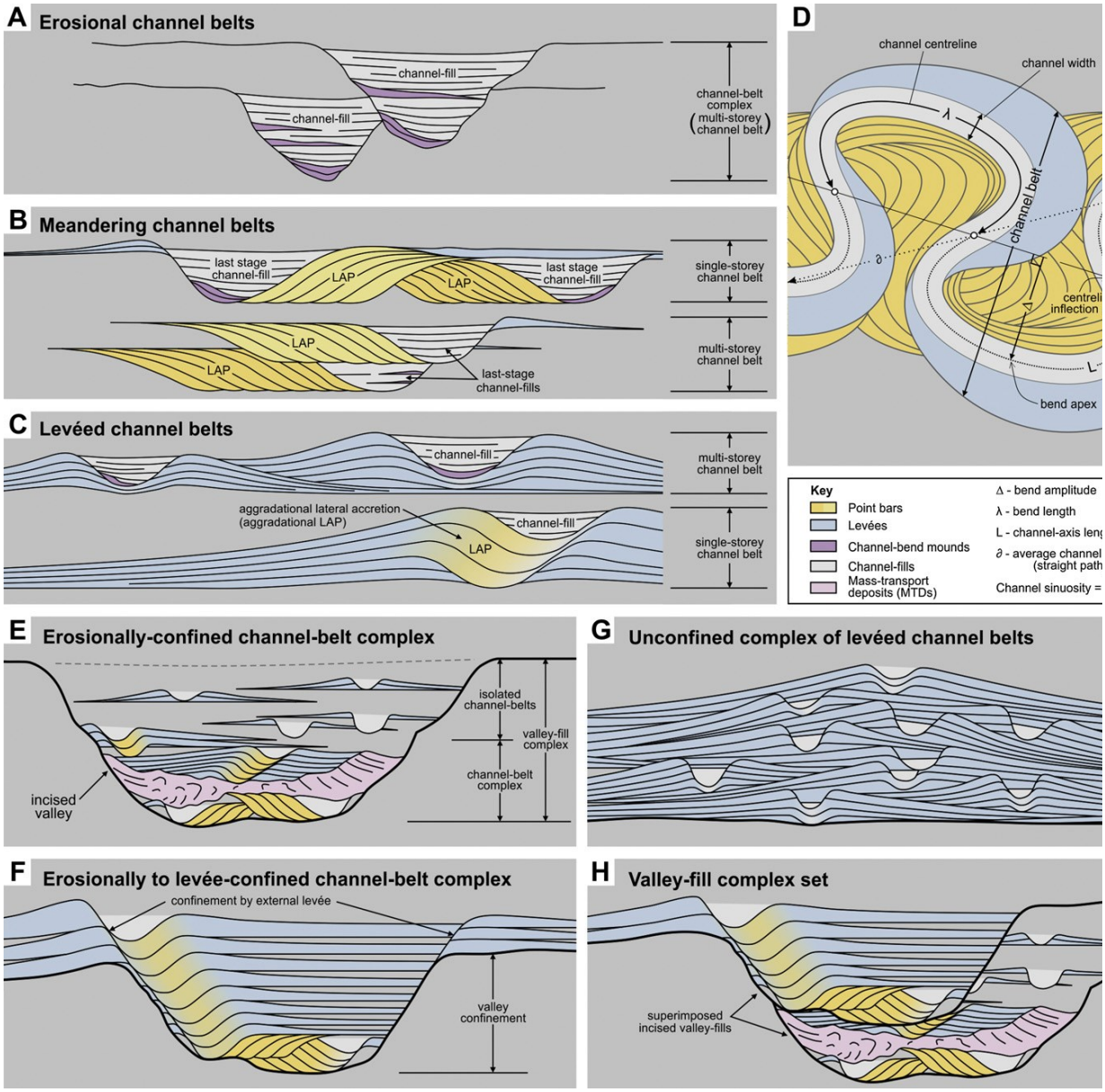

Fig. 21. Schematic diagrams illustrating basic terminology used for channel belts. (A) Erosional channel belts. (B) Non-aggradational meandering channel belts. (C) Aggradational levéed channel belts. (D) Descriptive geometrical parameters of sinuous channel planform. (E) Erosionally confined channel-belt complex. (F) Erosionally to levée-confined valley-fill complex. (G) Unconfined complex of vertically offset-stacked levéed channel belts. (H) Valley-fill complex set. From Janocko *et al.* (2013).

2.1.2.1. Meandering channel belts

Meandering channel belts are typically well detected in modern turbidite systems or in seismic maps, and are characterised by a high sinuosity conduit (i.e., > 1.2, Reimchen *et al.*, 2016), regular and smoothly curved meander bends, which show evidence of cut-offs (e.g., Janocko *et al.*, 2013). Channels in a meandering channel belts can display a complex architecture reflecting different evolutionary trends and can be highly heterogeneous in terms of channel fill facies (Kolla *et al.*, 2007; Janocko *et al.*, 2013; Gong *et al.*, 2020; Mayall & Kneller, 2021). Based on the

curvature direction of the channel bend, an inner and an outer bank can be recognised as representing the accreted bank and the eroded bank, respectively.

The most characteristic feature in meandering channel belts deposits is represented by lateral accretion packages (LAPs hereafter) on the inner bank of the channel bend. LAPs appear as closely-spaced to discontinuous and offlaping shingle-stratified channel fills, which are detectable both at seismic scale (if they are thicker than the seismic tuning thickness) and outcrop scale. In the most of cases, LAPs geometry is sigmoidal with planar base and top, although the lateral migration of the channel thalweg frequently involves uneven scouring and can result in local morphological irregularities of the channel base (e.g., Hansen *et al.*, 2017). The different parts of LAPs are termed as top-set, middle-set and toe-set, which chiefly consist of differently amalgamated (Abreu *et al.*, 2003) conglomerates and sandstones bedsets characterised by erosional bases, mud-clasts and bed-load tractive structures (i.e., dunes, ripples, traction carpets, plane parallel lamination). The top-set corresponds to mostly horizontally laying part of the bedsets deposited adjacent to or on top of the inner bank. The middle-set is represented by laterally accreted bedsets accumulating as the inner bank migrates. Finally, the toe-set represents the downlapping sigmoid termination towards the channel thalweg. LAPs are interpreted as point bar-like deposits formed by the lateral migration of the channel (e.g., Abreu *et al.*, 2003; Beaubouef, 2004a; Babonneau *et al.*, 2010; Pyles *et al.*, 2012; Janocko *et al.*, 2013). The planform evolution of point bar-like deposits, as well as the migration of the channel, is strongly dependent upon the local seafloor gradient (Pirmez *et al.*, 2000; Kneller, 2003; Samuel *et al.*, 2003) and substrate cohesiveness (Janocko *et al.*, 2013).

In outcrop examples (e.g., Navarro *et al.*, 2007; Wynn *et al.*, 2007; Dykstra & Kneller, 2009; Pyles *et al.*, 2012), LAPs are frequently overlain by thin-bedded heterolithics, described as to be the late stage plug capping the channel form deposited by means of waning turbidite gravity flows (McHargue *et al.*, 2011a), marking the progressive abandonment of the channel (May *et al.*, 1983; Mutti & Normark, 1987; Shanmugam & Moiola, 1988; Cook *et al.*, 1994).

Often, basal channel fill deposits in meandering channel belts can be characterised by bank-derived fine-grained slumps or mass-wasting (i.e., MTDs), possibly recording multiple instability

phenomena. These deposits can be either limited to a single bend of the channel or common to several channel bends.

2.1.2.2. Levéed channel belts

Conduits of levéed channel belts have sinuosity in the range 1.05-1.2 (Reimchen *et al.*, 2016) and are characterised by irregular bends, only occasionally sharp. They are confined by laterally extensive levées, showing a typical gull-wing shape on both side of the channel (e.g., Mutti & Normark, 1987; Mutti, 1992; Reading, 2009; Janocko *et al.*, 2013; Deptuck & Sylvester, 2018). The base of the confined channel belt is flat, but it can be slight uneven due to variable depth of the thalweg scour.

Channel belt deposits, especially if a levéed channel belt is isolated, consist of conglomerates and sandstones with a different degree of amalgamation. Because the single conduit of the channel belt is confined and thus not characterised by important lateral migration events, deposits of this type of channel belts typically lack LAPs. Furthermore, evidence of bends cut-off or collapse of channel-margins, with associated forms and deposits, are rarely recognised (Janocko *et al.*, 2013; Reimchen *et al.*, 2016). However, LAPs can occur as aggradational packages of channel belts in confined channel belt complexes.

2.1.2.3. Erosional channel belts

Erosional sinuous channel belts have a typical V- or U-shaped profile, particularly evident at seismic scale, and are characterised by mainly symmetrical banks with a crescent steepness as the sinuosity increases (Reading, 2009). Their sinuosity can vary from 1.05 to values higher than 1.2 (Janocko *et al.*, 2013). The base of these channel belts is smooth, but it typically shows a stepped profile if the channel belt is characterised by significant phases of erosional rejuvenation, (i.e., testified by several orders of palaeotopographic terraces; e.g., Deptuck *et al.*, 2003; Qin, 2017; Akindulureni *et al.*, 2018; Deptuck & Sylvester, 2018).

Commonly, channel fill deposits of erosional channel belts are composed of conglomerates and sandstones bedsets, with a typical high degree of amalgamation, passing upward to a late-stage infill characterised by less amalgamated sandstones and/or heterolithics. Differently from the

meandering channel belts (see Section 2.1.2.1), LAPs are lacking and bank collapse forms or MTDs are rare.

Furthermore, erosional channel belts usually do not develop levées, which may rarely occur associated to small-sized and few incised channel belts (Reading, 2009; Janocko *et al.*, 2013).

The thickness of this type of channel belt generally excees those of other channel belt varieties.

2.1.3. Hyperpycnal systems and their depositional elements

Unlikely from systems developed in deep-water, hyperpycnal systems in shallow marine environments are poorly understood in outcrop because of the difficult identification of the nature of their deposits and therefore the lack of an efficient classification (i.e., which ca be ubiquitously applied to every hyperpycnal accumulation).

Heller & Dickinson (1985) were the first to introduce the term “submarine ramp” aiming at distinguishing sandy turbidite fan systems directly connected to and fed by deltas from those fed by submarine canyons in the deep-water (see Section 2.1.2). Reading & Richards (1994) subsequently considered the term “clastic ramp” in a broader sense including all the architectural elements, both erosional and depositional, constituting hyperpycnal fan systems fed by deltas on a gently dipping seafloor profile, relatively shallower compared to the deep-water profile.

In contrary to deep-water turbidite fan systems fed by surge-like turbidity currents (see Section 1.1.1.1), hyperpycnal fan systems are deposited by means of sustained hyperpycnal discharges (see Section 1.1.1.2), which are able to travel for long distances, by pumping provided by river floods, on gentle ramp or slope profiles (Kneller & Buckee, 2000; Mulder *et al.*, 2001b; Plink-Björlrklund & Steel, 2004; Lamb & Mohrig, 2009; Azpiroz-Zabala *et al.*, 2017; Simmons *et al.*, 2020). Thus, the distance travelled by an hyperpycnal flow is directly dependent upon the duration of the river flood itself. According to this dependence, the size of an hyperpycnal fan system evolving downcurrent is a function of the river flood duration. The longer the river flood lasts, greater is the length of the developed hyperpycnal fan system (Zavala & Pan, 2018).

The understanding of the downcurrent evolution of an hyperpycnal flow is therefore fundamental to comprehend the resulting architectural elements (along with their geometries) that make the hyperpycnal fan system.

The initial path of an hyperpycnal flow is traced by the advance of the head of the flow which moves downcurrent along the depositional profile gradient reaching the lower topographic positions. In this view, if the topographic depositional profile is rough, closed topographic lows may result in flow trapping and forced accumulation of very thick and discontinuous massive sand deposits. If the topographic depositional profile is more regular depicting a gentle or flat landscape, the acceleration of the hyperpycnal flow (Fig. 22A) along its body leads to the erosion of the depositional surface and downcurrent transportation of sediments. High velocities at the hyperpycnal flow axis produces a flute-like basal scour (Fig. 22B. Hoyal *et al.*, 2003) with associated levée deposits, which result by lofting deposition from the suspension load cloud of the hypepycnal flow (i.e., Facies L in Section 1.1.2.2).

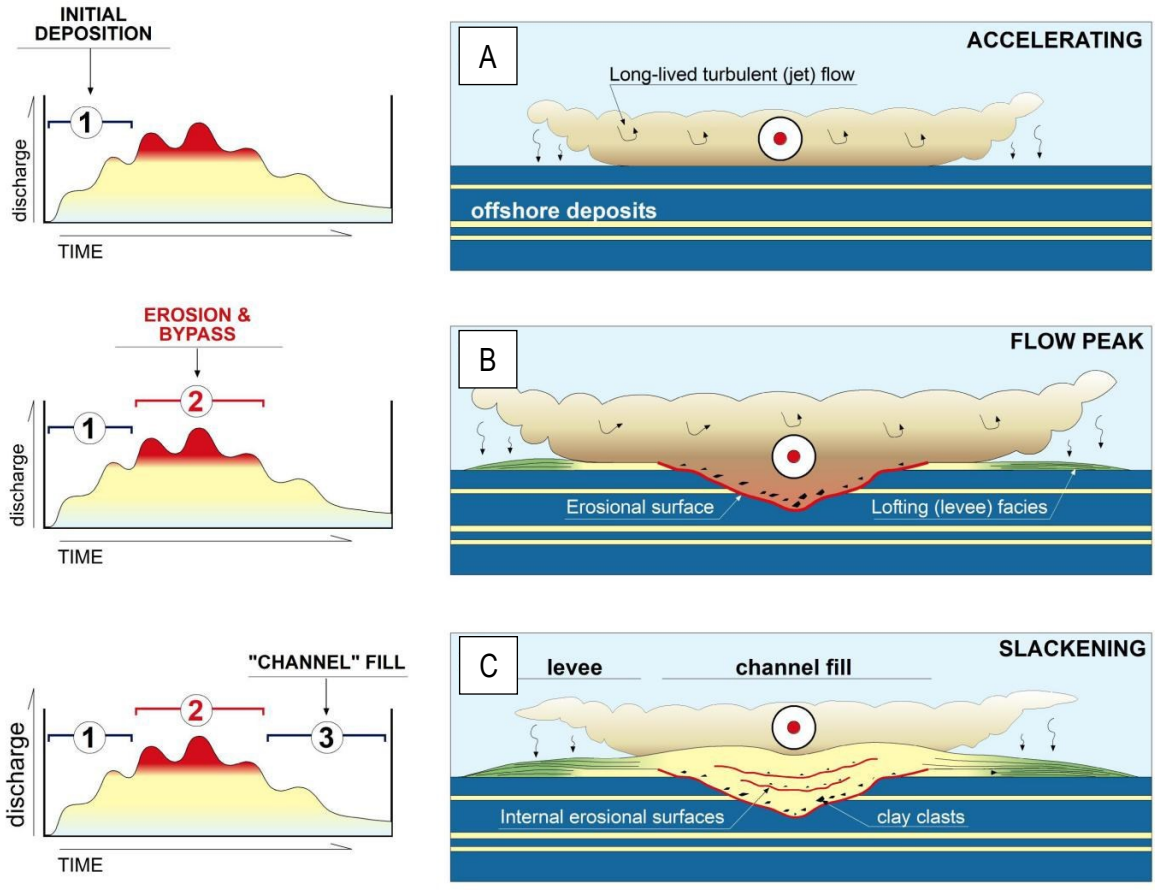

Fig. 22. Theoretical sketch illustrating the step-by-step evolution of an hyperpycnal channel belt. (A) Arrival of the flow head accumulated traction plus fall-out deposits; (B) High-velocities at flow axis produces a flute-like basal erosional feature; (C) The erosional features is deepened and the hyperpycnal flow infill deposited within the previous erosional relief. From Zavala & Pan (2018)

The interplay of erosion and bypass at this stage can result in bedload and suspended load at the channel bottom, which can be associated to lateral migration in case of sinuous meandering channels (Zavala & Pan, 2018), such as those of turbidite fan systems (see Section 2.1.2.1).

If the hyperpycnal flow is sustained through time by the persisting river flood, this basal scour will be deepened evolving into a channel incision (Fig. 22C). The channel fill at this stage is characterised by an overall thinning- and fining-upward trend depending upon an overall fluctuating waning flow (McHargue *et al.*, 2011a). The channel fill deposits typically involves gravel to sand-sized materials collapsed from the sustained hyperpycnal flow and are associated to finer-grained levée deposits at channel margins.

Taking into account these concerns, the term *hyperpycnal channel* (e.g., Ponce *et al.*, 2008; Ponce & Carmona, 2011; Pan *et al.*, 2017; Zavala & Pan, 2018) can be used to indicate a conduit formed by and conveying hyperpycnal flows (see Section 1.1.2.2), which typically deposit sediments both inside and outside the channel incision. The resulting channelised body is referred to broadly as *hyperpycnal channel belt*.

Differently from their fluvial counterparts, hyperpycnal channels generally develop a positive topography on the seafloor which will control the location of the future hyperpycnal channels resulting in compensation cycles (Mutti & Sonnino, 1981).

In this complex scenario due to compensation cycles, the transition from hyperpycnal channels to lobes occurs when hyperpycnal flows wane and lose their erosional capacity.

The deposition during this phase is controlled once again by the topographic surface profile. In topographically controlled depocentres, the hyperpycnal flow could be forced to wane and accumulate according to fill and spill processes (e.g., Winker, 1996; Sinclair & Tomasso, 2002; Toniolo *et al.*, 2006; Marini *et al.*, 2016). On the contrary, if the depositional surface topography is more regular, hyperpycnal channels are able to reach distances of hundreds of kilometres until their sediment load spread out depositing terminal lobe fringes.

CHAPTER III

Stratigraphic evolution of a spectacularly exposed turbidite channel belt from the Tachrift Turbidite System (Tortonian, NE Morocco)

Intentioanlly blank page

3. Stratigraphic evolution of a spectacularly exposed turbidite channel belt from the Tachrift Turbidite System (Tortonian, NE Morocco)

This chapter is based largely on a paper in review for Sedimentology, “Stratigraphic evolution of a spectacularly exposed turbidite channel belt from the Tachrift Turbidite System (Tortonian, NE Morocco)” by Reguzzi S., Marini M., Felletti F., El Kati I., Zuffetti C., Tabyaoui H.

In this chapter sedimentary architecture and controls on the evolution of a channel-levée complex of the Tachrift Turbidite System (Upper Miocene, the Melloulou Fm.), accumulated upon the southern slope of the Neogene Taza-Guercif Basin (Rifian Corridor of NE Morocco), are examined. The studied complex is spectacularly well exposed along an outcrop belt of ca. 3.4 km and it was detailed by acquiring and correlating sedimentological logs with cm-scale resolution and close spacing.

3.1. Introduction

Submarine channels are important geomorphological seafloor elements that traverse slopes and basin floors conveying sediments, organic matter, and pollutants transported by gravity flows to deep-water (Peakall & Sumner, 2015; Kane & Clare, 2019). As a result of overbanking from turbidity currents, they are laterally associated with levées and, locally, with crevasse splays (Mutti, 1992; Peakall *et al.*, 2000; Posamentier & Kolla, 2003; Wynn *et al.*, 2007; Kane & Hodgson, 2011; Janocko *et al.*, 2013). Up-dip, submarine channels can pass into a canyon that indents the shelf edge and can connect to a deltaic system acting as a trap for sediments being drifted along (e.g., Plink-Bjölrklund & Steel, 2004).

Although submarine channels show some morphological commonalities with fluvial channels, their sedimentary processes are fundamentally different from those governing their fluvial counterparts due to a range of controls (Peakall *et al.*, 2000; Kolla *et al.*, 2007; Sylvester *et al.*, 2011; Jobe *et al.*, 2016, 2020). While submarine channels host deposition from a range of flow types (from mass flows to highly dilute turbidity currents; Peakall & Sumner, 2015), locally modified by the action of contour currents (Fonnesu *et al.*, 2020 and references therein), the fill of fossil examples is dominated by turbidites and thus referred to as turbidite channels.

The planform of submarine channels, commonly described in terms of sinuosity (i.e., ratio of the centre line length to the corresponding straight-line distance; Bridge, 2003), show the tendency to vary down dip from relatively straight to sinuous (i.e., sinuosity greater than 1.05; Reimchen *et al.*, 2016) as the slope gradient reduces (Pirmez *et al.*, 2000; Kneller, 2003; Hodgson *et al.*, 2011), albeit tectonics and halokinesis can result in more complex patterns (Pirmez *et al.*, 2000; Kane *et al.*, 2010, 2012; Covault *et al.*, 2020; Tek *et al.*, 2021).

Yet, the along-dip depth profile of submarine channels and the associated slope gradient can change over time because of their tendency to attain a concave-up profile of equilibrium, at which the prevailing sediment discharge produces minimum aggradation or degradation (graded or equilibrium profile; Pirmez *et al.*, 2000). The tendency of a submarine channel to erode or aggrade at any point along its course, depends upon accommodation, which can be viewed as the space between the equilibrium profile (i.e., the slope profile of no net erosion or deposition) down the sediment transport pathway and the actual slope profile (Fig. 23) (Kneller, 2003; Samuel *et al.*, 2003b).

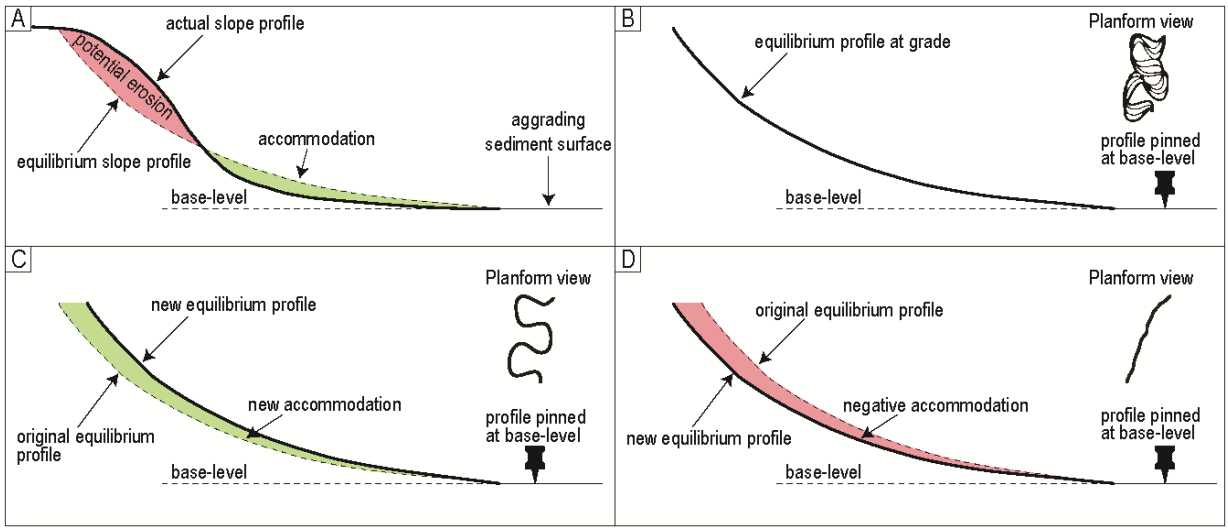

Fig. 23. Schematic illustration of equilibrium profile. (A) Equilibrium slope profile Vs. actual slope profile. (B) Graded channel profile with generalized planform view. Flow parameters remain constant with time. (C) Aggradational channel with generalized planform view. (D) Erosional channel with generalized planform view. Modified after Kneller (2003) and Samuel *et al.* (2003).

When the slope profile is close to grade, channels may establish as relatively straight conduits dominated by erosion and bypass but rapidly undergo a phase of meander development as the sediment input increases (Elliott, 2000; Peakall *et al.*, 2000; Babonneau *et al.*, 2010; Hodgson *et al.*, 2011). In meandering channels, the bends expand laterally (i.e., swing; Peakall *et al.*, 2000)

resulting in accrection of point bar-like deposits on the inner bank, commonly referred to as lateral accrection packages (LAPs hereafter, Abreu *et al.*, 2003; Dykstra & Kneller, 2009; Pyles *et al.*, 2012), and erosion of the outer cut-bank (Babonneau *et al.*, 2010). Upon reaching the equilibrium profile (i.e., graded or neutral channels of Kneller, 2003; Fig. 23B), channel sinuosity become relatively stable, albeit its bends may be subject to downstream translation (sweep; Peakall *et al.*, 2000; Labourdette & Bez, 2010). At this stage, the channel tends to aggrade as it acts dominanlty as a bypass zone (Peakall *et al.*, 2000), so that sweep result in superposition of LAPs with changing direction of accrection (e.g., Janbu *et al.*, 2007; Janocko *et al.*, 2013). Labourdette & Bez (2010) have suggested that sweep may dominate over swing when channels are erosionally entrenched into older deposits or in aggradational channels sided by high-relief levées.

The influence of flow parameters on submarine channel morphodynamics and sedimentation has been stressed by Kneller (2003) who proposed that, in a system at grade, changes in sediment input would induce adjustment of the along-dip channel profile to a new equilibrium. In this view, reduction in flow size, density, and efficiency should reflect in the tendency of a channel to aggrade (Fig. 23C). On the other hand, erosional channels would reflect a change toward higher efficiency, larger and denser flows (Fig. 23D).

Most of the understanding of how submarine channels modify their morphology derives from several decades of exploration of the seafloor and its subsurface, which has yielded incredibly detailed morphobathimetric and seismic imaging of present-day and hydrocarbon-bearing fossil examples (Weimer, 2000; Pettingill & Weimer, 2002; Weimer & Pettingill, 2007). Nonetheless, prediction of fine-scale heterogeneity of channelised turbidites still relies on outcrop investigations (Sprague *et al.*, 2005; Wynn *et al.*, 2007; Janocko *et al.*, 2013; García *et al.*, 2015; Reimchen *et al.*, 2016; Gong *et al.*, 2020), which can provide lithological and sedimentary facies calibration down to the scale of component event beds (Elliott, 2000; Navarro *et al.*, 2007; Kane & Hodgson, 2011; Pyles *et al.*, 2012; Arnott *et al.*, 2021).

Among the outcrop examples published to date, Elliott (2000) documented the stratigraphic variability of the Ross Sandstone Formation of western Ireland, recognizing an early incisional phase during which a low sinuosity channel with composite basal erosion (megaflute surface) was

established, and a late depositional phase of channel-axis infill, lateral expansion, and development of higher sinuosity and laterally migrating channels with laterally accreted bedsets.

Navarro *et al.* (2007) detailed the architecture of an up to 90 m-thick channel-levée complex from the Isaac Formation (Southern Canadian Cordillera). Correlations, detailing a bend of the channel belt, illustrate the stratigraphic transition from an inception phase dominated by axial bypass and development of low-relief asymmetric levées to a mature stage of channel aggradation, during which continued levées growth is accompanied with an increased in-channel deposition. Navarro *et al.* (2007) also proposed that the observed architectural complexity may largely reflect sediment input variations at a range of scales.

Hodgson *et al.* (2011) explained the sedimentary architecture of the Karoo Basin (South Africa) channel-levée system as the response to an equilibrium profile shift from low accommodation to high accommodation conditions, through an intermediate phase of at grade condition. This entails transition from formation of a basal master erosion, acting primarily as sediment bypass conduit, to its infilling with stacked and then vertically aggraded channel fills.

The role of sediment input variations was emphasized by McHargue *et al.* (2011), who proposed that the stratigraphic heterogeneity of channelised turbidites is partly due to cyclic changes of gravity flow energy at multiple time scales. This results in alternation of ‘waxing’ phases, during which relatively large, highly concentrated and relatively coarse flows drive erosion of channel conduits bypassing most of their load, and ‘waning’ phases in which in-channel deposition dominates as smaller volume, less concentrate and finer-grained flows are delivered to the system.

More recently, based on numerous channel trajectory measurements from 21 submarine systems, Jobe *et al.* (2016) have shown that adjustment of submarine channels to an equilibrium planform takes place in a two-phase evolution. The resulting depositional architecture is typified by a ‘hockey-stick’ channel-fill trajectory, whereby laterally stacked channel-fills are gradually replaced upward by vertically stacked channel fills.

Further complexity can arise from local modification of sea floor topography by tectonic tilting, halokinesis, and mass wasting, capable of forcing channel rerouting (Kane *et al.*, 2010), meander

development and cut-offs up-dip of topographic obstacles (Covault *et al.*, 2020), and retrogressive erosion associated to upstream migrating knickpoints (Tek *et al.*, 2021).

The aim of this contribution is threefold: (i) to document the stratigraphic variability of sedimentary architecture of a sinuous meandering slope channel at a sub-seismic scale, (ii) to highlight the possible role of sediment input variations in controlling the fine-scale lithological heterogeneity in similar systems and (iii) to investigate channel morphodynamics and test current models explaining stratigraphic changes of channel trajectory and depositional style.

To do this, a superbly exposed channel-levée complex belonging to the Tachrift Turbidite System of NE Morocco (Taza-Guarcif Basin, Late Tortonian-Early Messinian; Gelati *et al.*, 2000; Felletti *et al.*, 2020) was investigated, acquiring 84 closely spaced (ca. 50 m) sedimentary logs spanning a ca. 3.4 km-long outcrop belt oblique to the mean palaeoflow. Bed-by-bed correlations, constrained by marker beds, revealed a stratigraphically varied depositional architecture that, based on magnetochronology constrains (Krijgsman & Langereis, 2000), is thought to have developed over a time span of a few kyr. This begins with a thin but laterally extensive sand-prone unit characterised by laterally accreted channel fills with poorly developed levées, which make transition to a mud-prone and dominantly non-channelised package, and then to an upper unit of vertically aggraded channel fills with well-developed levées. It is proposed that this stratigraphic evolution reflected the response of the channel morphology and dynamics to perturbations of a graded profile induced by sediment input variations.

This study provides insights into likely controls on changes of architectural style that can be developed at a sub-seismic scale and are thus potentially underappreciated in subsurface analogues.

3.2. Geological setting

The Taza-Guercif Basin of NE Morocco (Fig. 24) is part of the Rifian Corridor (Flecker *et al.*, 2015; Capella *et al.*, 2018), a remnant of the Rif foreland basin system that acted as a seaway connecting the Atlantic Ocean to the Mediterranean Sea during the late Miocene (Bernini *et al.*, 1999; Gelati *et al.*, 2000; Sani *et al.*, 2000; Capella *et al.*, 2017, 2019). Together with its westerly equivalents, i.e. the Gharb and Fes-Maknes Basins (Fig. 24), the Taza-Guercif Basin has established since the early Tortonian as a result of a combination of flexural loading by the advancing thrust sheets of the Rifean system, and strike-slip tectonics in the Middle Atlas (Bernini *et al.*, 2000; Gelati *et al.*, 2000; Sani *et al.*, 2000; Capella *et al.*, 2017). These basins sit on top of a regional-scale unconformity which records the Cretaceous-early Miocene compressional reactivation of Jurassic rift faults of the Middle Atlas (Bernini *et al.*, 1999; de Lamotte *et al.*, 2009).

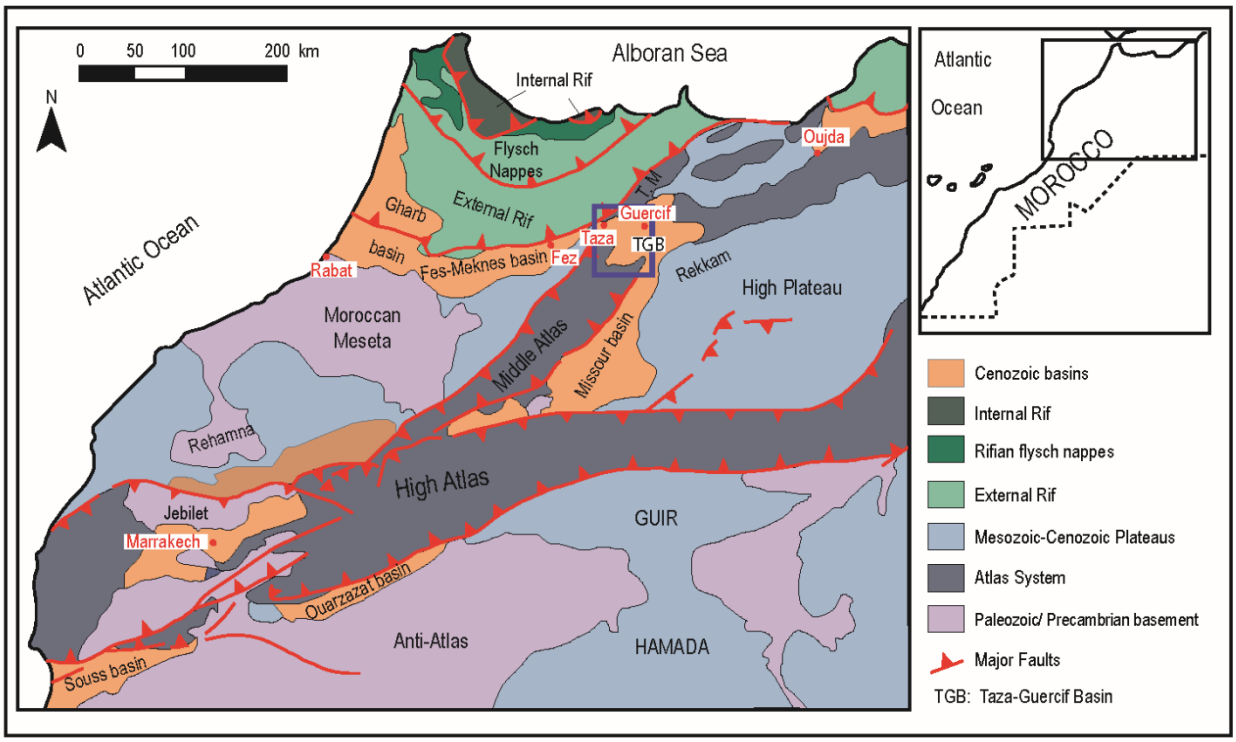

Fig. 24. Sketch map representing the regional geology of northern Morocco showing key structural elements and terrains, along with location of Gharb, Fes-Meknes and Taza-Guercif basins (modified after Hafid *et al.*, 2006). The blue frame locates the study area.

Marine transgression in the Taza-Guarcif Basin (Fig. 25A) began in the late Tortonian (Krijgsman *et al.*, 1999) with accumulation of the up to 500 m-thick shallow marine Ras el Ksar Formation, and is locally preceded by deposition of the alluvial Draa Sidi Saada Formation (Benzaquen, 1965;

Bernini *et al.*, 2000; Gelati *et al.*, 2000). The transgression culminates with the deposition of the Melloulou Formation (Section 3.2.1), a thick unit of interbedded hemipelagic marlstones and turbidites (Bernini *et al.*, 1999; Gelati *et al.*, 2000; Sani *et al.*, 2000) widespread in the Rifean Corridor (*cf.* with 'Marnes Bleues' of Benzaquen, 1965; 'Marnes Tortoniennes' of Colletta, 1977; 'Melloulou Unit' of Gelati *et al.*, 2000) and recording the deepening and sedimentation rate in the Taza-Guercif Basin during the Tortonian (Krijgsman & Langereis, 2000). One last sedimentary turnaround begins in the earliest Messinian, when a tectonically controlled regression (Krijgsman *et al.*, 1999) led first to deposition of the Gypsiferous marlstones of the upper Melloulou Formation and the shallow marine to continental Kef Ed Debe Formation (Gelati *et al.*, 2000; Sani *et al.*, 2000), and then (from 6.7 Ma onward) to the emersion of the Taza-Guercif Basin (Krijgsman *et al.*, 1999; Krijgsman & Langereis, 2000; Capella *et al.*, 2017, 2018).

3.2.1. The Tachrift Turbidite System

The Melloulou Formation contains two distinct turbidite sub-units in the study area, namely the El Rhirane Turbidite and the Tachrift Turbidite Systems (*cf*. with sub-units of Gelati *et al.*, 2000), the latter comprising the channel-levée Complex 4, which is the object of this study (Fig. 3B). El Rhirane and Tachrift Turbidite Systems crop out to the west and to the east of the Zobzit river course, respectively, but their stratigraphic relationship is poorly understood (Fig. 25C).

Gelati *et al.* (2000) suggested that the El Rhirane System is younger than the Tachrift System (Fig. 25C), albeit the two share a common southerly sediment source. Gelati *et al.* (2000) also recognised the channelised nature of the ca. 600 m-thick Tachrift System (to which the studied channel-levée Complex 4 belongs; Fig. 25B), reporting several individual sand-prone bodies separated each from another by hemipelagic blue marls.

The Tachrift Turbidite System was deposited between 7.7 and 7.2 Ma (Krijgsman *et al.*, 1999; Krijgsman & Langereis, 2000), with sedimentation rates between 0.4 m/kyr (Tortonian lower section) and of 1.7 m/kyr (Messinian upper section), and a Middle Atlas sediment source area (Pratt *et al.*, 2016).

The sand-prone component of the Tachrift Turbidite System comprises 9 individual channel-levée turbidite complexes (*sensu* Gardner *et al.*, 2003), interpreted as the product of a number of sinuous

channel belts developed along a north-dipping basinal slope (Felletti *et al.*, 2020). The turbidite system comprises four facies associations, i.e. sand-prone channel fills, heterolithic levée deposits, mass transport deposits, and hemipelagic marlstone bearing methane-derived authigenic carbonates (Felletti *et al.*, 2020).

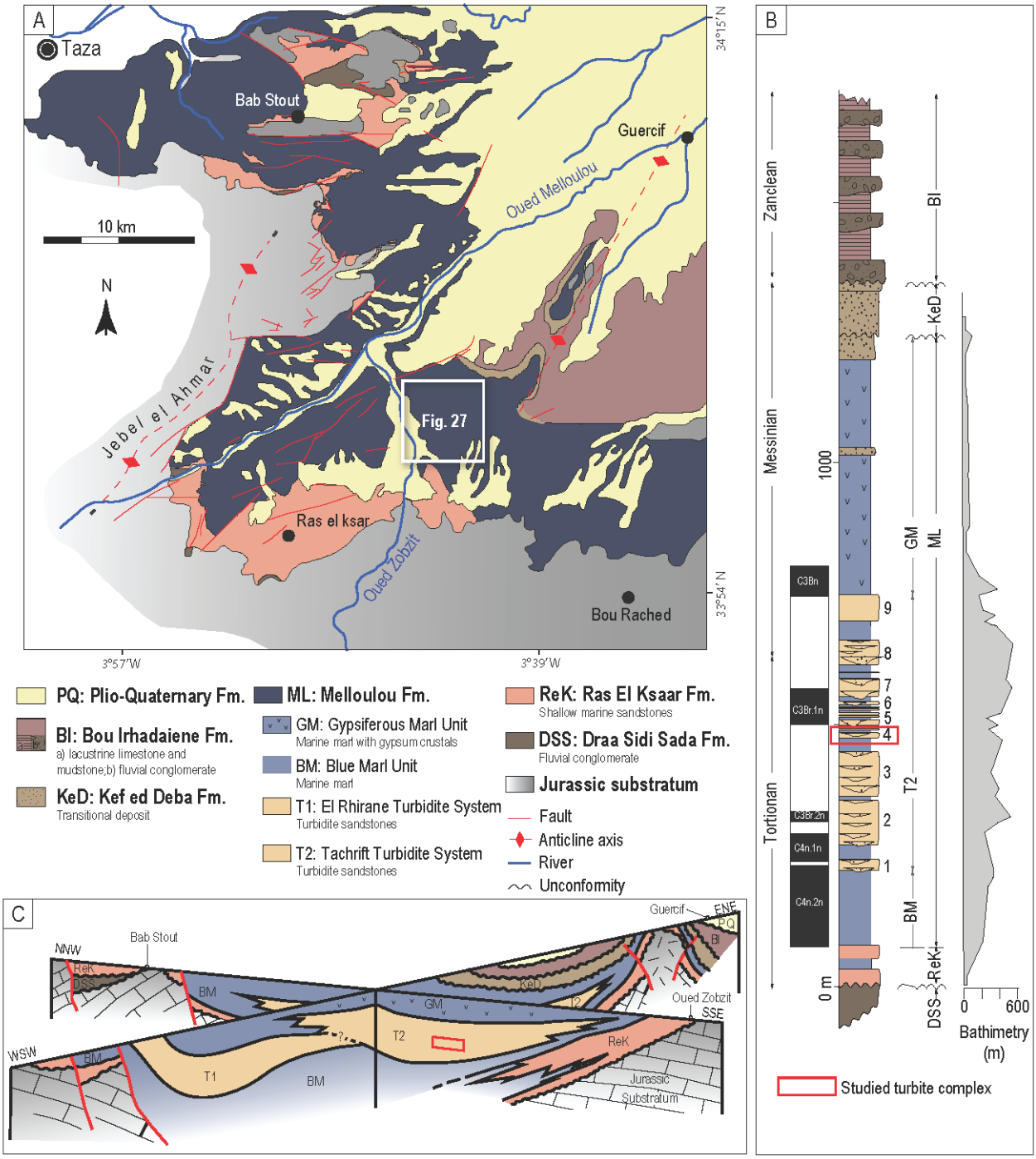

Fig. 25. (A) Schematic geological map of the Taza-Guercif basin (modified after Felletti *et al.*, 2020). (B) Stratigraphic column of the Taza-Guercif Basin fill, with palaeobathimetry and magnetostratigraphy (modified after Krijgsman *et al.*, 1999). (C) Fence diagram showing the stratigraphic relationships of the Neogene Units filling the Taza-Guercif basin. (modified after Gelati *et al.*, 2000). Red rectangle in panels B and C: the turbidite Complex 4 studied in this work.

3.3. Materials and methods

This work focuses on the turbidite channel-levée Complex 4, which occurs at medial stratigraphic position within the Tachrift System (Fig. 25B and Fig. 26). The complex is exposed along a ca. 3.4 km-long outcrop belt, which is largely oblique to palaeoflow and comprises three main outcrop sectors (Fig. 27).

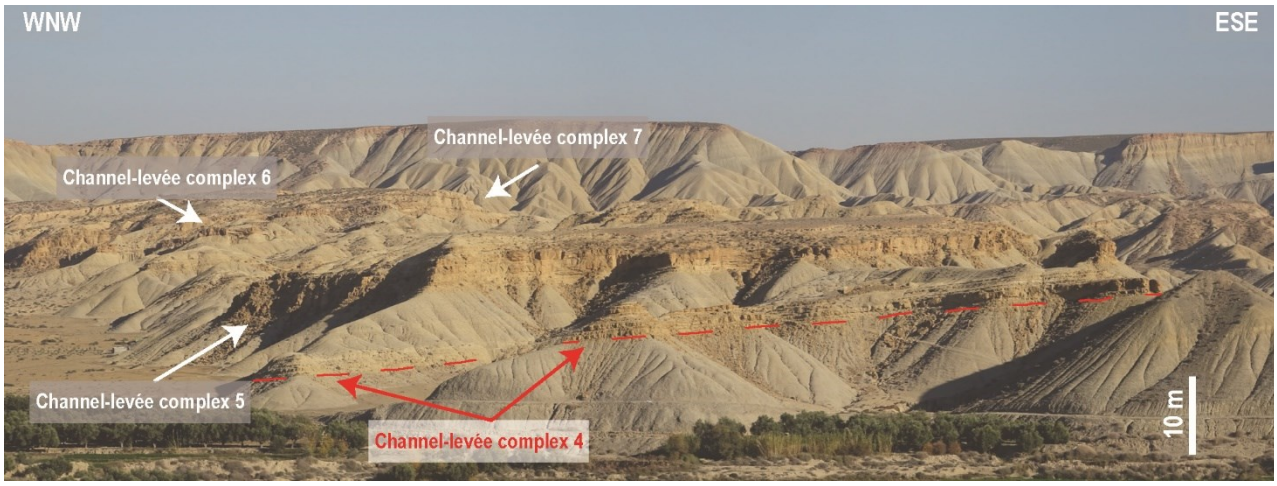

Fig. 26. Panoramic view of part of the Tachrift turbidite system exposed to the east to the Zobzit river, pointing out the stratigraphic position of the channel-levée Complex 4.

Complex 4 was detailed acquiring 84 closely spaced (i.e., ca. 50 m on average) sedimentary logs with an average thickness of ca. 20 m. To ensure spatial accuracy and faithful reproduction of depositional geometries, logs were measured by combining tape metre for individual beds thickness and a high-precision Jacob's staff with laser sighting capability (Patacci, 2016) for long-range measurements (e.g., cumulative thickness of very thick bedsets and monotonous marlstone intervals).

Logs were measured with cm-scale resolution (i.e., 1:20) taking note of lithology, chart-aided estimations of grain size (i.e., using a grain-size comparator) and sorting, sedimentary structures, palaeoflow directions from sole and ripple marks, and intensity of bioturbation. Because distinguishing turbidite mudstones from hemipelagic marlstone is unpractical and subjective in most situations, it was not attempted to do so.

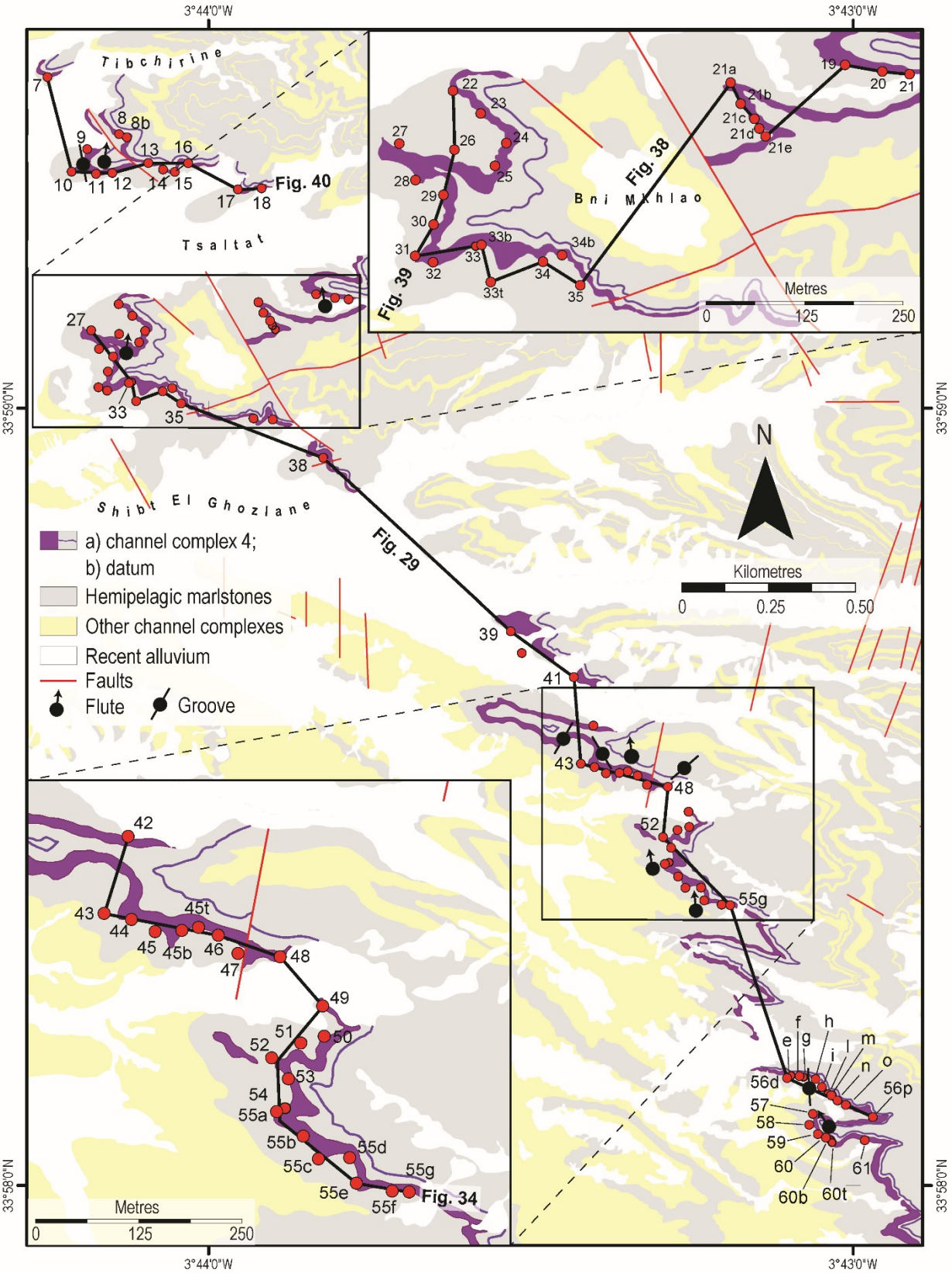

Fig. 27. Sketch map showing the outcrop belt of the channel-levée Complex 4 along with the location of logs and correlation panels discussed in the text (modified after Felletti *et al.*, 2020).

Adjacent logs were correlated physically, either walking out each event bed and stratigraphic surface in the field or by tracing them laterally on photo-panels of the few inaccessible cliffs. Subsets of sedimentary logs from different outcrops were instead correlated based on sedimentary trends after flattening their stratigraphy to a marker turbidite bedset (the datum, hereafter) occurring halfway within the hemipelagic marlstones (Section 3.4.1) separating Complex 4 from Complex 5 (Fig. 25B), which is characterised by a rather flat geometry.

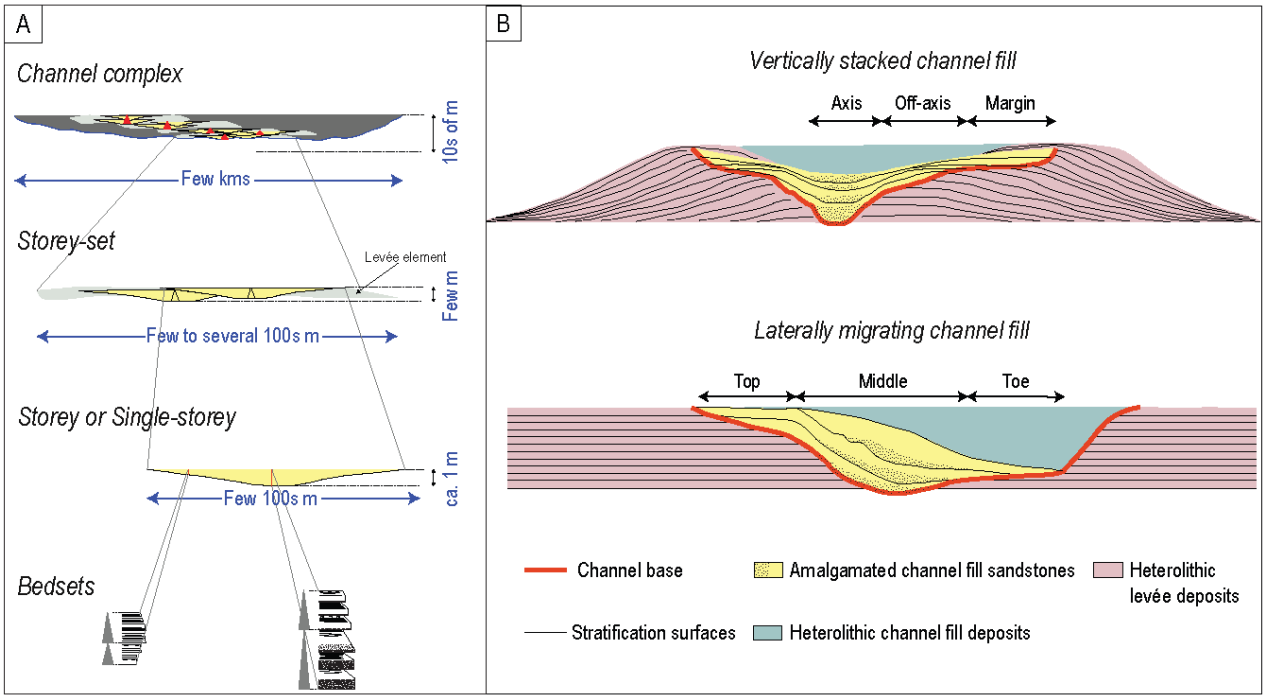

Fig. 28. (A) The hierarchical classification for channelised environments used in this work, showing the average dimensions of corresponding units. Modified after Sprague *et al.* (2005) and Pickering & Cantalejo (2015). (B) Channel-levée architecture for single-storey and storey-sets pointing out the different relations among architectural elements.

The hierarchical scheme by (Sprague *et al.*, 2005), with later amendments by Sprague and co-workers (Campion *et al.*, 2007, 2011; Flint *et al.*, 2008; Sprague *et al.*, 2008, see also Cullis *et al.*, 2018 for a review) is adopted in this paper, which applies to both channel fill and correlative levée deposits. Following this scheme, the terms *storey* and *single-storey* are used interchangeably to refer to a stack of bedsets showing a distinct latero-vertical facies association reflecting the lower rank cycle of depositional evolution, from erosion to bypass and, ultimately, channel infill and abandonment. A few to several semi-amalgamated to amalgamated storeys is here referred to as a *storey-set* (*cf.* with 'channel fill' of Sprague *et al.*, 2005). Finally, the term *complex* is used to refer

to a higher-rank unit, bounded below and above by relatively thick packages of hemiplegic deposits, comprised of a stack of a few to several storeys and/or storey-sets.

Degree of amalgamation, bedding patterns, and sedimentary facies are used in this work to subdivide the sedimentary fill of non-migrational channels into axis, off-axis, and margin portions (Fig. 28A), albeit their boundaries may be not always clear-cut. Besides, the largely sigmoidal bedset formed after lateral accretion of the inner bank and constituting the fill of sinuous meandering channels (Fig. 28B) are further subdivided into: i) a top-set, corresponding to the generally flat-laying and stratigraphically higher portion of the sigmoid, deposited adjacent to or on top of the inner bank-levée transition, ii) a middle-set, representing the relatively thicker-bedded and inclined part of the sigmoid, and iii) a toe-set, that is the downlapping termination of the sigmoid.

3.4. Results

3.4.1. Physical stratigraphy

The channel-levée Complex 4 is sandwiched between hemipelagic blue marlstones a few tens of metres-thick and is exposed in three main sectors of the study area (Fig. 27), which are presented in the following Sections.

3.4.1.1. Northern and central outcrops

Sedimentary logs allows subdividing Complex 4 into twenty-three sand-prone channelised bedsets hierarchically equivalent to single-storey channels (labelled with numbers in Fig. 29A), which locally amalgamate to form at least nine storey-sets (labelled with letters in Fig. 29A; see Section 0).

Complex 4 initiates with five storeys (labelled 1-5 in Fig. 29A and Fig. 30A), with sand-prone channel fills having lengths of a few hundred metres (Section 3.4.3.1) and thickness less than 1.5 m. These channel-fills are vertically stacked, with a slight eastward offset, and are separated each from another by decimetres to metres-thick mud-prone packages that are laterally continuous throughout the outcrop.

Up-section, subsequent storeys amalgamate to form at least four channel storey-sets (A to D, Fig. 30A, B, and C), which stack laterally, partially amalgamating, to form a ca. 4 m-thick unit that can be followed along-strike for at least ca. 1100 m toward the east, before fringing into thin-bedded deposits interpretable as levées (Section 3.4.3.2).

In the central outcrop, channel storey-sets A-D are replaced upward by a ca. 10 m-thick section of thin-bedded turbidites, intercalated by sparse channelised bodies (i.e., storey-set E and single-storey 12 in Fig. 29A) and partly correlative to four more storey-sets (labelled F to I in Fig. 29A) exposed in the northern outcrop (Fig. 27). Totalling a maximum thickness of ca. 8.5 m, storey-sets F to I constitute the uppermost part of Complex 4 (Fig. 31A, B and C) and appear to be vertically stacked with only minor lateral offset. Correlation with levée deposits (log 7, Fig. 29A) of the westernmost exposure of Complex 4 allows estimating the full width of the channel fill part of these storey-sets to be in the range 550-850 m.

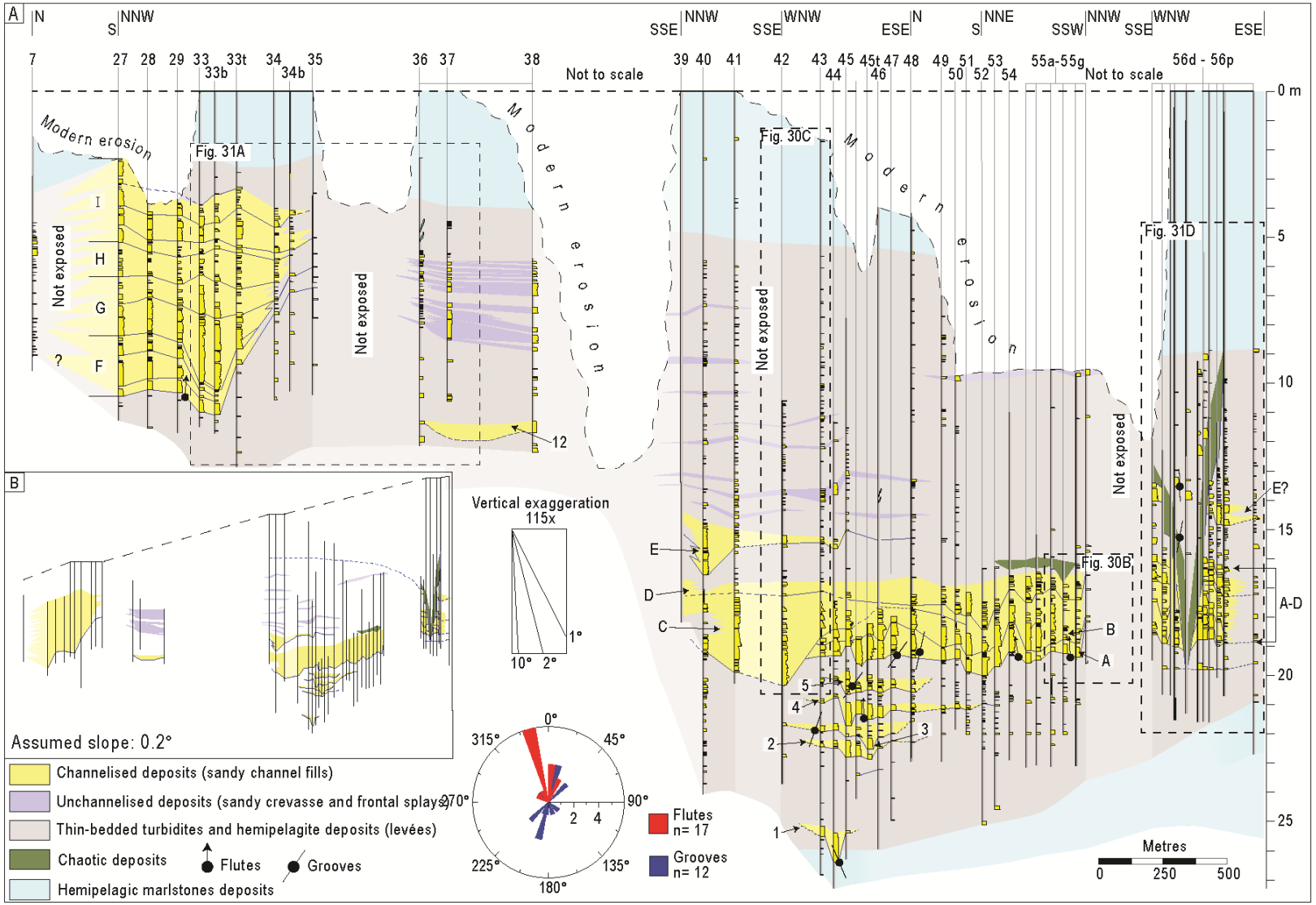

Fig. 29. (A) Correlation panel (see Fig. 27 for location) illustrating the stratigraphy, the facies associations, and the architectural elements (letters and numbers denote channel fills discussed in the text) of channel-levée Complex 4. The panel is oblique to the mean palaeoflow (flow is away from the reader and toward the left; see inset rose diagram). (B) The relative position of outcrops and logs, restored by assuming a seafloor dipping to the north by 0.2° at the time of deposition of the datum (dashed line).

3.4.1.2. Southern outcrop

In this sector, channel Complex 4 is characterised by the presence of a deep erosion (Fig. 29A and Fig. 31D), which is initially infilled with conglomerates and 'en masse' deposits (logs 56g-i; Fig. 29A) and subsequently with fine-grained thin-bedded turbidites (logs 56d-f and 56l-p; Fig. 29A). The erosion cut as deep as ca. 5 m into older channelised deposits, which consist of at least three distinct channel fill storey-sets with laterally accreted bedsets (Fig. 29A). Although these channelised deposits occur at a stratigraphic height similar to that of storey-sets A-D of the central outcrop (Section 3.4.1.1), the stratigraphic relationship between this outcrop and more northerly ones (Section 3.4.1.1) hinges only on the supposed correlation of a local marker bed with the datum and is thus weak (Fig. 29A). Therefore, data from the southernmost outcrop are not discussed further in this contribution.

Yet, it should be noted that if the datum is tilted so to account for the slope dip, assumed to be to the north (Felletti *et al.*, 2020) and in the order of 0.2° (e.g., Sinclair, 1994; Pirmez *et al.*, 2000; Reading, 2009; García *et al.*, 2012), the deepest point of the erosion is located at height comparable to that of the youngest stratigraphy of the northern outcrop, suggesting it might represent the product of a late phase of channel-belt reorganisation, most likely due to an up-dip avulsion relocating it to the east of the study area.

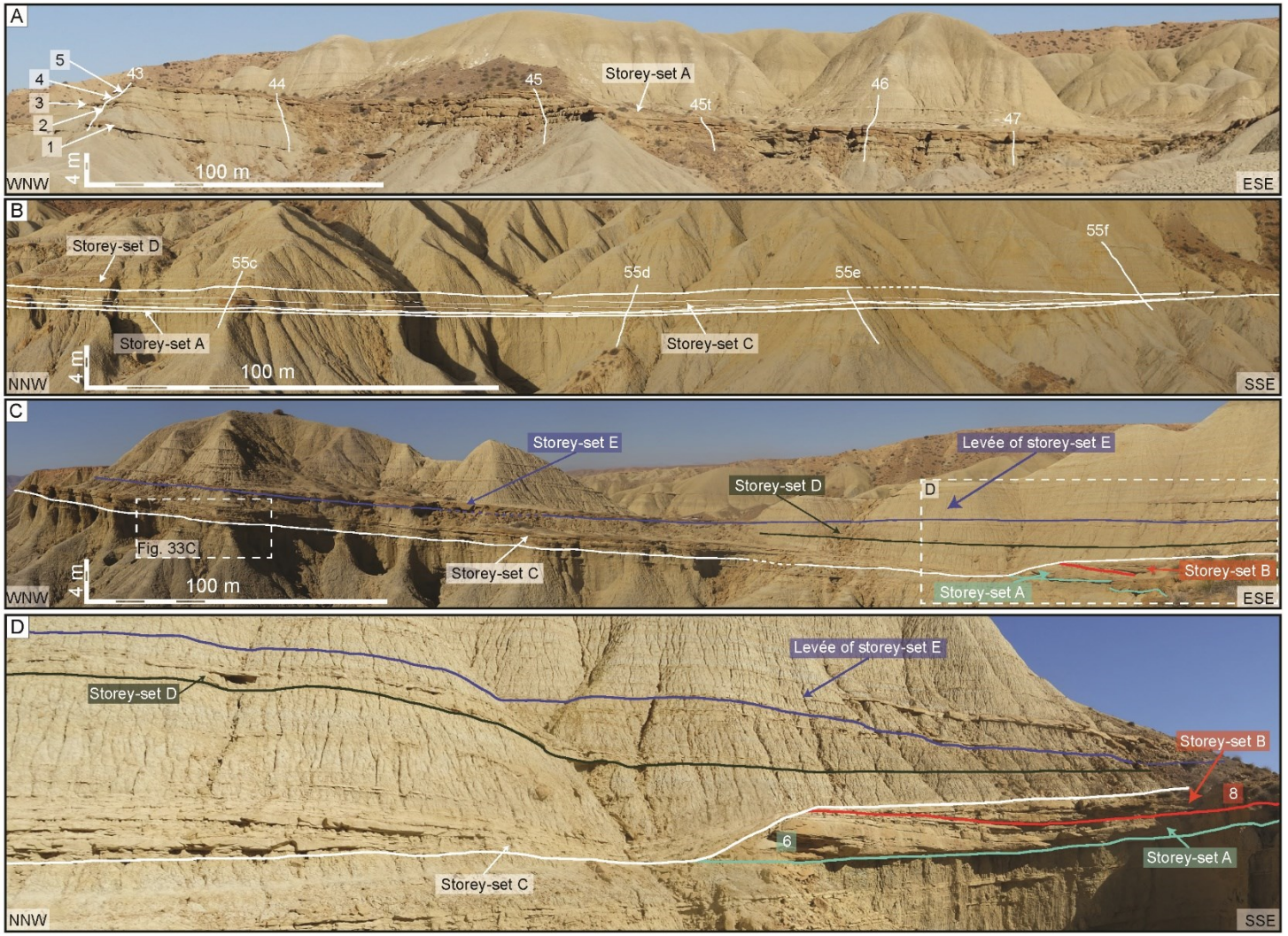

Fig. 30. Panoramic views (roughly orthogonal to mean palaeoflow) of the lower half of Complex 4 in the central outcrop area (see Fig. 27 and Fig. 29 for location). (A) Single-storey channel fills 1-5 and storey-set A. Note how single-storeys channel fill sandstones are vertically stacked and terminate toward ESE. (B) Lateral transition of storey-set A, C and D into their correlative levées toward SSE. (C) Storey-set A to E. Note how these are laterally stacked to result in interlayering of channel fill sandstones and heterolithics interpreted as levée deposits. (D) Detail showing how storey-set B rests on top of an erosional surface cutting storey-set A and the laterally accreted bedsets making single-storeys 6 and 7.

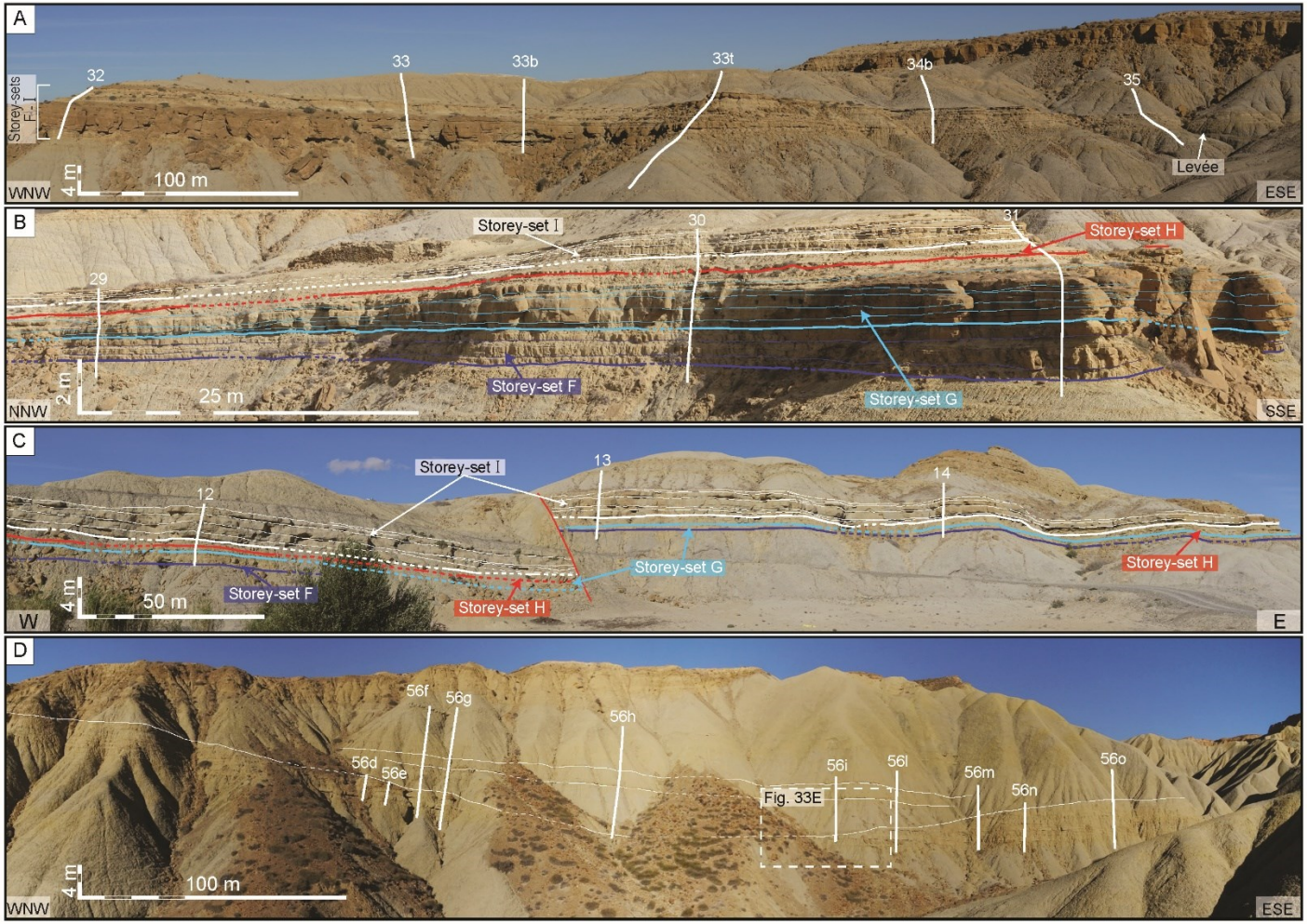

Fig. 31. Panoramic views of the upper half of Complex 4 (see Fig. 27 and Fig. 29 for locations) in the northern (A-C) and southern outcrops (D). (A) Strike section view (palaeoflow away from the reader) showing the lateral transition from sand-prone channel fills of storey-set F to I into correlative heterolithics interpreted as levées. (B) View slightly oblique to mean channel axis (mean palaeoflow toward the left and away from the viewer) of storey-set F to I showing their overall sigmoidal shape with a net lateral accretion toward the right. (C) Strike-section view (palaeoflow away from the reader) of storey-set F to I showing their vertical stacking in the northwestermost sector of the Complex 4. (D) Strike section view (palaeoflow away from the reader) of the deep erosion (see Fig. 29) characterizing the southern outcrop.

3.4.2. Sedimentary facies

Six sedimentary facies (Tab. 2) were defined based on lithology, grain size and vertical association of sedimentary structures. These include 4 turbidite sandstone facies (f1 to f4), named after their most distinctive and generally thickest division, mudstones (f5) and chaotic and slumped deposits (f6).

Facies	Lithology	Sedimentological Characteristics	Process Interpretation
f1	Sandstones with a basal massive division	Coarse/medium- to fine-grained, well to medium sorted, 15-100 cm-thick beds. Structureless or with traction carpets, horizontal planar parallel lamination, ripple cross-lamination. Small mud clasts may be present close to base or scattered with bed.	High-density turbidity currents. High suspended-load fallout rates, flow deceleration and bypass.
f2	Cross-stratified sandstones	Very coarse- to medium/fine-grained, well to medium sorted, 10-100 cm-thick beds. Trough-cross to cross-lamination, low-angle cross-lamination, ripple cross-lamination, horizontal plane-parallel lamination, traction carpets. Sometimes wavy top due to ripple-marks crests or bioturbation.	2D or 3D dune formation underneath waning high-density turbidity currents.
f3	Planar-parallel laminated sandstones	Medium- to fine-grained, well sorted, 15-100-cm thick beds. Horizontal plane-parallel lamination passing upward to ripple cross-lamination. Bioturbated top.	Waning flow deposition. Partial bypass of sediment load.
f4	Thin-bedded ripple laminated sandstones	Fine- to very fine-grained, medium sorted, 1-15 cm-thick beds. Ripple-cross lamination, or water-escape structures. Intensely bioturbated.	Waning low-density turbidity current deposition.
f5	Mudstones	Clay- to coarse silt, 0.5 to 200 cm-thick. Structureless of weakly laminated. It may include structureless hemipelagic marlstone.	Turbiditic and hemipelagic fall-out deposition.
f6	Chaotic deposits	Clay- to fine-grained sand with scattered cm- to dm-thick sandstones blocks, or slumped marlstones, 20-500 cm-thick.	Debris flows, mass wasting, levée failure.

Tab. 2 Features of the sedimentary facies recognised within the channel-levée Complex 4.

3.4.2.1. Sandstones with a basal massive division (f1)

The facies f1 consists of medium to very thick beds of coarse- to medium-grained sandstone, typically with scoured bases, which can include a basal mud-clast breccia (Fig. 32A- B). The basal division of f1 is represented by a massive interval, which may begin with traction carpets and grades upward into planar-parallel (Fig. 32C) to ripple-drift laminated tops so as to form a Bouma-like sequence. Less frequently, the basal massive division may be very thick and sharply overlain by a thin mudstone cap.

Facies f1 occurs almost exclusively as part of the sand-prone channelised units, albeit it may be sporadically found as single beds either in the marginal channel portions or in thin-beds mud-prone units.

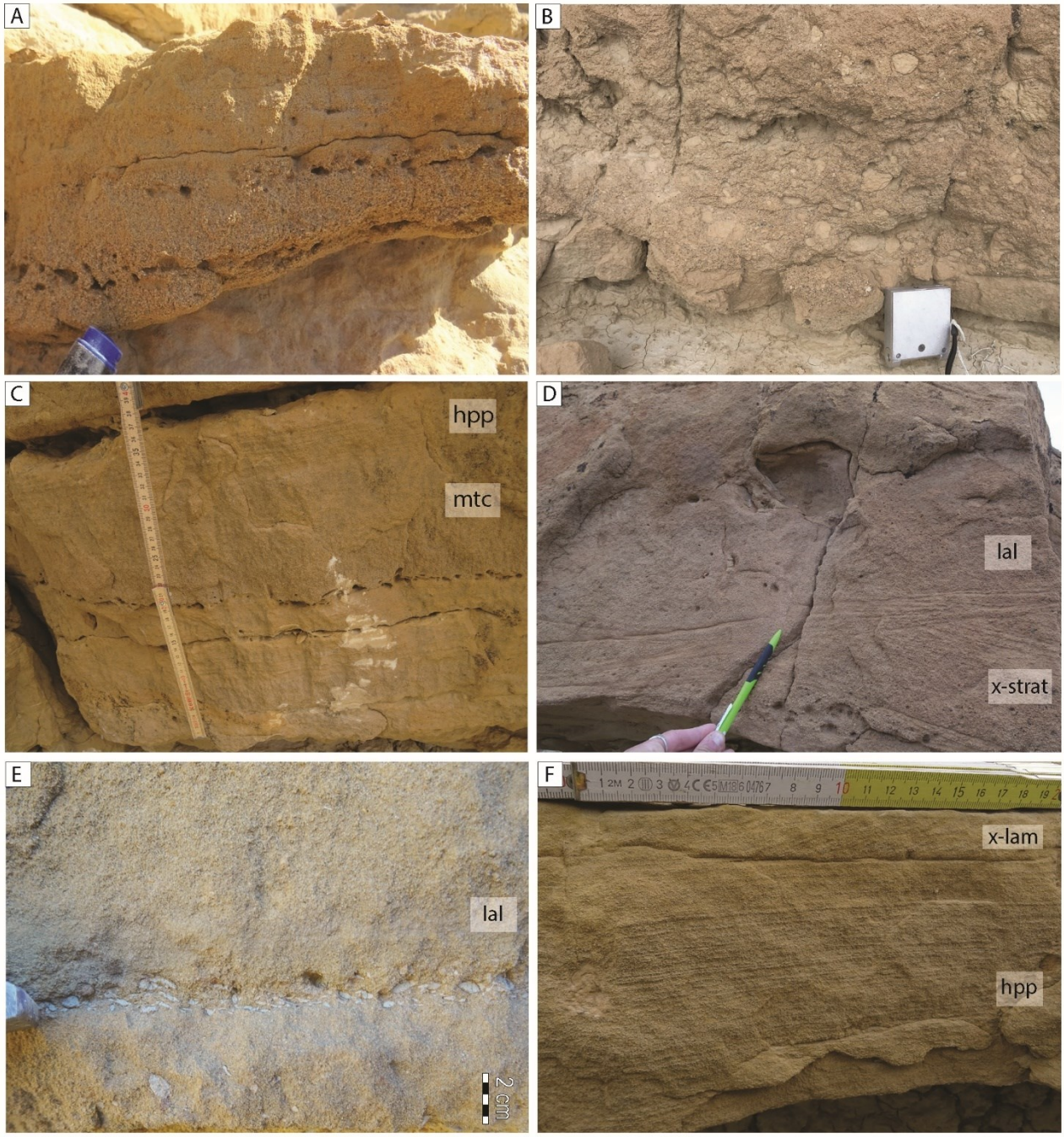

Fig. 32. (A) Massive sandstones with basal mud-chips (facies 1). (B) Massive very coarse- to medium-grained sandstones with cm-sized mud-chips (facies 1). (C) Basal massive sandstones interval characterised by traction carpets (*mtc*) evolving upward into a horizontal plane-parallel laminated (*hpp*) top (facies 1). (D) Cross-stratified sandstones in facies f2. (E) Low- angle cross laminated sandstones with mud-clast basal lag (facies f2). (F) Horizontal plane-parallel laminated sandstones sharply overlain by a very thin cross-laminated (*x-lam*) top in facies 3.

The basal division of f1 suggests that the rate of sediment fall-out from above was generally sufficiently high to suppress traction. The upward transition to finer-grained laminated tops suggests deposition from a decelerating flow becoming less concentrated in time to result in

establishment of traction plus-fall out conditions. Conversely, sharp capping of the very thick massive division by a mudstone cap can be interpreted as an evidence of sediment bypass.

3.4.2.2. Cross-stratified sandstones (f2)

The facies f2 consists of medium to thick beds of medium- to coarse-grained sandstones with a range of cross to trough cross-bedding (Fig. 32D-E). The cross-stratified beds pass upward to a mudstone cap either sharply or more transitionally, through an incompletely developed Bouma-like sequence. f2 occurs mostly as part of the sand-prone channelised units and, more rarely, within the relatively muddier units separating subsequent channel storeys.

The cross-stratification suggests that f2 represents the product of two- or three-dimensional small dunes forming underneath high-density flows.

3.4.2.3. Planar-parallel laminated sandstones (f3)

The facies f3 consists of medium- to thick beds of normally graded medium- to fine-grained sandstones and a co-genetic mudstone cap, characterised by a basal planar-parallel laminated division. The laminated basal division may either be sharply overlain by a co-genetic mudstone cap (facies f5) or, sometimes, it grades upward into a rippled or convoluted top (Fig. 32F), more rarely, it passes upward to a structureless sandstone with abundant millimetres-sized mud-clasts.

Albeit most commonly interbedded with facies having coarser-grained lithotextures as part of amalgamated sand-prone channel fills, the facies f3 is ubiquitous, occurring also in marginal channel settings and in the mud-prone units.

The facies f3 shows similarities with base-missing Bouma sequences with partly developed T_c-T_d divisions. It may be thus interpreted as the product of deposition from waning flows partly bypassing finer-grained sediments.

3.4.2.4. Thin-bedded ripple laminated sandstones (f4)

The facies f4 consists of well-sorted, fine- to very fine thin-bedded ripple-cross laminated sandstones which grade upward to a co-genetic mudstone cap (see facies f5 below) and are generally strongly bioturbated (Fig. 33A-B).

Although bioturbation and soft sediment deformation commonly obliterate primary sedimentary structures, these beds generally show cross and convolute lamination.

The facies f4 is typically interbedded with mudstones (facies f5, see below) forming either parallel-stratified packages (Fig. 33A), correlative to sand-prone channel fills and interpretable

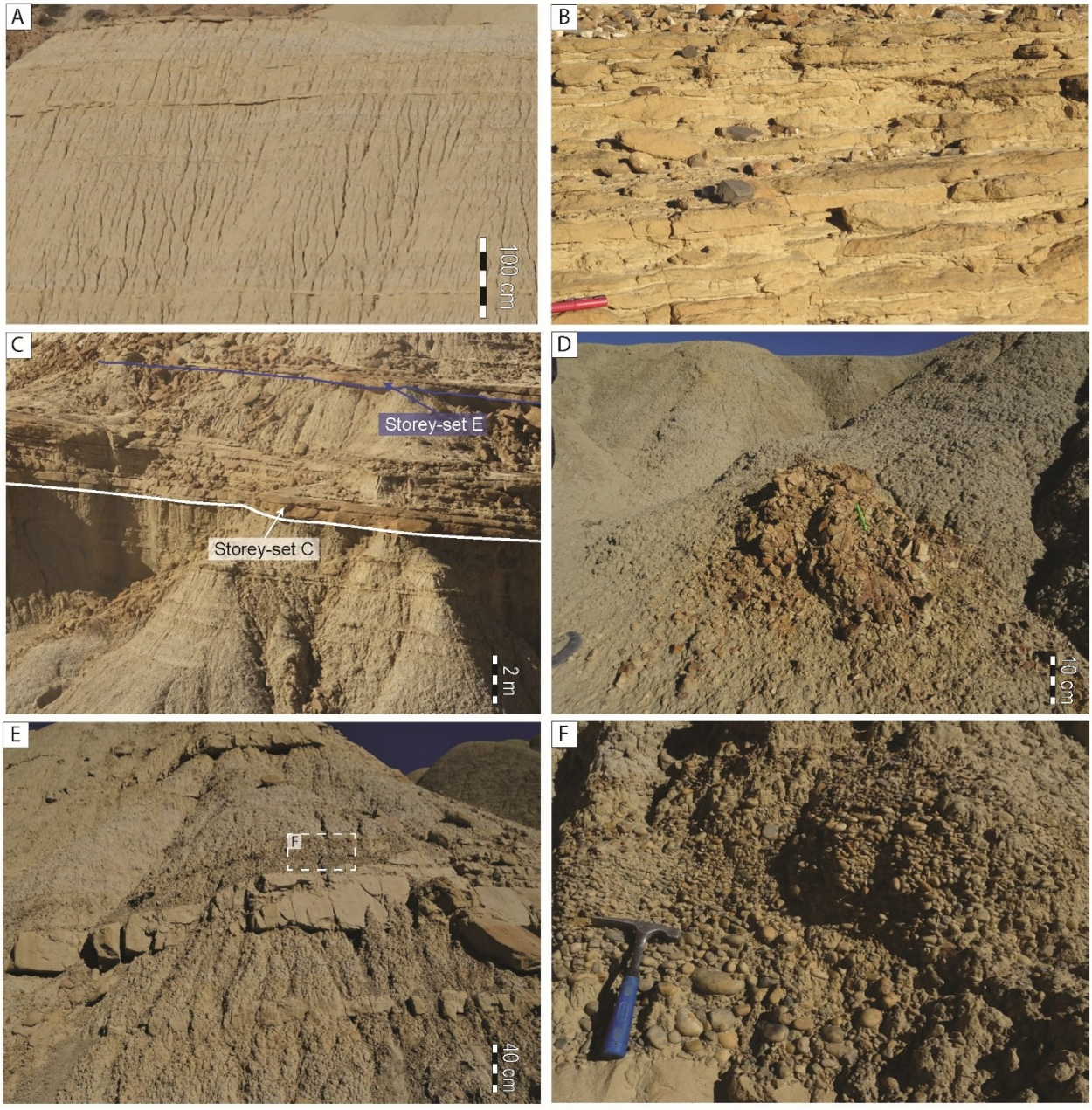

Fig. 33. Different proportions of thin-bedded fine-grained sandstone, mudstones, and subordinately marlstones form mud-prone(A) and sand-prone (B) intervals (facies f4). (C) Structureless siliciclastic turbidite mudstones and marlstones of facies f5, intercalated with rare very thin turbidite sandstone beds (see Fig. Fig. 30C for location). (D) A detail of a carbonate concretion within mudstones of facies f5. (E) Massive conglomerates of facies f6 sit above the deep erosion documented in the southernmost sector (see Fig. 31D for location). (F) Detail showing the well-rounded carbonate clasts making the conglomerate of facies f6.

as levées (Felletti *et al.*, 2020), or building cross-stratified bedsets in the uppermost channel fills (Fig. 33B).

The facies f4 show similarities with T_c and T_d-T_e Bouma sequences suggesting deposition from low-density waning flows in a relatively low-energy environment, favourable to colonization from taxa responsible for bioturbation.

3.4.2.5. Mudstones (f5)

The facies f5 comprises siliciclastic turbidite mudstones, which may cap turbidite sandstones or occur interbedded with very thin beds of hemipelagic marlstones. Interbedded turbidite mudstone and marlstones form up to few m-thick mud-prone units (Fig. 33C) which are typically found laterally to, and away from, channel fills. f5 can bear carbonate concretions and micrite beds (Fig. 33F) described by Felletti *et al.* (2020) and interpreted as methane derived authigenic carbonates.

The facies f5 is interpreted as the result of fall out deposition from the most dilute part of low-density turbidity currents and, subordinately, from hemipelagic fall-out.

3.4.2.6. Chaotic and slumped deposits (f6)

The facies f6 occurs as part of the infill of the deep erosion of the southernmost outcrop (Section 3.4.1.2; Fig. 29 and Fig. 31D) and in the central outcrop atop storey-set D (Fig. 34). In the former outcrop, f6 lays all along the erosional surface. In the deeper part of the incision fill, f6 comprises chaotic mudstone with scattered centimetre- to decimetre-sized sandstone clasts associated to an up to 1.5 thick pebble-grained conglomerate lag (Fig. 33D-F), in a ratio of about 4:1. Conversely, f6 is represented by chaotic marlstones on the incision border. This heterogeneity suggests that f6 likely resulted from repeated mass wasting events before backfilling of the incision by fines.

In the central outcrop f6 comprises a slumped package of thin-bedded turbidites (Fig. 29), which can be correlated to the stratigraphy of nearby levées (Fig. 34), suggesting episodic levée failure toward the channel thalweg.

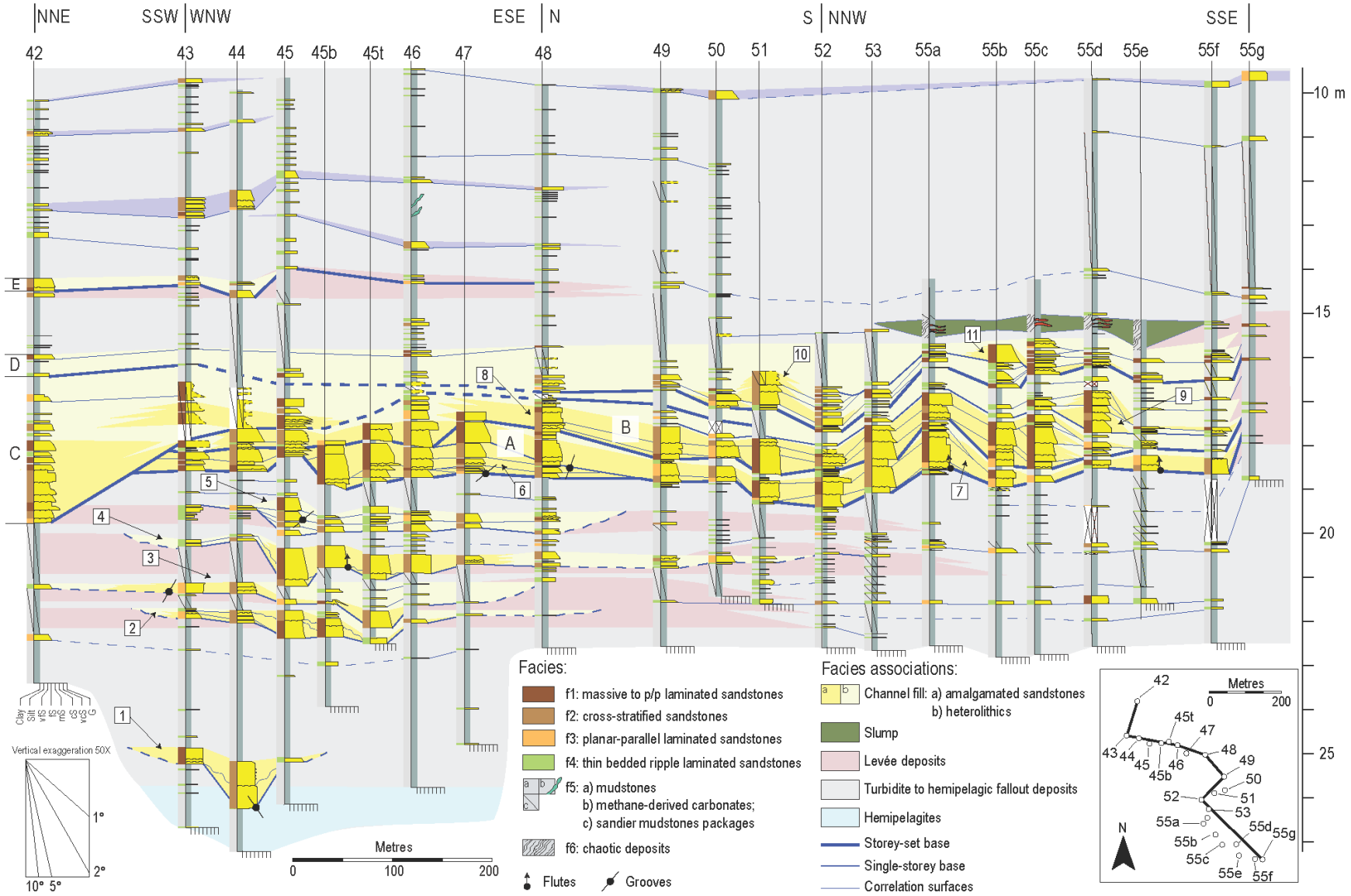

Fig. 34. Correlation panel of the lower half of Complex 4 (see Fig. 27 and inset map for location). The panel is largely oblique to palaeoflow (flow is away from the reader and toward the left).

3.4.3. Architectural elements and associated facies heterogeneity

3.4.3.1. Channel fills

The sand-prone channel fill of Complex 4 shows a considerable variability of size (see Tab. 3) and internal architecture. This variability will be addressed in the following sections, focusing on non-amalgamated single-storey channel fills first (Section 3.4.3.1), and then on storey-sets channel fills (Section 3.4.3.1), along with their elemental building blocks.

Single-storey channel fills

Single-storey channel fills are best observed in the lowermost part of Complex 4 (storeys 1-5) where they constitute relatively thin sand-prone bodies encased in mud-prone packages (Fig. 29 and Fig. 34). They have lateral extents in the range 200-450 m and aspect ratios in the range 185-1100 (Tab. 3). The sand-prone bodies have erosional bases, cutting as deep as ca. 1.5 m into the underlying mudstone, and relatively flat tops with a gentle dip toward the easterly quadrants (Fig. 34). Internally, they are made of few medium to thick sandstone beds with scoured bases, which stack vertically with either no or minor lateral offset toward the east (e.g., storey 2, Fig. 34). Component event beds are generally amalgamated, albeit the case point of storey 5 is comprised of non-amalgamated and relatively thinner event beds. The thickest, axial part of the channel fills is represented by amalgamated sandstones, either massive (facies f1) or cross-stratified (facies f2). Moving away from the channel axis these facies are replaced by less amalgamated and finer-grained beds of cross-stratified (facies f2), plane-parallel laminated (facies f3) and, more rarely, massive (facies f1) sandstones, some of which are capped by very thin co-genetic mudstone caps (facies f5). The less amalgamated character of this facies association (storeys 2-5, Fig. 34) indicates that sole erosion by subsequent flow was relatively low suggesting deposition in an off-axis setting. Farther away from channel fill axes, off-axis deposits are replaced by very thin- to thin-bedded channel margin heterolithics. These are alternations of horizontal plane-parallel (facies f3), ripple-laminated (facies f4) and cross-laminated (facies f2) fine to very fine-grained sandstones with co-genetic mud caps (facies f5) (single-storey 4, Fig. 34). Cm-thick massive and cross-laminated sandstones (facies f1 and f2,

respectively) may be present, suggesting occasional deposition by voluminous and concentrated flows (storeys 4 and 5, Fig. 34).

Single-storey channel fills

ID	Maximum observed thickness (m)	Maximum observed width (m)	Aspect ratio	Internal structure
1	**1.07**	**201**	**187**	Plane-parallel horizontal to sub-horizontal stratification
2	**0.63**	**413**	**651**	
3	**0.39**	**433**	**1101**	
4	**0.86**	**447**	**520**	
5	**0.85**	**375**	**440**	
6	1.20	512	428	Laterally accreted bedsets
7	1.09	444	409	
8	1.32	432	327	Laterally accreted bedsets
9	0.95	390	409	
10	1.10	411	372	Laterally accreted bedsets
11	2.14	387	181	
12	0.68	441	648	-
13	0.57	348	608	Laterally accreted bedsets
14	1.05	216	206	
15	0.72	174	240	
16	**2.54**	**436**	**172**	Laterally accreted bedsets
17	**2.84**	**447**	**157**	
18	**0.85**	**554**	**648**	Laterally accreted bedsets
19	**1.30**	**547**	**419**	
20	**0.99**	**312**	**316**	Laterally accreted bedsets
21	**0.84**	**448**	**531**	
22	**0.74**	**300**	**408**	
23	**2.44**	**472**	**194**	

Storey-sets

ID	Maximum observed thickness (m)	Maximum observed width (m)	Aspect ratio	Component storeys
A	1.90	502	264	6 and 7
B	1.77	429	242	8 and 9
C	3.07	393	118	Not distinguished
D	1.98	460	232	10 and 11
E	1.78	524	294	Not distinguished
F	2.04	851	417	13 to 15
G	3.88	80	209	16 and 17
H	1.65	641	387	18 and 19
I	3.47	566	163	19 to 22

Tab. 3. Maximum observed thickness and width for both single-storeys (above) and storey-sets. In bold, measurements and aspect ratios of fully exposed single-storey channel fills that are not cut by subsequent erosion.

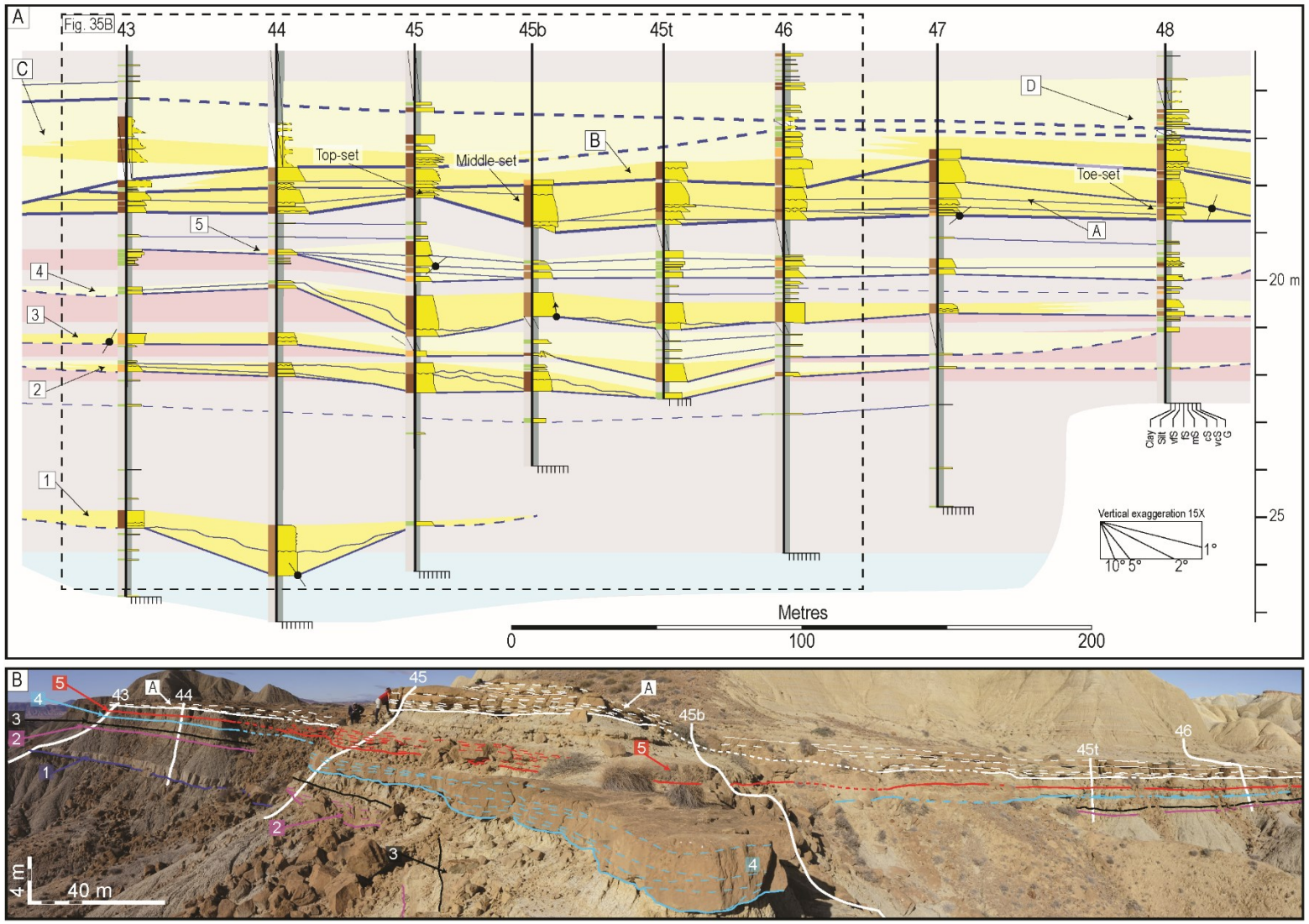

Fig. 35. (A) Detail of Fig. 34 illustrating the internal organisation and spatial stacking of channelised deposits of storeys 1-5 and storey-sets A-D. Note how single-storeys 1-5 are vertically stacked with minor lateral off-set. Differently from those above (storeys 6-7, sotreys-set A), they do not show appreciable internal lateral accrection. (B) Outcrop view of the represented correlation panel in picture A showing the lateral thickness variation and internal organisation of the storeys 1-5.

Storey-set channel fills

At the scale of storey-sets, channel fills are composed of two main types of bedsets, namely laterally accreted bedsets and heterolithic bedsets, differing each from another for internal bedding pattern and sand content. Their internal complexity (e.g., number of component event beds) suggests that their hierarchic rank is equivalent to that of single-storey channel fills, albeit amalgamation can locally make difficult to appreciate their boundaries.

Laterally accreted bedsets (Lateral Accretion Packages)

Laterally accreted bedsets are made of a few to several variably amalgamated event beds that stack laterally with coherent inclined bedding. They have sigmoidal cross-sectional shape (Fig. 28B) and can be interpreted as lateral accretion packages (LAPs hereafter; Abreu *et al.*, 2003; Wynn *et al.*, 2007; Pyles *et al.*, 2012; Arnott *et al.*, 2021). Within channel storey-sets, subsequent LAPs can be either locally amalgamated or intercalated with heterolithic bedsets (see below in this section).

Beautifully exposed examples of LAPs, cut at a range of angles with respect to the inferred direction of accretion, are those making channel storey-sets A to D from the lower part of Complex 4 (Fig. 34, Fig. 35A, Fig. 36, Fig. 37A), and channel storey-sets F, G, and I from the upper part of Complex 4 (Fig. 37B, Fig. 38, Fig. 39, and Fig. 40). It is anticipated that the aggradational nature of the upper part of channel Complex 4 (see Fig. 29, Section 3.4.1.1) makes difficult to disentangle the effects of early compaction (discussed in Section 3.4.3.3) from actual depositional geometries, thus preventing straightforward identification of LAPs.

The top-set facies association occupies the topographically higher part of the laterally accreted sigmoid, supposedly laying above the accreting inner channel bank (Fig. 28B). The top-set is generally a few tens of centimetres thick and displays an along-dip continuity of up to a few tens of metres (Fig. 35A and Fig. 36). It comprises very thin to thick sandstone beds, either amalgamated (storeys 8 and 16 in Fig. 36A and Fig. 38, respectively; storeys 13 and 14, Fig. 40) or partially preserving mudstone caps (storey 9 in Fig. 36A), which form fining- and thinning-upward sets. The most common sedimentary facies include massive (facies f1) and cross-

stratified (facies f2) sandstones and, subordinately, horizontal plane-parallel laminated (facies f3) to ripple-laminated (facies f4) very fine- to medium-grained sandstones.

The middle-set facies association constitutes the medial and thickest part of the sigmoid. It is composed of medium to very thick amalgamated sandstone beds (storeys 8-9, Fig. 36 and Fig. 37; storeys 16 and 17, Fig. 38 and Fig. 39, respectively), shows thicknesses in the range 1.0-3.5 m and along-dip extents in the range of 50-130 m. Because of the amalgamated nature of middle-sets, internal patterns in grain size, facies, and bed thickness are highly variable, albeit there are a few examples (storey 8, Fig. 36; storey 17, Fig. 38 and Fig. 39; storey 14, Fig. 40) with a basal thickening-coarsening upward and a top thinning- and fining-upward bedset. The most frequent sedimentary facies are massive (facies f1) or cross-stratified (facies f2), medium- to coarse-grained sandstones (storeys 16-17 and 22- 23, Fig. 38 and Fig. 39, respectively). In some cases, it solely comprises horizontal plane-parallel laminated (facies f3) or massive (facies f1) amalgamated sandstones (storeys 13-15, Fig. 38 and Fig. 39). In few cases, middle-sets were observed to terminate upward with cm-thick beds of fine- to medium-grained sandstones with horizontal plane-parallel (f3) and ripple laminations (facies f4) (storeys 8 and 17, Fig. 36 and Fig. 39, respectively).

The toe-set facies association shows thicknesses in the range 10-50 cm and along-dip lateral extents of few tens of metres (storey 9, Fig. 36). It comprises very thin to thin beds of fine- to medium-grained, horizontal plane-parallel and ripple-cross, laminated (facies f4) and massive (facies f1) sandstones with co-genetic mudstone caps (facies f5), generally organised into coarsening-thickening upward sets (storeys 6, 8, and 9, Fig. 35; storey 23, Fig. 40).

The direction of accretion of the LAPs varies across the Complex 4. In the lower part of Complex 4 (storey-sets A-D, Fig. 34), accretion is mostly toward easterly quadrants (storeys 8-9, Fig. 34 and Fig. 36), albeit there are examples in which bedding shows no apparent dip along the outcrop belt (these LAPs are cut along accretion strike), thus suggesting a more northerly directed accretion (storeys 6 to 8, Fig. 34, Fig. 35A and Fig. 36A). Conversely, in the upper part of Complex 4, the direction of lateral accretion seems to point toward the westerly quadrants (e.g.,

storeys 13 to 17 Fig. 38, Fig. 39, and Fig. 40) and to change in storeys 22-23, which display a main component of accretion toward the east.

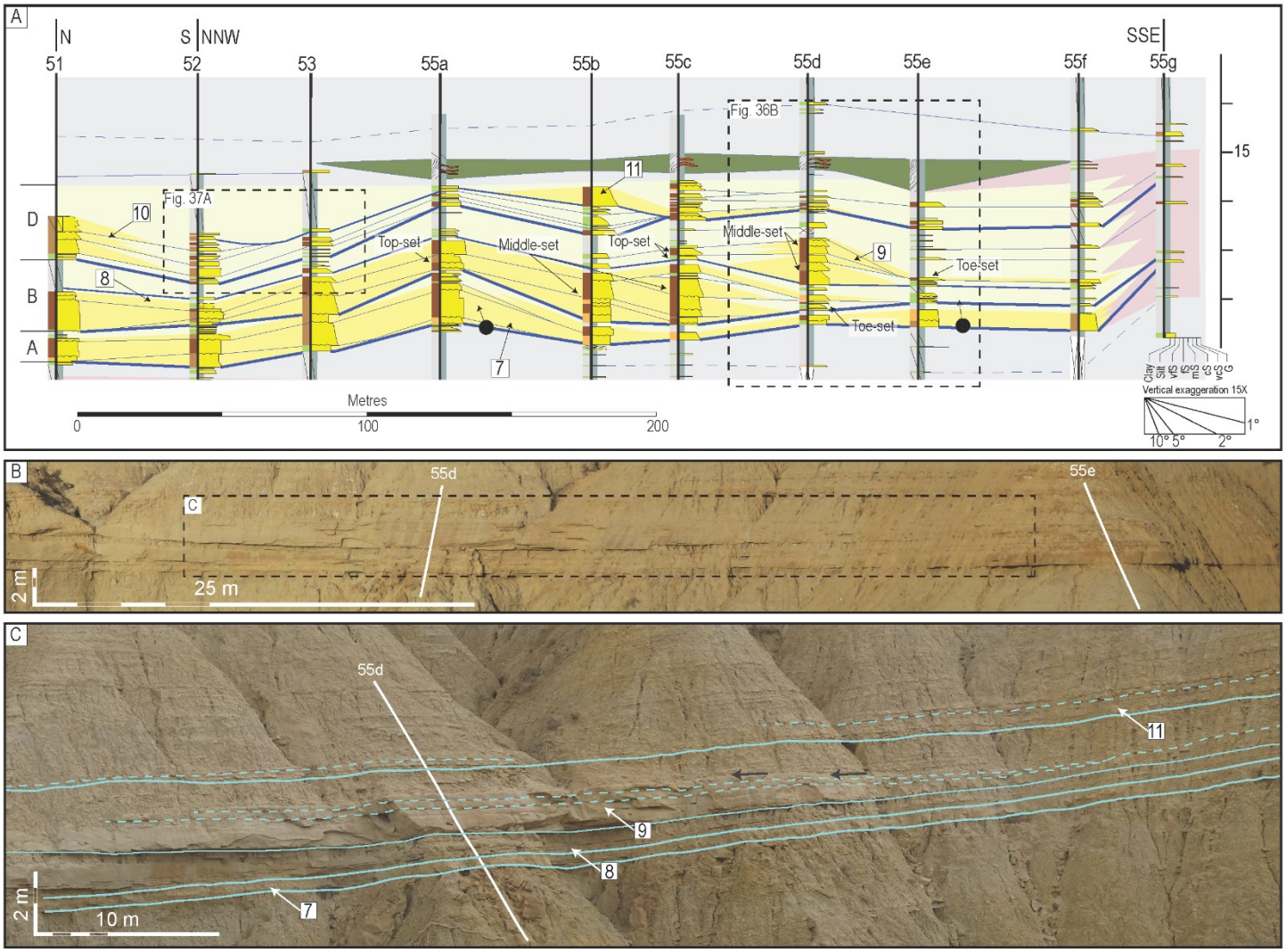

Fig. 36. (A) Detail of Fig. 34 showing the internal architecture of the single-storeys 8, 9, 10, and 11. Note how these are made of laterally accreted bedsets (LAPs; see Section 3.4.3.1) having largely sigmoidal shape and directed toward the easterly quadrants. Top-, middle-, and toe-sets identify differet portions of the sigmoid (see text for details). (B) Outcrop view of the correlation panel in picture A. (C) A detail of the outcrop view in picture B showing the lateral stacking of the single-storeys. Note how heterolithic deposits close in onlap while overlying storey 9 (see black arrows).

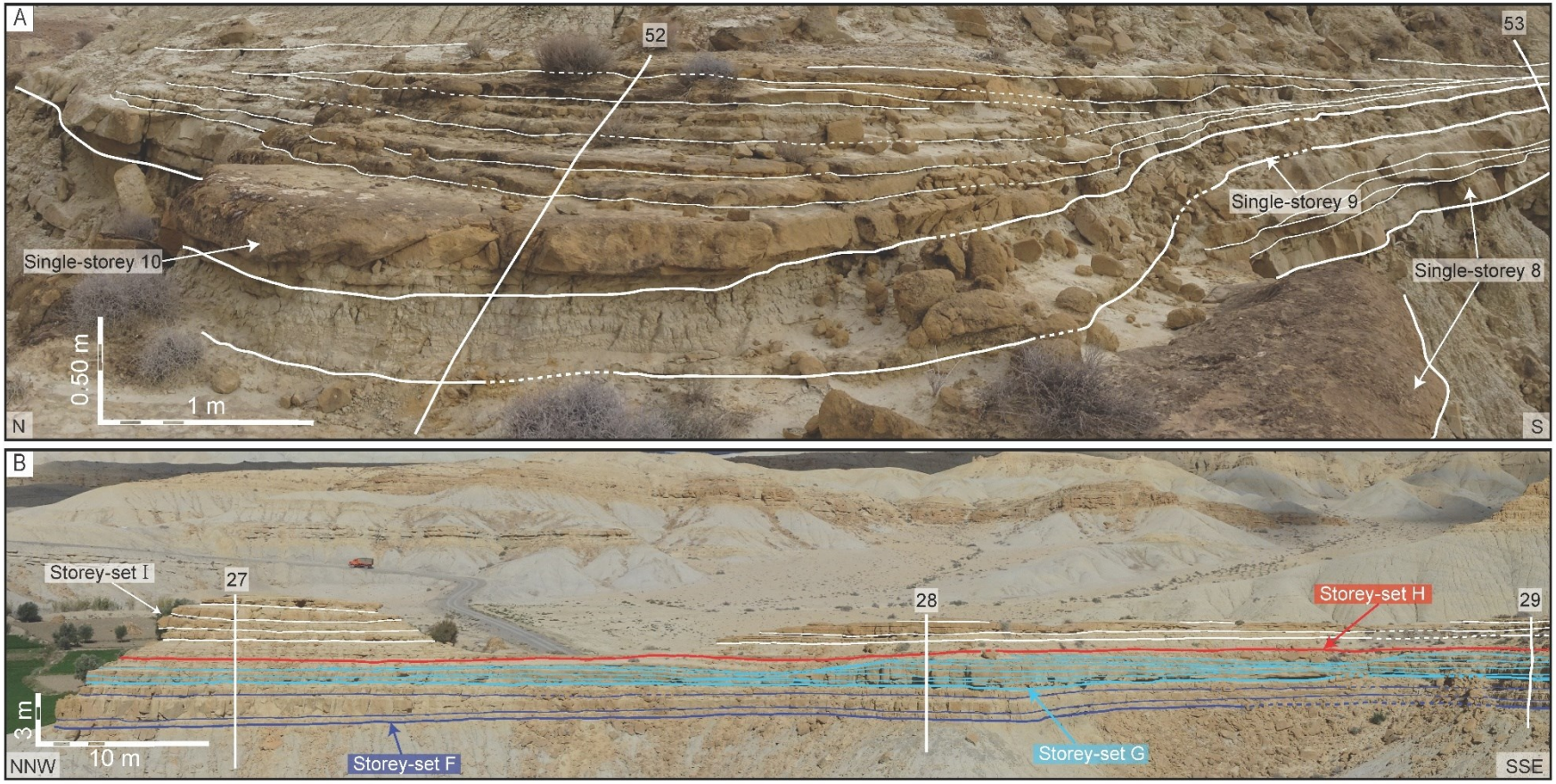

Fig. 37. (A) Single-storeys 8 to 10 from the lower half of Complex 4 (see Fig. 27, Fig. 29, and Fig. 36A for location). Note the sigmoidal shape of the laterally accreted bed set making storey 10 and how subsequent beds stack latoward the southeast. (B) Storey-sets F to I from the upper half of Complex 4 (see Fig. 29 for location). Note the component lateral accrected bedsets of these storey-sets along a transect oriented NNW-SSE (see Fig. 27).

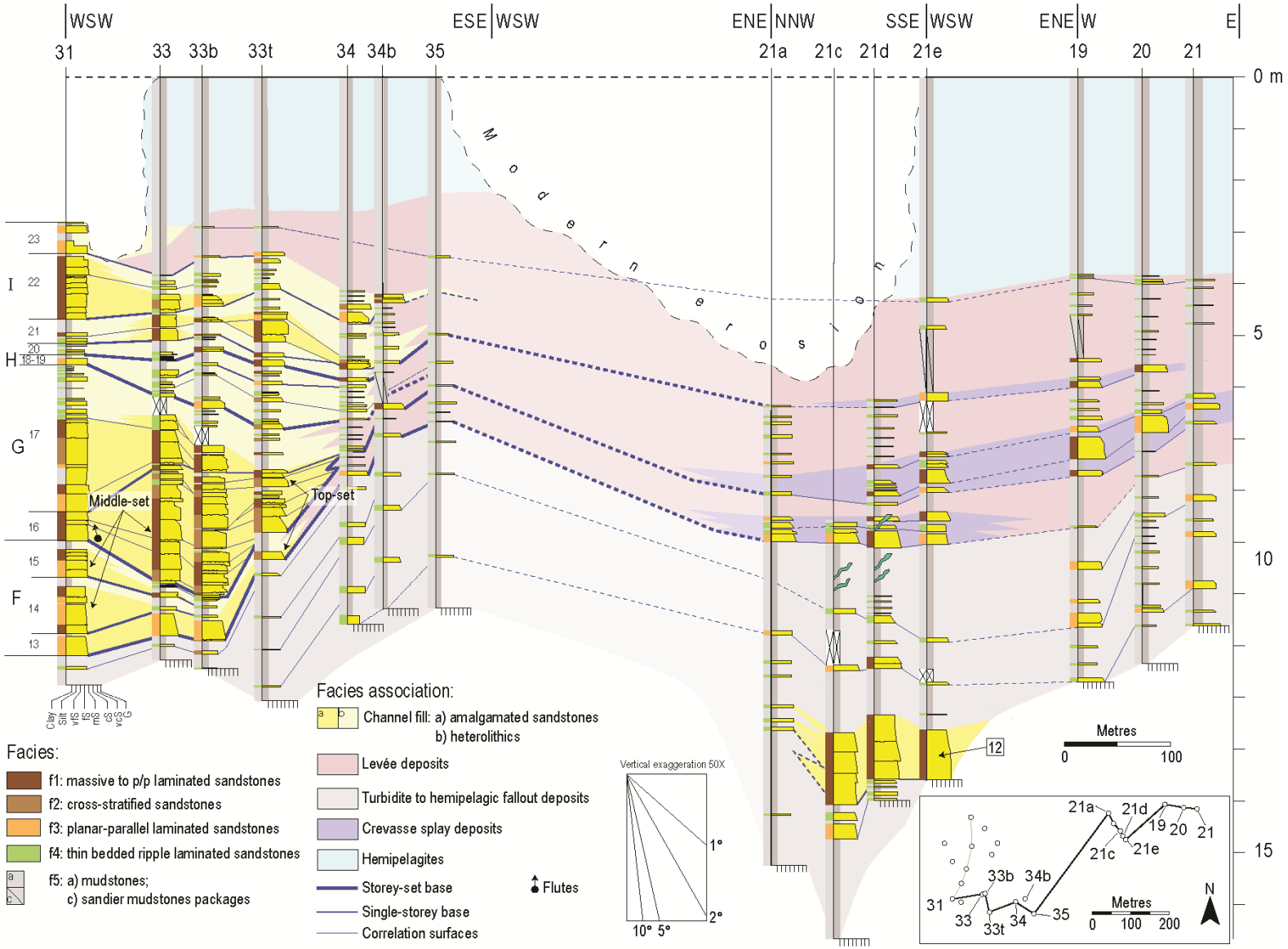

Fig. 38. Correlation panel of the upper half of Complex 4 (see Fig. 27 and the inset map for location). Note that the levées of storey-sets F to I are intercalated with sand-prone crevasse splay deposits (see Section 3.4.3.2).

Heterolithic channel fills

Subsequent single-storeys (e.g., storeys 10-11, Fig. 34 and Fig. 36) can be separated by decimetre-thick heterolithic packages consisting of very thin- to medium-bedded co-genetic sandstone-mudstone couplets. Heterolithics compensate the topography of the deposits below (e.g., storey 9, Fig. 36A and C; storey 20, Fig. 38), abutting on them with onlap geometry. The heterolithic packages are laterally contained by, or make transition to, the levée deposits (Section 3.4.3.2). The facies assemblage of the heterolithic channel fills comprises fine-grained horizontal plane-parallel (facies f3) to ripple- (facies f4) laminated sandstone, which typically grade upward into a co-genetic mud cap (facies f6). It suggests deposition from a range of high- to low-density waning flows.

A metre-thick example of heterolithic package (labelled H in Fig. 38, Fig. 39, and Fig. 40) is that separating the storey-set G from the storey-set I of the upper half of Complex 4. It can be widely correlated across the entire channel fill with little facies and thickness changes and traced laterally into correlative levée deposits (Section 3.4.3.2). It differs from the thinner equivalents separating single-storeys, because it contains a greater proportion of sandstone (Fig. 40), represented by relatively thicker and coarser-grained beds with a massive basal division.

3.4.3.2. Levée deposits

The best exposed levée deposits of Complex 4 belong to the storey-sets A to D (logs 55f and 55g, Fig. 34) and to the storey-sets F to I (Fig. 29, Fig. 38, Fig. 39, Fig. 40).

The levée deposits of storey-sets A to D crop to the southeast of these channel fills and are up to ca. 3 m-thick (Fig. 34). Internally, they are represented by mud-prone heterolithic deposits with a sand/mud ratio of ca. 0.25. They consist of alterations of very thin to thin beds of fine-grained sandstone (facies f4) and, subordinately, plane-parallel laminated fine to medium-grained sandstones (facies f3), and decimetre- to metre-thick mudstone beds (facies f5). Based on the direction of lateral accretion of the channel fill sandstones (Section 3.4.3.1), these can be interpreted as outer bank levées. The presence of a deformed to chaotic heterolithic package up to ca. 1 m-thick atop of the channel fill storey-set D (Fig. 36), with a locally preserved stratigraphy

matching that of nearby levée deposits in place, suggests these were locally prone to mass wasting.

The levée deposits of the storey-sets F to I (Fig. 29) are exposed on both sides of the correlative channel fills but best preserved to the east, where they can be followed along-strike for ca. 500 m. The westerly directed accretions of storey-set channel fills F and G (Section 3.4.3.1) implies that the correlative heterolithics to the west and to the east might represent outer and inner bank levées, respectively (Fig. 38, Fig. 39, and Fig. 40). Component facies of the inner bank levées of these storeys sets are similar to those of storeys-sets A to D, albeit thicker and coarser sandstones beds are relatively more frequent, thickening toward the east. Consequently, in the same direction, sand/mud ratio and cumulative levée thickness increase from ca. 0.25 to ca. 1.1 and from 1.8 m to 2.8 m, respectively (Fig. 38). The thicker and coarser sandstone beds are up to 0.9 m-thick and can be massive (facies f1), with horizontal plane-parallel laminations (facies f3) and ripple cross-lamination (facies f4). Facies f1, f3 and f4 are separated by mudstone caps (facies f5) and stack vertically to form bedsets with a minimum lateral continuity of ca. 600 m (Fig. 38 and Fig. 40), locally characterised by coherent thickening- and coarsening- and then thinning- and fining-upward trends. Similarity with analogue deposits interbedded with levée deposits (Beaubouef, 2004b; Wynn *et al.*, 2007) suggests that these bedsets represent crevasse splays.

When crevasse splay deposits are removed, sand-mud ratio is ca. 0.45. The outer bank levée of storey-sets F and G is only partly exposed, but its upper part appears devoid of sand intercalations interpretable as crevasse splay deposits and is characterised by a sand to mud ratio of ca. 0.22.

The easterly-directed accretion of the storey-set channel fill I indicates that the correlative heterolithics to the west and to the east may represent inner and outer bank levées, respectively (Fig. 40). The inner bank levée shows a sand to mud ratio of ca. 0.4 and a thickening-coarsening to thinning- and fining-upward trend. Conversely, the outer bank levée is up to 2.8 m-thick in the most proximal section and thins to 2.2 m over a distance of ca. 70 m to the east, while the sand to mud ratio decreases from 0.18 and 0.07 (Fig. 40).

Because of the relatively less sandy character of the lowermost part of Complex 4, cover from regolith makes impractical to precisely establish correlation between channel fills and laterally associated heterolithics. Nonetheless, these heterolithics constitute most of the stratigraphy of easterly sections (see right and side of Fig. 34), which, together with the vertically stacked arrangement of single-storey channel fills 2-5, is suggestive of establishment of a relatively stable channel belt, albeit with subtle muddy levées (see discussion in Section 3.5.2).

The inner bank levée is solely correlated for single-storey 5 (logs 43 and 44, Fig. 34), where it is up to 0.5 m-thick, with a sand to mud ratio varying between 0.4 and 0.1 from more proximal to distal positions. Conversely, the thickness of the outer bank levée varies in the range 0.3 and 0.75 m in storeys 2 to 5 (Fig. 34), thinning away from the channel-axis. The outer bank levée shows a sand to mud ratio between 0.71 and 0.1 from proximal to distal locations (Fig. 34).

The single-storey levée types of component facies are similar to those of storeys-sets levées, except for the higher sand content nearby the channel margins, especially in the outer bank.

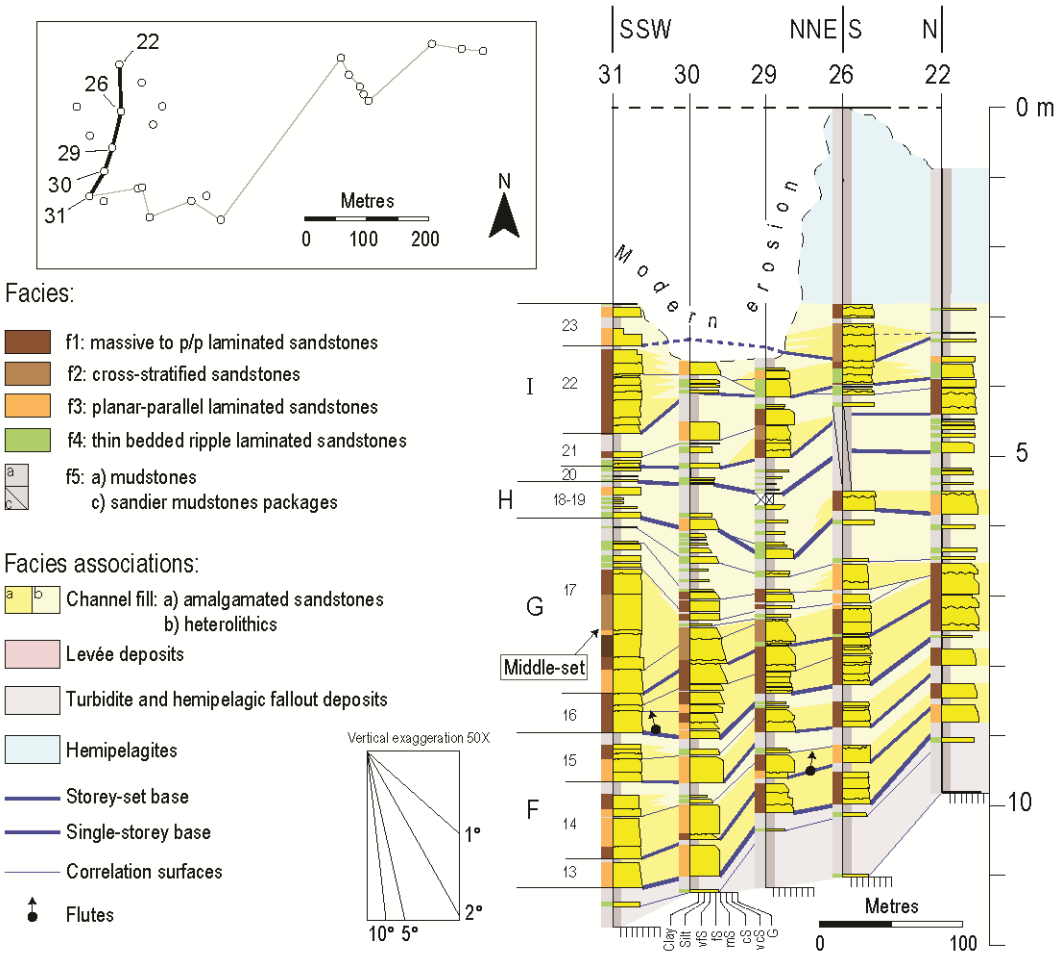

Fig. 39. Correlation panel of the upper half of Complex 4 in the central outcrop area (see the insert map and Fig. 27 for location). The represented fence is oriented ca. parallel to the mean palaeoflow (i.e., ca. towards NNE).

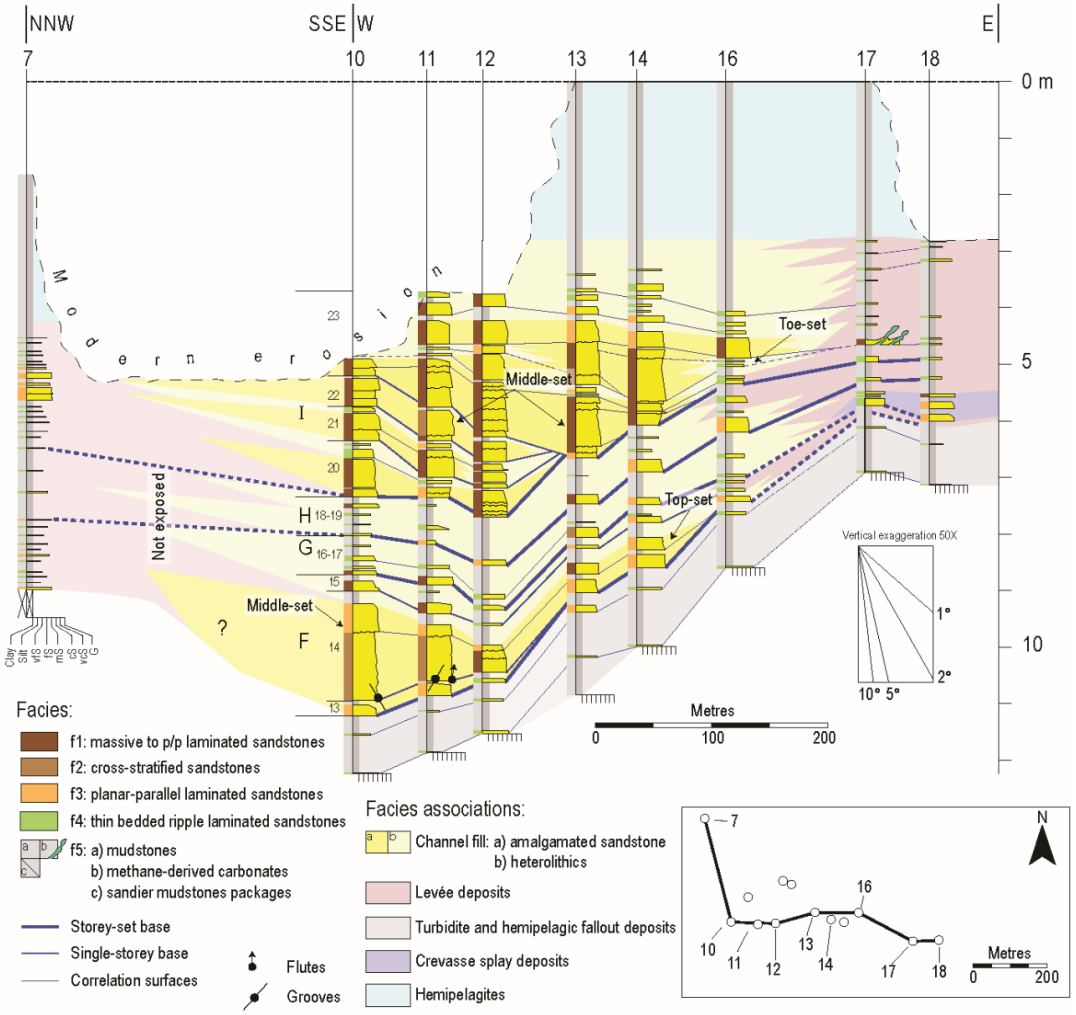

Fig. 40. Correlation panel of the upper half of Complex 4 in the central north-western outcrop area (see the insert map and Fig. 27 for location). The represented fence is oriented almost perpendicular compared to the mean palaeoflow (i.e., ca. NNW-NNE). Note how storey-sets F to I are here confined between their levées.

3.4.3.3. Storey-set spatial stacking

The spatial stacking of the storey-sets varies stratigraphically. The storey-set channel fills of the lower Complex 4 (A to D in Fig. 27, Fig. 29, and Fig. 34) are laterally stacked and amalgamated to form a larger sand-prone body. This is up to ca. 5 m-thick and at least ca. 1100 m wide (its width exceeds that of total length of the central outcrop; Fig. 27). It is bounded by a composite basal surface eroding up to at least 1.5 m into the underlying deposits. These storey-sets are internally made of variably amalgamated LAPs with locally preserved heterolithics intercalations (see Section 3.4.3.2). The direction of LAPs accretion is toward easterly quadrants.

Stratigraphic superimposition indicates that storey-sets A and B constitute the oldest channelised sets. The lack of significant grain size and facies breaks in between may indicate that these storey-sets were deposited in continuity. They are cut to the west by storey-set C (Fig. 30C-D and Fig. 34), which means a westward shift of the channel form and local re-incision of previous deposits. Storey-set C (not detailed because mostly exposed along an inaccessible cliff; Fig. 30C and Fig. 33C) is comparatively thicker than all other storey-sets of Complex 4 (Tab. 3), suggesting it may in reality encompass e few to several storey-sets. Deposition continues with establishment of the relatively less sandy and amalgamated storey-set D (Fig. 34, Fig. 36, and Fig. 37A), which records a reduction in sand content and a further shift of the active channel toward the east.

The upper part of Complex 4, superbly exposed to the west of the Zobzit river course (Fig. 27, Fig. 31A-C, and Fig. 37B), is composed of four storey-set channel fills (labelled F to I; Fig. 29) which can be either relatively sand-rich and amalgamated (storey-sets F, G, and I), or mud-prone and heterolithic (storey-set H). Because of differential early compaction, the geometry, internal structure, and spatial stacking of these storey-sets is elusive unless sedimentary logs are flattened on appropriate datum planes (i.e., which can be reasonably assumed to be flat at time of deposition). Flattening to such a datum (Fig. 41), highlights that the base of these storey-sets is typically slightly to non-erosional on what is thought to represent the inner bank, as well as below at any location below the heterolithic channel fill of storey-set H, and relatively more incisional elsewhere. On the other hand, storey-sets tops show upward convexity (Fig. 41) and some small-scale rugosity (amplitude less than few metres and wavelength is in the order of a pair of metres, which is far less

than average log spacing; Fig. 38, Fig. 39, and Fig. 40) related to presence of medium to large scale bed forms (facies f2). Despite the geometry of the top surface of the deposit below, subsequent storey-set channel fills and correlative levées appear to stack mostly vertically (Fig. 38, Fig. 39), with very minor off-set toward the east up-section (i.e., storey-set I; Fig. 40). As a result, the overall architecture of the upper part of Complex 4 is one of a largely aggradational type with well-developed levées.

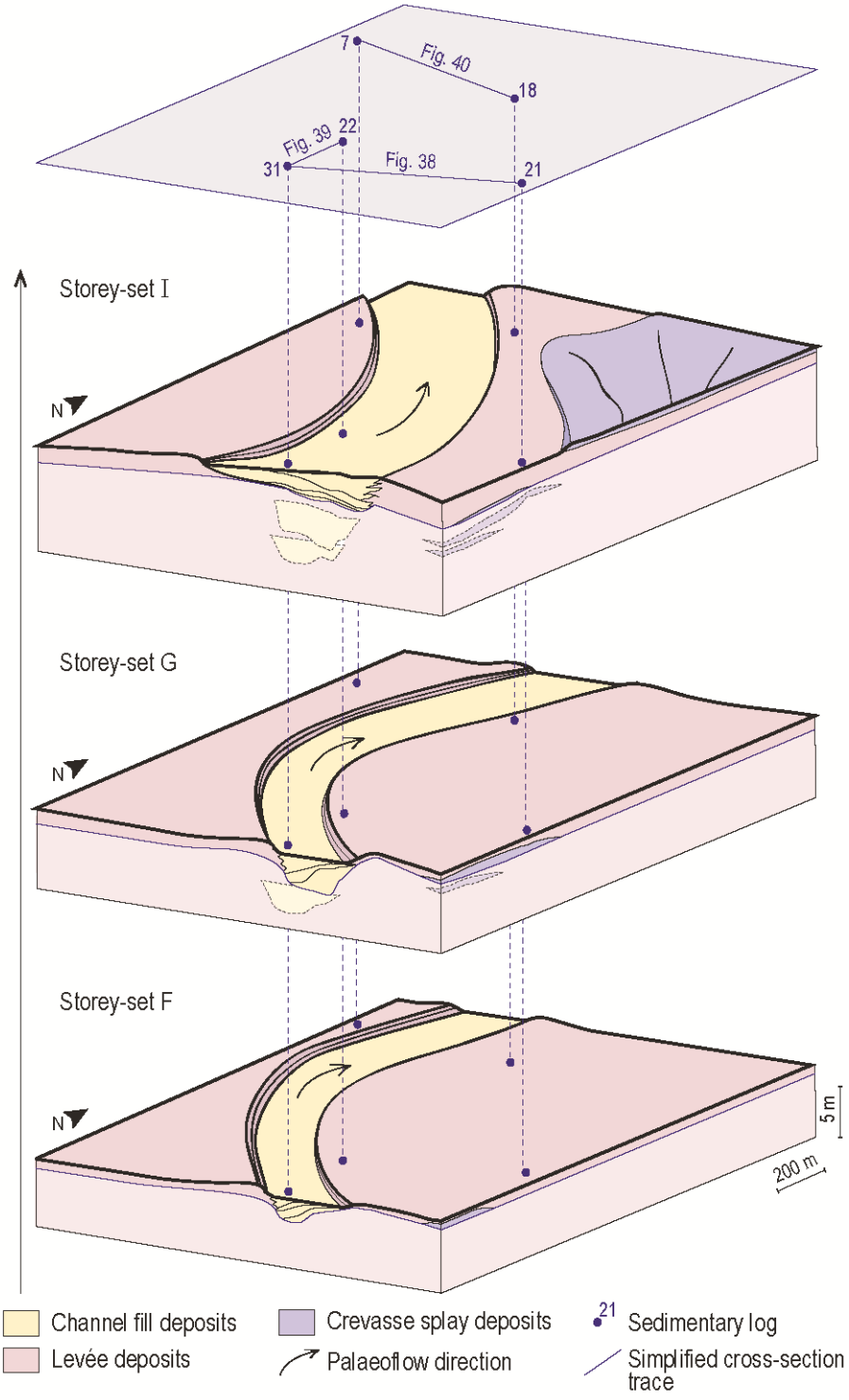

Fig. 41. Block diagrams representing Complex 4 evolution between storey-sets F and I. Each storey-set was flattened on a local marker datum to show the original depositional architecture net of compaction. Storey-set F and G LAPs were flattened on their top-set. Storey-set I is flattened on the datum bed for the Complex 4 (see Fig. 29). Note the different LAPs direction of accretion and downcurrent sweep of the meander between storey-sets F-G and I.

3.5. Discussion

3.5.1. Depositional hierarchy and its likely meaning

Refining the existing hierarchical classification of the sedimentary architecture of channelised turbidites (see Cullis *et al.*, 2018 for a review), some of which proposing likely time durations for each rank (e.g., Mutti & Normark, 1987, 1991; Ghosh & Lowe, 1993), is beyond the aim of this contribution. Nonetheless, the availability of constraints from magnetochronology (Krijgsman *et al.*, 1999; Krijgsman & Langereis, 2000) on depositional rates, allow to loosely estimate the time duration of channel-levée Complex 4 and speculate on the meaning of its component sedimentary units, which can be paralleled with the existing hierarchical schemes.

Separated by several decimetre- to metre-thick mud-prone intervals, single-storeys 1-5 from the lowermost part of Complex 4 can be unequivocally recognised as the product of many distinct pulses of coarse sediment input to the studied part of the system (waxing-waning cycles of McHargue *et al.*, 2011, *cf.* with 'build-cut-fill-spill' sequences of Gardner & Borer, 2000). Their scale and internal complexity (i.e., they are bedsets composed of a few to several event beds), comparable to that of 'elementary' or 'single story' channel fills reported by Gardner & Borer (2000) from the Brushy Canyon (Fig. 20) and the 'channel storeys' of Sprague *et al.* (2005), suggests they represent the elemental building blocks of the studied channelised complex.

Nonetheless, it has been shown (Section 3.4.3.1) how the character of this elemental building blocks may vary stratigraphically, reflecting changes in channel morphodynamics (see Section 3.5.2). For instance, single-storeys constituting the remainder part of Complex 4 are represented by LAPs that are often amalgamated and problematic to delimit. A case point is the sedimentary package of storey-sets A to D, in which the relatively low aggradation of the channel belt (see Section 3.4.3.3) resulted in widespread amalgamation and likely less than complete sedimentary record. However, there are cases where subsequent LAPs, both at the scale of single storeys (e.g., storeys 9 and 11, Fig. 36; storeys 14 and 15, Fig. 38 and Fig. 40) and storey-sets (e.g., storey-sets G and I, separated by the heterolithic storey-set H; Fig. 38, Fig. 39, and Fig. 40), are separated by mud-prone heterolithics that are continuous throughout the entire channel fill and reflect lapses of reduced sediment input. This indicates that, although lateral accretion itself reflects an autocyclical process of channel bend

expansion, the building up and the sedimentary heterogeneity of higher-rank laterally accreted bodies can be modulated by sedimentary input variations (McHargue *et al.*, 2011). A similar variability in degree of LAPs amalgamation has been reported by Abreu *et al.* (2003) who explained it as a response to changes in magnitude, energy, variability of discharge and sediment load composition of the turbidity currents.

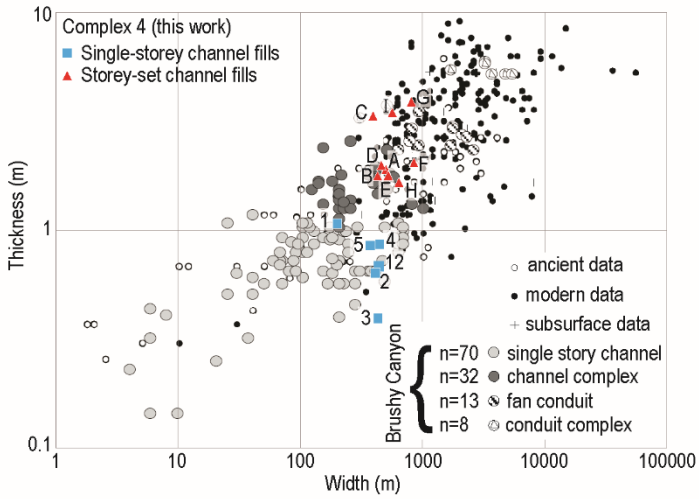

Fig. 42. Bi-logarithmic plot of thickness Vs. width of channels-fills comparing data from the present study (single storeys and storeys-sets as per legend, identified with numbers and letters, respectively; see Tab. 3) to those from the Brushy Canyon and other ancient systems, and modern analogues (modified after Gardner & Borer, 2000).

At least 9 storey-sets (10, acknowledging that, although non-amalgamated, single-storeys 1-5 form a set of similar thickness and temporal scale to that of the storey-sets above) and 23 single-storeys were recognised within the channel-levée Complex 4, albeit amalgamation and erosion suggest their number can be larger (especially that of single-storeys).

An estimation of the time duration of Complex 4 can be derived by the magnetochronology (Krijgsman & Langereis, 2000), who attributed the sedimentary package containing it to the magnetochron C3Br.2n. This corresponds to an average depositional rate of 0.84 m/kyr that, however, encompasses both the hemipelagic and the turbidite components. Therefore, the time duration of the ca. 30 m-thick Complex 4 can be loosely constrained to be <36 kyr, albeit it might have been significantly shorter since turbidite accumulation rates are typically much higher than those of hemipelegic deposits. It can be thus concluded that if single-storeys and storey-sets of Complex 4 were actually the result of changes in sediment input (albeit not necessarily cyclical), these might have developed over scales

of several hundred to a few thousand years, respectively (*cf*. with Payros & Martínez-Braceras, 2014; Catuneanu, 2019, 2020; Marini *et al.*, 2020).

3.5.2. Stratigraphic evolution of channel-levée complex 4

The stratigraphic organisation of channelised sandstones vs. mud-prone levée facies and of hemipelagic deposits composing Complex 4 (Fig. 29) can be used as constraints for devising an evolutionary model of the channel belt and inferring likely control on its development.

As detailed below, three main evolutionary steps can be envisaged, consisting of an early phase of channel belt inception and a late phase of aggradation, separated by a relatively long intervening phase of lateral migration.

3.5.2.1. Channel belt inception

Complex 4 begins with five single-storey channel fills (Section 3.4.3; Fig. 29, Fig. 34, Fig. 35, and Fig. 43A) separated from one another by metres-thick mud-prone intervals that become progressively thinner up-section. Although vertically stacked with minor lateral off-set, these channel fills are not contained either within a master erosion nor high-relief levées. Rather, their vertical stacking suggests that in subsequent waxing phases (McHargue *et al.*, 2011a) the denser and erosive part of the flow was trapped within the under-filled (though veneered by fines) channel form of the preceding single-storey. Thus, single-storey channel fills 1-5 are best interpreted to collectively represent the down-dip continuation of a relatively more incisional channel (e.g., Cronin *et al.*, 2000; Navarro *et al.*, 2007; Marini *et al.*, 2020), which established as turbidity currents were first delivered to the studied section of the slope and remained active through multiple waxing phases (McHargue *et al.*, 2011a). It is reasonable to assume that, further down-stream, the channel hosting deposition of single-storey channel fills 1-5, progressively lost confinement and become more distributive, resulting in a dispersed and offset channel fill pattern (Labourdette & Bez, 2010; *cf.* with ‘disorganised pattern’ in Funk *et al.*, 2012).

A similar architectural style witnessing an early phase of channel inception are those of the channelised deposit of Ross Sandstones Formation of western Ireland (see formation of megaflute in Elliott, 2000). An inception phase characterised by relatively straight conduits has been also

reported, albeit developed at large scales, from the modern Congo system (Babonneau *et al.*, 2010) and the Pleistocene Mississippi system (Peakall *et al.*, 2000).

3.5.2.2. Channel belt migration

Up-section, Complex 4 continues with the variously amalgamated storey-sets A-D, which are internally characterised by LAPs and stack spatially so as to suggest a relatively prolonged phase of lateral migration and minor aggradation of the channel belt.

Direction of LAPs accretion indicates that storey-sets A-B were deposited in substantial continuity on the inner bank of a bend as it expanded toward the east relatively thin levées accumulated at the outer bank (Fig. 34). Instead, by capping with erosional contact previous deposits, storey-set C marks a relocation of the channel to the west, followed by a further phase of east-directed bend swing and consequent accretion at the inner bank (Fig. 43B). This change in the channel course may reflect either a process of channel sweep with consequent erosion of previous deposits in the outer cut-bank or, alternatively, be the result of an up-dip avulsion. However, the first model seems unlikely, as it might require a contemporaneous westward shift of the channel axis to explain the lateral continuity of storey-set C (in excess of ca. 260 m; see Fig. 29 and Tab. 3).

Direction of accretion of LAPs and a decrease in grain size and degree of amalgamation from storey-set C through storey-set D would suggest that, although continuing its westward expansion, the channel belt started to aggrade, as progressively finer sediments were delivered to the system. Laterally migrating channels producing LAPs similar to those of storey-sets A-D are documented both in outcrop (Elliott, 2000; Abreu *et al.*, 2003; Navarro *et al.*, 2007; Wynn *et al.*, 2007; Li *et al.*, 2018; Arnott *et al.*, 2021) and in the subsurface (Babonneau *et al.*, 2010; Labourdette & Bez, 2010; Janocko *et al.*, 2013; Reimchen *et al.*, 2016), and are commonly interpreted to reflect a low sediment accommodation regime. This may relate to a local bathymetric control (e.g., due to halokinesis, MTDs deposition, and tectonic deformation; Janbu *et al.*, 2007; Kane *et al.*, 2012; Tek *et al.*, 2021) or signify that the channel profile is close to be at grade (Kneller, 2003). Whichever the case, while LAPs formation indicates that some of the sediment load was trapped in the studied section of the

system, the low degree of channel aggradation signifies that a proportionally greater volume of sediments might have been bypassed to be deposited downcurrent.

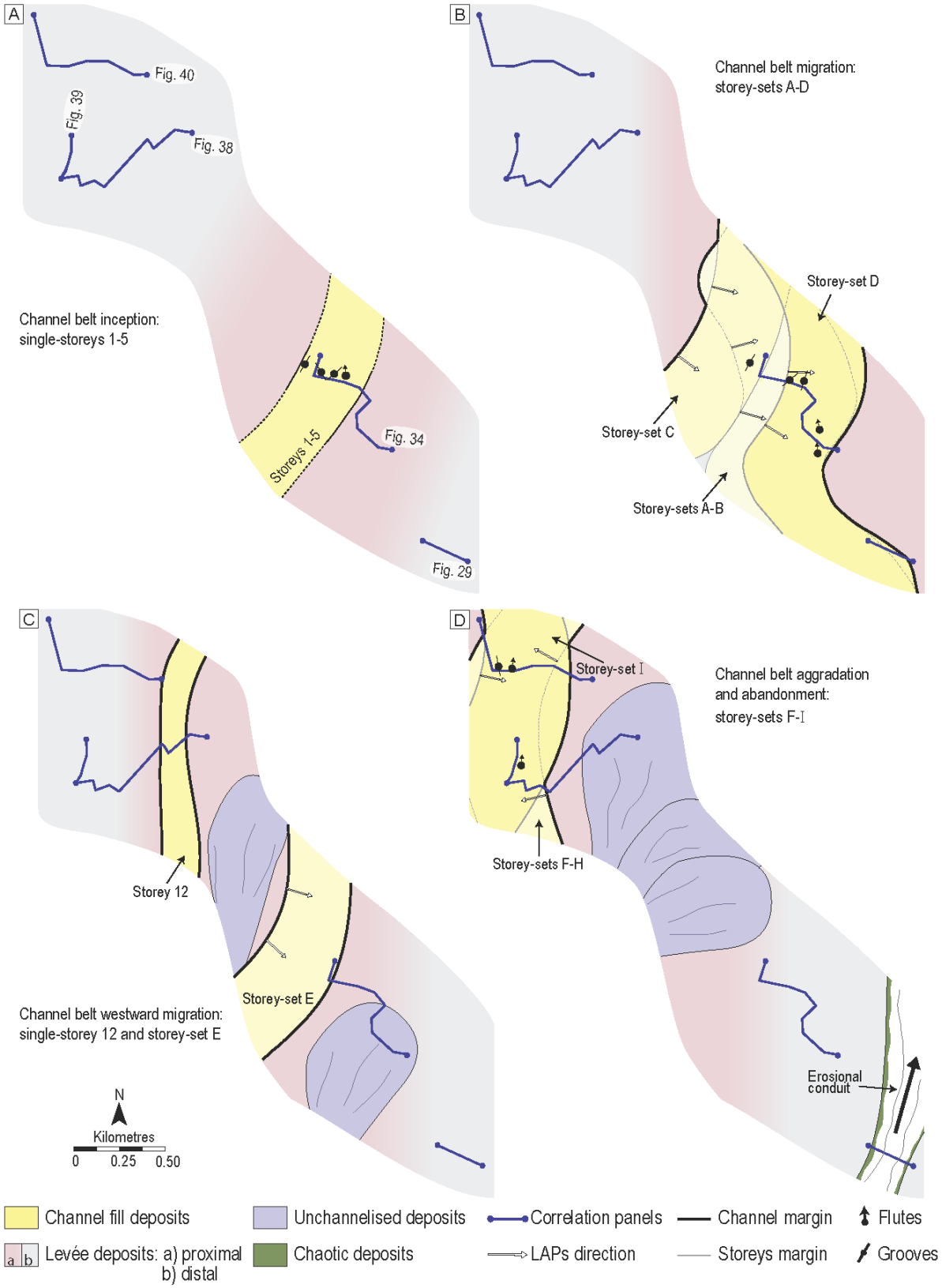

Fig. 43. Sketch map illustrating the inferred evolution of the levéed channel belt of Complex 4 with location of correlation panels, palaeocurrents, and direction of accretion of LAPs used as constraints for interpretation.

3.5.2.3. Channel belt aggradation and abandonment

Establishment of the channel belt of storey-sets F-I (Fig. 29) is preceded by a ca. 6 m-thick relatively muddy interval, in which interbedded non-channelised turbidites and hemipelagites are locally intercalated by sparse channel fills (e.g., storey-set E and single storey 12; Fig. 29). Although the mudstone (i.e., turbidite and hemipelagic) fraction is significant (ca. 64%), this interval is typically sandier than levée packages observed elsewhere (Section 3.4.3.2), which makes it hardly interpretable as laterally correlative to coeval channels located elsewhere along strike. Rather, its non-channelised turbidite component might represent relatively muddy terminal splays that veneered the previous channel belt during a relatively prolonged phase of reduced sediment input to the slope. In this view, the relatively less frequent channelised deposits may represent the fill of ephemeral distributive channels that reached this far at phases of increased sediment input.

Thus, following this interval of relatively condensed turbidite deposition, the uppermost section of Complex 4 records an increase of sediment input accompanied with the onset of an aggradational channel with well-developed levées. These confined an active channel with an estimated width in the range 560-850 m.

The storey sets F-I channel fills are made of LAPs with stratigraphically variable direction of accretion, which indicates that, while aggrading, the channel was not only subject to swing (at the scale of single-storeys and storeys-sets) but also to sweep (e.g., see the contrasting direction of accretion of storey-sets F-G and I; Fig. 41).

A similar aggradational architecture, with vertically stacked LAPs having contrasting direction of accretion, has been documented at different scales, both in outcrop (e.g., the Kusuri Formation form the Sinop Basin of Turkey; Janbu *et al.*, 2007) and in the subsurface (Babonneau *et al.*, 2010; Labourdette & Bez, 2010; Janocko *et al.*, 2013), locally accompanied with variability in degree of LAPs size, lithological fractions, and amalgamation (Abreu *et al.*, 2003).

Aggradational channels generally forms in the lower tract of out-of-grade systems tending to achieve an equilibrium profile (Pirmez *et al.*, 2000; Kneller, 2003; Samuel *et al.*, 2003b; Hodgson *et al.*, 2011) or up-dip of topographic obstacles in systems with an evolving bathymetry, as a result of flow blocking by growing tectonic structure and salt diapirs, MTDs, and a combination thereof (Kane

et al., 2012; Hansen *et al.*, 2015, 2017; Torres Carbonell & Olivero, 2019; Watson *et al.*, 2020; Park *et al.*, 2021; Tek *et al.*, 2021). Alternatively, Kneller (2003) proposed that changes in flow parameters toward less dense, thick, and finer-grained flows might force a channel to aggrade, disregarding of its along dip depth profile.

The last step of the stratigraphic evolution of channel-levée Complex 4 is its deactivation with consequent veneering by marlstones. Albeit cover hampers tracking to the north the erosional conduit of the southern outcrop (logs 56d-p, Fig. 29), it is believed that this might correlate to the abandonment of the aggradational channel of storey-sets F-I. Particularly, the conduit may have formed following breeching of the right-bank levée up-dip (Fig. 43D), as turbidity currents were rerouted toward a lower-lying seafloor to the N-NE (i.e., away from the levéed channel of the storey-sets) eroding and channelling into older deposits.

3.5.3. Can an equilibrium profile model explain the observed changes of architectural styles?

The stratigraphically tripartite architectural style of channel-levée Complex 4 is intriguing, as it reflects changes in channel morphodynamics occurring over a time-scale that is most likely in the order of a few kyr (see Section 3.5.1). This stratigraphic change of architectural style is developed over a thickness of ca. 30 m, which suggest that similar organisation of channelised deposits might be underappreciated in subsurface analogues.

Stratigraphic transitions from relatively small incisional channel fills similar to that of the inception phase (see section 3.5.2.1) to larger and more stable channels with LAPs, such those of the channel belt migration phase (see section 3.5.2.2), have been documented elsewhere both at outcrop (e.g., Elliott, 2000; Navarro *et al.*, 2007; Hodgson *et al.*, 2011; Funk *et al.*, 2012) and in the subsurface (e.g., Peakall *et al.*, 2000; Babonneau *et al.*, 2010; Labourdette & Bez, 2010). Several Authors suggested that this stratigraphic evolution might reflect the initial adjustment of a channel to an ‘equilibrium’ planform as it establishes onto a slope that is close to grade. Once the equilibrium state is reached, neither significant deposition nor erosion occur (Pirmez *et al.*, 2000; Kneller, 2003; Hodgson *et al.*, 2011), so that the equilibrium planform will remain stable and the channel itself acts dominantly as a bypass zone.

In the studied example, the channel belt migration phase (see section 3.5.2.2) seems to encompass a relatively short period of high sediment supply, during which rapid channel bend swing, accompanied with avulsion events, were capable of forming laterally extensive sandstones, >1 km wide and ca. 4 m-thick. This implies that, while a significant amount of sand was deposited by lateral accretion processes at the inner bank, a similar volumetric fraction of previous slope deposit (i.e., hemipelagites and previously formed levée deposits) undergone degradation in the outer cut bank. In keeping with the existing models (Pirmez *et al.*, 2000; Kneller, 2003; Deptuck et al., 2007; McHargue et al., 2011), the transition from the inception phase to the migrational phase can be viewed as the response of channel morphodynamics to an augmented sedimentary input, whereby the channel adjusted its sinuosity in order to reduce the local slope gradient.

Observations made on numerous submarine channels and channel kinematics modelling (Peakall *et al.*, 2000; Deptuck *et al.*, 2007; McHargue *et al.*, 2011a; Jobe *et al.*, 2016) would predict that, once at equilibrium, overbanking of fines would promote levée growth, discourage avulsion, and ultimately result in channel aggradation (Jobe *et al.*, 2016). It can be said that the resulting depositional architecture is one with a 'hockey stick' trajectory (*sensu* Jobe *et al.*, 2016) of channel fills that are initially laterally staked and evolve stratigraphically into a vertically stacked pattern.

However, the stratigraphic evolution of channel-levée Complex 4 does not fit a simple a 'hockey stick' model, in that establishment of its late aggradational phase is preceded by a relatively prolonged phase of reduced sediment delivery to the studied section of the slope. Whether this reflected either a diminished sediment availability in the catchment area (e.g., reduced run-off?) or augmented shelf sediment storage (e.g., due to a relative sea level rise) is unclear.

Nonetheless, it is likely that, all in all, this phase resulted in increased trapping of sediments on the slope up-dip of the studied outcrop, which aggraded to adjust to equilibrium.

Thus, it can be argued that, following the flow parameter model of Kneller (2003), the aggradational phase of channel-levée Complex 4 reflected the response of the channel to an upturn of sediment input, which might have forced degradation of the slope profile in up-dip locations and establishment of a high-accommodation regime in the lower tract of its course.

3.6. Conlusions

The up to ca. 30 m-thick channel-levée Complex 4 constitutes part of the Tachrift Turbidite System (Late Tortonian-Messinian) and was accumulated onto the south-bounding slope of the Taza-Guercif Basin of NE Morocco, which hosted contemporaneous deposition of hemipelagic marlstones. As it turned out by physical correlation of 84 sedimentary logs spanning an outcrop belt ca. 3.4 km-long oblique to palaeoflow, the studied units is characterised by stratigraphic changes of sedimentary architectural style linked to the evolution of a levéed sinuous channel. Results provide the following insights into kinematics of channel belt evolution and sedimentary heterogeneity of the resulting deposits:

- The elemental building blocks of the channel-levée Complex 4 are single-storey channel fills and associated levées. These are sets of several event beds that can stack vertically with minor off-set or form laterally accretion packages (LAPs) interpreted to result from channel bend expansion.
- Single-storeys can be locally amalgamated but are often separated one form another by relatively muddier intervals. They are interpreted to reflect phases of high sediment supply and can group into larger units (storey-sets) showing a common migration pathway.
- Internal facies variability allows subdividing LAPs into a thin-bedded and generally heterolithic top-set, a middle set made of medium-grained massive to cross-stratified sandstones, and a toe set represented by fine-grained laminated, plane parallel to ripple, sandstones.
- The spatial stacking of single-storeys and storey-sets reflect a range of processes, including relatively prolonged phases of channel bend expansion (swing), down-slope translation of channel bends (sweep), channel avulsion, and variable degree of channel (and levée) aggradation.
- Overall, the complex show a threefold stratigraphic organisation including: i) a lowermost mud-prone interval with relatively small (a few hundred of metres across and metre-thick) and vertically stacked channels fills, ii) a middle ca. 4 m-thick and >1 km-wide dominantly amalgamated sandstone made of eastward-directed LAPs, passing upward into a 6 m-thin

interval of thin-bedded turbidites, hemipelagic deposits with sparse channel-fills, and iii) an uppermost package of vertically aggraded channel fills with variously directed LAPs and well-developed levées.

- The above sedimentary packages are interpreted as the product of an early *phase of inception,* a subsequent *phase of increased sediment input and channel lateral migration* and a late *phase of channel aggradation*.
- The stratigraphic organisation reflects the response to an equilibrium profile shift from a low accommodation regime (inception phase), through an at grade condition (migrational phase), to a high accommodation regime (aggradational phase). These evolution is modulated through time by sediment input variation.
- The Complex 4 was likely deposited over a time <36 kyr allowing to estimate the time duration of its elemental building blocks equal to several hundreds to few thousand years.

CHAPTER IV

Depositional analogue for delta-fed hyperpycnal systems: insights from the Monastero Fm. (Oligocene, Tertiary Piedmont Basin, NW Italy)

Intentionally blank page

4. Depositional analogue for delta-fed hyperpycnal systems: insights from the Monastero Fm. (Oligocene, Tertiary Piedmont Basin, NW Italy)

This chapter is largely based on a draft of a paper in preparation for Sedimentary Geology, "Depositional analogue for delta-fed hyperpycnal systems: insights from the Monastero Fm. (Oligocene, Tertiary Piedmont Basin, NW Italy)" by Reguzzi S., Marini M., Maron M., Felletti F., and Rossi M.

In this chapter facies, architectures, and controls on a delta-fed turbidite unit, the Monastero Fm. of the Tertiary Piedmont Basin (Rupelian), are examined. Even though the studied turbidite system is not well-exposed, the acquired stratigraphic logs, complemented by photopanel interpretation and geological mapping, provided sedimentological insights along a thick and sufficiently exposed section. The further combination of sedimentological data with novel magnetostratigraphic data and biostratigraphic data from the literature has allowed to roughly estimate the sedimentation rate function for the unit.
The integration of 2D seismic lines has also provided insights into Monastero Fm. depositional model.

4.1. Introduction

Sediment gravity flows generated at river mouths have been long recognised to largely contribute to clastic deposition in seas and lakes (Bates, 1953; Mulder & Syvitski, 1995; Nemec, 1995; Mulder *et al.*, 1997, 1998b, 2001a; b, 2003; Mulder & Alexander, 2001; Lamb & Mohrig, 2009; Steel *et al.*, 2018). When entering a water body, the density contrast between the sediment-laden river effluent and ambient fluid will determine whether the flow will i) plunge and continue as a seafloor hugging turbulent underflow (i.e., inflow density > ambient fluid density, hyperpycnal flow; Mulder *et al.*, 2003; Piper & Normark, 2009; Zavala *et al.*, 2011a), ii) form a buoyant plume spreading off-shoreward (i.e., inflow density < ambient fluid density, hypopycnal flow; Mulder *et al.*, 2003; Zavala *et al.*, 2011a; Mutti, 2019), or iii) mix with the ambient fluid so to rapidly die out (i.e., inflow density = ambient fluid density; homopycnal flow; Mulder & Syvitski, 1995; Allaby, 2008). Albeit these three flow types generally co-exist, deposition by hyperpycnal flows is generally dominant volumetrically (e.g., Mulder *et al.*, 2001a, 2003; Zavala *et al.*, 2011a) and can form clastic accumulations with a close genetic link with adjacent deltaic systems that are commonly referred to as hyperpycnal systems (*sensu* Zavala *et al.*, 2011a).

On the other hand, deposition by homopycnal flows is generally unimportant and limited to the close proximity of river mouths, whereas hypopycnal deposition encompasses for the slow hemipelagic settling of very fine- rained (clay-grade)particles (Bates, 1953; Mulder *et al.*, 2003).

Hyperpycnal flows can form either during normal floods, or seasonal floods, or following catastrophic events (e.g., jökulhaups, lahars, dam breaking and draining; Mulder *et al.*, 2003; Plink-Bjölrklund & Steel, 2004). Typically, low-density hyperpycnal flows are initiated by normal river floods, whereas high-density hyperpycnal flows are initiate by seasonal or catastrophic floods (Plink-Bjölrklund & Steel, 2004; Clare *et al.*, 2018).

Several workers (Chikita, 1989; Mulder & Syvitski, 1995; Hoyal *et al.*, 1999; Mulder *et al.*, 2001a, 2003; Parsons *et al.*, 2001; Petter & Steel, 2006; Steel *et al.*, 2018) addressed the ignition conditions of hyperpycnal flows, highlighting that a critical sediment concentration of the riverine water is required for generating a plunging plume at sea. Experimental results by Parsons *et al.* (2001) suggest that this critical concentration is relatively high and in the range 30-45 kg/m^3, a condition rarely met in the marine environment (Mulder & Syvitski, 1995; Mulder *et al.*, 2003). However, other factors can contribute to hyperpycnal flows generation, either reducing the critical concentration required for ignition or determining high suspended sediment loads in rivers. Hoyal *et al.* (1999) suggested that convective instability of sediment-laden riverine waters entering the sea can considerably reduce the density contrast threshold required for hyperpycnal flow generation. Mulder *et al.* (2003) proposed that this same threshold can be lowered as a result of dilution of sea water by fresh water during long-lasting river floods, which would thus favour hyperpycnal flow generation. Several authors (Wright *et al.*, 1990; Mulder *et al.*, 1998a among other) have shown how drainage basins characterised by relatively soft and easily erodible rocks or even loose deposits (e.g., loess deposits, black shales) can result in floods with unusual high suspended sediment concentrations and generation of long-lasting hyperpycnal flows.

The recurrence rates of hyperpycnal flows in modern systems is highly variable (form a few tens of years to more than 10kyr; Mulder & Syvitski, 1995) as a result of a number of interplaying factors, with some authors (Johnson et al., 2001) reporting recurrence rates as low as 2.5–3 years.

Mulder *et al.*, (2001a) first recognised that a complete vertical facies sequence might ideally reflect the hydrograph of the flood from which the parent hyperpycnal flow was generated. Thus, an hyperpycnite event bed would start with a coarsening upward basal interval (*cf.* with Ha unit of Mulder *et al.*, 2003) deposited during the waxing phase of the flood, and terminate upward with a fining-upward division (*cf.* with Hb unit of Mulder *et al.*, 2003) recording the waning phase of the flood. The contact between the two divisions is generally erosional and associated to the coarsest sediment fraction in proximal flow deposits, corresponding to the discharge peak of the flood (Mulder *et al.*, 2001a; Mulder *et al.*, 2003; Zavala *et al.*, 2011a; Mutti, 2019). Conversely, this erosional contact commonly lacks in distal flow deposits (e.g., Martini & Sandrelli, 2015).

However, since second-order discharge variations can superimpose on a simple flood hydrograph, the vertical sequence of sedimentary divisions within an hyperpycnite event bed is difficult to generalise and may include several intrasequence erosional contacts and the lacking of such sedimentary features (Mutti *et al.*, 1996; Mulder *et al.*, 2003; Lamb & Mohrig, 2009).

There is general agreement (Mulder *et al.*, 2001a, 2003; Plink-Björlrklund & Steel, 2004; Petter & Steel, 2006; Zavala *et al.*, 2011a; Gobo *et al.*, 2015; Mutti, 2019) that one of the most distinctive features of hyperpycnite-prone successions is their tightly packed and heterolithic structure, made of relatively thin alternations of sandstones and mudstones reflecting fluctuations of flow velocity and grain-size of sediments being detrained from suspension (Hesse & Chough, 1980; Zavala *et al.*, 2011a). Other common features of hyperpycnites are their generally good sorting (Mulder *et al.*, 2003; Zavala *et al.*, 2011a), local presence of basal bed load facies made of mud intraclasts (Zavala *et al.*, 2011a; Zavala & Pan, 2018) and fine-grained tops with frequent ripple-drift cross lamination (Mulder *et al.*, 2003; Mutti *et al.*, 2003; Gobo *et al.*, 2015), abundant plant debris and micas (Zavala & Pan, 2018) and trace fossils from opportunistic taxa (Buatois *et al.*, 2011).

More recently, Zavala *et al.* (2011a; b, 2012) and Zavala & Pan (2018) proposed an hyperpycnite facies tract organised in three main facies groups (Fig. 44B-C), namely (from proximal to distal), a ‘bed load’ facies B, a ‘suspended load’ facies S and a ‘lofting plume’ facies L. Facies B, (Fig. 44B-C) is made of coarse-grained sandstone and pebbly-sandstone characterised by metre-scale bed forms deposited underneath an overpassing long-lived hyperpycnal flow. Facies S (Fig. 44B-C) is

represented by structureless to ripple-drift laminated sandstones resulting from traction plus fall-out deposition from a turbulent hyperpycnal flow. Finally, facies L (Fig. 44B-C) consist of interbedded very fine sandstone- to claystone-grained sediments with abundant plant debris and micas and is the product of fall out deposition from a lofting plume.

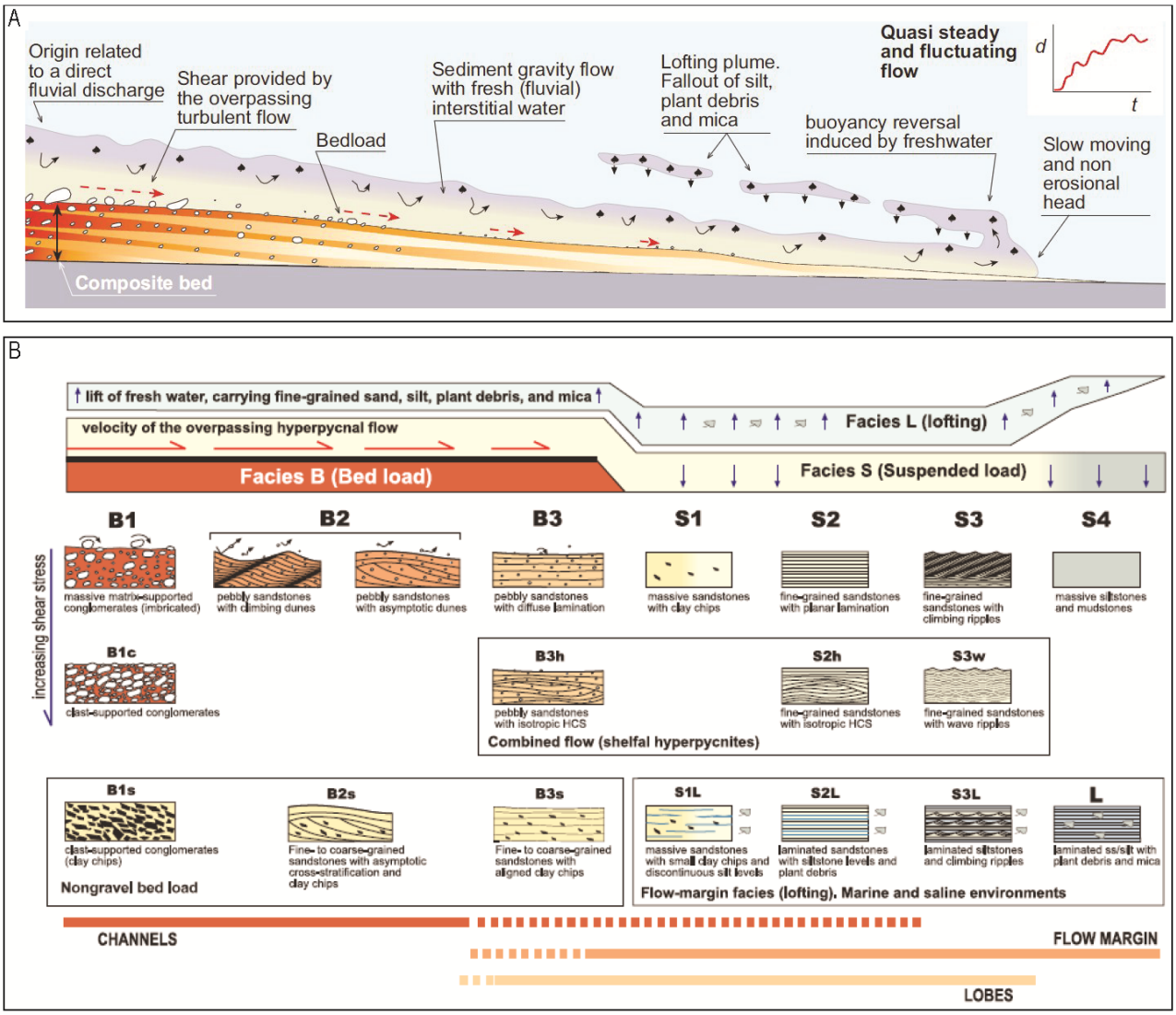

Fig. 44. (A) Main characteristics of long-lived hyperpycnal flows and their typical deposits. The complexity of these flows results in the accumulation of composite beds d = discharge; t = time. From Zavala *et al.* (2011a). (B) Conceptual sketch for the genetic classification of clastic facies associated with hyperpycnal systems. HCS = hummocky cross-stratification; ss/silt = sandstone/silt. From Zavala *et al.* (2011a).

Facies composition and geometry of architectural elements of hyperpycnal systems are relatively poorly constrained.

Petter & Steel (2006) proposed an evolutionary model of architectural elements as related to a single hyperpycnal flow hydrograph. At the beginning of the waxing phase of the hyperpycnal flow, l waxing

lobes are deposited, displaying a coarsening-upward depositional profile made of thin rippled, wavy, to flat laminated beds. At the peak of the waxing phase, the channel incision is created and channel deposits are typically composed of different order of erosional surfaces, lateral accretions (*sensu* Abreu *et al.*, 2003), blocky grain-size profiles (Mulder *et al.*, 2003), and thick sets of plane-parallel laminations and ungraded to fining-upward beds (e.g., Plink-Björlrklund & Steel, 2004; Zavala *et al.*, 2011a). When the hyperpycnal flow starts to die out, waning lobes associated with minor distributary channels (Steel *et al.*, 2018), composed of relatively thick beds decreasing in amalgamation downcurrent (Zavala *et al.*, 2011a), are deposited.

This humble contribution documents the Rupelian Monastero Formation (Tertiary Piedmont Basin, NW Italy; Gelati, 1977; Mutti *et al.*, 1995, 2003), which represents a turbidite unit partly coeval to a heteropic fan delta system (named Savignone Conglomerate, Ibbeken, 1970; Bellinzona & Boni, 1971; Bellinzona *et al.*, 1971; Gelati & Gnaccolini, 1978a; Mutti *et al.*, 1995). The Monastero Fm. was deposited upon a south-eastward dipping clastic ramp (Gelati, 1977) and conists of an apperently monotonous succession made of thin-bedded sandstone-mudstones couplets, for the most of its thickness (885 m out of 1100 m), interbedded to channel fill and lobe deposits. Even though extensively studied, the Monastero Fm. nature has never been completely understood in terms of depositional processes and its relationship with the adjacent deltaic system.

Thus, this study aims to investigate facies and architecture of depositional elements of the delta-fed Monastero Fm. by acquiring detailed sedimentological logs, coupled with photopanels interpretation, in order to assess if the nature of these deposits can be grouped under the category of hyperpycnal flows deposits (*sensu* Mulder *et al.*, 2003).

The collected sedimentological data were combined with biostratigraphic and magnetostratigraphic data in order to provide constraints on depositional rates and return time of sedimentary gravity flows. Furthermore, three 2D seismic lines were interpreted to better constrain the depositional setting of Monastero Fm. and comparing it with analogue systems occurring in the subsurface.

The study provides insights into delta-fed turbidite systems analogues in terms of return periods of sedimentary gravity flows, internal heterogeneity of architectural elements and their spatial arrangement.

4.2. Geological framework

The Tertiary Piedmont Basin (TPB hereafter) of NW Italy is an episutural basin developed on top of the Alps-Apennines junction (also known as the 'Ligurian knot'; Fig. 45A) (Laubscher *et al.*, 1992; Federico *et al.*, 2009; Maino *et al.*, 2013; Capponi *et al.*, 2016), a kinematically highly complex area recording the dynamics of two intimately related orogenic systems and relative motion of Adria and Europe (Fig. 45B) (Trümpy, 1960; Boccaletti *et al.*, 1980; Vanossi, 1986; Castellarin, 2001; Carminati *et al.*, 2004, 2012; Malusá *et al.*, 2009). The age of the oldest sedimentary units (ca. 35 Ma; Gelati, 1977; de Voogd *et al.*, 1991; Rollet *et al.*, 2002; Ghibaudo *et al.*, 2019) of the up to 4000 m-thick mainly deep-water clastic fill of the TPB indicates that the basin was established at least in the Late Eocene. The mechanism of formation and meaning of the TPB is still debated (see Molli *et al.*, 2010 for a review), with some authors suggesting it represents a retro-foreland basin of southern Alps (Carrapa *et al.*, 2003, 2016; Carrapa & Garcia-Castellanos, 2005) and some other emphasizing the role of the extensional regime affecting this sector of the western Mediterranean (Carrapa *et al.*, 2003, 2016; Maino *et al.*, 2013).

As a matter of fact, deposition in the TPB is largely coeval to rifting and subsequent spreading of the Liguro-Provençal oceanic basin (Horvath *et al.*, 1981; Rollet *et al.*, 2002; Le Breton *et al.*, 2021; Piana *et al.*, 2021), a back-arc basin of the Apennines (Fig. 45B).

Based on its character, the infill of the southern and most subsiding part of the TPB can be subdivided into two different sub-depocentres, the Langhe sub-depocentre to the west and the Borbera-Curone sub-depocentre to the east (Pieri & Groppi, 1981; Mosca, 2006; Rossi *et al.*, 2009; Maino *et al.*, 2013; Ghibaudo *et al.*, 2014, 2019; Rossi & Craig, 2016), separated until the early late Burdigalian by the Alto Monferrato structural high (Fig. 46).

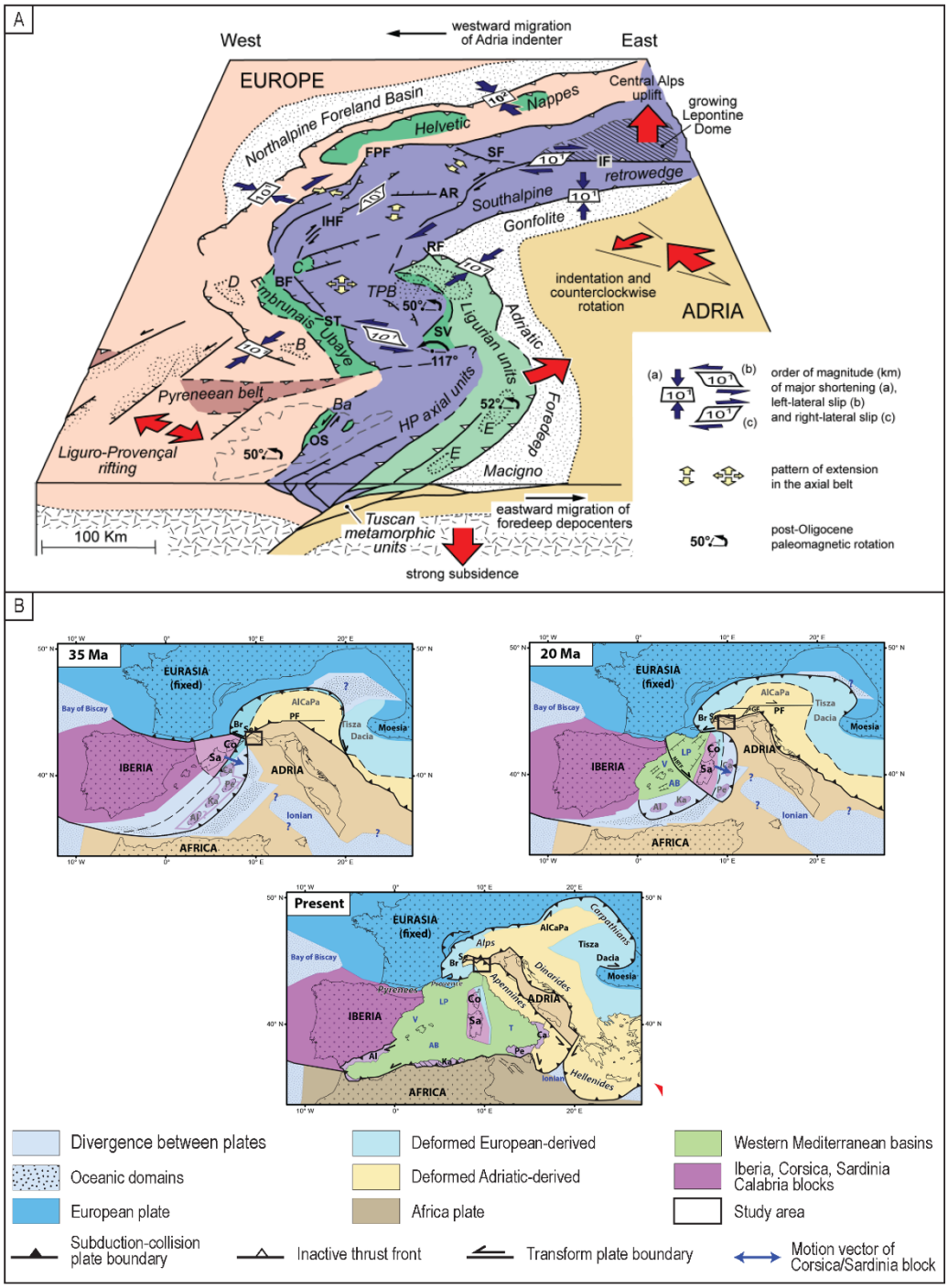

Fig. 45. (A) Conceptual 3D reconstruction of the Western Alps-Northern Apennine junction area at the latest Oligocene earliest Miocene (Molli *et al.*, 2010). (B) Simplified tectonic maps of the Western Mediterranean–Alpine from 35 Ma to present (convergent phase – right panels), relative to Eurasia (fixed), showing the main plate boundaries and divergence between Europe–Corsica and Adria (blue vectors). Note that these maps do not show intraplate deformation and rifting along the continental margins but the divergence between plates when considered rigid. Present-day coastlines are represented for orientation. Abbreviations: AB– Algerian Basin; Al – Alboran; AlCaPa – Alpine–Carpathians–Pannonian unit; Br – Briançonnais; Ca – Calabria; Co – Corsica; GF –Giudicarie Fault; Ka – Kabylides; LP – Liguro-Provençal Basin; NBTZ – North Balearic Transform zone; Pe – Peloritani; PF – Periadriatic Fault; PL – Piemont–Liguria (Basin and Ocean); Sa – Sardinia; SCRZ – Sicily Channel rift zone; Se – Sesia; Tu – Tuscany; T – Tyrrhenian Sea; V – Gulf of Valencia; Va – Valais Basin. Modified after Le Breton *et al.*, 2021.

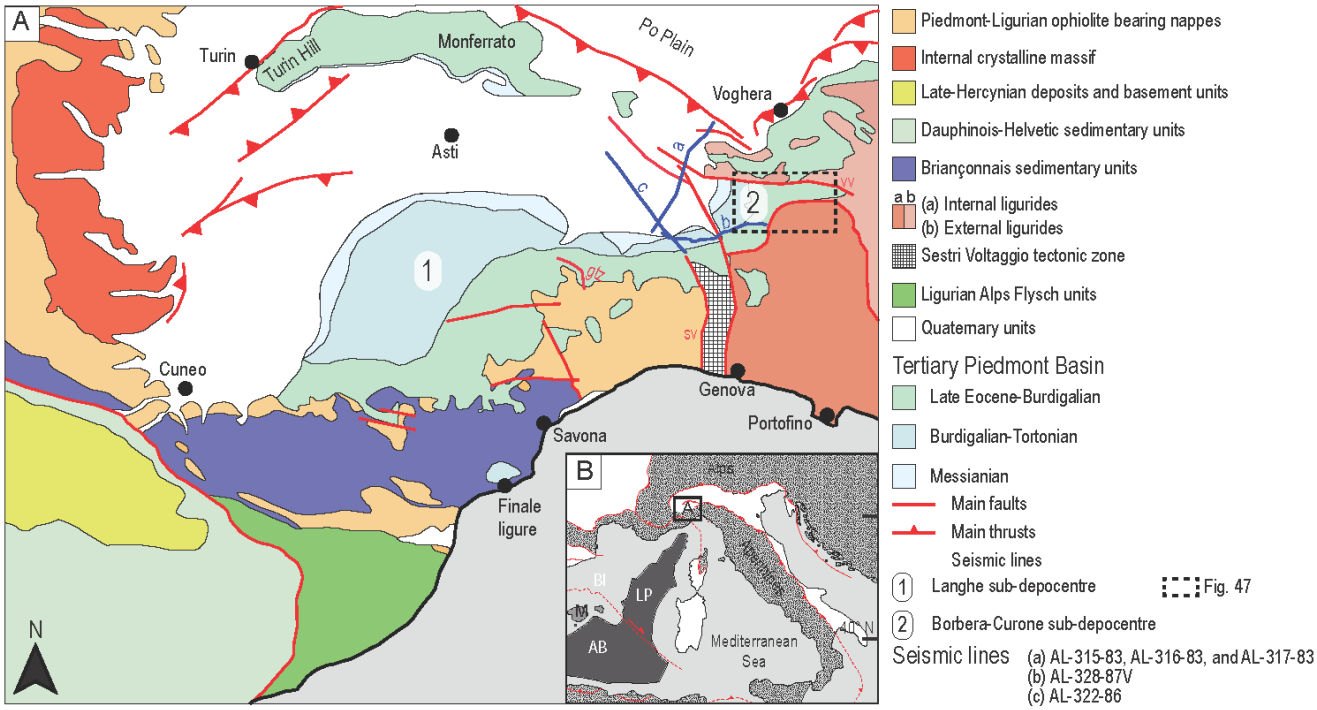

Fig. 46. (A) Geological sketch map of the north-western sector of Alps and Apennines (modified after Mosca *et al.* (2010) and Maino *et al.* (2013). sv = Sestri-Voltaggio line; gtz= Grognardo Thrust Zone; vv= Villavernia-Varzi line). (B) Schematic representation of the circum-Mediterranean area modified after v. LP= Liguro-Provençal Basin; AB= Algerian Basin; BI= Balearic Islands; M= Mallorca Island.

4.2.1. Stratigraphy framework of the Borbera-Curone sub-depocentre

The Monastero Fm. is part of the sedimentary fill of the Borbera-Curone sub-depocentre (Fig. 46, Fig. 47 and Fig. 48, Andreoni *et al.*, 1981; Mosca *et al.*, 2010; Ghibaudo *et al.*, 2014, 2019), which disconformably overlies a basement made of deformed oceanic units (the Internal Ligurides; Fig. 46 and Fig. 47) and terminates to the north and the to the east against the Villalvernia-Varzi tectonic line (Fig. 47), a polyphasic fault system active since the Late Eocene (Gelati, 1974; Felletti, 2002; Festa *et al.*, 2015) separating the TPB from the northern Apennines. The sedimentary fill of the Borbera-Curone sub-depocentre is ca. 3500 m-thick and comprises a range of relatively shallow water to deep-water clastic deposits whose stratigraphic arrangement reflects the interplay of tectonics, sediment supply, and eustatic sea level variations (Di Giulio, 1991; Rossi *et al.*, 2009; Rossi & Craig, 2016). Based on stratigraphic changes in sandstone petrography, Cavanna et al. (1989) and Di Giulio (1991) subdivided the late Eocene to Chattian section into three depositional units (labelled S1 to S3, from older to younger). Together with the partly coeval fan-delta deposits of early Rupelian age (Savignone Conglomerate), the Rupelian Monastero Fm. belongs to the S3 sequence of Di Giulio (1991) and

makes an upward transition to slope to basinal mudstones of Chattian age (Gremiasco Fm.), forming a higher rank unit with an overall transgressive organisation interpreted to record the Oligocene collapse of western Alps (*cf.* with Unit II of Rossi *et al.*, 2009; Mosca *et al.*, 2010; Rossi & Craig, 2016). In the Miocene, sedimentation proceeded with fast accumulation of confined to unconfined turbidite systems (Castagnola Fm., Aquitanian-Burdigalian; Marini *et al.*, 2016b, 2020), which to the west are overlain by shelfal deposits of Langhian to Messinian age (i.e., Cessole Fm., Serravalle Sandstones, and Sant'Agata Fossili Fm., Fig. 47 and Fig. 48).

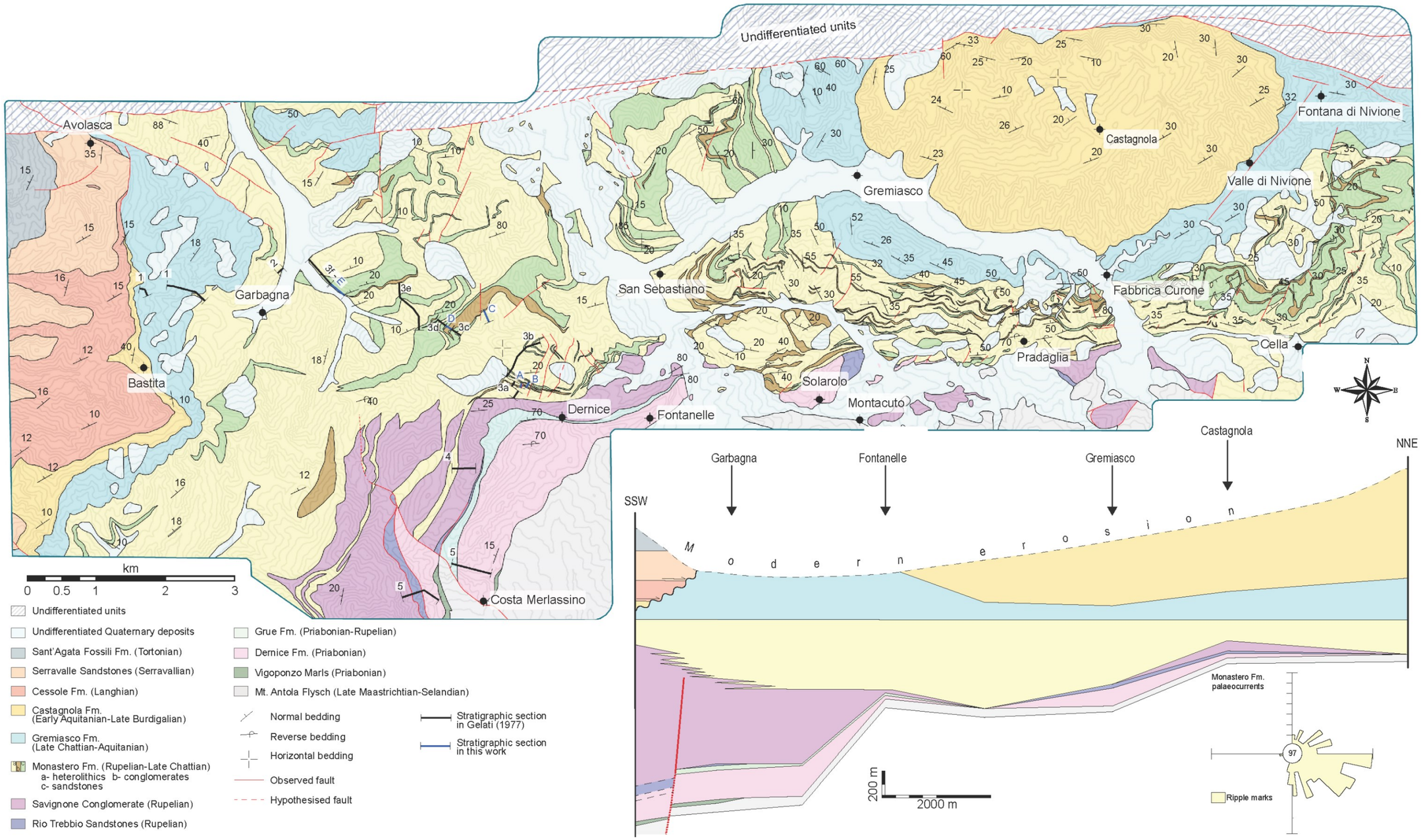

Fig. 47. Summary geological map and stratigraphic scheme of the Borbera-Curone sub-depocentre obtained after merging Gelati (1977), Cavanna *et al.* (1989), Marroni *et al.* (2010), and Festa *et al.* (2015) works. The stratigraphic scheme represents the situation at the time of deposition of the Monastero Fm.

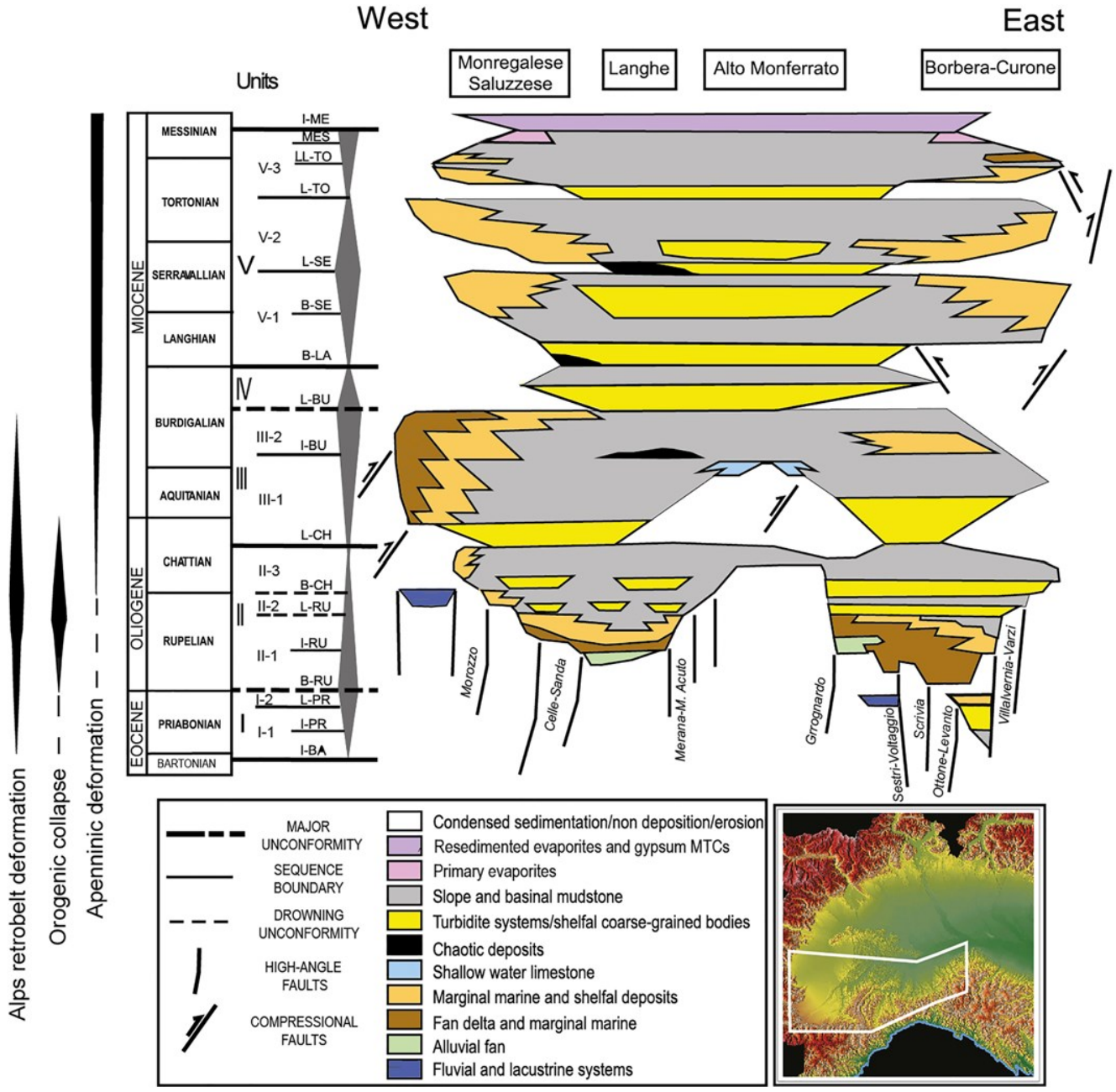

Fig. 48. Late Eocene–Miocene tectono-stratigraphic framework of Tertiary Piedmont Basin (from Rossi & Craig, 2016). Grey triangles define regressive v. transgressive stacking patterns. Thick solid lines mark the boundaries of major unconformity-bounded stratigraphic units; intermediate lines mark the boundaries of allogroups (solid lines represent sequence boundaries; dashed lines represent drowning unconformities); thin lines mark minor sequence boundaries. I-BA, Intra-Bartonian unconformity; I-PR, Intra-Priabonian sequence boundary; L-PR, Late-Priabonian allogroup boundary; B-RU, Base Rupelian unconformity; I-RU, Intra-Rupelian sequence boundary; L-RU, Late Rupelian allogroup boundary; B-CH, Base Chattian allogroup boundary; L-CH, Latest Chattian unconformity; I-BU, Intra-Burdigalian allogroup boundary; L-BU, Late Burdigalian unconformity; B-LA, Base Langhian unconformity; B-SE, Base Serravallian sequence boundary; L-SE, Late Serravallian allogroup boundary; L-TO, Late Tortonian allogroup boundary; LL-TO, Latest Tortonian sequence boundary; MES, Messinian sequence boundary; I-ME, Intra-Messinian unconformity.

4.2.2. The Monastero Fm. depositional system

The Monastero Fm. (Bellinzona et al. 1971; *cf*. with 'Arenarie di Ranzano' of Cavanna et al. 1989; 'Unità Monastero' of Mutti et al. 1995; and 'Membro di San Sebastiano' of Martelli *et al.*, 1998) is a relatively thick deep-water coarse-grained unit, interpreted as a series of turbidite systems fed from the S-SW by adjacent conglomeratic fan-deltas (Gelati, 1974, 1977; Gnaccolini, 1974; Gelati & Gnaccolini, 1984; Cavanna *et al.*, 1989; Di Giulio, 1991; Festa *et al.*, 2015). It crops out to the south of Villalvernia-Varzi line, forming an outcrop belt that extends for ca. 15 km between the Scrivia Valley to the west and the Staffora Valley to the east (Fig. 47). The unit terminates against the Val Scrivia Fault to the west (Ghibaudo *et al.*, 1985) and thickens rapidly eastward from ca. 200 m (Scrivia Valley) to 1100 m (San Guadenzio section, Borbera Valley; Gelati, 1977), before thinning again toward its eastern termination against the Villalvernia-Varzi line (Staffora Valley).

To the west the unit overlies with transitional contact the fan-delta deposits of the Savignone Conglomerate (Grue and Borbera valleys; Gelati, 1977; Uchman *et al.*, 2015) and the Molare Fm. (Scrivia Valley; Gnaccolini, 1974; Ghibaudo *et al.*, 1985), whereas to the east it sits with disconformable contact on top of the Ligurian units. Upwards, the Monastero Fm. passes to slope to basinal hemipelagic marlstones (Gremiasco Fm.; Fig. 47 and Fig. 48) containing a range of channelised to unchannelised sandstone bodies (Cavanna et al. 1989; Stocchi *et al.*, 1992; Marini *et al.*, 2019).

Early sedimentological studies described the Monastero Fm. as comprised dominantly by thin-bedded turbidites with mudstone to sandstone thickness ratio <1, intercalated with channelised conglomerates and sandstones, turbidite sandstone lobes (e.g., “Lobi di San Gaudenzio”; Gelati, 1977), and subordinately mass transport deposits (Gelati, 1977; Ghibaudo *et al.*, 1985; Cavanna et al. 1989). Several authors documented the interfingering of the conglomeratic facies belonging to the Conglemerato di Savignone Fm. and the lowermost deposits of the Monastero Fm. (e.g., to the north of Costa Merlassino village Fig. 47), suggesting the two units are partly heteropic (Gelati, 1977; Gelati & Gnaccolini, 1984, Ghibaudo *et al.*, 1985; Uchman *et al.*, 2015). At a larger scale, the Monastero Fm. onlaps to the south and to the west the top of the Conglomerato Savignone Fm., forming what

has been interpreted as a drowning unconformity (*sensu* Rossi *et al.*, 2018), e.g. a flooding surface recording basin subsidence induced by the Oligocene collapse of western Alps (*cf.* with Unit II of Rossi *et al.*, 2009; Mosca *et al.*, 2010; Rossi & Craig, 2016).

Based on thickness changes, previous workers (Ghibaudo *et al.*, 1985; Cavanna et al. 1989; Martelli *et al.*, 1997) suggested that the Monastero Fm was structurally confined by the Val Scrivia Fault to the west and the Villalvernia-Varzi line to the north (Fig. 47 and Fig. 61B). The confined character of the unit is reflected by the paleocurrent pattern (Cavanna et al. 1989; Di Giulio, 1991, Martelli *et al.*, 1997), which includes a main cluster of palaeoflow indicators directed toward the east, interpreted to result from deflection of incoming flows parallel to the Villalvernia-Varzi line. Cavanna et al. (1989) also reported several conglomeratic channel fills with N-S-striking axes suggestive of sediment feeding the system from the south.

The modal composition of the Monastero Fm. sandstones suggests they are litharenites, and subordinately feldspatic litharenites, composed of clasts of metamorphic schists, quartz, volcanics and sedimentary rocks derived from the Ligurides metamorphic rocks (Fig. 46) and their sedimentary covers (e.g., Antola Flysch; Fig. 47) (Di Giulio, 1991; Martelli *et al.*, 1997; Cibin et al., 2003).

Planktonic foraminifera biostratigraphy (Gelati, 1977; Gelati & Gnaccolini, 1978; Mancin & Pirini, 2001) indicates a Rupelian age (biozones O2 to O5, Wade *et al.*, 2011, corresponding to an age range of ca. 31-27.5 Ma; Fig. 49). To the west the base of the Monastero Fm tends to rejuvenate slightly (biozone O3; Gelati & Gnaccolini, 1978) reflecting the onlap onto the relict morphology of the fan-deltas below (i.e., Savignone Conglomerate).

Benthic foraminifera assemblages and planktonic to benthic/planktonic ratio (Mancin & Pirini, 2002) suggest that the unit was likely deposited in a middle to lower bathyal environment, within a depth range of 600-1500 m.

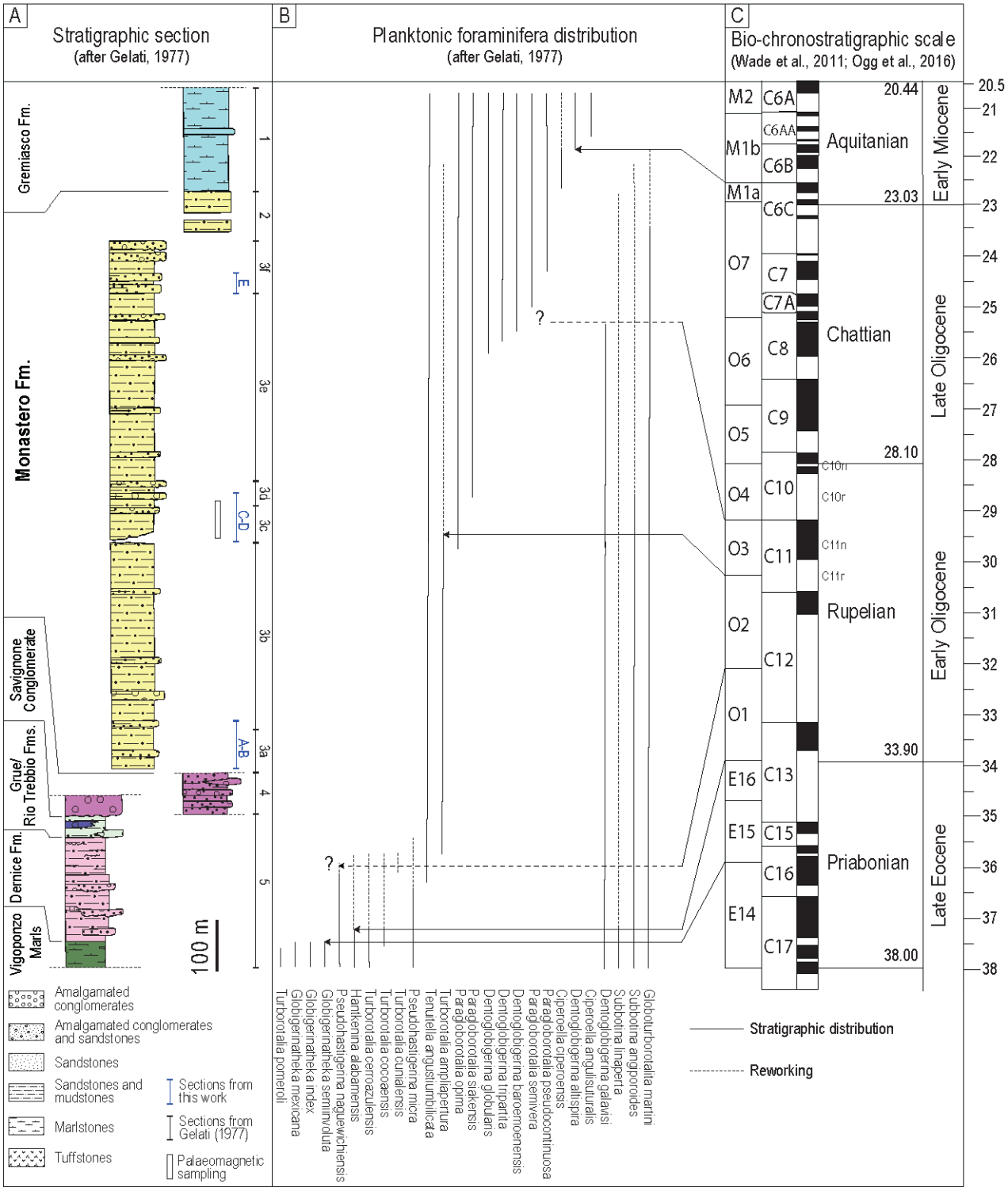

Fig. 49. Chronostratigraphic scheme of the studied succession. (A) Simplified sedimentary log of the studied section (modified, after Gelati, 1977) with lithostratigraphy after Marroni *et al.* (2010). (B) Planktonic foraminifera distribution, reviewed after Gelati (1977) (see Appendix I for the review). (C) Bio-chronostratigraphic scale by Wade *et al.* (2011) and Ogg *et al.* (2016).

In summary, the current depositional model for the Monastero Fm. (Fig. 50) is one of a structurally confined turbidite system supplied with sediments from coeval conglomeratic fan-delta systems (part

of which constituting the Savignone Conglomerate and Molare Fms.) developed along the southern margin of the Borbera-Curone sub-basin (Gelati, 1974, 1977; Gnaccolini, 1974; Gelati & Gnaccolini, 1984; Cavanna *et al.*, 1989; Di Giulio, 1991; Festa *et al.*, 2015).

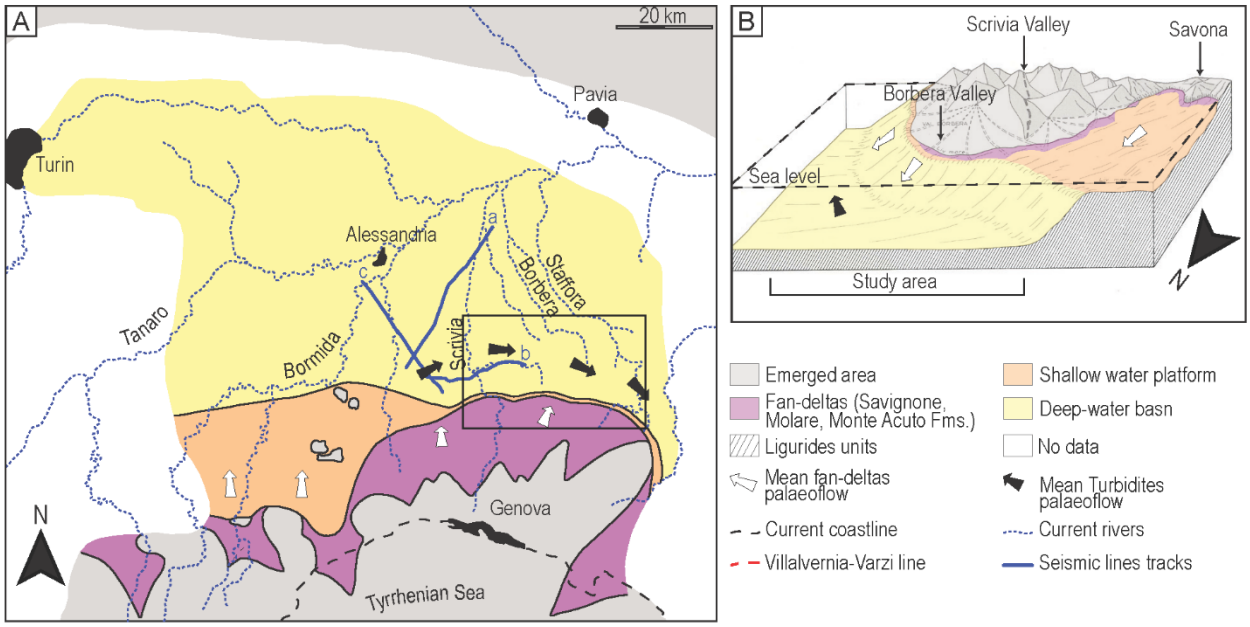

Fig. 50. (A) and (B) Inferred palaeogeographic map (modified after Gelati & Gnaccolini, 1984) and 3D block diagram for the Tertiary Piedmont Basin during the middle part of the Oligocene showing the distribution of depositional environments. The black square indicates the study are represented in Fig. 47.

4.3. Materials and methods

4.3.1. Sedimentary logging, field mapping, and seismic data interpretation

Due to the generally poor exposure of the Monastero Fm. and the inaccessibility of some of the best exposures, the characterization of the architectural element of the Monastero Fm. was achieved by combining sedimentary logging, physical correlation of key sedimentary bodies, and interpretation of photopanels.

Five sedimentary logs were acquired, detailing the lower, middle and upper parts of the Monastero Fm. (see Section 4.4). Logs were measured with cm-scale resolution (1:20 scale) taking note of lithology, chart-aided estimations of grain size and sorting, sedimentary structures, palaeoflow directions from sole marks and sedimentary structures, and intensity of bioturbation. Sedimentary divisions were classified following the facies schemes of Lowe (1982) and Bouma (1962) for coarse-grained and relatively finer-grained turbidite facies, respectively (Fig. 51). Bed and intrabed division thickness was measured using a tape meter, whereas long-range measurements (e.g. thickness of very thick monotonous or covered stratigraphic intervals) were accomplished using a high-precision Jacob's staff with laser sighting capability (Patacci, 2016).

Key sedimentary bodies were tracked laterally across adjacent sections in order to estimate their minimum widths and aid log correlation.

Finally, to better constrain the western boundary of the studied units and explore whether analogue systems were present in the subsurface to the west of the study area, three seismic sections (2D pre-stack data, fully migrated in time, Appendix II) acquired in the early 1980s by Eni S.p.A were interpreted using DecisionSpace®365 (https://www.landmark.solutions/ds365). After tying them to surface geology (Ghibaudo *et al.*, 1985, 2019; Festa *et al.*, 2015), the horizons originally defined by Rossi & Craig (2016) (corresponding to major unconformity surfaces) were tracked proceeding from the shallow subsurface to deeper levels, particularly focussing on bounding surfaces of the Oligocene Unit II of Rossi *et al.* (2009).

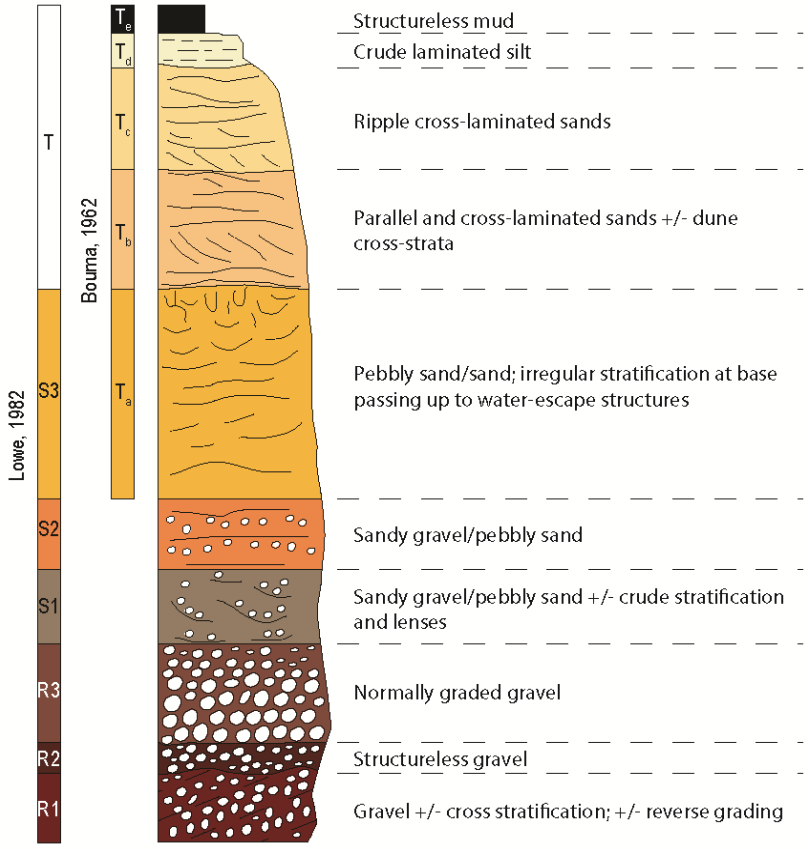

Fig. 51. Classifications by Lowe (1982) and Bouma (1962) used to categorize sedimentary divisions of the Monastero Fm. deposits.

4.3.2. Magnetochronology and biostratigraphy

Aiming at providing insights into age and accumulation rates of the Monastero Fm., one of the logged sections (section 'D', along the SP 122 connecting Garbagna to Dernice, see Fig. 47 for location) was sampled for a pilot magnetostratigraphic investigation. This section was chosen because it is relatively less prone to channelisation and, presumably, more continuous in terms of sedimentary and biostratigraphic record. Sixteen standard (10 cc) drill-core samples, spanning a stratigraphic interval of ca. 70 m (see Section 4.4.4), were collected using a water-cooled drill, selectively targeting mudstones.

Isothermal remanent magnetization (IRM) acquisition experiments and hysteresis loops were performed at the Laboratory of Magnetostratigraphy and Paleogeography (PalMag) of the University of Milan (Segrate, Milan). A sub-set of 2 samples (SC2b and SC12) was analysed for hysteresis and IRM, using a Microsense EZ7 Vibrating Sample Magnetometer (VSM). Thermal demagnetization of a three-component IRM (Lowrie, 1990) was performed on one representative sample adopting 2.5T,

0.4T and 0.15T orthogonal fields, using an ASC IM-10-30 pulse magnetizer to impart the IRM and a 2G Enterprises 755 DC-SQUID (Direct Current – Superconducting Quantum Interference Device) cryogenic magnetometer for measurements.

The natural remanent magnetization (NRM) of all samples was analysed at the the Laboratory of Paleomagnetism of the Istituto Nazionale di Geofisica e Vulcanologia (Rome, Italy). Samples were thermally demagnetized from room temperature up to 630°C at 120, 180, 230, 280°C and then in steps of 40°C with an ASC TD48 furnace. The natural remanent magnetization (NRM) was measured after each demagnetization step with a 2G Enterprises 755 DC-SQUID cryogenic magnetometer hosted in a magnetically shielded room. The directions of the NRM were plotted on standard vector end-point demagnetization diagrams (Zijderveld, 1967). After removing the viscous component of magnetization (typically up to an unblocking temperature of ~200°C), the direction of the characteristic remanent magnetization (ChRM) was extracted with standard least square analysis for samples showing a relatively stable magnetic direction (4 samples) and by means of a great circles analysis (McFadden & McElhinny, 1988) when multiple superimposed components were present (9 Samples). A virtual geomagnetic pole (VGP) was calculated for each ChRM component direction in tilt-corrected coordinates, and the VGP latitudes (relative to the north geographic pole; positive for normal polarity, negative for reverse polarity) were used for interpreting magnetic polarity stratigraphy.

The thus obtained polarity stratigraphy of section D was correlated to the Geomagnetic Polarity Timescale (Ogg *et al.*, 2016) with the aid of literature biostratigraphic data from the same section (Gelati, 1977), after reviewing them for taxonomy and age distribution of reported species. The taxonomy review was accomplished using *Mikrotax*, a database combining data from previous databases and syntheses works (Huber *et al.*, 2016) and providing taxonomy, identification, and age range information for planktoninc foraminifers. For marker species, age ranges were derived by most recent review works of mediterranean foraminiferal assemblages (Wade *et al.*, 2011; Lirer *et al.*, 2019 and references therein). The reviewed biostratigraphic data are provided in Appendix I and summarised in Section 4.4.4.

4.4. Results

4.4.1. Sedimentary facies

Six sedimentary facies were defined based on lithology, grain size and vertical association of sedimentary structures. These include 1 conglomeratic and pebbly-sandstone facies (facies CP, Section 4.4.1.1) and 5 turbidite sandstones facies (facies mlS, rS, pcS-r, mlS-r, SM-r, Sections 4.4.1.2, 4.4.1.3, 4.4.1.4) named after their most distinctive and generally thickest division, and mass transport deposits (facies MTD, Section 4.4.1.5).

4.4.1.1. Conglomerates and pebbly sandstones (facies CP)

This facies consists of structureless to stratified conglomerates and pebbly sandstones, and more rarely of pebbly-mudstones (Fig. 52A-D). It forms erosionally-based beds with thickness in the range 0.20-1.50 m, that can occur either interbedded to other non-channelised facies, or in sets of a few to several beds as part of channel-fills. The grain size of the coarsest fraction varies between medium-coarse and fine-very fine gravel (Fig. 52A). This is accompanied with variable proportions of sand and mud, resulting in a generally very poor to moderate sorting. The texture is clast-supported for conglomerates and pebbly sandstones (Fig. 52A-B), and matrix supported for the relatively less frequent pebbly mudstones (Fig. 52D), which are characterised by a volumetric fraction of matrix around 80%. Beds are generally normally graded (Fig. 52C), being represented by a lower conglomerate division and an upper pebbly sandstone. Conglomerates are generally structureless or crudely stratified (*cf.* with facies R2 and R3 of Lowe, 1982), whereas pebbly sandstones show a range of crude to horizontal plane parallel and cross-stratifications, accompanied with presence of traction carpets (cf. with facies S1, S2 and S3 of Lowe, 1982; Fig. 52B-C).

Compositionally, the gravel component of this facies is represented by (in decreasing order of abundance) schists and ophiolitic rock fragments, polycrystalline quartz, rare carbonate clasts, and shell fragments.

Interpretation: This facies represents the product of deposition from a range of flow types including debris flows, hyperconcentrated flows and a high-density turbidity currents (Mulder & Alexander, 2001) transitioning one into another, as a result of water ingestion and progressive dilution (*cf*. with facies F of Sohn *et al.*, 2002).

4.4.1.2. *Massive to laminated sandstones with sharp tops (facies mlS)*

This facies consists of cm- to dm-thick normally graded beds of medium- to fine-grained laminated sandstones, locally with a relatively thin structureless to crudely laminated basal division (*cf*. with facies S3 of Lowe, 1982 and facies T_a of Bouma, 1962; Fig. 52E-F). Where present, the structureless division is a very coarse- to coarse-grained sandstone, rarely with sparse pebbles at its base (*cf*. with T_a division of Bouma, 1962). The remained of the sandstone is parallel to cross-stratified, frequently with traction carpets (*cf*. with T_b division of Bouma, 1962), grading upward into a cross-laminated or convoluted top of fine sandstones (*cf*. with T_c division of Bouma, 1962; Fig. 52E). The top of the sandstone has flat to wavy geometry and is sharply overlain by a cm- to dm-thick mudstone cap, with the coarse silt fraction notably missing.

Interpretation: these beds represent the product of deposition from high- to low-density waning flows (*sensu* Lowe, 1982). The sharp transition to a relatively thin mudstone cap can be interpreted to reflect by-pass of most of the very fine sand-mud.

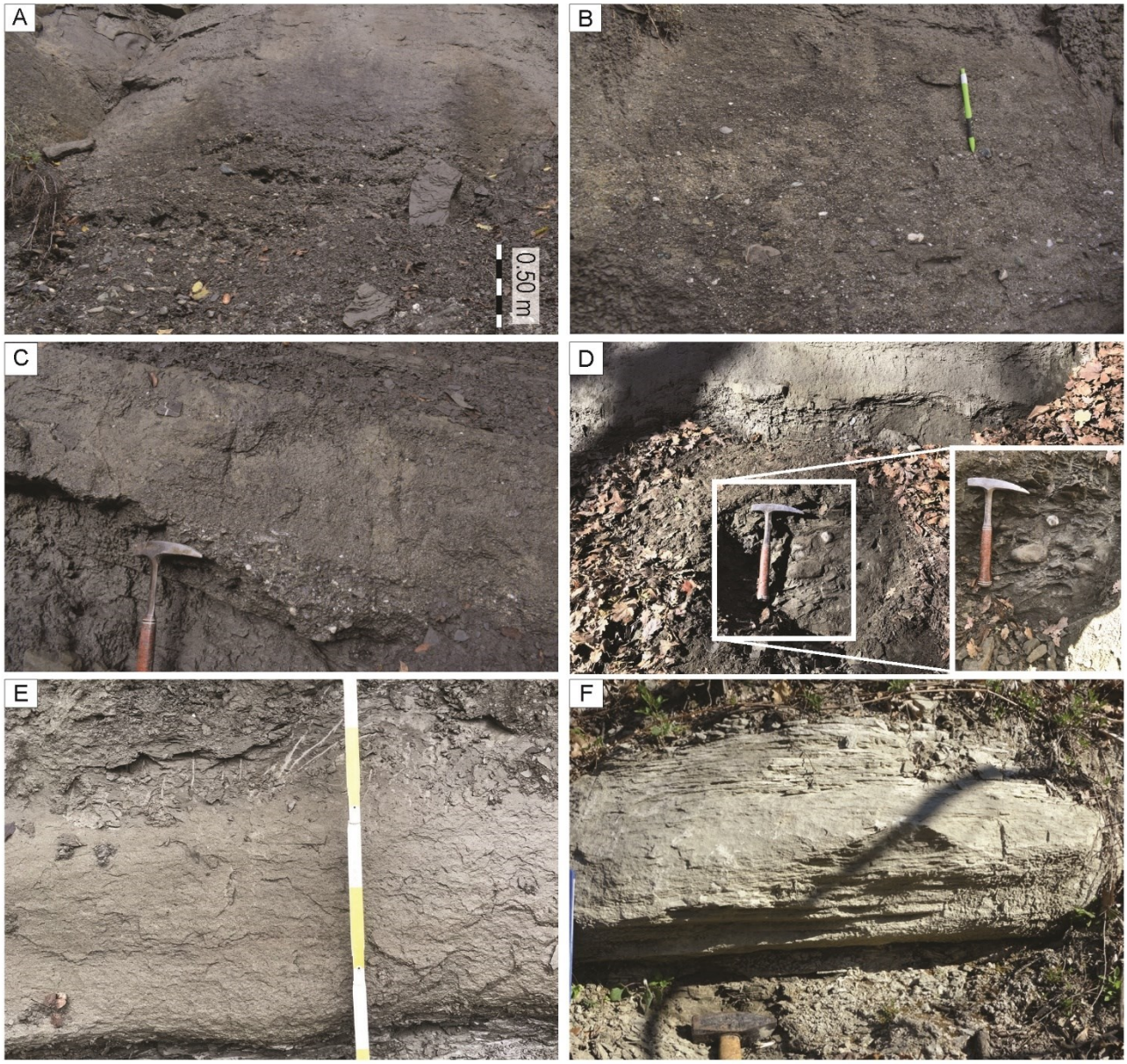

Fig. 52. (A) Crudely bedded conglomerates rapidly grading upward into crudely- to well-bedded pebbly sandstones (facies CP). (B) Normally graded conglomerates passing upward into pebbly sandstones (facies CP). (C) Pebbly sandstones bed characterised by an erosive base overlain by a traction carpets interval (facies CP). (D) Detail of the facies CP, showing the contact between pebbly mudstones and pebbly sandstones. The inset highlights the matrix-supported texture of the pebbly mudstone layer. (E) Massive to laminated sandstone bed characterised by slightly erosional base (facies mlS; *cf.* with T_{a-c} of Bouma, 1962). (F) Plane parallel- to ripple cross-laminated, sandstone bed (facies mlS; *cf*. with T_{b-c} divisions of Bouma, 1962).

4.4.1.3. *Ripple laminated sandstones (facies rS)*

This facies consists of relatively well-sorted fine- to very fine-grained mm- to cm-thick sandstone beds that grade upward into their co-genetic mudstone cap (Fig. 53A). It is characterised by a range of cross to sinusoidal and planar-parallel laminations (*cf*. with T_{c-d} divisions of Bouma, 1962; Fig. 53A) locally deformed to give rise to convoluted laminations (Fig. 53B). Where they are preserved,

ripple-cross laminations indicate paleocurrents toward south-easternly quadrants. Transition to the capping mudstone (typically mm- to cm-thick) can be either sharp or more gradational via a relatively thick division of coarse silt (Fig. 53A-B).

Interpretation: this facies corresponds to the T_{c-d} divisions of Bouma (1962) and is interpreted to reflect deposition by waning low-density turbidity currents and partial by-pass of the finest sediment fraction.

Fig. 53. (A) Ripple cross-laminated bed passing upward to the co-genetic mud cap (facies rS). (B) Ripple cross-laminated bed gradually passing to their mud cap. Look how the deformation at the top of the bed (facies rS). (C) Metres-thick parallel to low-angle cross-stratified sandstone-grained repetitions. Gray dashed lines point out the base of each normal grading interval (facies pcS-r). (D) Mud-clast breccia interval at the base of bed made of parallel to cross-stratified sandstone-grained repetitions (facies pcS-r). (E) Plane-parallel laminated sandstones sharply passing to a cm-thick mud-clast interval characterising the base of the overlying coarser-grained interval (facies pcS-r).

4.4.1.4. Beds with repeated sedimentary divisions

This facies group is comprised of beds with multiple grading and vertically repeated sedimentary structures, suggestive of pulsating flow conditions (*sensu* Mulder *et al.*, 2003 and Zavala & Pan, 2018).

4.4.1.4.1. *Parallel to cross-stratified sandstone repetitions (facies pcS-r)*

This facies consists of alternations of medium/coarse to fine/very fine-grained sandstones with low-angle cross-stratification, traction carpets, and horizontal plane-parallel lamination (Fig. 53C). These alternations are organised so as to form beds with thickness in the range of 0.20 - 1.50 m with multiple normal grading repetitions. Although component divisions tend to become thinner and finer-grained upward (Fig. 53C) there are cases where they vertically arrange to form coarsening-upward sets. Close to bed base (Fig. 53D) and to the bases of coarser grained divisions (Fig. 53E), alignments of outsized clasts and/or intraformational mud-clasts can be present suggesting bed load transport. On the other hand, the top of beds and of finer-grained parallel-laminated divisions can bear abundant phytoclasts laying in the plane of lamination (Fig. 54A). At the top, sandstone bedsets can be sharply overlain by a mud-clast breccia interval which passes upward to a laminated mudstone cap.

Interpretation: Repetitions in this facies are interpreted as the product of high-density pulsating flows. The thinning and fining-upward trend suggests a waning flow, which becomes progressively less concentrated in time to result in establishment of traction conditions. The laminated mudstone cap is the result of the final fall-out from a lofting plume, typical of hyper-hypopycnal deposition (Zavala *et al.*, 2012). The presence of mud-clasts breccia intervals can be interpreted as an evidence of bed load and sediment by-pass (Cunha *et al.*, 2017).

4.4.1.4.2. *Massive to laminated sandstone repetitions (facies mlS-r)*

This facies consists of cm-to dm-thick beds with an erosive base, cutting into underlying deposits as deep as ca. 10 cm, and a commonly rippled top (Fig. 54B), passing upward to cm- to dm-thick laminated mudcap. These beds are made of coarse- to medium-grained sandstone to siltstone repetitions, which are homogeneous in grain size, internal structures, and have a normal grading

trend (Fig. 54B-C), which can be also separated one from another by a mm-thick mud veil or can be distinguished on the basis of grain size breaks. These repetitions are made of structureless (*cf.* with T_a division of Bouma, 1962), plane parallel-laminated (*cf.* with T_b division of Bouma, 1962), sometimes with traction carpets, and ripple cross-laminated (*cf.* with T_c division of Bouma, 1962) sandstones (Fig. 54B-C). Often, the rippled-interval is deformed to give rise to convoluted laminations or is obliterated by bioturbation. The repetitions are organised to form inverse to normal grading beds (Fig. 54D).

Interpretation: Despite these repetitions could be interpreted as the effect of flow rebounds (e.g., Marini *et al.*, 2016a) or propagation of internal waves (Patacci *et al.*, 2015), the lack of ripple cross-laminas with opposite directions, bilobate structures, and very thick mud caps leads to interpret them as the product of pulsating low-energy hyperpycnal flows (Mulder *et al.*, 2003; Gobo *et al.*, 2014; Zavala & Pan, 2018). The occurrence of thicker and coarser-grained beds is representative of higher energy hyperpycnal flows (Mulder *et al.*, 2003). Mudcap laminas can be interpreted as the fall-out of river-derived hypopycnal lofting plumes (Gobo *et al.*, 2014; Zavala & Pan, 2018).

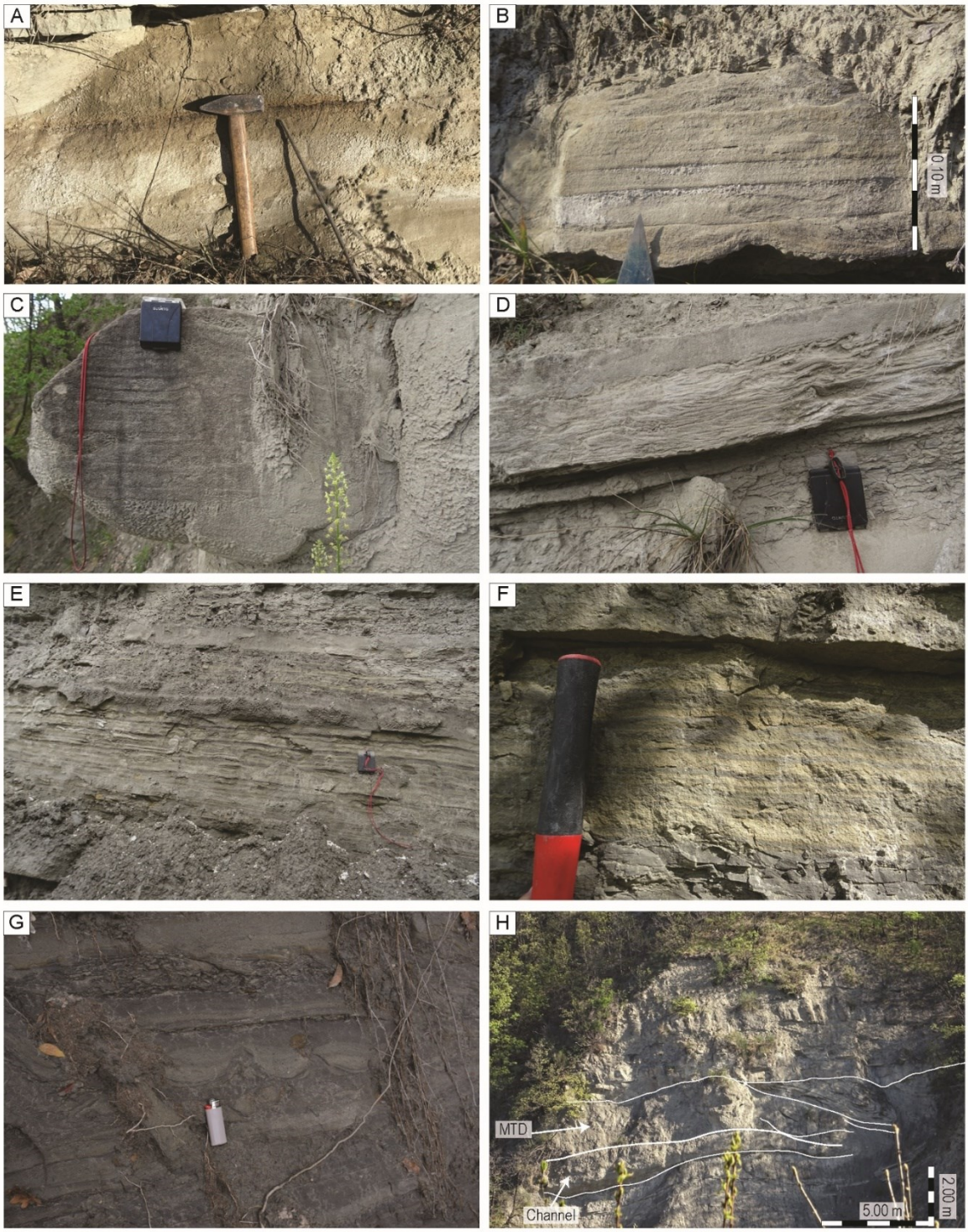

Fig. 54. (A) A detail of the plane-parallel laminated sandstone-grained repetitions characterised by cm-thick vegetal fragments lamina (facies pcS-r). (B) Cm-thick massive to laminated sandstone-grained repetitions. The base is erosional filled up by cross-laminas (facies mlS-r). (C) Cm-thick massive to laminated sandstone-grained repetitions, characterised by a coarse-grained sandstone lag, constituting a pulsate bed (facies mlS-r). (D) Cm-thick massive to laminated sandstone-grained repetitions constituting an inversely grading bed (facies mlS-r). (E) Fine sandstone-mudstone repetitions organised in a ca. 50 cm-thick inverse to normal graded bed pattern (facies SM-r). (F) A detail of fine sandstone-mudstone repetitions organised to form a tight alternation. (G) Soft sediment deformation in fine sandstones-mudstones repetitions (facies SM-r). (H) Metric-scale MTD overlying a conglomeratic channel fill.

4.4.1.4.3. *Fine sandstone-mudstone repetitions (facies SM-r)*

This facies consists of dm- to m-thick inversely to normally graded beds internally made by multiple mm- to cm-thick sandstone-mudstone couplets (Fig. 54E-F). The sandstone component is characterised by cross and, more rarely, ripple and convolute laminations and grades upward into a capping mudstone that can bear abundant micas and phytoclasts having their long axes laying in the lamination plane (*cf*. with facies S4 and L of Zavala & Pan, 2018). Where this facies form thick beds and bedsets, soft sediment deformations are common (Fig. 54G).

Interpretation: The inverse to normal grading trend of these beds reflects an accelerating-decelerating flow over time (e.g., Mulder *et al.*, 2003; Zavala *et al.*, 2011a). Grain size and sedimentary structures indicate that this facies is derived by low-density flows.

Therefore, due to the lack of ripple cross laminas with opposite directions and hummocky structures, these repetitions are interpreted as the result of a pulsate low-density sustained flow with a river-derived origin (Nemec, 1995; Mulder *et al.*, 2003; Gobo *et al.*, 2014; Zavala & Pan, 2018).

Mudstone caps with abundant micas and phytoclasts laminas are interpreted as the result of the fall-out of a lofting plume derived by a pulsate hyperpycnal flow (Gobo *et al.*, 2014), with each lamina that indicatively representing a pulse (Zavala & Pan, 2018).

4.4.1.5. Mass Transport Deposits

This facies could not be inspected directly as it crops out along an inaccessible cliff (Fig. 54H). It consists of a metre-thick mass transport deposit (MTD) with a minimum lateral continuity of ca. 20 m made of variable proportions of thin- to thick-bedded sandstones and mudstones. Beds are folded but deformation is locally sufficiently pervasive to obliterate the original stratigraphy. The MTD can be traced laterally into undeformed beds representing the stratigraphy in place.

Interpretation: This facies testifies mass wasting processes likely favoured by local over steepening of the slope due to high sedimentation rates.

4.4.2. Architectural elements and facies heterogeneity

Based on component facies and depositional geometries observed at outcrop and/or constrained by correlations, different architectural elements were recognised, whose sedimentary heterogeneity and meaning is detailed hereafter.

4.4.2.1. Channel-fills

A total of three of such channel fills were observed, two in the lower part (i.e., a few tens of metres above the top of the underlying fan-delta deposits of the Savignone Conglomerate) and one in the middle part of the studied sections (Fig. 55 and Fig. 56). They are encased in heterolithic muddy deposits (Section 4.4.2.3) and alternate with depositional lobes with varying sand content (Section 4.4.2.2), both characterised by hyperpycnal facies (Section 4.4.1.4).

They are composed of a few to several amalgamated beds of conglomerates and pebbly-sandstones of facies CP (see Section 4.4.1.1) and, subordinately, of parallel to cross-stratified sandstone repetitions (facies pcS-r, Section 4.4.1.4.1).

Correlations suggest these channels fills are flat-topped and are characterised by vertically stacked beds with an overall fining- and thinning-upward trend. They have a maximum observed thickness in the range 2-18 m (Fig. 56) and width in the range of ca. 200-500 m, and thin sideways both to the WNW and ESE as the basal erosion shallows, suggesting NNW-SSE directed channel axes and likewise palaeoflow. Moving away from the deeper part of the channel fill, the event beds decrease in thickness passing to dm-thick beds of either facies CP or facies mlS (see Sections 4.4.1.1 and 4.4.1.2).

The lateral extent of these channels fills is in the order of several hundred of metres along strike. Cavanna *et al.* (1989) mapped several tens of these channel fills (*cf.* with ‘facies c’) in the Monastero Fm. to the east of the studied section, whose geometry and range of lateral continuity is suggestive of palaeoflow directed toward the south-easternly quadrants.

Petrographic and textural analogies with the conglomerates of the Conglomerato di Savignone Fm., suggest these sedimentary bodies represent the fill of incisional channels indenting and terminanting landward into a coeval conglomeratic fan-delta. The size of these channel fills spans

across a range of hierarchical ranks, potentially from that of ‘channel storey’ to that of ‘channel fill’ of Sprague *et al.* (2005).

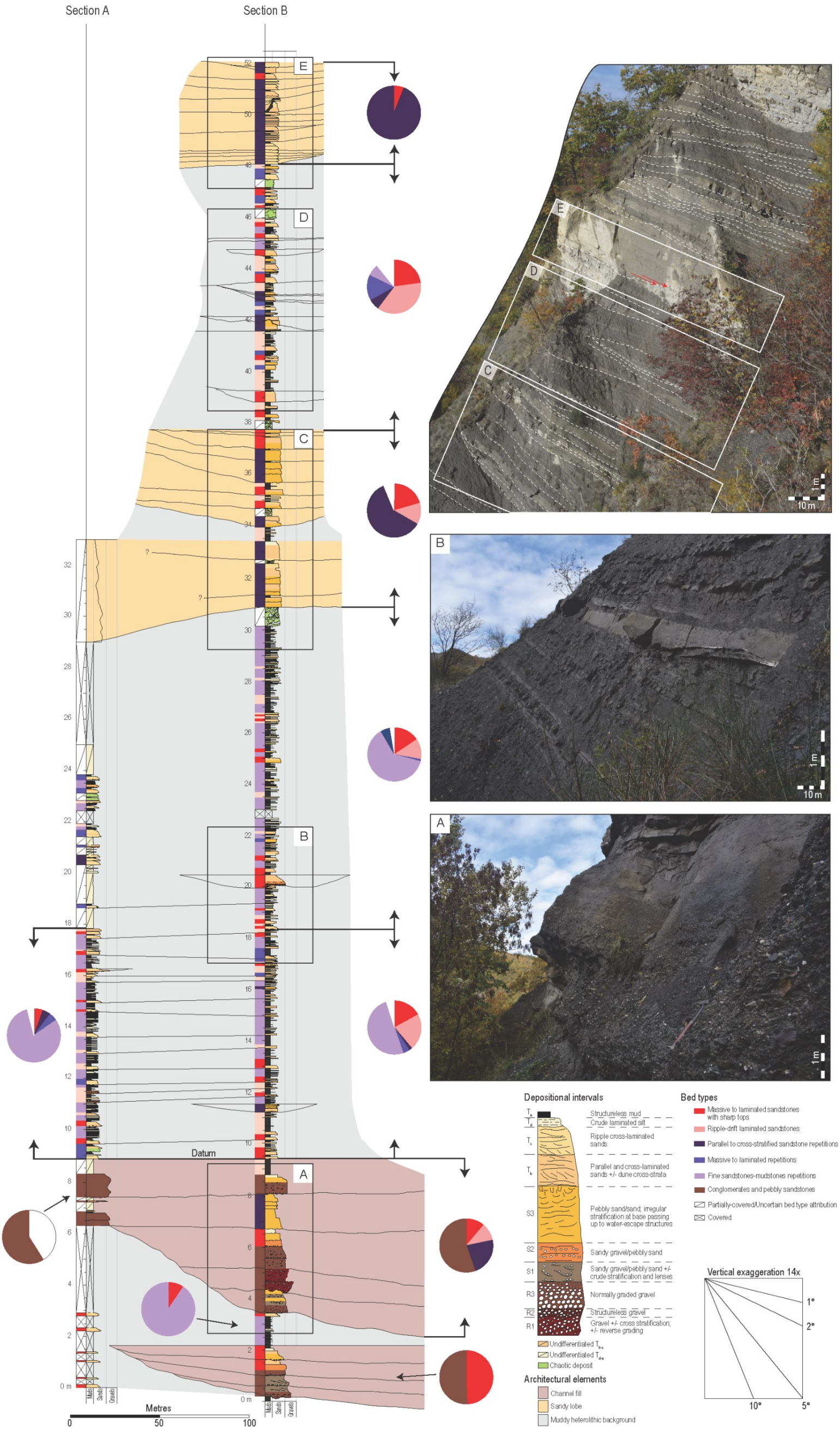

Fig. 55. Correlation panel of the lowermost part of the Monastero Fm. (for logs location see Fig. 47, the panel is oriented along an ENE-WSW transect, ca. orthogonal to mean orientation of channel axes). (A) A detail of channel fill deposits consisting of facies CP (see Section 4.4.1.1). (B) Decimetres thick bed of facies mIS (see Section 4.4.1.2) filling a metres-scale erosional surfaces, interpreted as distributary channels. (C) A detail of an amalgamated sandy lobe deposits. Note the compensation geometries between beds. (D) Thin-bedded heterolithic background characterised by unconformable bed surfaces. (E) Lower part of an amalgamated sandy lobe. Note the onlap closure of the beds onto the base (red arrows).

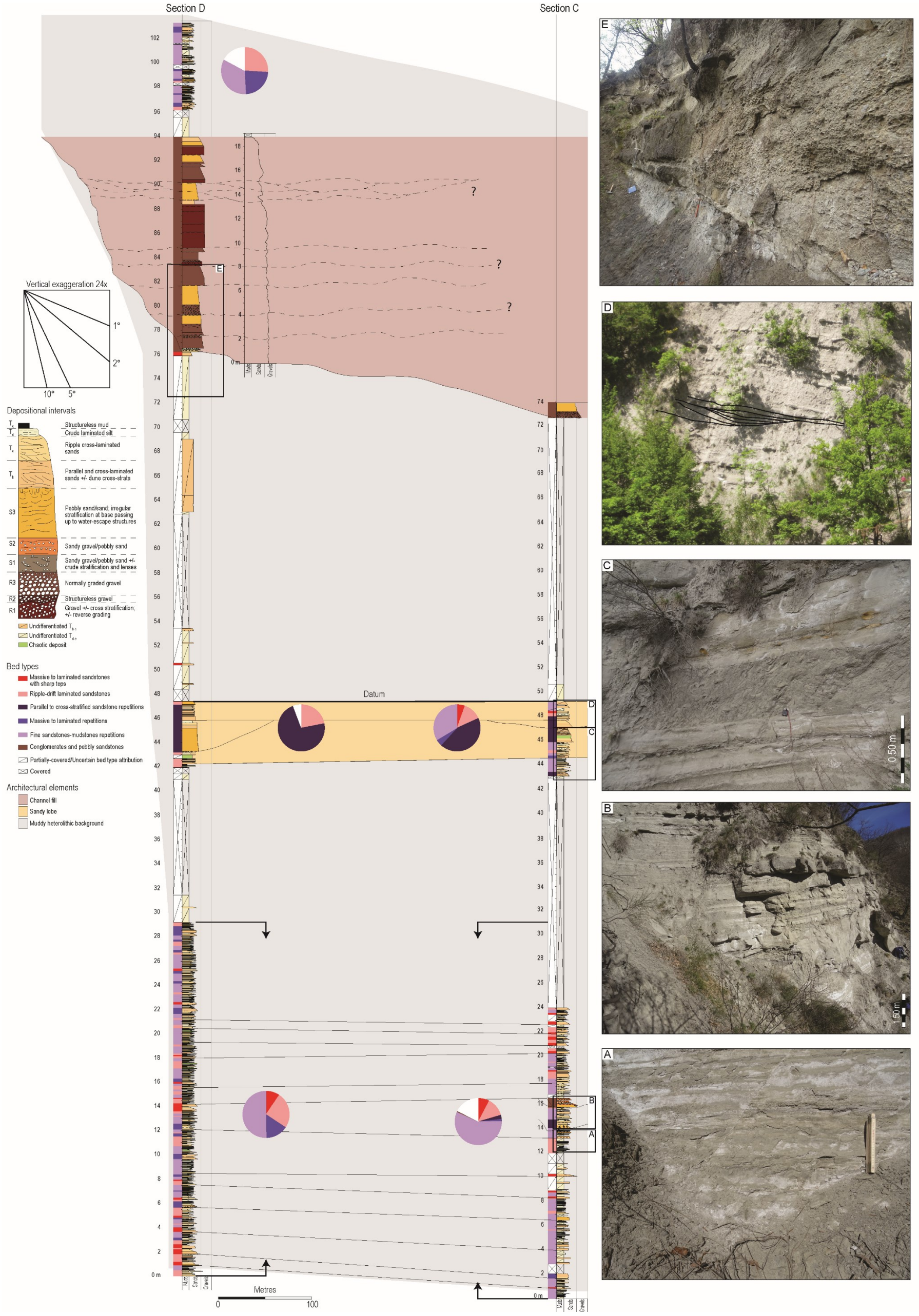

Fig. 56. Correlation panel of the middle part of the succession the Monastero Fm (for logs location see Fig. 47, the panel is oriented along an ENE-WSW transect, ca. orthogonal to mean orientation of channel axis). (A) Very thin-bedded sandstone-mudstone couplets constituting the heterolithic background (See Section 4.4.2.3). (B) Decimetre-thick beds of facies pcS-r and mlS-r (see Sections 4.4.1.4.1 and 4.4.1.4.2) forming the fill of a metre-scale erosional feature interpreted as distributary channel form. (C) Detail of a thin-bedded interval characterised by soft sediment deformation within an amalgamated sandy lobe. (D) A detail of a distributary channel within an amalgamated sandy lobe. (E) Detail of the base of the channel fill consisting of facies CP (see Section 4.4.1.1).

4.4.2.2. Depositional lobes

Depositional lobes first occur in the lower part of the studied section, encased in heterolithic muddy deposits (Section 4.4.2.3) and alternate with channel fills (Section 4.4.2.1), but become dominant in the uppermost part of the Monastero Fm. (Fig. 55, Fig. 56, Fig. 57, Fig. 58, and Fig. 59) where they were early recognized and mapped accordingly (*cf.* with "Lobi di San Gaudenzio" of Gelati, 1977 and Cavanna *et al.*, 1989).

4.4.2.2.1. Amalgamated sandy lobes

Four amalgamated lobes were encountered along the studied section (Fig. 55, Fig. 56, and Fig. 57), from which three could be logged in detail. Their base can be flat or irregular with erosional scours ca. 1 m-deep and is often associated to soft-sediment deformation of underlying thin-bedded deposits (e.g., Fig. 55C).

They are composed (see pie charts in Fig. 55 and Fig. 56) for most of their thickness by parallel to cross-stratified sandstone repetitions (i.e., 44-72% of facies pcS-r; see Section 4.4.1.4.1), and subordinately by fine sandstones-mudstone repetitions (i.e., 34% of facies SM-r, see Section 4.4.1.4.3) and massive to laminated sandstones (i.e., 13-22% of facies mlS, see Section 4.4.1.2), which can be arranged so as to form thickening-coarsening and then thinning- and fining- trends (e.g., Fig. 55C-E, Fig. 56). However, more frequently the geometry of component beds is lenticular, either because of sole erosion or compensation of the underlying deposit, which results in more complex bedding patterns.

Locally, basal erosion can be more focused and deep resulting in a channelised structure of the lobe, with the fill of erosional features (e.g., Fig. 56D) being made of a range of fine-grained conglomerates of facies CP (see Section 4.4.1.1), massive to laminated sandstones of facies mlS (see Section 4.4.1.2) and plane parallel to cross-stratified sandstone repetitions of facies pcS-r (see Section 4.4.1.4.1). The thickness of these lobes ranges between 4 and 6 m, whereas their minimum observed length (estimated along a WNW-ESE-directed outcrop belt) is in the order of 3 km (*cf.* with 'facies a' of Cavanna *et al.* 1989). Lateral terminations could not be observed directly, but mapping suggests a rapid fringing into less amalgamated and relatively thin-bedded deposits.

Facies composition and geometry suggest that these sedimentary bodies may represent sandy hyperpycnal lobes (*sensu* Zavala *et al.*, 2011a), crossed in their most proximal part by small-scale ephemeral distributary channels.

By a hierarchical standing point, the size of these lobes is comparable to that of turbidite 'lobe storeys' of Sprague *et al.* (2005).

4.4.2.2.2. Heterolithic lobes

Three heterolithic lobes are present along the studied section, all exposed on inaccessible cliffs (Fig. 57A-B) a few metres to several tens of metres above Sections B (Fig. 12). They show thicknesses in the range of 1.5-3 m, rather flat geometry, and minimum lateral continuity of ca. 1.5 km. Internally they are parallel-stratified and made of a several to a few tens of sandstone-mudstone couplets belonging mostly to facies SM-r (Fig. 57B) with an overall sand to mud ratio close to 1.

A sandier variety of this lobe type is that portrayed in Fig. 58A, which crops out immediately above Section B in the lower part of the Monastero Fm. Differently from other examples, this sedimentary body show a sigmoidal shape with flat base and convex top. It is up to 4 m thick and likely made of three fining- and thinning-upward bed sets (likely belonging to facies mlS-r and SM-r, see Sections 4.4.1.4.2 and 4.4.1.4.3, respectively), separated one from another by erosional surfaces (Fig. 58B-C), with flaser-bedding and soft-sediment deformations (Fig. 58C-D).

Facies composition suggests these sedimentary bodies represent parts of hyperpycnal lobes, comparatively less-sandy and of smaller lobes than amalgamated sandy lobes described in Section 4.4.2.2.1.

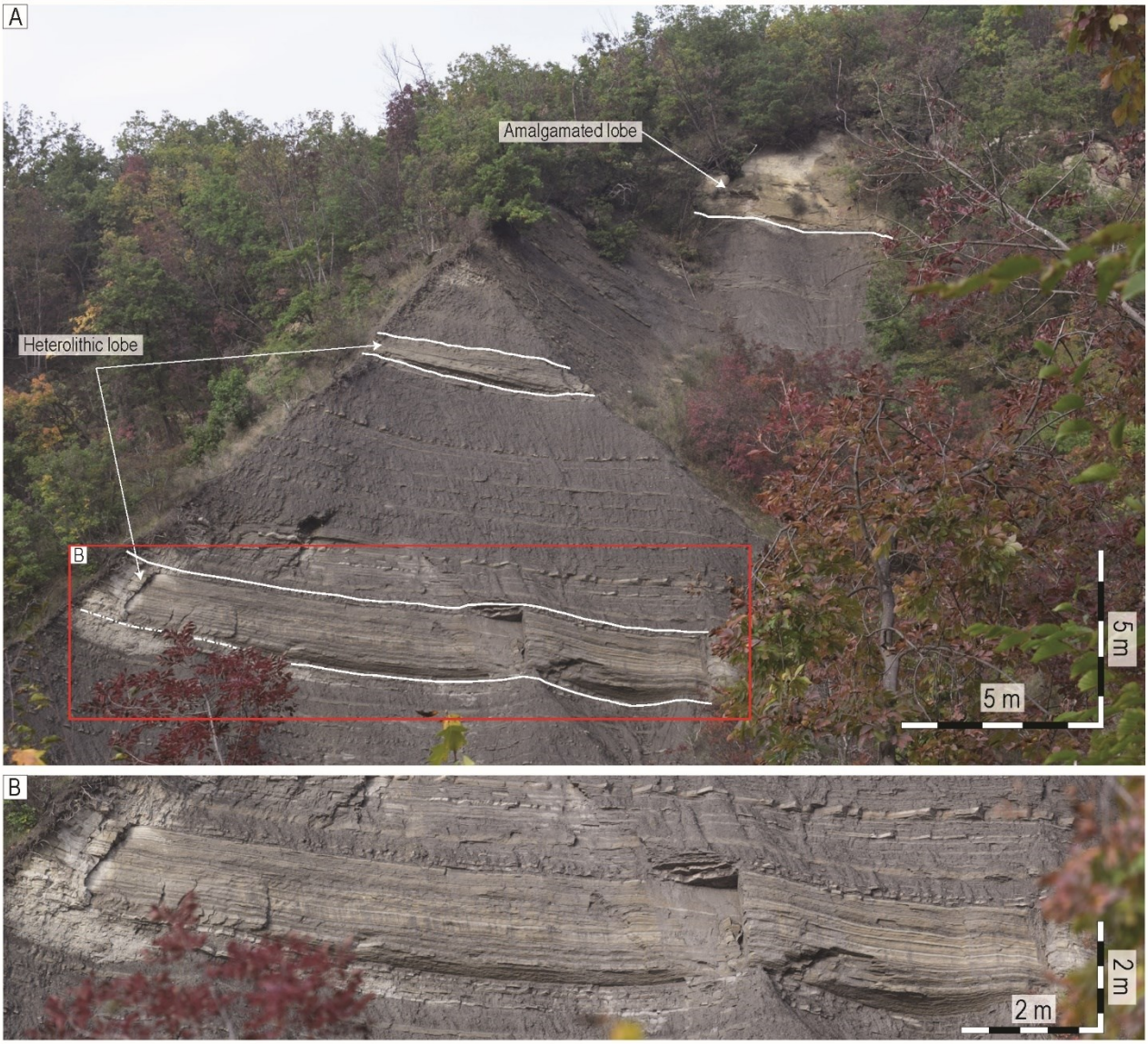

Fig. 57. (A) Panoramic view of the north-eastern cliff along the road between Dernice and Garbagna villages, nearby Section C (i.e., middle part of the Monastero Fm.) ca.-oriented transverse to the mean palaeoflow (Fig. 47). Two metres-thick heterolithic lobes and an amalgamated lobe are enveloped in the thin-bedded heterolithic background. Note flat geometries of heterolithic lobe base and top. (B) Detail of picture A showing the internal stacking pattern of heterolithic lobe deposits. Note the abundance of thin-bedded sandstones-mudstones couplets constituting them.

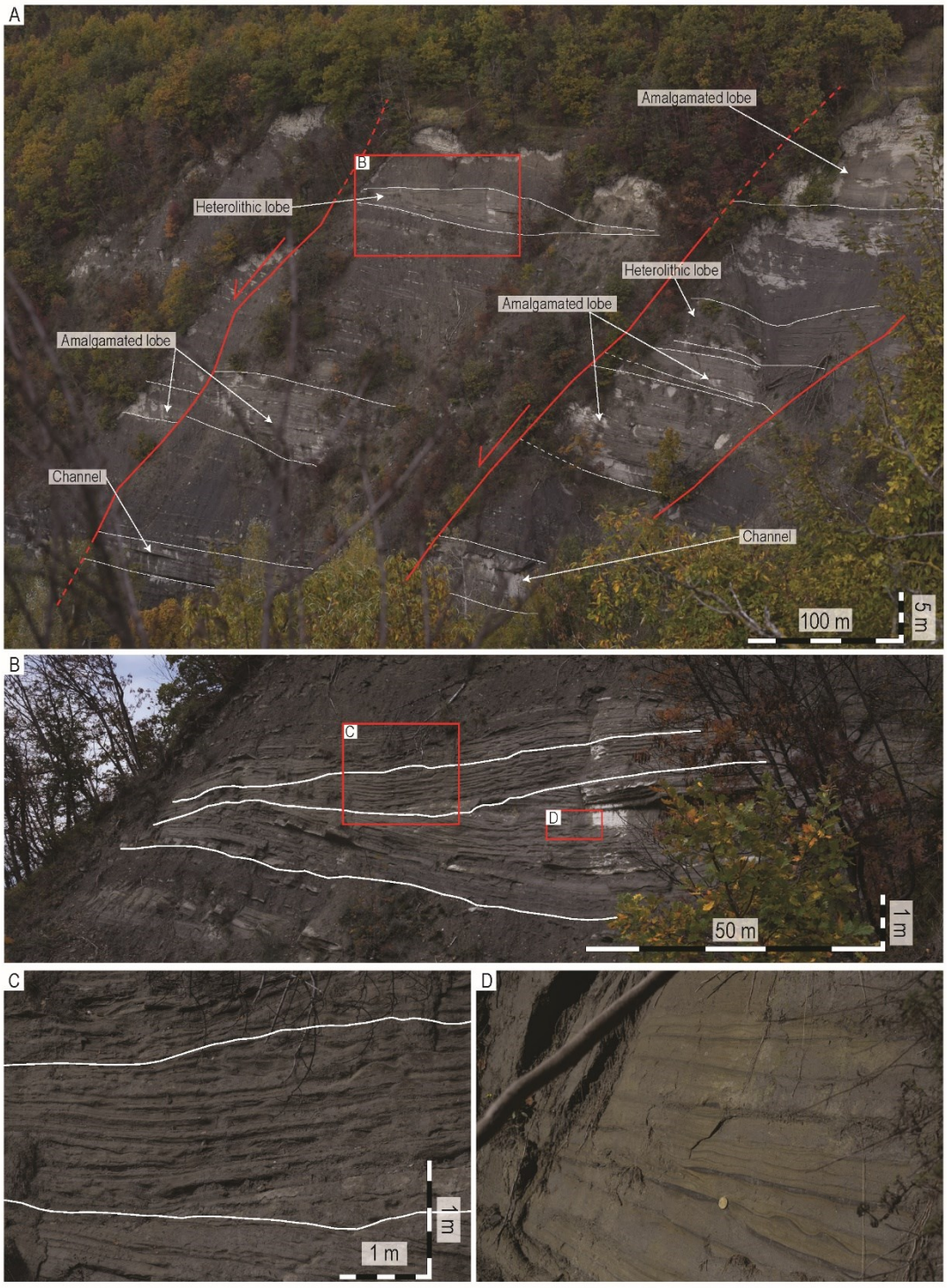

Fig. 58. (A) Panoramic view of the cliff to the north of Dernice (roughly orthogonal to mean channel axes; palaeoflow is directed towards the reader Fig. 47). Channel fill (see Section 4.4.2.1) and lobe deposits (see Section 4.4.2.2) are encased in the muddy heterolithic background (see Section 4.4.2.3). The red frame indicates the sigmoidal-shaped heterolithic lobe (see Section 4.4.2.2.2). Red lines are faults. (B) Detail of the sigmoidal heterolithic lobe. Note the three sequences and the erosional characteristic of their base. (C) Detail of the erosional surfaces pointed out in picture B. Note how surfaces above them are erosive. (D) Alternated sandstones-mudstones couplets constituting the heterolithic lobe (facies SM-r, see Section 4.4.1.4.3). Sandstones are plane-parallel and ripple cross-laminated, sometimes convoluted due to soft-sediment deformation. Mudstone caps are frequently preserved in mm- to sub-mm thick laminas (coin for scale).

4.4.2.2.3. Non-amalgamated sandy lobes

Two out of the several depositional lobes characterizing the upper most part of the Monastero Fm in the studied section (*cf.* with “Lobi di San Guadenzio” reported by Gelati, 1977, e.g., Fig. 59A) were logged at one single locality (Section E in Fig. 59) to assess facies composition contrast with that of other lobe type describe so far (Section 4.4.2.2.1 and 4.4.2.2.2).

Both logged examples have a thickness of ca. 5 m and a minimum width of ca. 1500 m (estimated along a E-W oriented outcrop belt; see Fig. 47), across which they appear to be bounded by rather flat bases and tops. Internally, these lobes are chiefly comprised of parallel to cross-stratified sandstone repetitions (22-27%; facies pcS-r, see Section 4.4.1.4.1) and, subordinately, rippled laminated (15-35%; facies mlS, see Section 4.4.1.2) and massive to laminated sandstones (12-16%; facies rS, see Section 4.4.1.3). Furthermore, conglomerates of facies CP (see Section 4.4.1.1) are present in a percentage of 30% of the total thickness in the lower lobe (e.g., between 6 m and 10 m along Section E of Fig. 59).

All these depositional events are stacked to form and aggradational arrangement with each event non-amalgamated to the one below.

In the logged section, the two lobes are separated one from another by a ca. 1 m thick interval made of thin-bedded ripped laminated sandstone (facies rS, see Section 4.4.1.3) and parallel to cross-stratified sandstone repetitions (facies mlS-r, see Section 4.4.1.4.2) (e.g., Fig. 59B).

Cavanna *et al.* (1989) mapped non-amalgamated lobe deposits (*cf.* with facies “a” of their work) in a greater area of the Borbera-Curone sub-depocentre, indicating that palaeoflows are directed toward south-easternly quadrants.

Facies composition suggests these sedimentary bodies represent parts of non-amalgamated hyperpycnal lobes. From a hierarchical standing point, the size of these lobes is comparable to that of turbidite ‘lobe storeys’ of Sprague *et al.* (2005).

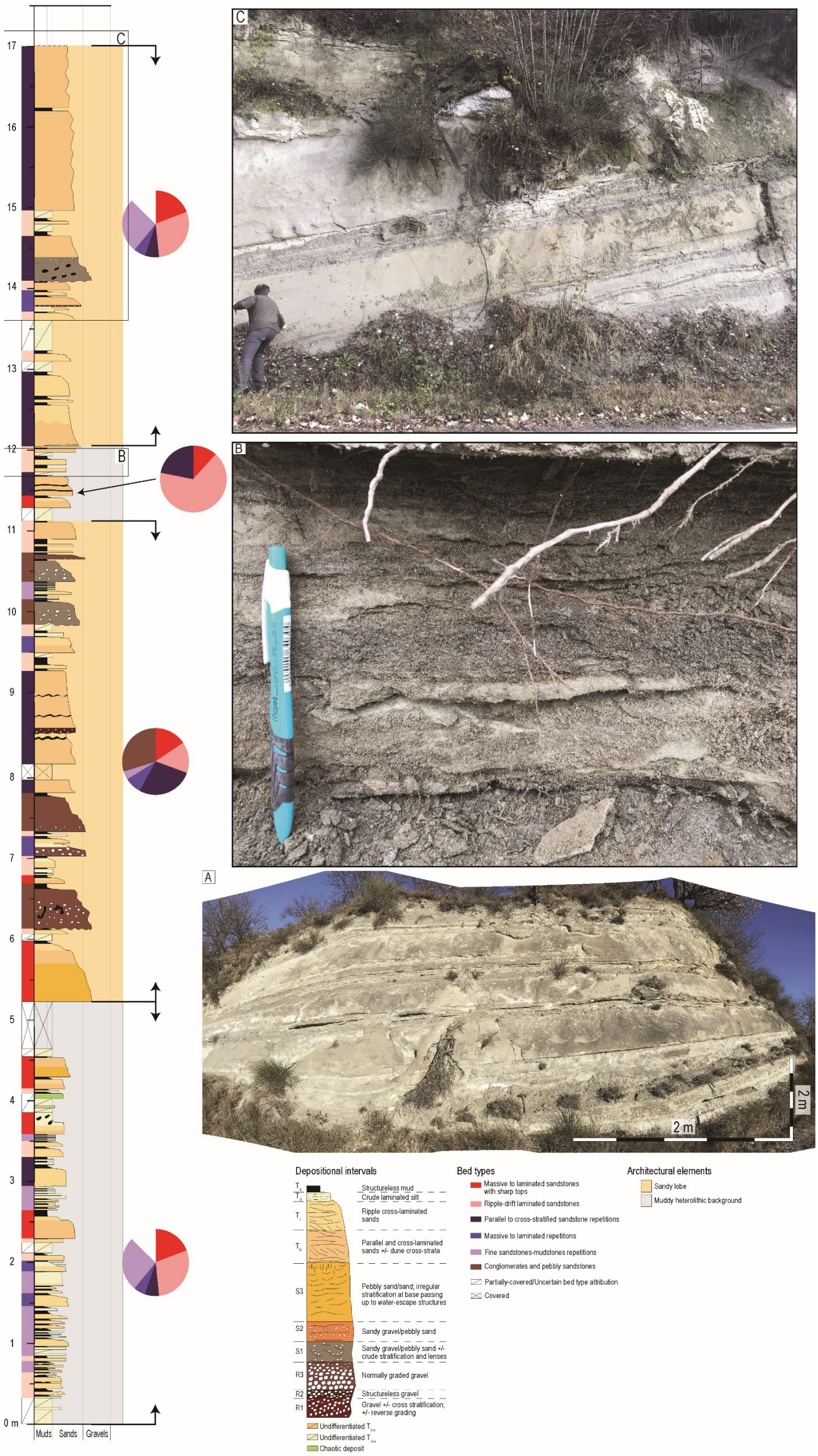

Fig. 59. Detail sedimentological “Section E”, measured in the upper part of the Monastero Fm. (see Fig. 47 for location). (A) Outcrop view of non-amalgamated lobe named by Gelati (1977) as “Lobi di San Gaudenzio”. Note the tabular shape and facies pattern made of parallel to cross-stratified sandstone repetition (facies pcS-r, see Section 4.4.1.4.1). (B) A detail of ripple laminated sandstone-mudstone couplets (facies rS, see Section 4.4.1.3) intercalated to lobe deposits. (C) Non-amalgamated lobe deposits consisting of parallel to cross-stratified sandstone repetitions (facies pcS-r, see Section 4.4.1.4.1).

4.4.2.3. Muddy heterolithic background

The depositional elements described so far are embedded within a muddy heterolithic background that corresponds to the 'facies s' of Cavanna *et al.* (1989) and constitutes more ca. 60% of the total logged thickness (i.e., 94 m out of 155 m).

This background is chiefly comprised of very thin to thin beds of fine-grained sandstone-mudstone repetitions (i.e., 50-81%, facies SM-r, see Section 4.4.1.4.3), ripple laminated sandstones (13-25%, facies rS), massive to laminated sandstone repetitions (4-15%, facies mlS-r, see Section 4.4.1.4.2), and massive to laminated sandstones with sharp tops (6-17%, facies mlS, see Section 4.4.1.2) (see pie charts in Fig. 55 and Fig. 56), often displaying soft-sediment deformations (Fig. 54G). Beds are tightly packed, with a total number of event bed per metre of ca. 3.

Locally, massive to laminated sandstone (facies mlS-r) and parallel to cross-stratified (facies SM-r) repetitions and, more, rarely pebbly sandstones of facies CP (see Section 4.4.1.1) can have basal scours up to 0.5 m-deep and 100-m across (Fig. 55B and Fig. 56B).

These beds are laterally continuous for few tens to a few hundreds of metres, closing by progressive pinch out.

The muddy heterolithic background also contains rare trace fossils belonging to a range of taxa. These include *Paleodictyon sp.*, *Cosmorhaphe sp.*, *Scolicia sp.*, *Udichnia sp.*, *Taenidium sp.*, *Cladichnus sp. ?, Glockerichnus sp. ?, Thalassinoides sp.? Ophiomorpha sp.?* (Fig. 60).

Focused erosion, sediment remobilization and a combination thereof, can impart an overall poorly stratified appearance to this thin-bedded background facies association (Fig. 55D).

Facies composition suggest the muddy heterolithic background is chiefly the product of deposition by frequent hyperpycnal flows and turbidity currents, locally capable of channelising into previously deposited sediments. The occurrence of *Thalassinoides sp*. ? and *Ophiomorpha sp*. suggests opportunistic colonization during times of decreased sedimentation rate (Buatois *et al.*, 2011).

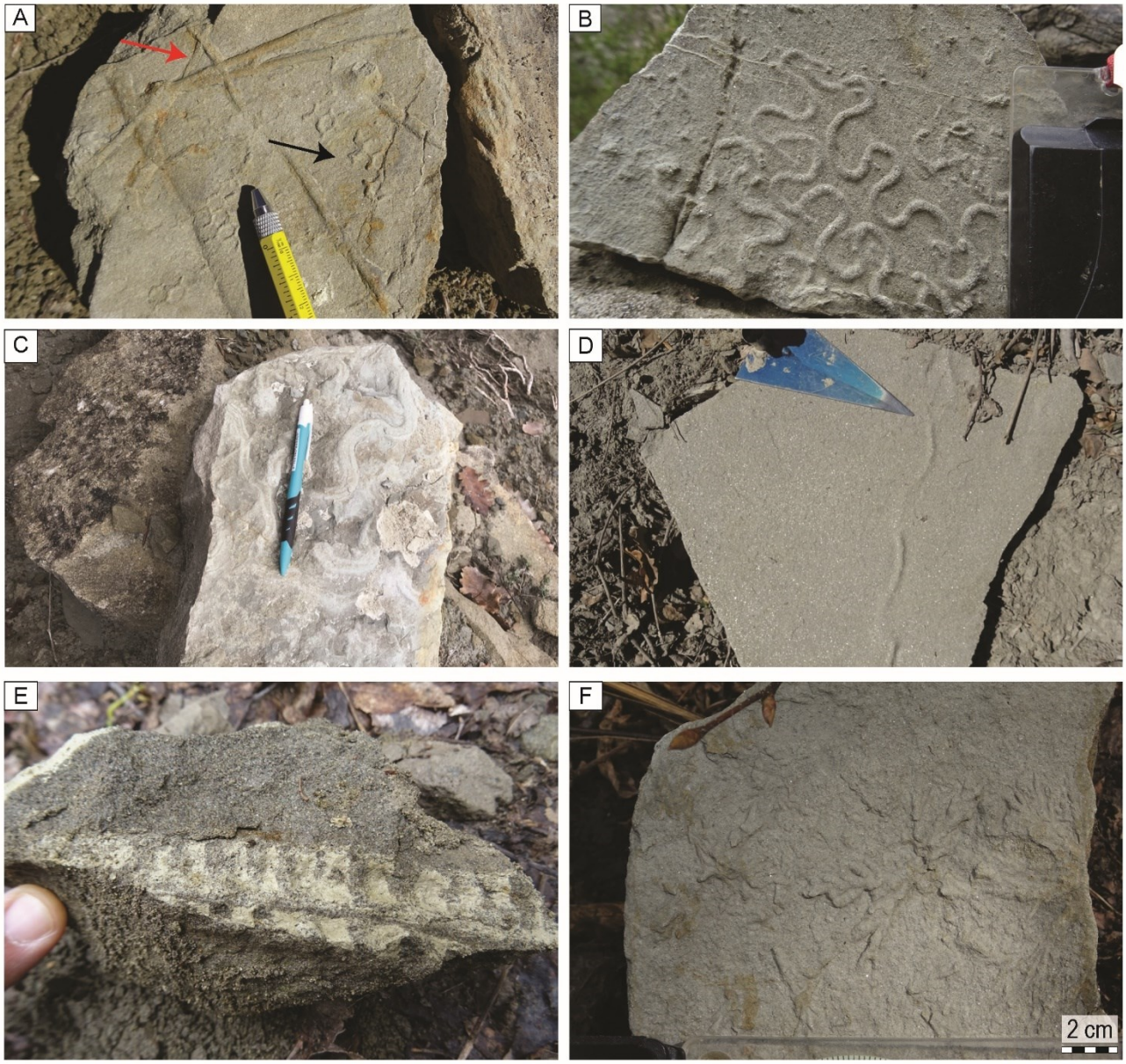

Fig. 60. Ichnogenera recognised in the thin-bedded sandstone-mudstone background. (A) Paleodictyon (black arrow) and Thalassinoides/Ophiomorpha (red arrow). (B) Cosmorhaphe. (C) Scolicia. (D) Udichnia. (E) Taenidium (uncertain attribution). (F) Cladichnus/Glockerichnus.

4.4.3. The Savignone Conglomerate-Monastero Fm. system in the subsurface

Seismic sections of Fig. 61A-C are located to the west of the Scrivia Valley Fault, in a sector representing the western bound of the Savignone-Ranzano Oligocene Basin (Rossi *et al.*, 2009). Here, at surface the Rupelian succession lies with disconformable contact (lower-Rupelian unconformity) upon basement rocks and is represented by the fan-delta conglomerates and sandstones of the Molare Fm., the largely coeval westerly equivalent of the Savignone Conglomerate (Gnaccolini, 1974; Gelati & Gnaccolini, 1984; Ghibaudo *et al.*, 1985, 2019; Barbieri *et al.*, 2001). On

the other hand, the seismic section of Fig. 61B straddles the Scrivia Valley Fault, highlighting the role of this fault in controlling the western boundary of the Monastero Fm. basin during the Rupelian.

The early Rupelian unconformity is tied to outcrops located along the southward continuation (not shown) of the sections of Fig. 61A and C. Due to the generally poor quality of the seismic data at depth, this unconformity was recognized and tracked with confidence in sections of Fig. 61C and Fig. 60B only. The late-Chattian unconformity, representing the upper boundary of the Oligocene overall transgressive unit (Unit II of Rossi *et al.*, 2009) to which the Monastero Fm. and time-equivalent systems belong, could be tied to surface geology in section of Fig. 61B, and is generally clearly expressed (Fig. 61A and C), as it separates a relatively transparent facies below (Gremiasco Fm.-like slope to basinal mudstones; *cf*. with Rocchetta Fm. of Ghibaudo *et al.*, 2019) from a package with locally high amplitude reflectors with onlap terminations (i.e., confined turbidite systems of Aquitanian age equivalent to the Castagnola Fm.; Marini *et al.*, 2016b).

The early-Rupelian unconformity is difficult to locate in the southern part of section of Fig. 60A, whereas to the north it separates the Oligocene succession from a layered seismic facies attributable to late Eocene turbidites (Dernice Fm.). It is noteworthy that the Oligocene deposits tend to thicken northward before rapidly thinning out across the Villarvernia-Varzi flower structure. This geometry suggests that early (intra-Rupelian) deformation along the Villarvernia-Varzi line (Festa *et al.*, 2015) was able to generate sufficient submarine relief to confine to the north the Oligocene depositional systems, most likely represented by deep-water clastics at this location (Rossi *et al.*, 2009).

In the section of Fig. 60C, the mounded morphology at the toe of Rupelian fan-delta systems suggests the presence of a basin floor turbidite fan that is veneered by Chattian mudstones and onlapped to the NW by Lower Miocene deposits.

The section of Fig. 60B shows the termination of the Monastero Fm. against the Val Scrivia Fault. To the east, it can be seen how the passage between the Savignone Conglomerate and the Monastero Fm. occurs across a relatively high-amplitude reflector (laterally continuous coarse-grained body embedded in the thin-bedded heterolithic background, see Section 4.4.2.3) and is locally more subtle, possibly due to lateral heteropy between the two units.

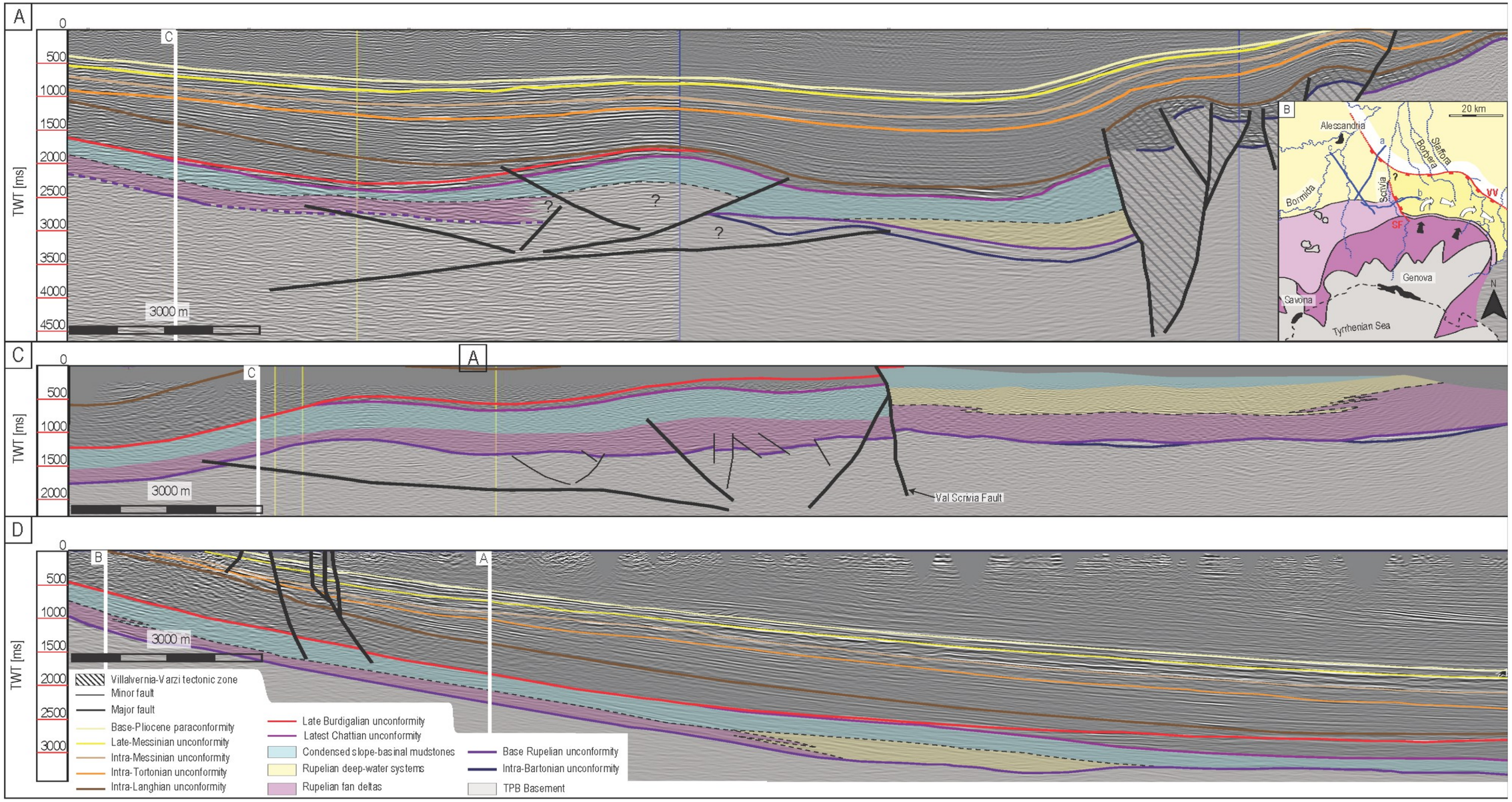

Fig. 61. Two-Way Time seismic sections from the eastern Tertiary Piedmont Basin (see Fig. 46 and inset map of this figure for location). (A) SSW-NNE oriented seismic section showing the lateral confinement of the Bartonian-Aquitanian succession by the Villalvernia Varzi tectonic zone. (B) Inset palaeogeographic map showing the depositional setting at the time of the Monastero Fm. and location of sismic lines (see Fig. 64 for details). (C) E-W oriented seismic section showing in detail the Savignone Conglomerate-Monastero Fm. depositional system. Note the heterophy relation between these two units to the east of the Val Scrivia Fault. (D) NNW-SSE oriented seismic section showing the evolution of the Oligo-Miocene units toward the basin depocentre. Uninterpreted seismic lines in Appendix II.

4.4.4. Rock magnetism and magnetostratigraphy

IRM backfield acquisition on samples SC2b and SC12 indicates that the main carriers of remanence are low-coercivity minerals (H_{cr} ≈ 25-35 mT) with saturation reached between 120-160 mT (Fig. 62C). The shapes of hysteresis loops of samples SC2b and SC12 (Fig. 62D), corrected for paramagnetic contribution, are typical of pseudo single-domain (PSD) grains (Tauxe *et al.*, 2002). The slenderer and more inclined slope in sample SC2b suggest coarser ferromagnetic grains. This is confirmed also by the position of the samples in the Day plot (Day et al., 1977; Dunlop, 2002). Non-corrected hysteresis loops (Appendix III) indicate the minor contribution of paramagnetic and superparamagnetic (SP) particles, much more evident in sample SC12 (potbellied shape; Tauxe et al., 1996). Thermal demagnetisation of three-axis IRM (Lowrie, 1990) shows a main unblocking temperature of ~300°C on both the 0.12 and 0.4 T curves, with complete demagnetisation at ~550-575°C (Fig. 62E). The 1.5 T curve shows a negligible contribution of high-coercivity minerals. The unblocking temperatures in the Lowrie diagram are coherent with the presence of pyrrhotite and magnetite, the latter partially originated from the oxidation of pyrrhotite.

The ChRM polarity was obtained for 4 samples out of 16. ChRM directions were extracted with principal component analisys (PCA) on samples SC4, SC9, SC10, and SC12bis (see Fig. 62 for location).

In 9 out of the remaining 11 samples ChRM is highly overprinted by a secondary component, but remagnetisation circles are well recognisable, all of them showing a trend from viscous normal polarity component to reverse polarity. Unfortunately, the ChRM is not directly measurable.

In Section ‘D’ no samples provided normal polarity ChRM, thus we can confidently interpret the entire stratigraphic interval as reverse polarity.

When plotted on an equal-area stereo-plot after tilt-correction, ChRM component directions form a relatively well-defined cluster oriented southeast-and-up suggestive of a reverse polarity.

The in situ and tilt-corrected ChRM mean directions were calculated by applying the mixed remagnetisation circles statistics of McElhinny & McFadden (1998) (Fig. 63; Tab. 4).

MEAN DIRECTIONS									
		In Situ				Tilt-Corrected			
Site	N	k	α_{95}	Dec.	Inc.	k	α_{95}	Dec.	Inc.
Section 'D'	13	11.8	12.9°	146.5°E	-43.6°	11.8	12.9°	143.1°E	-25.2°

PALEOMAGNETIC POLE AND ROTATION					
Site	Lat.	Long.	k	A_{95}	Rotation
Section 'D'	45.6°N	245.6°E	11.8	7.5°	32.2° ± 8.2° CCW
Oligocene Reference Pole (Africa-Adria)[1]	77.8°N	208.1°E	470	5.7°	

Note: N: number of samples Dec.: mean Declination Inc.: mean Inclination
k: Fisher precision parameter α_{95}: radius of the 95% confidence cone
Lat.: Latitude Long.: Longitude A_{95}: radius of the 95% confidence cone around the pole
References: [1]Muttoni *et al.* (2013)

Tab. 4. Paleomagnetic mean directions and pole of the Section 'D'

The tilt-corrected mean direction yielded a paleomagnetic pole at Latitude = 45.5°N, Longitude = 245.6°E (A95 = 7.5°) that is rotated by ca. 32° counter-clockwise with respect to the Miocene reference pole of Adria/Africa (Muttoni et al., 2013). This result is in substantial agreement with previous data from other sedimentary units of comparable age from the TPB (Kie, 1988; Maffione *et al.*, 2008; see Table 1), and reflect the generalized counter-clockwise rotation of northern Apennines thrust sheets during the Neogene (e.g., Muttoni *et al.*, 1998).

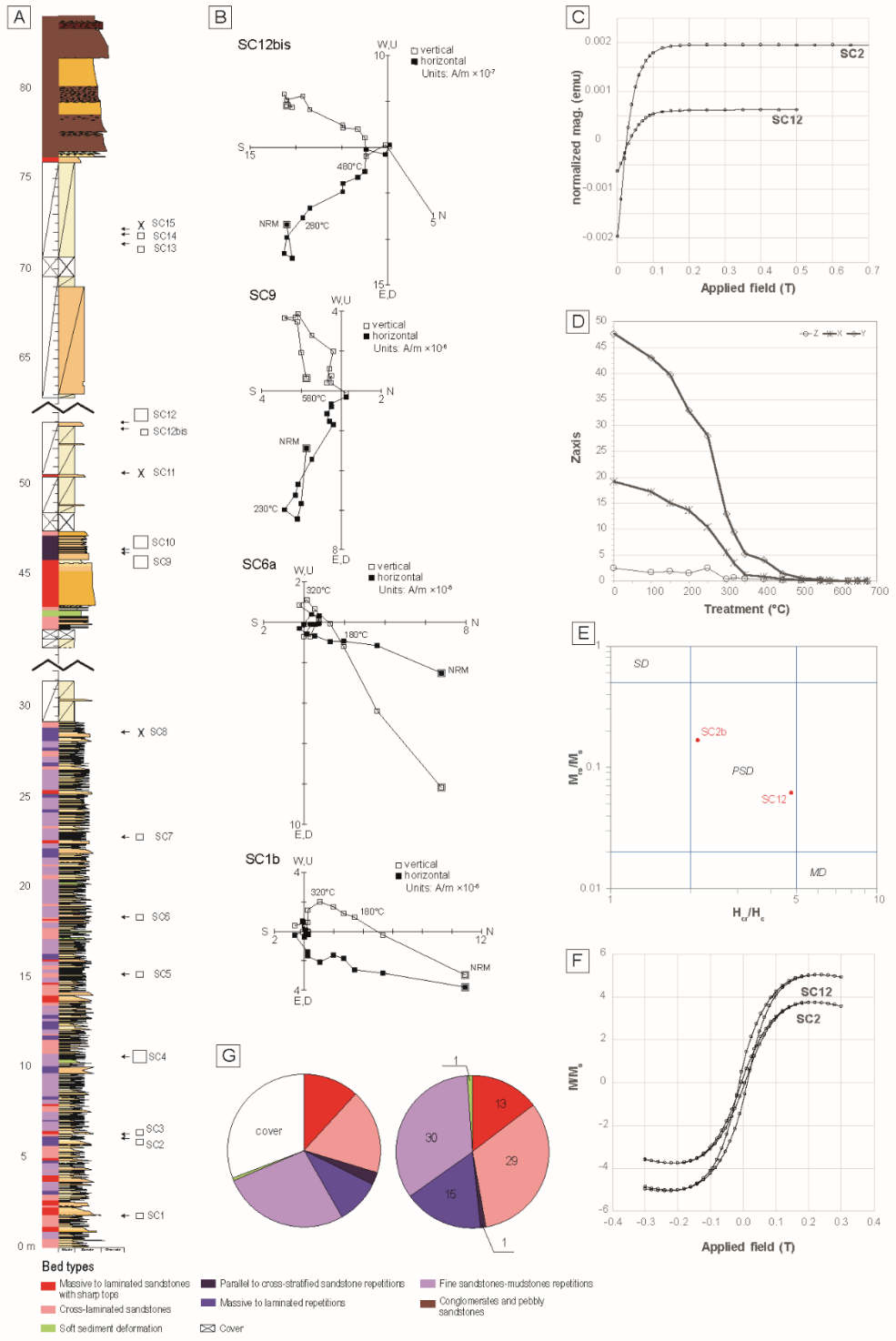

Fig. 62. (A) Lithostratigraphy of section 'D', Monastero Fm. (B) Vector end-point demagnetisation diagrams for representative samples in *in situ* coordinates. Closed squares are projections onto the horizontal plane, and open squares are projections onto the vertical plane. (C) IRM backfield acquisition curves of samples SC2b and SC12; (D) Hysteresis loops of samples SC2b and SC12, corrected for paramagnetic component. (E) Day plot. Note how Samples SC2b and SC12 fall in the pseudo single-domain area (PSD). (F) Thermal demagnetisation path of three-axes IRM on representative samples. (G) Pie charts showing the breakdown by bed type of cumulative thickness (left) and number of component beds (right) of the sampled section.

The planktonic foraminifer assemblage characterising this reversed polarity interval comprises reworked *Turborotalia ampliapaertura*, *Paragloborotalia opima*, *Tenuitella angustiumbilicta*, *Dentoglobigerina galavisi*, *Subbotina angiropoides*, and *Globoturborotalia martini* (Gelati, 1977). Together with the the first occurrence of *Paragloborotalia siakensis* a few metres above the sampled interval (Fig. 62), biostratigraphy suggests section D belongs to the biozone O3 (Wade *et al.*, 2011) and is thus part of the reverse polarity magnetochron C11r (Ogg *et al.*, 2016).

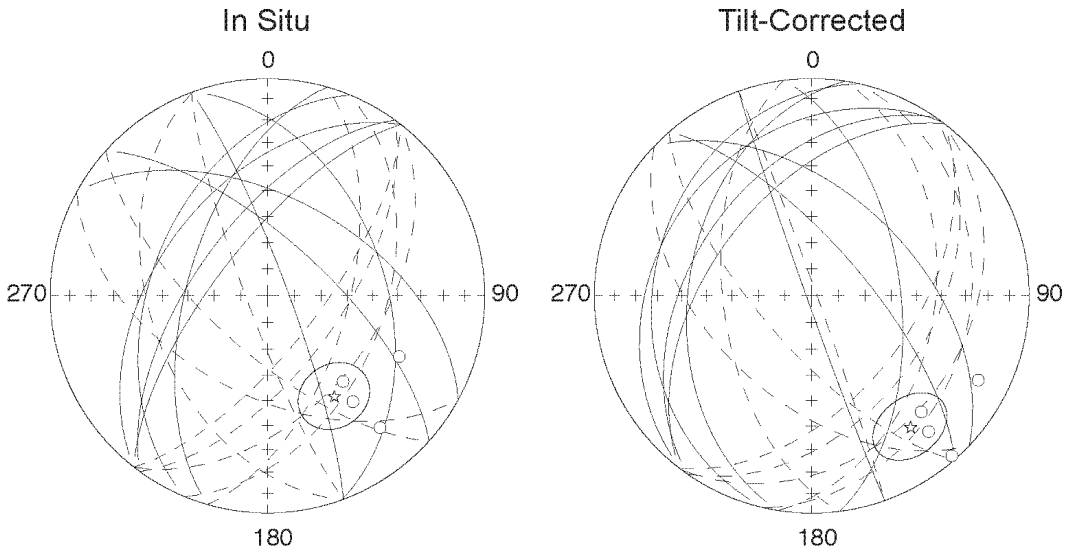

Fig. 63. Stereographic projection showing in situ (left) and tilt-corrected (right) ChRM directions obtained by PCA (empty dots, 4 samples) and remagnetization great circles of the remaining 9 samples. Mean ChRM direction (star) and its ellipse of 95% confidence have been calculated using the method of McElhinny & McFadden (1998).

4.5. Discussion

4.5.1. Hyperpycnal origin of the Monastero Fm

Facies analysis results show that a significant fraction (ca. 65%) of the event beds of the measured section of the Monastero Fm. are composed of repeated sedimentary divisions characterised by range of features (e.g., inversely graded bases, bed-load transport fabrics, plant debris- and mica-rich fine-grained tops; see Zavala *et al.*, 2011 for a review) that are hard to explain as deposited by 'classical' turbidity currents (e.g., Mulder & Syvitski, 1995; Shanmugam, 2000; Mulder *et al.*, 2003).

Although it could be argued that repetitions might represent the result of flow confinement by basin morphobathimetry (e.g., due to generation of reflected flows and sloshing internal waves; Pickering & Hiscott, 1985; Patacci *et al.*, 2015) this seems unlikely, since other sedimentary features typical of confined turbidites (e.g., sedimentary structures with large dispersion of orientation or even opposing direction, oscillatory-flow and combined-flow bed forms and anomalously thick event beds with relatively thick mudstone caps; Van Andel & Komar, 1969; Hiscott & Pickering, 1984; Pickering & Hiscott, 1985; Haughton, 1994, 2000; Marini *et al.*, 2016a; b) are notably rare or missing.

Rather, the many analogies with hyperpycnites reported in the literature (Mutti *et al.*, 1996, 2000, 2002b; Plink-Bjölrklund & Steel, 2004; Petter & Steel, 2006; Zavala *et al.*, 2011a; Gobo *et al.*, 2015; Zavala & Pan, 2018) suggest that the event beds with repeated sedimentary divisions (Section 4.4.1.4) might represent the deposit of pulsating hyperpycnal flows arising from riverine floods with a complex discharge hydrograph (Junk *et al.*, 1989; Wolski & Murray-Hudson, 2006; Pricope, 2013; Rosen & Xu, 2014; Hansford *et al.*, 2020). This would include an overall waxing-to-waning component (Mulder *et al.*, 2003) explaining the locally preserved coarsening and then fining trends, and second-order variations (see experimental works by Duringer *et al.*, 1991; Lamb & Mohrig, 2009) responsible for the multiple grading (*cf.* with facies B3 and S2 in Zavala & Pan, 2018 and facies association 3a in Bourget *et al.*, 2010).

The relatively small range of grain size variability of the beds with repeated sedimentary divisions is an acessory feature supporting their hyperpycnal origin. Despite these beds are rarely thicker than several tens of centimetres, in fact their moderately to well-sorted nature may indicate a parent

flow with an underlying sustained character, capable of hydraulically selecting sedimentary particles (Bridge, 1981; Khan *et al.*, 2005).

Hyperpycnites of the Monastero Fm. are interbedded with coarse-grained channel fills (Section 4.4.2.1) and 'classical' turbidite beds (Sections 4.4.1.2 and 4.4.1.3). The small lateral continuity of beds, partly due to soft-sediment deformation and local channelisation, together with the generally less than perfect outcrop exposures of the Monastero Fm., hamper the precise establishment of a relationship between hyperpycnite beds and other facies. Nonetheless, it can be speculated that, except for mass transport deposits (Section 4.4.1.5), the facies of the Monastero Fm are all part of a hyperpycnite continuum. Coarse-grained sediments, similar to the conglomerates and pebbly sandstones of facies CP (Section 4.4.1.1), were reported elsewhere associated with typical hyperpycnites (Mutti *et al.*, 2002b; Plink-Björlrklund & Steel, 2004; Petter & Steel, 2006), whereas many authors (Piper *et al.*, 1999b; Mutti *et al.*, 2003; Zavala *et al.*, 2011) suggested that 'classical' turbidites can result from the downcurrent transformation of hyperpycnal flows.

Though the abundance of hyperpycnal facies in the Monastero Fm. could be questioned (see discussion in Shanmugam, 2000), it must be borne in mind that the Oligocene basin physiography is extremely favourable to the development of hyperpycnal flows. In fact, the Monastero Fm. was hosted in a tectonically active basin (Carrapa, 2002; Carrapa & Garcia-Castellanos, 2005) characterised by a reduced shelf which was closely interconnected to its feeding deltaic system. As suggested by Mutti *et al.* (1996, 2000), all these factors result in small drainage basins with high relief and sediment runoff attached to a shelf break closely passing to deep water environments.

4.5.2. A revised depositional model for the Monastero Fm.

This work provides novel sedimentological, stratigraphic and subsurface data that can be used to propose a revised depositional model for the Rupelian-aged Monastero Fm. and insights into facies and architectural elements of what can be regarded as a hyperpycnal clastic ramp.

Beside confirming the structurally confined nature and relatively small size (the preserved part is estimated to be ca. 50x20 km) of the host basin (Ghibaudo *et al.*, 1985; Cavanna *et al.*, 1989; Di

Giulio, 1991; Festa *et al.*, 2015), bounded to the north and to the west by the Villalvernia-Varzi tectonic line and the Scrivia Fault, respectively, the interpretation of three 2D seismic lines (Section 4.4.3) highlights how systems similar to the Monastero Fm. might occur in the subsurface, down-dip of partly coeval fan-delta conglomerates (Savignone Conglomerate and Molare Fms.) cropping out to the south.

The stratigraphic logs acquired as part of this work, complemented by photopanel interpretation and geological mapping, provided insights into sedimentary facies and architectural elements of the lowermost, middle and upper part of Val di Grue-San Guadenzio section (Gelati, 1977), the thickest and best exposed of the Monastero Fm.

Results show that the lowermost and middle part of the Monastero Fm. is characterised by conglomeratic channel fills (Section 4.4.2.1) that are several metre-thick and up to ca 1 km across and become relatively less frequent up-section, in favour of depositional lobes (Section 4.4.2.2). Channel fills and lobes are surrounded by a thin-bedded and relatively muddier heterolithic background (Section 4.4.2.3).

The latero-vertical stratigraphic relationship with the Savignone Conglomerate (a few tens of metres below in the studied section) along with a common petrographic composition of the gravelly fraction (*cf.* with Di Giulio, 1991; Martelli *et al.*, 1998; Marroni *et al.*, 2010), indicates that these conglomeratic bodies of the Monastero Fm. might represent the sedimentary fills of the distal section of channels indenting a coeval fan-delta system developed on the shelf to the south of the Borbera-Curone sub-basin (Fig. 64). The vertically layered nature of these channel fills, along with the lack of associated levées, suggests that the parent submarine channel was incisional, behaving as a by-pass conduit before being filled at a later stage.

The size and composition of lobes of the Monastero Fm. varies stratigraphically. In the lower section, the thickness of lobes is in the range ca. 1-6 m, with thicker lobes (typically up to 8 m-thick, Section 4.4.2.2.1) being comparatively sandier and amalgamated compared to thinner examples (generally less than ca. 2.5 m-thick; Section 4.4.2.2.2), which are instead typically heterolithic and

muddier (sand to mud ratio is ca. 1). Moving upward, amalgamated sandy lobes appear to become relatively less frequent in favour of heterolithic muddy lobes. In keeping with their hyperpycnal origin, these two lobe end member-types are both characterised by a relatively narrow grain size range.

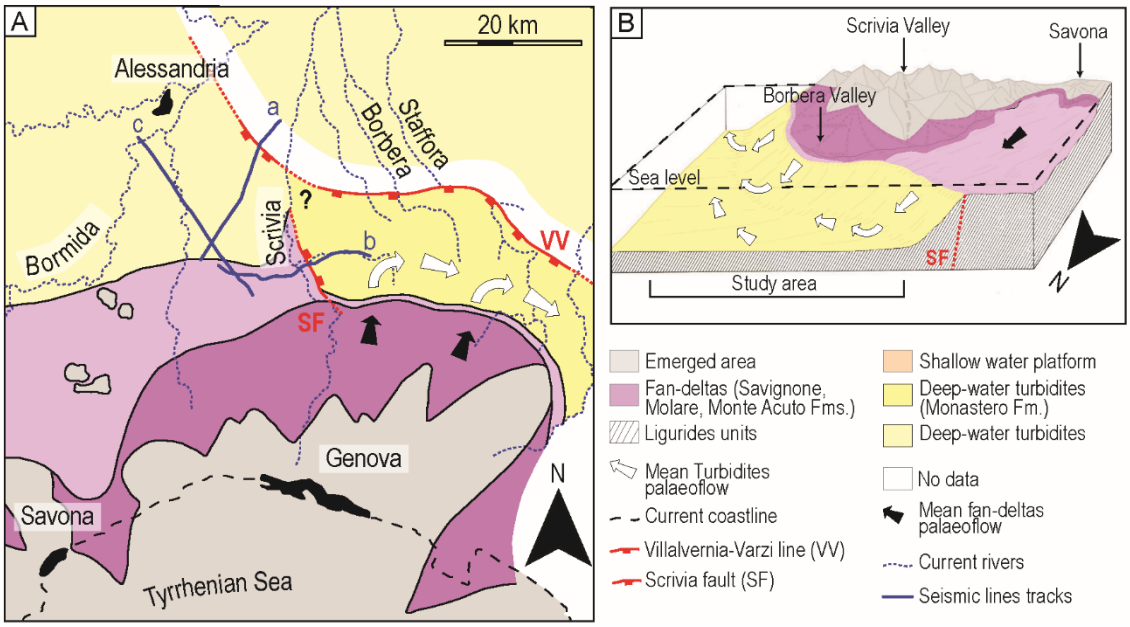

Fig. 64. (A) and (B) Revised palaeogeographic map for the Borbera-Curone sub-depocentre and 3D block diagram for the Tertiary Piedmont Basin during the middle part of the Oligocene showing the distribution of depositional environments (modified after Gelati & Gnaccolini, 1984).

It is unclear whether the thinner and muddier lobes represent either the lateral or distal fringes of sandier amalgamated examples but, given the size of the basin, this seems unlikely. Rather, the sand content and degree of amalgamation, the thickness and ultimately the type of hyperpycnal lobes (i.e., amalgamated sandy vs. heterolithic and muddy) most likely reflect stratigraphic changes in average grain size composition, volume, and efficiency of flows.

The lobes dominating the upper part of the Monastero Fm. (*cf.* with "Lobi di San Gaudenzio" of Gelati, 1977) represent a lobe type on their own. In fact, albeit showing thicknesses and sand to mud ratio similar to that of the amalgamated sandy lobes of the lower section, they are typically coarser grained and made of non-amalgamated sandstones separated by relatively thick mudstone caps.

However, the most intriguing stratigraphic component of the studied section is by far the heterolithic muddy background (Section 4.4.2.3) encasing the channel fills and lobes of the Monastero Fm. It

has an average sand to mud ratio of ca. 0.45 and represents ca. 52% of the cumulative thickness of the logged sections. Geological maps (Ghibaudo *et al.*, 1985; Cavanna *et al.*, 1989) indicates that the facies is equally abundant in other sections of the Monastero Fm. As it turns out from facies analysis, this heterolithic facies association is composed by tightly packed very thin to medium beds with small lateral continuity (a few ten to a few hundreds of metres), frequent soft sediment deformation and rare bioturbation by opportunistic taxa (Section 4.4.2.3), most of which (ca. 75%) of hyperpycnal origin (see Section 4.4.2.3). Locally, coarse turbidite beds with deeply scoured bases occur, suggesting episodic channelisation by larger volume and denser flows. Estimations made on a cumulative thickness of ca. 30 m indicate an average number of event beds per metre in the order of 3, albeit lateral continuity of beds suggest this can be significantly larger (Fig. 62; see Section 4.4.2.3).

If sedimentary facies (Section 4.4.1.4), stratigraphic distribution of architectural elements (Fig. 55, Fig. 56, Fig. 57, Fig. 59 and Section 4.4.2) and relationship with partly coeval units are considered, the Monastero Fm. can be viewed as a structurally confined hyperpycnal system developed seaward of conglomeratic fan deltas (e.g., the Savignone Conglomerate and Molare Fms.) at a water depth in the range 400-700 m (Mancin & Pirini, 2002). The sand to mud ratio of the measured section varies from 0.45 to 1.5. Compared to other deep-water systems (e.g., Gottero, Forties, Gull Island, Peira Cava; Reading & Richards, 1994), the Moastero Fm is relatively sand-rich (it would correspond to sand/mud- to sand-rich systems of Reading & Richards, 1994). This would indicate either that the average sediment calibre delivered to the system was relatively coarse-grained or most of the mud by-passed, or a combination thereof.

Alternations of architectural elements and the heterolithic muddy background containing them would indicate changes in sediment input, with channels and lobes reflecting the system forestepping at time of high sediment input and the background indicating lapses of reduced sediment input. Yet, the channels and lobes appear to form three stratigraphic clusters which, as suggested by Di Giulio (1991), might reflect 10^4 to 10^5 eustatic cycles (*sensu* Catuneanu, 2019). However, further investigations are required to confirm this hypothesis.

On the other end, sedimentary facies associations mapped by Cavanna *et al.* (1989) would suggest that the stratigraphic transition from a lower channelised to an uppermost unchannelised part seen in the studied section is reflected over the whole host basin, likely indicating an overall backstepping of the system. This is agreement with the overall regressive trend of the Oligocene deposits of the Borbera-Curone sub-depocentre (*cf*. with Unit II of Rossi *et al.*, 2009), interpreted to record the western Alps collapse (Mosca *et al.*, 2010; Rossi & Craig, 2016).

4.5.3. Accumulation rates and implications for hyperpycnal deposition

The biostratigraphic data from Gelati (1977), revised as part of this work (see Section 4.3.2 and Appendix I) and supported by the pilot magnetostratigraphic study (belonging entirely to the magnetochron C11r) presented in Section 4.4.4, indicate that the Rupelian Monastero Fm. has a time duration of ca. 3.5 Ma and accumulated with a relatively constant rate in order of 400 m/Ma. The lower part of the studied section appears to reflect relatively lower accumulation rates (in the range 350-390 m/Ma) compared to the upper part of the section (460 m/Ma), especially considering that the last occurrence of the *Pseudohastigerina naguewichiensis* can be related to sedimentary facies control (e.g., establishment of restricted marine environment of the Rio Trebbio Sandstones Fm.). This change in accumulation rate is in agreement with the partly channelised nature of the lower part of the studied section, which suggests that some of the sediment are by-passed and deposited elsewhere. Conversely, the uppermost part of the Monastero Fm. would record a significant reduction of accumulation rates (55 m/Ma), which correlates to a reduction of sand content in the whole system. A similar trend has been document in the western Tertiary Piedmont Basin and culminates with formation of a drowning unconformity and a landward shift of coeval fluvio-deltaic systems (Rossi & Craig, 2016). Thus, the reduction in sand delivery to the studied section can reflect trapping of coarse-grained sediments up-dip, e.g., within basins perched on the slope to the south (not preserved today).

Considering the tight bedding pattern of the heterolithic muddy background (corresponding to an estimated bed density of ca. 3 beds/m) and the limited lateral continuity of component beds (which represent ca. 60% the total thickness of studied section), the return period of sediment gravity flows

for the studied section can be estimated to less than a few thousand years. However, this period is most likely underestimated because the estimation does not account for erosion, by-pass, and undetected beds (not intersected by the logged sections). This return period estimation for hyperpycnal flows of the Monastero Fm. is within the range proposed by Mulder & Syvitski (1995) for moderately clean rivers.

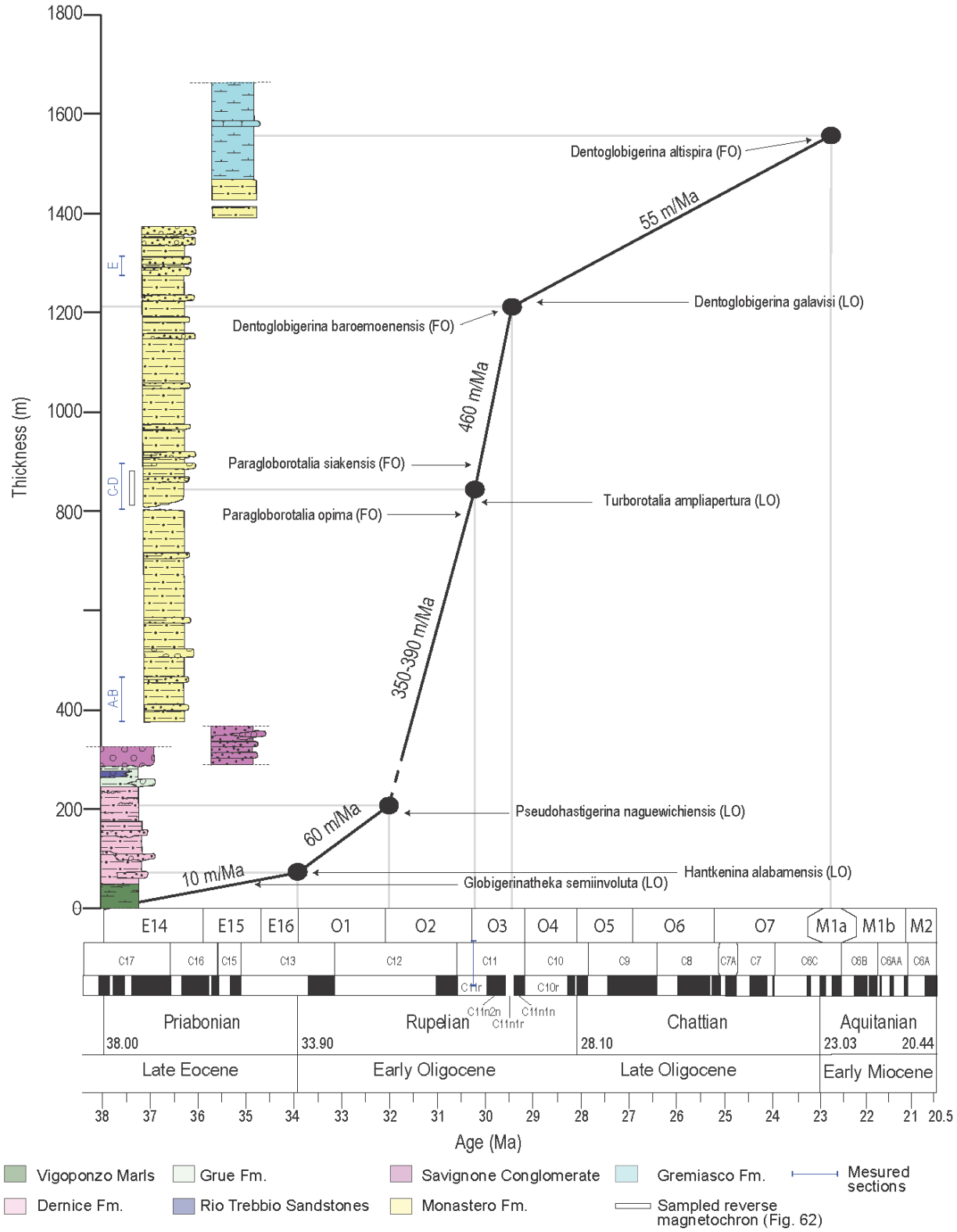

Fig. 65. Sedimentation rate of the Rupelian-Chattian succession of the Borbore-Curone sub-depocentre from the Val di Grue-San Guadenzio section of Gelati (1977). Sedimentation rates are plotted Vs. foraminiferal datum events. For locations of the measured sections see Fig. 47.

4.6. Conclusions

This study investigated the sedimentology of the thickest section (Val di Grue-San Guadenzio section, up to ca. 1100 m) of the deep-water Monastero Fm. from the Tertiary Piedmont Basin (NW, Italy), which was deposited partly heteropic to fan-delta conglomerates in a structurally confined basin during the Rupelian. To frame the results in larger stratigraphic and paleogeographic context, sedimentary logging and facies analysis were complemented with a thorough revision of biostratigraphic data, acquisition of novel magnetostratigraphic data and analysis of 2D seismic section made available by Eni S.p.A.

As it turned out from correlation of the best-exposed parts of the section, facies analysis and interpretation of photopanels, the Monastero Fm. is characterised by peculiar sedimentary facies and architectural elements, which are hard to fit into ‘classical’ models of turbidite systems. Rather, facies features and relationship with coeval conglomeratic fan-deltas indicate that the Monastero Fm. is best interpreted as a delta-fed turbidite system.

Results provide the following insights into facies and architecture of analogues systems:

- A significant fraction (65%) of the Monastero Fm. is represented by facies with repeated sedimentary divisions and grading interpreted as the result of deposition by pulsating hyperpycnal flows.
- The co-existence of hyperpycnite facies and ‘classical’ turbidite facies indicates that one type may pass into the other over short distance as a result of parent flow transformations.
- The investigated stratigraphy is dominated (60% of the total logged section) by a muddy heterolithic background made of tightly packed thin beds (3 event beds per metre, on average), embedding conglomeratic channel fills and hyperpycnal lobes.
- Coarse-grained channelised bodies (up to 20 m-thick and 500 m-wide) are interpreted as the fills of channels indenting a coeval fan-delta.
- Lobes show a great variety of dimensional parameters, sand to mud content and facies composition which is thought to chiefly reflect changes in flow parameters and longitudinal profile of the system.

- The revised biostratigraphy, supported by novel magnetostratigraphic data, suggests an average accumulation rate of 400 m/Ma slightly increasing up section as more channelised facies are replaced by lobes. The tightly packed nature of the Monastero Fm. suggests that the return period of sediment gravity flows was lower than a few thousand years, which is within the range proposed for moderately clean rivers.
- Seismic interpretation confirms the confined nature of the Monastero Fm. and highlights that similar systems may be present in the subsurface to the west and north of the study area.

CHAPTER V

Final remarks

Intentionally blank page

5. Insights from this work

This doctoral work investigated the sedimentology of two deep-water clastic units, namely the channel-levée Complex 4 of the Tachrift Turbidite System (Tortonian; Taza-Guercif Basin of NE Morocco) and the partly channelised Monastero Fm. (Rupelian; Tertiary Piedmont Basin of NW Italy), differing one from another in scale, time duration, dominant architectural elements, and sedimentary facies.

The Complex 4 of the Tachrift Turbidite System is characterised by a tripartite channel system, consisting of an initial incisional phase, followed by a middle migrational phase and an uppermost aggradational phase. This evolution is interpreted as the response to an equilibrium profile shift from a low accommodation regime to a high accommodation regime, passing through an at grade condition, which is modulated through time by sediment input variation.

Differently, the Monastero Fm. turbidite system is a confined thin-bedded system, characterised by interbedded channel lobe complexes, with an hyperpycnal origin and sedimentation rates in the range 350-460 m/Ma.

Despite their remarkably different nature, the two investigated units show an internal complexity which needed to be time-constrained in order to fully understand the stratigraphic meaning of each of their architectural components. As a matter of fact, turbidite systems are often lacking reliable time frameworks on their deposition due to the intrinsically incomplete record of deep-water flow events and accumulations.

If the time variable is not taken into account in combination with the spatial arrangement of deposits (i.e., 4D scale analysis), a reliable interpretation for turbidite systems evolution cannot be obtained. Thus, the understanding of factors controlling turbidite systems, and their changes over time, cannot be advanced significantly (e.g., system morphodynamics and self-organisation, changes in sediment input, tectonics, etc.).

This doctoral work has pursued the goal of complementing the obtained sedimentary facies dataset with biostratigraphic and magnetostratigraphic data (revised from the literature or newly-acquired), in order to construct a time framework on the depositional evolution of the studied turbidite units.

Even though sedimentological results from both case studies point out a remarkable heterogeneity and difference between these turbidite deposits, a common return period of sediment gravity flows in the scale of less than a few thousand years is recognised and is linked to variations of sediment input.

These very similar sedimentary inputs characterise two totally different deep-water systems, which have just only one commonality, that is, being fed by an adjacent deltaic system.

Whether these variations are cyclical or not has still to be demonstrated, although preliminary estimations indicate that they might have an interval in the range of 10^3-10^4 years (comparable with 3rd-4th order cycles, e.g., Payros & Martínez-Braceras, 2014; Catuneanu, 2019) and they may also represent a record of climate changes.

However, as detailed in several other case studies in the literature (e.g., Ten Kate & Sprenger, 1993; Reijmer *et al.*, 1994; Krijgsman *et al.*, 1999; Heard *et al.*, 2008; Mawson & Tucker, 2009; Payros & Martínez-Braceras, 2014), understanding if turbidite successions record cyclical-astronomical variations or, alternatively, whether they simply reflect an incomplete sedimentary record produced by flow bypass and erosion is often difficult.

Nevertheless, it has been recognised that return periods of turbidity currents and sediment input variations are both key controls on the spatial arrangement and internal heterogeneity of deep-water systems (*cf*. Drummond, 1999 and Prélat & Hodgson, 2013).

What could be done to improve age models of turbidite systems deals with decreasing the uncertainty related to the incompleteness of the sedimentary record. This could be pursued by focusing the bio-magnetostratigraphic analyses on the fine-grained portions of turbidite systems, such as levées and hemipelagic accumulations occurring in-between the more channelised portions. These fine-grained deposits preserve a more complete age record and, being the correlative of more channelised and incomplete accumulations, they might represent the tool to track hypothetical timelines within the channelised part of turbidite systems through bed-by-bed correlations.

Other suggestions concern with the biostratigraphic tools used for the investigations. If possible, the integration between different biostratigraphic tools could prove to have potential for constraining the sedimentation rates of studied successions. This approach could be coupled with an increase of the

sampling frequency for both magnetostratigraphic and biostratigraphic analyses, within both channelised and unchannelised deposits, to better refine the produced age model.

Finally, the detailed lateral correlation between a large number of sections acquired within the same turbidite system would allow a better evaluation of depositional rates across the host basin, providing information on possible control factors and depositional trends at basin scale.

It is thus concluded that more effort should be done to retrieve age constraints on deposition in order to advance our understanding of deep-water clastic sedimentary systems.

Intentionally blank page

References

Abreu, V., **Sullivan, M.**, **Pirmez, C.** and **Mohrig, D.** (2003) Lateral accretion packages (LAPs): An important reservoir element in deep water sinuous channels. *Mar. Pet. Geol.*, **20**, 631–648.

Akindulureni, J.O., **Adepelumi, A.A.** and **Benjamin, U.K.** (2018) Evolution, Geometry and Formative Processes of Depositional Elements in Niger Delta Slope Settings. *Univers. J. Geosci.*, **6**, 118–129.

Al Ja'Aidi, O.S., **McCaffrey, W.D.** and **Kneller, B.C.** (2004) Factors influencing the deposit geometry of experimental turbidity currents: Implications for sand-body architecture in confined basins. *Geol. Soc. Spec. Publ.*, **222**, 45–58.

Allaby, M. (2008) Dictionary of earth sciences, 3rd edn. *Oxford University Press*.

Allen, J.R.L. (1971) Mixing at turbidity current heads, and its geological implications. *J. Sediment. Petrol.*, **41**, 97–113.

Altinakar, M.S., **Graf, W.H.** and **Hopfinger, E.J.** (1996) Flow structure in turbidity currents. *J. Hydraul. Res.*, **34**, 713–718.

Alves, T.M., **Cartwright, J.** and **Davies, R.J.** (2009) Faulting of salt-withdrawal basins during early halokinesis: Effects on the paleogene rio doce canyon system (Espírito Santo Basin, Brazil). 617–652 pp.

Alves, T.M., **Strasser, M.** and **Moore, G.F.** (2014) Erosional features as indicators of thrust fault activity (Nankai Trough, Japan). *Mar. Geol.*, **356**, 5–18.

Amy, L., **Kneller, B.** and **McCaffrey, W.** (2000) Evaluating the Links Between Turbidite Characteristics and Gross System Architecture: Upscaling Insights from the Turbidite Sheet-System of Peïra Cava, SE France. *Deep. Reserv. World 20th Annu.*, 1–15.

Amy, L.A., **McCaffrey, W.D.** and **Kneller, B.C.** (2004) The influence of a lateral basin-slope on the depositional patterns of natural and experimental turbidity currents. *Geol. Soc. Spec. Publ.*, **221**, 311–330.

Arnott, R.W.C., **Tilston, M.**, **Fraino, P.**, **Navarro, L.**, **Dumouchel, G.** and **Miklovich, N.** (2021) Laterally accreting sinuous channels and their deposits: The goldilocks of deep-water slope systems. *J. Sediment. Res.*, **91**, 451–463.

Artoni, A., **Di Biase, D.**, **Mutti, E.** and **Tinterri, R.** (2000) Control of thrust propagation on turbidite sedimentation. In: *EAGE Conference on Geology and Petroleum Geology of the Mediterranean and Circum-Mediterranean Basins*, *European Association of Geoscientists & Engineers*, cp-109.

Azpiroz-Zabala, M., **Cartigny, M.J.B.**, **Talling, P.J.**, **Parsons, D.R.**, **Sumner, E.J.**, **Clare, M.A.**, **Simmons, S.M.**, **Cooper, C.** and **Pope, E.L.** (2017) Newly recognized turbidity current structure can explain prolonged flushing of submarine canyons. Sci Adv. doi: 10.1126/sciadv.1700200

Baas, J.H., **Best, J.L.** and **Peakall, J.** (2011) Depositional processes, bedform development and hybrid bed formation in rapidly decelerated cohesive (mud-sand) sediment flows. *Sedimentology*, **58**, 1953–1987.

Baas, J.H., **Best, J.L.**, **Peakall, J.** and **Wang, M.** (2009) A phase diagram for turbulent, transitional, and laminar clay suspension flows. *J. Sediment. Res.*, **79**, 162–183.

Babonneau, N., **Savoye, B.**, **Cremer, M.** and **Bez, M.** (2010) Sedimentary Architecture in Meanders of a Submarine Channel: Detailed Study of the Present Congo Turbidite Channel (Zaiango Project). *J. Sediment. Res.*, **80**, 852–866.

Bagnold, R.A. (1962) Auto-suspension of transported sediment; turbidity currents. *Proc. R. Soc. London. Ser. A. Math. Phys. Sci.*, **265**, 315–319.

Barbieri, C., **Carrapa, B.**, **Di Giulio, A.** and **Wijbrand, J.** (2001) A provenance study of a post-collisional transgressive sequence (Molare Formation, Italy) through integrated facies analysis, mineral chemistry and 40Ar/39Ar dating. *Abstr. XI EUG Conf.*, **6**, 534.

Barnes, H.A., **Hutton, J.F.** and **Walters, K.** (1989) An introduction to rheology. *Elsevier*.

Bates, C.C. (1953) Rational theory of delta formation. *Am. Assoc. Pet. Geol. Bull.*, **37**, 2119–2162.

Beaubouef, R.T. (2004a) Deep-water leveed-channel complexes of the Cerro Toro Formation, Upper Cretaceous, southern Chile. *Am. Assoc. Pet. Geol. Bull.*, **88**, 1471–1500.

Beaubouef, R.T. (2004b) Deep-water leveed-channel complexes of the Cerro Toro Formation, Upper Cretaceous, southern Chile. *Am. Assoc. Pet. Geol. Bull.*, **88**, 1471–1500.

Bell, D., **Kane, I.A.**, **Pontén, A.S.M.**, **Flint, S.S.**, **Hodgson, D.M.** and **Barrett, B.J.** (2018) Spatial variability in depositional reservoir quality of deep-water channel-fill and lobe deposits. *Mar. Pet. Geol.*, **98**, 97–115.

Bellinzona, G. and **Boni, A.** (1971) Stratigrafia e tettonica della zona tra il T Scrivia e il T. *Atti dell'Istuto di Geol. dell'Università di Pavia*, **21**, 21–137.

Bellinzona, G., **Boni, A.**, **Braga, G.** and **Marchetti, G.** (1971) Note illustrative della Carta Geologica d'Italia in scala 1: 100.000, Foglio 71, Voghera. *Serv. Geol. d'Italia, Roma*, 121.

Benzaquen, M. (1965) Etude stratigraphique préliminaire des formations du bassin de Guercif. Verlag nicht ermittelbar

Bernini, M., **Boccaletti, M.**, **Gelati, R.**, **Moratti, G.**, **Papani, G.** and **Mokhtari, J. El** (1999) Tectonics and sedimentation in the Taza-Guercif Basin, northern Morocco: Implications for the Neogene evolution of the Rif-Middle Atlas Orogenic System. *J. Pet. Geol.*, **22**, 115–128.

Bernini, M., **Boccaletti, M.**, **Moratti, G.** and **Papani, G.** (2000) Structural development of the Taza-Guercif Basin as a constraint for the Middle Atlas Shear Zone tectonic evolution. *Mar. Pet. Geol.*, **17**, 391–408.

Bersezio, R., **Felletti, F.**, **Riva, S.** and **Micucci, Lu.** (2009) Trends in Bed Thickness and Facies of Turbiditic Sandstone Bodies: Unravelling the Effects of Basin Confinement, Depositional Processes, and Modes of Sediment Supply. *Extern. Control. Deep. Depos. Syst.*, **92**, 303–321.

Bertrand, G. (1897) Sur l'intervention du manganèse dans les oxydations provoquées par la laccase. *G. Masson*.

Blanpied, C. and **Stanley, D.J.** (1981) Uniform mud (unifite) deposition in the Hellenic Trench, Eastern Mediterranean.

Boccaletti, M., **Coli, M.** and **Napoleone, G.** (1980) Landsat lineation pattern in the Apennines and its geodynamic significance. **7**, 95–103.

Booth, J.R., **DuVernay, A.E.**, **Pfeiffer, D.S.** and **Styzen, M.J.** (2000) Sequence stratigraphic framework, depositional models, and stacking patterns of ponded and slope fan systems in the Auger Basin: Central Gulf of Mexico slope. In: *Global deep-water reservoirs: Gulf Coast Section SEPM Foundation 20th Annual Bob F. Perkins Research Conference* (Ed. P. Weimer, R.M. Slatt, J.L. Coleman, N.C. Rosen, C.H. Nelson, A.H. Bouma, and D.T. Lawrence), 127–151.

Bouma, A.H. (1962) Sedimentology of some flysch deposits.

Bouma, A.H. (1964) Turbidites. In: *Developments in sedimentology*, *Elsevier*, 3, 247–256.

Bouma, A.H., **Normark, W.R.** and **Barnes, N.E.** (2012) Submarine fans and related turbidite systems. *Springer Science & Business Media*.

Bouma, A.H. and **Stone, C.G.** (2000) Fine-grained, mud-rich turbidite systems: model and

comparison with coarse-grained, sand-rich systems. *SEPM J. Sediment. Res.*, **68**, 9–20.

Bourget, J., **Zaragosi, S.**, **Mulder, T.**, **Schneider, J.L.**, **Garlan, T.**, **Van Toer, A.**, **Mas, V.** and **Ellouz-Zimmermann, N.** (2010) Hyperpycnal-fed turbidite lobe architecture and recent sedimentary processes: A case study from the Al Batha turbidite system, Oman margin. *Sediment. Geol.*, **229**, 144–159.

Bridge, J.S. (2003) Rivers and floodplains. Forms, Processes and Sedimentary RecordBlackwell Science. 512 pp.

Bridge, J.S. (1981) Hydraulic interpretation of grain-size distributions using a physical model for bedload transport. *J. Sediment. Res.*, **51**, 1109–1124.

Bryn, B.K.L. (1998) Sedimentology of Monte Jaizkibel Formation: an Early Eocene Turbiditic Fan in the Basque-Cantabrian Basin. Bergen University, Norway

Buatois, L.A., **Saccavino, L.L.** and **Zavala, C.** (2011) Ichnologic Signatures of Hyperpycnal Flow Deposits in Cretaceous River-dominated Deltas, Austral Basin, Southern Argentina. Sediment Transf from Shelf to Deep Water—Revisiting Deliv Syst. doi: 10.1306/13271355st611948

Bull, S., **Browne, G.H.**, **Arnot, M.J.** and **Strachan, L.J.** (2020) Influence of mass transport deposit (MTD) surface topography on deep-water deposition: an example from a predominantly fine-grained continental margin, New Zealand. *Geol. Soc. London, Spec. Publ.*, **500**, 147–171.

Burke, K. (1972) Longshore drift, submarine canyons, and submarine fans in development of Niger Delta. *Am. Assoc. Pet. Geol. Bull.*, **56**, 1975–1983.

Camacho, H., **Busby, C.J.** and **Kneller, B.** (2002) A new depositional model for the classical turbidite locality at San Clemente State Beach, California. *Am. Assoc. Pet. Geol. Bull.*, **86**, 1543–1560.

Campion, K.M., **Sprague, A.R.** and **Sullivan, M.D.** (2007) Architecture and lithofacies of the Miocene Capistrano Formation, San Clemente State Beach, California, U.S.A. *Atlas Deep. Outcrops, AAPG Stud. Geol.*, **56**, 395–400.

Capella, W., **Barhoun, N.**, **Flecker, R.**, **Hilgen, F.J.**, **Kouwenhoven, T.**, **Matenco, L.C.**, **Sierro, F.J.**, **Tulbure, M.A.**, **Yousfi, M.Z.** and **Krijgsman, W.** (2018) Palaeogeographic evolution of the late Miocene Rifian Corridor (Morocco): Reconstructions from surface and subsurface data. *Earth-Science Rev.*, **180**, 37–59.

Capella, W., **Flecker, R.**, **Hernández-Molina, F.J.**, **Simon, D.**, **Meijer, P.T.**, **Rogerson, M.**, **Sierro, F.J.** and **Krijgsman, W.** (2019) Mediterranean isolation preconditioning the Earth System for late Miocene climate cooling. *Sci. Rep.*, **9**, 1–8.

Capella, W., **Matenco, L.**, **Dmitrieva, E.**, **Roest, W.M.J.**, **Hessels, S.**, **Hssain, M.**, **Chakor-Alami, A.**, **Sierro, F.J.** and **Krijgsman, W.** (2017) Thick-skinned tectonics closing the Rifian Corridor. *Tectonophysics*, **710**–**711**, 249–265.

Capponi, G., **Crispini, L.**, **Federico, L.** and **Malatesta, C.** (2016) Geology of the Eastern Ligurian Alps: a review of the tectonic units. *Ital. J. Geosci.*, **135**, 157–169.

Carey, S.N. and **Sigurdsson, H.** (1980) The Roseau ash: Deep-sea tephra deposits from a major eruption on Dominica, Lesser Antilles arc. *J. Volcanol. Geotherm. Res.*, **7**, 67–86.

Carminati, E., **Doglioni, C.** and **Scrocca, D.** (2004) Alps vs Apennines. *Spec. Vol. Ital. Geol. Soc. IGC 32 Florence-2004*, 141–151.

Carminati, E., **Lustrino, M.** and **Doglioni, C.** (2012) Geodynamic evolution of the central and western Mediterranean: Tectonics vs. igneous petrology constraints. Tectonophysics. doi: 10.1016/j.tecto.2012.01.026

Carnevale, M., **Felletti, F.**, **Marini, M.**, **Patacci, M.**, **Fonnesu, M.** and **McCaffrey, W.D.** (2018) Outcrop-Based Quantification of Short-Scale Heterogeneity in Hybrid Event Beds (HEBs) to Inform Modelling of HEBs-Prone Turbidite Reservoirs. In: *AAPG ACE 2018*,

Carrapa, B. (2002) Tectonic evolution of an active orogen as reflected by its sedimentary record - An integrated study of the Tertiary Piedmont Basin. Vrije Universiteit

Carrapa, B., **Bertotti, G.** and **Krijgsman, W.** (2003) Subsidence, stress regime and rotation (s) of a tectonically active sedimentary basin within the western Alpine Orogen: the Tertiary Piedmont Basin (Alpine domain, NW Italy). *Geol. Soc. London, Spec. Publ.*, **208**, 205–227.

Carrapa, B., **Di Giulio, A.**, **Mancin, N.**, **Stockli, D.**, **Fantoni, R.**, **Hughes, A.** and **Gupta, S.** (2016) Tectonic significance of Cenozoic exhumation and foreland basin evolution in the Western Alps. *Tectonics*, **35**, 1892–1912.

Carrapa, B. and **Garcia-Castellanos, D.** (2005) Western Alpine back-thrusting as subsidence mechanism in the Tertiary Piedmont Basin (western Po Plain, NW Italy). *Tectonophysics*, **406**, 197–212.

Castellarin, A. (2001) Alps-Apennines and Po Plain-frontal Apennines relations. In: *Anatomy of an Orogen: the Apennines and Adjacent Mediterranean Basins* (Ed. G.B. Vai and I.P. Martini), *Springer Netherlands*, Dordrecht, 177–195.

Catuneanu, O. (2020) Sequence stratigraphy of deep-water systems. *Mar. Pet. Geol.*, **114**, 104–238.

Catuneanu, O. (2019) Scale in sequence stratigraphy. *Mar. Pet. Geol.*, **106**, 128–159.

Cavanna, F., **Di Giulio, A.**, **Galbiati, B.**, **Mosna, S.**, **Perotti, C.R.** and **Pieri, M.** (1989) Carta geologica dell'estremità orientale del Bacino Terziario Ligure-Piemontese.

Chen, S., **Steel, R.J.** and **Olariu, C.** (2016) Upper-slope to shelf-edge delta architecture, miocene cruse formation, orinoco shelf margin, trinidad. *J. Sediment. Res.*, **86**, 87–106.

Chikita, K. (1989) Dynamic processes of sedimentation by river-induced turbidity currents. I. Relations between their hydrodynamics and grain size of sediment. *Trans. Japan. Geomorph. Union*, **10**, 155–177.

Clare, M.A., **Le Bas, T.**, **Price, D.M.**, **Hunt, J.E.**, **Sear, D.**, **Cartigny, M.J.B.**, **Vellinga, A.**, **Symons, W.**, **Firth, C.** and **Cronin, S.** (2018) Complex and cascading triggering of submarine landslides and turbidity currents at volcanic islands revealed from integration of high-resolution onshore and offshore surveys. *Front. Earth Sci.*, **6**, 223.

Colletta, B. (1977) Evolution neotectonique de la partie meridionale du bassin de Guercif (Maroc Oriental). Université Scientifique et Mèdicale de Grenoble

Collinson, J.D. (1986) Submarine ramp facies model for delta-fed, sand-rich turbidite systems: discussion. *Am. Assoc. Pet. Geol. Bull.*, **70**, 1742–1743.

Cook, T.W., **Bouma, A.H.**, **Chapin, M.A.** and **Zhu, H.** (1994) Facies architecture and reservoir characterization of a submarine fan channel complex, Jackfork Formation, Arkansas.

Covault, J.A., **Sylvester, Z.**, **Hudec, M.R.**, **Ceyhan, C.** and **Dunlap, D.** (2020) Submarine channels 'swept' downstream after bend cutoff in salt basins. *Depos. Rec.*, **6**, 259–272.

Cronin, B.T., **Hurst, A.**, **Celik, H.** and **Türkmen, I.** (2000) Superb exposure of a channel, levee and overbank complex in an ancient deep-water slope environment. *Sediment. Geol.*, **132**, 205–216.

Cullis, S., **Colombera, L.**, **Patacci, M.** and **McCaffrey, W.D.** (2018a) Hierarchical classifications of the sedimentary architecture of deep-marine depositional systems. 38–71 pp.

Cullis, S., **Colombera, L.**, **Patacci, M.** and **McCaffrey, W.D.** (2018b) Hierarchical classifications of

the sedimentary architecture of deep-marine depositional systems. *Earth-Science Rev.*, **179**, 38–71.

Cunha, R.S., **Tinterri, R.** and **Muzzi Magalhaes, P.** (2017) Annot Sandstone in the Peïra Cava basin: An example of an asymmetric facies distribution in a confined turbidite system (SE France). *Mar. Pet. Geol.*, **87**, 60–79.

Dailly, P., **Henderson, T.**, **Hudgens, E.**, **Kanschat, K.** and **Lowry, P.** (2013) Exploration for Cretaceous stratigraphic traps in the Gulf of Guinea, West Africa and the discovery of the Jubilee Field: a play opening discovery in the Tano Basin, Offshore Ghana. *Geol. Soc. London, Spec. Publ.*, **369**, 235–248.

Daly, R.A. (1936) Origin of submarine canyons. *Am. J. Sci.*, **5**, 401–420.

Day, R., **Fuller, M.** and **Schmidt, V.A.** (1977) Hysteresis properties of titanomagnetites: grain-size and compositional dependence. *Phys. Earth Planet. Inter.*, **13**, 260–267.

de Lamotte, D.F., **Leturmy, P.**, **Missenard, Y.**, **Khomsi, S.**, **Ruiz, G.**, **Saddiqi, O.**, **Guillocheau, F.** and **Michard, A.** (2009) Mesozoic and Cenozoic vertical movements in the Atlas system (Algeria, Morocco, Tunisia): an overview. *Tectonophysics*, **475**, 9–28.

de Voogd, B., **Nicolich, R.**, **Olivet, J.L.**, **Fanucci, F.**, **Burrus, J.**, **Mauffret, A.**, **Pascal, G.**, **Argnani, A.**, **Auzende, J.M.**, **Bernabini, M.**, **Bois, C.**, **Carmignani, L.**, **Fabbri, A.**, **Finetti, I.**, **Galdeano, A.**, **Gorini, C.Y.**, **Labaume, P.**, **Lajat, D.**, **Patriat, P.**, **Pinet, B.**, **Ravat, J.**, **Lucchi, F.R.** and **Vernassa, S.** (1991) First deep seismic reflection transect from the Gulf of Lions to Sardinia (ECORS-crop profiles in Western Mediterranean). *Cont. Lithosph. Deep Seism. reflections*, **22**, 265–274.

Deptuck, M.E., **Steffens, G.S.**, **Barton, M.** and **Pirmez, C.** (2003) Architecture and evolution of upper fan channel-belts on the Niger Delta slope and in the Arabian Sea. *Mar. Pet. Geol.*, **20**, 649–676.

Deptuck, M.E. and **Sylvester, Z.** (2018) Submarine Fans and Their Channels, Levees, and Lobes. *Springer Geol.*, 273–299.

Deptuck, M.E., **Sylvester, Z.**, **Pirmez, C.** and **O'Byrne, C.** (2007) Migration-aggradation history and 3-D seismic geomorphology of submarine channels in the Pleistocene Benin-major Canyon, western Niger Delta slope. *Mar. Pet. Geol.*, **24**, 406–433.

Di Giulio, A. (1991) Detritismo della parte orientale del Bacino Terziario Piemontese durante l'Eocene-Oligocene: composizione delle arenarie ed evoluzione tettono-stratigrafica. *Atti Ticinensi di Sci. della Terra*, **34**, 21–22.

Drummond, C.N. (1999) Bed-thickness structure of multi-sourced ramp turbidites: devonian brallier formation, central appalachian basin. *J. Sediment. Res.*, **69**, 115–121.

Dunlop, D.J. (2002) Theory and application of the Day plot (Mrs/Ms versus Hcr/Hc) 1. Theoretical curves and tests using titanomagnetite data. *J. Geophys. Res.*, **107**, 1–22.

Duringer, P., **Paicheler, J.C.** and **Schneider, J.L.** (1991) Un courant d'eau continu peut-il générer des turbidites? Résultats d'expérimentations analogiques. *Mar. Geol.*, **99**, 231–246.

Dykstra, M. and **Kneller, B.** (2009) Lateral accretion in a deep-marine channel complex: Implications for channellized flow processes in turbidity currents. *Sedimentology*, **56**, 1411–1432.

Eberli, G.P. (1991) Calcareous turbidites and their relationship to sea-level fluctuations and tectonism. *Cycles events Stratigr.*, **340**, 359.

Elliott, T. (2000) Depositional architecture of a sand-rich, channelized turbidite system: the Upper Carboniferous Ross Sandstone Formation, western Ireland. In: *Deep-water reservoirs of the world: Gulf Coast Section Society for Sedimentary Geology, GCSSEPM Foundation Annual Bob*

F. Perkins Research Conference Proceedings, 20, 342–373.

Falcini, F., **Marini, M.**, **Milli, S.** and **Moscatelli, M.** (2009) An inverse problem to infer paleoflow conditions from turbidites. *J. Geophys. Res*, **114**, 10019.

Federico, L., **Spagnolo, C.**, **Crispini, L.** and **Capponi, G.** (2009) Fault-slip analysis in the metaophiolites of the Voltri Massif: constraints for the tectonic evolution at the Alps/Apennine boundary. *Geol. J.*, **44**, 225–240.

Felletti, F. (2002) Complex bedding geometries and facies associations of the turbiditic fill of a confined basin in a transpressive setting (Castagnola Fm., Tertiary Piedmont Basin, NW Italy). *Sedimentology*, **49**, 645–667.

Felletti, F. and **Bersezio, R.** (2010) Quantification of the degree of confinement of a turbidite-filled basin: A statistical approach based on bed thickness distribution. *Mar. Pet. Geol.*, **27**, 515–532.

Felletti, F., **Marini, M.**, **El Kati, I.** and **Tabyaoui, H.** (2020) The Tachrift channel-levée turbidite complexes (Tortonian) of the Taza-Guercif basin (South Rifian Corridor, NE Morocco). *J. Maps*, **16**, 902–917.

Festa, A., **Fioraso, G.**, **Bissacca, E.** and **Petrizzo, M.R.** (2015) Geology of the Villalvernia – Varzi Line Between Scrivia and Curone valleys (NW Italy). *J. Maps*, **11**, 39–55.

Flecker, R., **Krijgsman, W.**, **Capella, W.**, **de Castro Martíns, C.**, **Dmitrieva, E.**, **Mayser, J.P.**, **Marzocchi, A.**, **Modestou, S.**, **Ochoa, D.**, **Simon, D.**, **Tulbure, M.**, **van den Berg, B.**, **van der Schee, M.**, **de Lange, G.**, **Ellam, R.**, **Govers, R.**, **Gutjahr, M.**, **Hilgen, F.**, **Kouwenhoven, T.**, **Lofi, J.**, **Meijer, P.**, **Sierro, F.J.**, **Bachiri, N.**, **Barhoun, N.**, **Alami, A.C.**, **Chacon, B.**, **Flores, J.A.**, **Gregory, J.**, **Howard, J.**, **Lunt, D.**, **Ochoa, M.**, **Pancost, R.**, **Vincent, S.** and **Yousfi, M.Z.** (2015) Evolution of the Late Miocene Mediterranean–Atlantic gateways and their impact on regional and global environmental change. *Earth-Science Rev.*, **150**, 365–392.

Flint, S., **Hodgson, D.**, **Sprague, A.** and **Box, D.** (2008) A physical stratigraphic hierarchy for deep-water slope system reservoirs 1: super sequences to complexes. In: *American Association of Petroleum Geologists International Conference and Exhibition, Cape Town, South Africa, Abstracts*,

Fonnesu, M. (2016) Hybrid event bed processes, facies trends and distribution in deep-water turbidite systems - Volume I. University College Dublin

Fonnesu, M. and **Felletti, F.** (2019) Facies and architecture of a sand-rich turbidite system in an evolving collisional-trench basin: A case history from the upper Cretaceous-Palaeocene Gottero system (NW Apennines). *Riv. Ital. di Paleontol. e Strat.*, **125**, 449–487.

Fonnesu, M., **Felletti, F.**, **Haughton, P.D.W.**, **Patacci, M.** and **McCaffrey, W.D.** (2018) Hybrid event bed character and distribution linked to turbidite system sub-environments: The North Apennine Gottero Sandstone (north-west Italy). *Sedimentology*, **65**, 151–190.

Fonnesu, M., **Haughton, P.**, **Patacci, M.**, **Felletti, F.** and **McCaffrey, W.** (2015) Towards a classification of hybrid event beds. In: *BSRG*,

Fonnesu, M., **Palermo, D.**, **Galbiati, M.**, **Marchesini, M.**, **Bonamini, E.** and **Bendias, D.** (2020) A new world-class deep-water play-type, deposited by the syndepositional interaction of turbidity flows and bottom currents: The giant Eocene Coral Field in northern Mozambique. *Mar. Pet. Geol.*, **111**, 179–201.

Fryer, R.C., **Jobe, Z.R.**, **Laugier, F.**, **Pettinga, L.A.**, **Gilbert, J.C.**, **Shumaker, L.E.**, **Smith, J.E.** and **Sullivan, M.** (2021) Submarine lobe deposits of the Point Loma Formation, California: Quantifying event-bed architecture and lateral heterogeneity. *Depos. Rec.*, **7**, 374–391.

Funk, J.E., **Slatt, R.M.** and **Pyles, D.R.** (2012) Quantification of static connectivity between deep-

water channels and stratigraphically adjacent architectural elements using outcrop analogs. *Am. Assoc. Pet. Geol. Bull.*, **96**, 277–300.

Gao, S., **Wang, D.**, **Yang, Y.**, **Zhou, L.**, **Zhao, Y.**, **Gao, W.**, **Han, Z.**, **Yu, Q.** and **Li, G.** (2016) Holocene sedimentary systems on a broad continental shelf with abundant river input: Process-product relationships. *Geol. Soc. Spec. Publ.*, **429**, 223–259.

García, M., **Dowdeswell, J.A.**, **Ercilla, G.** and **Jakobsson, M.** (2012) Recent glacially influenced sedimentary processes on the East Greenland continental slope and deep Greenland Basin. *Quat. Sci. Rev.*, **49**, 64–81.

García, M., **Ercilla, G.**, **Alonso, B.**, **Estrada, F.**, **Jané, G.**, **Mena, A.**, **Alvés, T.** and **Juan, C.** (2015) Deep-water turbidite systems: A review of their elements, sedimentary processes and depositional models. Their characteristics on the iberian margins. *Boletín Geológico y Min.*, **126**, 189–218.

Garcia, M.H. (1989) Depositing and eroding sediment-driven flows: turbidity currents. University of Minnesota

García, M.H. (1993) Hydraulic jumps in sediment-driven bottom currents. *J. Hydraul. Eng.*, **119**, 1094–1117.

Garcia, M.O. and **Hull, D.M.** (1994) Turbidites from giant Hawaiian landslides: results from Ocean Drilling Program site 842. *Geology*, **22**, 159–162.

Gardner, M.H. and **Borer, J.M.** (2000) Submarine channel architecture along a slope to basin profile, Brushy Canyon Formation, West Texas. *Bouma, A.H., Stone, C.G. (Eds.), Fine-Grained Turbid. Syst. AAPG Mem. 72 SEPM Spec. Publ. 68*, 195–214.

Gardner, M.H., **Borer, J.M.**, **Melick, J.J.**, **Mavilla, N.**, **Dechesne, M.** and **Wagerle, R.N.** (2003) Stratigraphic process-response model for submarine channels and related features from studies of Permian Brushy Canyon outcrops, West Texas. *Mar. Pet. Geol.*, **20**, 757–787.

Garrett, S.W., **Atherton, T.** and **Hurst, A.** (2000) Lower Cretaceous deep-water sandstone reservoirs of the UK Central North Sea. *Pet. Geosci.*, **6**, 231–240.

Gelati, R. (1977) La successione eo-oligocenica di Garbagna (Alessandria) al margine orientale del Bacino Terziario Ligure Piemontese. *Riv. Ital. di Paleontol. e Stratigr.*, **83**, 103–136.

Gelati, R. (1974) Il limite Eocene-Oligocene nella successione stratigrafica di Costa Merlassino (Alessandria). *Riv. Ital. di Paleontol. e Stratigr.*, **80**, 49–83.

Gelati, R. and **Gnaccolini, M.** (1978a) I conglomerati della Val Borbera, al margine orientale del Bacino terziario ligure-piemontese. *Ist. di Geol. e Paleontol. dell'Università degli Stud. di Milano*, **84**, 701–728.

Gelati, R. and **Gnaccolini, M.** (1984) Evoluzione tettonico-sedimentaria della zona limite tra Alpi ed Appennini tra l'inizio dell'Oligocene ed il Miocene medio. *Mem. della Soc. Geol. Ital.*, **24**, 183–191.

Gelati, R. and **Gnaccolini, M.** (1978b) I conglomerati della Val Borbera, al margine orientale del Bacino Terziario Ligure-Piemontese. *Riv. Ital. di Paleontol. e Stratigr.*, **84**, 701–728.

Gelati, R., **Moratti, G.** and **Papani, G.** (2000) The Late Cenozoic sedimentary succession of the Taza-Guercif Basin, South Rifian Corridor, Morocco. *Mar. Pet. Geol.*, **17**, 373–390.

Georgiopoulou, A. and **Cartwright, J.A.** (2013) A critical test of the concept of submarine equilibrium profile. *Mar. Pet. Geol.*, **41**, 35–47.

Ghibaudo, G. (1992) Subaqueous sediment gravity flow deposits: practical criteria for their field description and classification. *Sedimentology*, **39**, 423–454.

Ghibaudo, G., **Clari, P.** and **Perello, M.** (1985) Litostratigrafia, sedimentologia ed evoluzione tettonico-sedimentaria dei depositi miocenici del margine sud-orientale del bacino terziario ligure-piemontese (Valli Borbera, Scrivia e Lemme). In memoria di Carlo Sturani. *Boll. della Soc. Geol. Ital.*, **104**, 349–397.

Ghibaudo, G., **Massari, F.**, **Chiambretti, I.** and **D'Atri, A.** (2014) Oligo-Miocene tectono-sedimentary evolution of the Tertiary Piedmont Basin southern margin, Roccaverano area-Langhe Sub-basin (NW Italy). *J. Mediterr. Earth Sci.*, **6**, 1–51.

Ghibaudo, G., **Massari, F.**, **Chiambretti, I.**, **d'Atri, A.** and **Fornaciari, E.** (2019) Birth and tectono-sedimentary evolution of the Tertiary Piedmont Basin (NW Italy).

Ghosh, B. and **Lowe, D.R.** (1993) The architecture of deep-water channel complexes, Cretaceous Venado sandstone member, Sacramento Valley, California.

Gihm, Y.S. and **Hwang, I.G.** (2016) Lacustrine hyperpycnal flow deposits after explosive volcanic eruptions, Cretaceous Beolkeum Member, Wido Island, Korea. *Geosci. J.*, **20**, 157–166.

Gillet, H., **Mazières, A.**, **Mulder, T.** and **Cremer, M.** (2013) High resolution morphobathymetric analysis and short-term evolution of the upper part of the Capbreton submarine canyon (south-east Bay of Biscay-French Atlantic coast). In: *EGU General Assembly Conference Abstracts*, EGU2013-10012.

Gnaccolini, M. (1974) Osservazioni sedimentologiche sui conglomerati oligocenici del settore meridionale del Bacino terziario ligure-piemontese. *Riv. Ital. di Paleontol. e Stratigr.*, **80**, 85–100.

Gobo, K. (2014) Development of Gilbert-type deltas: sedimentological case studies from the Plio-Pleistocene of Corinth Rift, Greece. University of Bergen

Gobo, K., **Ghinassi, M.** and **Nemec, W.** (2015) Gilbert-type deltas recording short-term base-level changes: Delta-brink morphodynamics and related foreset facies. *Sedimentology*, **62**, 1923–1949.

Gobo, K., **Ghinassi, M.** and **Nemec, W.** (2014) Reciprocal changes in foreset to bottomset facies in a gilbert-type delta: Response to short-term changes in base level. *J. Sediment. Res.*, **84**, 1079–1095.

Gong, C., **Steel, R.J.**, **Qi, K.** and **Wang, Y.** (2020) Deep-water channel morphologies, architectures, and population densities in relation to stacking trajectories and climate states. *Bull. Geol. Soc. Am.*, **133**, 287–306.

Hafid, M., **Zizi, M.**, **Bally, A.W.** and **Salem, A.A.** (2006) Structural styles of the western onshore and offshore termination of the High Atlas, Morocco. *Comptes Rendus Geosci.*, **338**, 50–64.

Hampton, M.A. (1972) The role of subaqueous debris flow in generating turbidity currents.

Hansen, L., **Janocko, M.**, **Kane, I.** and **Kneller, B.** (2017) Submarine channel evolution, terrace development, and preservation of intra-channel thin-bedded turbidites: Mahin and Avon channels, offshore Nigeria. *Mar. Geol.*, **383**, 146–167.

Hansen, L.A.S., **Callow, R.H.T.**, **Kane, I.A.**, **Gamberi, F.**, **Rovere, M.**, **Cronin, B.T.** and **Kneller, B.C.** (2015) Genesis and character of thin-bedded turbidites associated with submarine channels. *Mar. Pet. Geol.*, **67**, 852–879.

Hansford, M.R., **Plink-Björklund, P.** and **Jones, E.R.** (2020) Global quantitative analyses of river discharge variability and hydrograph shape with respect to climate types. *Earth-Science Rev.*, **200**, 102977.

Haughton, P., **Davis, C.**, **McCaffrey, W.** and **Barker, S.** (2009) Hybrid sediment gravity flow deposits - Classification, origin and significance. *Mar. Pet. Geol.*, **26**, 1900–1918.

Haughton, P.D.W. (2000) Evolving turbidite systems on a deforming basin floor, Tabernas, SE Spain. *Sedimentology*, **47**, 497–518.

Haughton, P.D.W. (1994) Deposits of deflected and ponded turbidity currents, Sorbas Basin, Southeast Spain. *J. Sediment. Res.*, **64**, 233–246.

Heard, T.G., **Pickering, K.T.** and **Robinson, S.A.** (2008) Milankovitch forcing of bioturbation intensity in deep-marine thin-bedded siliciclastic turbidites. *Earth Planet. Sci. Lett.*, **272**, 130–138.

Heezen, B.C. and **Ewing, W.M.** (1952) Turbidity currents and submarine slumps, and the 1929 Grand Banks [Newfoundland] earthquake. *Am. J. Sci.*, **250**, 849–873.

Heller, P.L. and **Dickinson, W.R.** (1985a) Submarine Ramp Facies Model for Delta-Fed, Sand-Rich Turbidite Systems. *Am. Assoc. Pet. Geol. Bull.*, **69**, 960–976.

Heller, P.L. and **Dickinson, W.R.** (1985b) Submarine ramp facies model for delta-fed, sand-rich turbidite systems. *Am. Assoc. Pet. Geol. Bull.*, **69**, 960–976.

Hesse, R. and **Chough, S.K.** (1980) The Northwest Atlantic Mid-Ocean Channel of the Labrador Sea: II. Deposition of parallel laminated levee-muds from the viscous sublayer of low density turbidity currents. *Sedimentology*, **27**, 697–711.

Hesse, R., **Rashid, H.** and **Khodabakhsh, S.** (2004) Fine-grained sediment lofting from meltwater-generated turbidity currents during Heinrich events. *Geology*, **32**, 449–452.

Hiscott, R.N. and **Pickering, K.T.** (1984) Reflected turbidity currents on an Ordovician basin floor, Canadian Appalachians. *Nature*, **311**, 143–145.

Hodgson, D.M. (2009) Distribution and origin of hybrid beds in sand-rich submarine fans of the Tanqua depocentre, Karoo Basin, South Africa. *Mar. Pet. Geol.*, **26**, 1940–1956.

Hodgson, D.M., **Di Celma, C.N.**, **Brunt, R.L.** and **Flint, S.S.** (2011) Submarine slope degradation and aggradation and the stratigraphic evolution of channel-levee systems. *J. Geol. Soc. London.*, **168**, 625–628.

Hopkins, J.L., **Wysoczanski, R.J.**, **Orpin, A.R.**, **Howarth, J.D.**, **Strachan, L.J.**, **Lunenburg, R.**, **McKeown, M.**, **Ganguly, A.**, **Twort, E.** and **Camp, S.** (2020) Deposition and preservation of tephra in marine sediments at the active Hikurangi subduction margin. *Quat. Sci. Rev.*, **247**, 106500.

Horvath, F., **Stegena, L.** and **Berckhemer, H.** (1981) Models of Mediterranean back-arc basin formation. *Philos. Trans. R. Soc. London. Ser. A, Math. Phys. Sci.*, **300**, 383–402.

Hoyal, D., **Van Wagoner, J.C.**, **Adair, N.L.**, **Deffenbaugh, M.**, **Li, D.**, **Sun, T.**, **Huh, C.** and **Giffin, D.E.** (2003) Sedimentation from jets: a depositional model for clastic deposits of all scales and environments. *Search Discov. Artic.*, **40082**, 1–9.

Hoyal, D.C.J.D., **Bursik, M.I.** and **Atkinson, J.F.** (1999) Settling-driven convection: A mechanism of sedimentation from stratified fluids. *J. Geophys. Res. Ocean.*, **104**, 7953–7966.

Hsü, K.J. (1970) The meaning of the word flysch: A short historical search.

Huber, B.T., **Petrizzo, M.R.**, **Young, J.R.**, **Falzoni, F.**, **Gilardoni, S.E.**, **Bown, P.R.** and **Wade, B.S.** (2016) Pforams@microtax: A new online taxonomic database for planktonic foraminifera. *Micropaleontology*, **62**, 429–438.

Ibbeken, H. (1970) Das ligurische Tongriano, eine resedimentierte Molasse-des Nordapennin. *Geol. Jahrb.*, **93**, 1–139.

Janbu, N.E., **Nemec, W.**, **Kirman, E.** and **Özaksoy, V.** (2007) Facies anatomy of a sand-rich channelized turbiditic system: the Eocene Kusuri Formation in the Sinop Basin, north-central

Turkey. In: *Special Publication 38: International Association of Sedimentologists*, *International Association of Sedimentologists*, 38, 457–517.

Janocko, M., **Nemec, W.**, **Henriksen, S.** and **Warchoł, M.** (2013) The diversity of deep-water sinuous channel belts and slope valley-fill complexes. *Mar. Pet. Geol.*, **41**, 7–34.

Jobe, Z.R., **Howes, N.C.** and **Auchter, N.C.** (2016) Comparing submarine and fluvial channel kinematics: Implications for stratigraphic architecture. *Geology*, **44**, 931–934.

Jobe, Z.R., **Howes, N.C.**, **Straub, K.M.**, **Cai, D.**, **Deng, H.**, **Laugier, F.J.**, **Pettinga, L.A.** and **Shumaker, L.E.** (2020) Comparing Aggradation, Superelevation, and Avulsion Frequency of Submarine and Fluvial Channels. *Front. Earth Sci.*, **8**, 53.

Johnson, A.M. (1970) Physical processes in geology: A method for interpretation of natural phenomena; intrusions in igneous rocks, fractures, and folds, flow of debris and ice. *Freeman, Cooper*.

Johnson, D. (1939) The origin of submarine canyons. *Columbia University Press*.

Johnson, K.S., **Paull, C.K.**, **Barry, J.P.** and **Chavez, F.P.** (2001) A decadal record of underflows from a coastal river into the deep sea. *Geology*, **29**, 1019–1022.

Junk, W., **Bayley, P.** and **Sparks, R.** (1989) The flood pulse concept in river-floodplain systems. In: *Geology*, *Proceedings of the International Large River Symposium. Can. Spcc. Publ. Fish. Aquat- Sci*, 106, 110–127.

Kane, I.A., **Catterall, V.**, **McCaffrey, W.D.** and **Martinsen, O.J.** (2010) Submarine channel response to intrabasinal tectonics: The influence of lateral tilt. *Am. Assoc. Pet. Geol. Bull.*, **94**, 189–219.

Kane, I.A. and **Clare, M.A.** (2019) Dispersion, accumulation, and the ultimate fate of microplastics in deep-marine environments: A review and future directions. Front Earth Sci. doi: 10.3389/feart.2019.00080

Kane, I.A. and **Hodgson, D.** (2009) Stratigraphic Stacking of Deepmarine Channel Levee Turbidites: Scales of Cyclicity and their Origin. Examples from the Laingsburg Fm.(Karoo, South Africa) and the Rosario Fm.(Baja, Mexico). In: *AGU Fall Meeting Abstracts*, 2009, EP53A-0611.

Kane, I.A. and **Hodgson, D.M.** (2011) Sedimentological criteria to differentiate submarine channel levee subenvironments: Exhumed examples from the Rosario Fm. (Upper Cretaceous) of Baja California, Mexico, and the Fort Brown Fm. (Permian), Karoo Basin, S. Africa. *Mar. Pet. Geol.*, **28**, 807–823.

Kane, I.A., **Mcgee, D.T.** and **Jobe, Z.R.** (2012) Halokinetic effects on submarine channel equilibrium profiles and implications for facies architecture: Conceptual model illustrated with a case study from magnolia field, Gulf of Mexico. *Geol. Soc. Spec. Publ.*, **363**, 289–302.

Kane, I.A. and **Pontén, A.S.M.** (2012) Submarine transitional flow deposits in the Paleogene Gulf of Mexico. *Geology*, **40**, 1119–1122.

Kassem, A. and **Imram, J.** (2001) Simulation of turbid underflows generated by the plunging of a river. *Geology*, **29**, 655–658.

Khan, S.M., **Imran, J.**, **Bradford, S.** and **Syvitski, J.** (2005) Numerical modeling of hyperpycnal plume. *Mar. Geol.*, **222**–**223**, 193–211.

Kie, T.H. (1988) Magnetotectonics in the Piemont Tertiary basin. *Phys. earth Planet. Inter.*, **52**, 308–319.

Kneller, B. (2003) The influence of flow parameters on turbidite slope channel architecture. *Mar. Pet. Geol.*, **20**, 901–910.

Kneller, B. (1995a) Beyond the turbidite paradigm: physical models for deposition of turbidites and their implications for reservoir prediction. *Geol. Soc. London, Spec. Publ.*, **94**, 31–49.

Kneller, B. (1995b) Beyond the turbidite paradigm: Physical models for deposition of turbidites and their implications for reservoir prediction. *Geol. Soc. Spec. Publ.*, **94**, 31–49.

Kneller, B. and **Buckee, C.** (2000) The structure and fluid mechanics of turbidity currents: A review of some recent studies and their geological implications. *Sedimentology*, **47**, 62–94.

Kneller, B.C., **Bennett, S.J.** and **McCaffrey, W.D.** (1997) Velocity and turbulence structure of density currents and internal solitary waves: Potential sediment transport and the formation of wave ripples in deep water. *Sediment. Geol.*, **112**, 235–250.

Kneller, B.C. and **Branney, M.J.** (1995) Sustained high-density turbidity currents and the deposition of thick massive sands. *Sedimentology*, **42**, 607–616.

Kneller, B.C. and **McCaffrey, W.D.** (2003) The interpretation of vertical sequences in turbidite beds: The influence of longitudinal flow structure. *J. Sediment. Res.*, **73**, 706–713.

Kolla, V. (2007) A review of sinuous channel avulsion patterns in some major deep-sea fans and factors controlling them. *Mar. Pet. Geol.*, **24**, 450–469.

Kolla, V., **Posamentier, H.W.** and **Wood, L.J.** (2007) Deep-water and fluvial sinuous channels—Characteristics, similarities and dissimilarities, and modes of formation. *Mar. Pet. Geol.*, **24**, 388–405.

Komar, P.D. (1971) Hydraulic jumps in turbidity currents. *Geol. Soc. Am. Bull.*, **82**, 1477–1488.

Krijgsman, W. and **Langereis, C.G.** (2000) Magnetostratigraphy of the Zobzit and Koudiat Zarga sections (Taza-Guercif basin, Morocco): implications for the evolution of the Rifian Corridor. *Mar. Pet. Geol.*, **17**, 359–371.

Krijgsman, W., **Langereis, C.G.**, **Zachariasse, W.J.**, **Boccaletti, M.**, **Moratti, G.**, **Gelati, R.**, **Iaccarino, S.**, **Papani, G.** and **Villa, G.** (1999) Late Neogene evolution of the Taza–Guercif Basin (Rifian Corridor, Morocco) and implications for the Messinian salinity crisis. *Mar. Geol.*, **153**, 147–160.

Kuenen, P.H. (1948) Turbidity currents of high density. In: *18th International Geological Congress (1948), London, Reports, pt*, 8, 44–52.

Kuenen, P.H. (1937) Experiments in connection with Daly's hypothesis on the formation of submarine canyons. *Leidse Geol. Meded.*, **8**, 327–351.

Kuenen, P.H. and **Migliorini, C.I.** (1950) Turbidity currents as a cause of graded bedding. *J. Geol.*, **58**, 91–127.

Labourdette, R. and **Bez, M.** (2010) Element migration in turbidite systems: Random or systematic depositional processes? *Am. Assoc. Pet. Geol. Bull.*, **94**, 345–368.

Lamb, M.P. and **Mohrig, D.** (2009) Do hyperpycnal-fl ow deposits record river-fl ood dynamics? *Geology*, **37**, 1067–1070.

Laubscher, H.P., **Biella, G.C.**, **Cassinis, R.**, **Lozey, A.**, **Scarascia, S.** and **Tobacco, I.** (1992) The Ligurian Knot. Tethys. *Geol. Rundsch*, **81**, 275–289.

Le Breton, E., **Brune, S.**, **Ustaszewski, K.**, **Zahirovic, S.**, **Seton, M.** and **Dietmar Müller, R.** (2021) Kinematics and extent of the Piemont-Liguria Basin-implications for subduction processes in the Alps. *Solid Earth*, **12**, 885–913.

Lewis, T., **Lamoureux, S.F.**, **Normandeau, A.** and **Dugan, H.A.** (2017) Hyperpycnal flows control the persistence and flushing of hypoxic high conductivity bottom water in a High Arctic lake. *Arct.*

Sci., **41**, 25–41.

Li, P., **Kneller, B.**, **Thompson, P.**, **Bozetti, G.** and **dos Santos, T.** (2018) Architectural and facies organisation of slope channel fills: Upper Cretaceous Rosario Formation, Baja California, Mexico. *Mar. Pet. Geol.*, **92**, 632–649.

Lirer, F., **Foresi, L.M.**, **Iaccarino, S.M.**, **Salvatorini, G.**, **Turco, E.**, **Cosentino, C.**, **Sierro, F.J.** and **Caruso, A.** (2019) Mediterranean Neogene planktonic foraminifer biozonation and biochronology. *Earth-Science Rev.*, **196**, 102869.

Lowe, D.R. (1982) Sediment gravity flows; II, Depositional models with special reference to the deposits of high-density turbidity currents. *J. Sediment. Res.*, **52**, 279–297.

Lowrie, W. (1990) Identification of ferromagnetic minerals in a rock by coercivity and unblocking temperature properties. *Geophys. Res. Lett.*, **17**, 159–162.

Maffione, M., **Speranza, F.**, **Faccenna, C.**, **Cascella, A.**, **Vignaroli, G.** and **Sagnotti, L.** (2008) A synchronous Alpine and Corsica-Sardinia rotation.

Maino, M., **Decarlis, A.**, **Felletti, F.** and **Seno, S.** (2013) Tectono-sedimentary evolution of the Tertiary Piedmont Basin (NW Italy) within the Oligo–Miocene central Mediterranean geodynamics. *Tectonics*, **32**, 593–619.

Malusá, M.G., **Polino, R.** and **Zattin, M.** (2009) Strain partitioning in the axial NW Alps since the Oligocene. Tectonics. doi: 10.1029/2008TC002370

Mancin, N. and **Pirini** (2001) Middle Eocene to early Miocene foraminiferal Biostratigraphy in the epiligurian succession (Northern Apennines, Italy). *Riv. Ital. di Paleontol. e Stratigr.*, **107**, 371–397.

Mancin, N. and **Pirini, C.** (2002) Benthic and planktonic foraminifera of the Paleogene Epiligurian Succession (Northern Apennines, Italy): a tool for paleobathymetric reconstruction. *Boll. della Soc. Paleontol. Ital.*, **41**, 187–214.

Marini, M., **Felletti, F.**, **Milli, S.** and **Patacci, M.** (2016a) The thick-bedded tail of turbidite thickness distribution as a proxy for flow confinement: Examples from tertiary basins of central and northern Apennines (Italy). *Sediment. Geol.*, **341**, 96–118.

Marini, M., **Maron, M.**, **Petrizzo, M.R.**, **Felletti, F.** and **Muttoni, G.** (2020) Magnetochronology applied to assess tempo of turbidite deposition: A case study of ponded sheet-like turbidites from the lower Miocene of the northern Apennines (Italy). *Sediment. Geol.*, **403**, 105654.

Marini, M., **Patacci, M.**, **Felletti, F.** and **McCaffrey, W.D.** (2016b) Fill to spill stratigraphic evolution of a confined turbidite mini-basin succession, and its likely well bore expression: The Castagnola Fm, NW Italy. *Mar. Pet. Geol.*, **69**, 94–111.

Marini, M., **Porta, G. Della**, **Felletti, F.**, **Grasso, B.M.**, **Franzini, M.** and **Casella, V.** (2019) Insight into heterogeneous calcite cementation of turbidite channel-fills from UAV photogrammetry. *Geosci.*, **9**, 9–17.

Marroni, M., **Ottria, G.** and **Pandolfi, L.** (2010) Note Illustrative della Carta Geologica d'Italia alla scala 1: 50,000 Foglio 196 Cabella Ligure.

Martelli, L., **Cibin, U.**, **Di Giulio, A.** and **Catanzariti, R.** (1998) Litostratigrafia della formazione di Ranzano (Priaboniano-Rupeliano, Appennino settentrionale e Bacino Terziario Piemontese). *Boll. della Soc. Geol. Ital.*, **117**, 151–185.

Martini, I. and **Sandrelli, F.** (2015) Facies analysis of a pliocene river-dominated deltaic succession (Siena Basin, Italy): Implications for the formation and infilling of terminal distributary channels. *Sedimentology*, **62**, 234–265.

Maury, M.F. (1860) The Physical Geography of the Sea, and Its Meteorology. Being a Reconstruction and Enlargement of the Eighth Edition of" The Physical Geography of the Sea". *Sampson Low*.

Mawson, M. and **Tucker, M.** (2009) High-frequency cyclicity (Milankovitch and millennial-scale) in slope-apron carbonates: Zechstein (Upper Permian), North-east England. *Sedimentology*, **56**, 1905–1936.

May, J.A., **Warme, J.E.** and **Slater, R.A.** (1983) Role of submarine canyons on shelfbreak erosion and sedimentation: modern and ancient examples.

Mayall, M. and **Kneller, B.** (2021) Seismic interpretation workflows for deep-water systems: A practical guide for the subsurface. *Am. Assoc. Pet. Geol. Bull.*, **105**, 2127–2157.

Mccaffrey, W. and **Kneller, B.** (2001) Process controls on the development of stratigraphic trap potential on the margins of confined turbidite systems and aids to reservoir evaluation. *Am. Assoc. Pet. Geol. Bull.*, **85**, 971–988.

McCave, I.N. and **Jones, K.P.N.** (1988) Deposition of ungraded muds from high-density non-turbulent turbidity currents. *Nature*, **333**, 250–252.

McCracken, W.A. (1969) Sedimentary Structures and Paleocurrent Analysis of Sespe Formation, Ventura Basin, California. *Am. Assoc. Pet. Geol. Bull.*, **53**, 463.

McElhinny, M.W. and **McFadden, P.L.** (1998) The magnetic field of the earth: paleomagnetism, the core, and the deep mantle. *Academic Press*.

McHargue, T., **Pyrcz, M.J.**, **Sullivan, M.D.**, **Clark, J.D.**, **Fildani, A.**, **Romans, B.W.**, **Covault, J.A.**, **Levy, M.**, **Posamentier, H.W.** and **Drinkwater, N.J.** (2011a) Architecture of turbidite channel systems on the continental slope: Patterns and predictions. *Mar. Pet. Geol.*, **28**, 728–743.

McHargue, T., **Pyrcz, Mi.J.**, **Sulllivan, M.D.**, **Clark, J.**, **Fildani, A.**, **Levy, M.**, **Drinkwater, N.**, **Posamentier, H.**, **Romans, B.** and **Covault, J.** (2011b) Event-Based Modeling of Turbidite Channel Fill, Channel Stacking Pattern, and Net Sand Volume. *Outcrops Revital.*, 163–173.

Meirovitz, C.D., **Stright, L.**, **Hubbard, S.M.** and **Romans, B.W.** (2021) The influence of inter-and intra-channel architecture on deep-water turbidite reservoir performance. Pet Geosci. doi: 10.1144/petgeo2020-005

Middleton, G. V (1966) Experiments on density and turbidity currents: I. Motion of the head. *Can. J. Earth Sci.*, **3**, 523–546.

Middleton, G. V (1993) Sediment deposition from turbidity currents. *Annu. Rev. Earth Planet. Sci.*, **21**, 89–114.

Middleton, G. V and **Hampton, M.A.** (1973) Sediment gravity flows: mechanics of flow and deposition. In, G.V. Middleton and A.H. Bouma (Eds.) Turbidites and Deep-water Sedimentation. *Short course notes. Soc. Econ. Paleontol. Mineral.*, 88.

Migliorini, C.I. (1943) Sul modo di formazione dei complessi tipo macigno. *Boll. della Soc. Geol. Ital.*, **62**, 48–49.

Molli, G., **Crispini, L.**, **Malusà, M.G.**, **Mosca, P.**, **Piana, F.** and **Federico, L.** (2010) Geology of the Western Alps-Northern Apennine junction area: a regional review. J Virtual Explor. doi: 10.3809/jvirtex.2010.00215

Morley, C.K., **King, R.**, **Hillis, R.**, **Tingay, M.** and **Backe, G.** (2011) Deepwater fold and thrust belt classification, tectonics, structure and hydrocarbon prospectivity: A review. *Earth-Science Rev.*, **104**, 41–91.

Morris, W. and **Busby-Spera, C.** (1990) A submarine-fan valley-levee complex in the Upper Cretaceous Rosario Formation: Implication for turbidite facies models. *Bull. Geol. Soc. Am.*, **102**,

900–914.

Mosca, P., **Polino, R.**, **Rogledi, S.** and **Rossi, M.** (2010) New data for the kinematic interpretation of the Alps–Apennines junction (Northwestern Italy). *Int. J. Earth Sci.*, **99**, 833–849.

Mueller, P., **Patacci, M.** and **Di Giulio, A.** (2017) Hybrid event beds in the proximal to distal extensive lobe domain of the coarse-grained and sand-rich Bordighera turbidite system (NW Italy). *Mar. Pet. Geol.*, **86**, 908–931.

Mulder, T. and **Alexander, J.** (2001) The physical character of subaqueous sedimentary density flow and their deposits. *Sedimentology*, **48**, 269–299.

Mulder, T., **Migeon, S.**, **Savoye, B.** and **Faugères, J.C.** (2001a) Inversely graded turbidite sequences in the deep Mediterranean: A record of deposits from flood-generated turbidity currents? *Geo-Marine Lett.*, **21**, 86–93.

Mulder, T., **Migeon, S.**, **Savoye, B.** and **Jouanneau, J.M.** (2001b) Twentieth century floods recorded in the deep Mediterranean sediments. *Geology*, **29**, 1011–1014.

Mulder, T., **Savoye, B.**, **Piper, D.J.W.** and **Syvitski, J.P.M.** (1998a) The Var submarine sedimentary system: understanding Holocene sediment delivery processes and their importance to the geological record. *Geol. Soc. Spec. Publ.*, **129**, 145–166.

Mulder, T., **Savoye, B.**, **Syvitski, J.P.M.** and **Parize, O.** (1997) Des courants de turbidité hyperpycnaux dans la tête du canyon du Var? Données hydrologiques et observations de terrain. *Ocean. Acta*, **20**, 607–626.

Mulder, T. and **Syvitski, J.P.M.** (1995) Turbidity currents generated at river mouths during exceptional discharges to the world oceans. *J. Geol.*, **103**, 285–299.

Mulder, T., **Syvitski, J.P.M.**, **Migeon, S.**, **Faugères, J.C.** and **Savoye, B.** (2003) Marine hyperpycnal flows: Initiation, behaviorand related deposits. A review. *Mar. Pet. Geol.*, **20**, 861–882.

Mulder, T., **Syvitski, J.P.M.** and **Skene, K.I.** (1998b) Modeling of erosion and deposition by turbidity currents generated at river mouths. *J. Sediment. Res.*, **68**, 124–137.

Mulder, T., **Weber, O.**, **Anschutz, P.**, **Jorissen, F.J.** and **Jouanneau, J.M.** (2001c) A few months-old storm-generated turbidite deposited in the Capbreton Canyon (Bay of Biscay, SW France). *Geo-Marine Lett.*, **21**, 149–156.

Mutti, E. (1985) Turbidite systems and their relations to depositional sequences. In: *Provenance of arenites*, D. Reidel (Ed. G.G. Zuffa), *Springer*, 65–93.

Mutti, E. (1992) Turbidite sandstones. *Agip - Ist. di Geol. Univ. di Parma, Italy, Spec. Publ.*, 275.

Mutti, E. (2019) Thin-bedded plumites: An overlooked deep-water deposit. *J. Mediterr. Earth Sci.*, **11**, 61–80.

Mutti, E. (1979) Turbidites et cones sous-marins profonds. *Sédimentation détritique (fluviatile, littorale Mar.*, **1**, 353–419.

Mutti, E., **Bernoulli, D.**, **Lucchi, F.R.** and **Tinterri, R.** (2009) Turbidites and turbidity currents from alpine ‘flysch’ to the exploration of continental margins. *Sedimentology*, **56**, 267–318.

Mutti, E., **Davoli, G.**, **Mora, S.** and **Papani, L.** (1994) Internal stacking patterns of ancient turbidite systems from collisional basins. In: *Submarine fans and turbidite systems: Gulf Coast Section SEPM Proceedings, 15th Annual Research Conference*, 15, 257–268.

Mutti, E., **Davoli, G.**, **Tinterri, R.** and **Zavala, C.** (1996) The importance of ancient fluvio-deltaic systems dominated by catastrophic flooding in tectonically active basins. *Mem. di Sci. Geol.*, **48**, 233–291.

Mutti, E. and **Ghibaudo, G.** (1972) Un esempio di torbiditi di conoide sottomarina esterna: le Arenarie di San Salvatore (Formazione di Bobbio, Miocene) nell'Appennino di Piacenza. *Mem. Acc. Sci. Torino, Cl. Sci. Fis. Mat. Nat.*, **16**, 1–40.

Mutti, E. and **Lucchi, F.R.** (1975) Turbidite facies and facies associations. In: *IX Int. Cong. I.A.S, Field Trip, All., Nizza* (Ed. M. E., P. G.C., R.L. F., S. M., Z. G., G. G., and I. S.), *Verlag nicht ermittelbar*, 21–36.

Mutti, E., **Lucchi, F.R.** and **Roveri, M.** (2002a) Revisiting turbidites of the Marnoso-arenacea formation and their basin-margin equivalents: problems with classic models. *Excursion Guideb. Turbid. Work. …*, 27–30.

Mutti, E. and **Normark, W.R.** (1991) An integrated approach to the study of turbidite systems. In: *Seismic facies and sedimentary processes of submarine fans and turbidite systems*, *Springer*, 75–106.

Mutti, E. and **Normark, W.R.** (1987) Comparing examples of modern and ancient turbidite systems: problems and concepts. In: *Marine clastic sedimentology*, *Springer*, 1–38.

Mutti, E., **Papani, L.**, **Di Biase, D.**, **Davoli, G.**, **Mora, S.**, **Segadelli, S.** and **Tinterri, R.** (1995) Il Bacino Terziario Epimesoalpino e le sue implicazioni sui rapporti tra Alpi ed Appennino. *Mem. di Sci. Geol. di Padova*, **47**, 217–244.

Mutti, E. and **Ricci Lucchi, F.** (1974) La signification de certaines unites sequentielles dans les series a turbidites. *Bull. la Société Geol. Fr.*, **7**, 577–582.

Mutti, E. and **Ricci Lucchi, F.** (1972) Le torbidite dell'Apennino Setlentrionale: introduzione all'analisi di facies: SocietaGeologica Italiana. *Memorie*, **11**, 161–199.

Mutti, E., **Ricci Lucchi, F.** and **Roveri, M.** (2002b) Revisiting turbidites of the Marnoso-arenacea Formation and their basin-margin equivalents: problems with classic models. In: *Turbidite Workshop organized by Dipartimento di Scienze della Terra, Università di Parma, and Eni-Agip Division for the 64th EAGE Conference and Exhibition, Florence, Italy, 27-30 May 2002*, 35.

Mutti, E. and **Sonnino, M.** (1981) Compensation cycles: a diagnostic feature of turbidite sandstone lobes. In: *International Association of Sedimentologists—European regional meeting.*, 120–123.

Mutti, E., **Tinterri, R.**, **Benevelli, G.**, **Biase, D. di** and **Cavanna, G.** (2003) Deltaic, mixed and turbidite sedimentation of ancient foreland basins. *Mar. Pet. Geol.*, **20**, 733–755.

Mutti, E., **Tinterri, R.**, **Di Biase, D.**, **Fava, L.**, **Mavilla, N.**, **Angella, S.** and **Calabrese, L.** (2000) Delta-front facies associations of ancient flood-dominated fluvio-deltaic systems. *Rev. la Soc. Geológica España*, **13**, 165–190.

Mutti, E., **Tinterri, R.**, **Remacha, E.**, **Mavilla, N.**, **Angela, S.** and **Fava, L.** (1999) An Introduction to the Analysis of Ancient Turbidite Basins from an Outcrop Perspective: AAPG Continuing Education Course Note, No. 39. *AAPG*.

Muttoni, G., **Argnani, A.**, **Kent, D. V.**, **Abrahamsen, N.** and **Cibin, U.** (1998) Paleomagnetic evidence for Neogene tectonic rotations in the northern Apennines, Italy. *Earth Planet. Sci. Lett.*, **154**, 25–40.

Muttoni, G., **Dallanave, E.** and **Channell, J.E.T.** (2013) The drift history of Adria and Africa from 280Ma to Present, Jurassic true polar wander, and zonal climate control on Tethyan sedimentary facies. *Palaeogeogr. Palaeoclimatol. Palaeoecol.*, **386**, 415–435.

Myrow, P.M., **Lamb, M.P.**, **Lukens, C.**, **Houck, K.** and **Strauss, J.** (2008) Proximal to distal facies relationships in deposits of wave-influenced hyperpycnal flows. In: *JJ Ponce and EB Olivero, conveners, Sediment transfer from shelf to deepwater—Revisiting the delivery mechanisms: Conference Proceedings, AAPG Hedberg Conference*,

Nardin, T.R., **Hein, F.J.**, **Gorsline, D.S.** and **Edwards, B.D.** (1979) A review of mass movement processes sediment and acoustic characteristics, and contrasts in slope and base-of-slope systems versus canyon-fan-basin floor systems. *SEPM Spec. Publ.*, **27**, 61–73.

Navarro, L., **Khan, Z.** and **Arnott, R.W.C.** (2007) Depositional Architecture and Evolution of a Deep-marine Channel-levee Complex: Isaac Formation (Windermere Supergroup), Southern Canadian Cordillera. 22 pp.

Nemec, W. (1995) The dynamics of deltaic suspension plumes. In: *Geology of Deltas* (Ed. M.N. Oti and G. Postma), *A.A. Balkem, Rotterdam, Brookfield*, 31–93.

Neuberger, D.J. (1987) Swastika (Upper Pennsylvanian) shelf-margin deltas and delta-fed turbidites, Flowers" Canyon Sand" Field area, Stonewall County, Texas.

Nichols, G. (2009) Sedimentology and stratigraphy. *John Wiley & Sons*.

Normark, W.R. (1970) Growth patterns of deep-sea fans. *Am. Assoc. Pet. Geol. Bull.*, **54**, 2170–2195.

Normark, W.R., **Posamentier, H.** and **Mutti, E.** (1993) Turbidite systems: state of the art and future directions. *Rev. Geophys.*, **31**, 91–116.

Ogg, J.G., **Ogg, G.M.** and **Gradstein, F.** (2016) A Concise Geologic Time Scale. *Elsevier*, 229 pp.

Oms, O., **Dinarès-Turell, J.** and **Remacha, E.** (2003) Magnetic stratigraphy from deep clastic turbidites: An example from the Eocene Hecho group (Southern Pyrenees). *Stud. Geophys. Geod.*, **47**, 275–288.

Palozzi, J., **Pantopoulos, G.**, **Maravelis, A.G.**, **Nordsvan, A.** and **Zelilidis, A.** (2018) Sedimentological analysis and bed thickness statistics from a Carboniferous deep-water channel-levee complex: Myall Trough, SE Australia. *Sediment. Geol.*, **364**, 160–179.

Pan, S., **Liu, H.**, **Zavala, C.**, **Liu, C.**, **Liang, S.**, **Zhang, Q.** and **Bai, Z.** (2017) Sublacustrine hyperpycnal channel-fan system in a large depression basin: A case study of Nen 1 Member, Cretaceous Nenjiang Formation in the Songliao Basin, NE China. *Pet. Explor. Dev.*, **44**, 911–922.

Park, Y., **Yoo, D.**, **Kang, N.**, **Yi, B.** and **Kim, B.** (2021) Tectonic control on mass-transport deposit and canyon-fed fan system in the Ulleung Basin, East Sea (Sea of Japan). *Basin Res.*, **33**, 991–1016.

Parsons, J.D., **Bush, J.W.M.** and **Syvitski, J.P.M.** (2001) Hyperpycnal plume formation from riverine outflows with small sediment concentrations. *Sedimentology*, **48**, 465–478.

Parsons, J.D., **Friedrichs, C.T.**, **Traykovski, P.A.**, **Mohrig, D.**, **Imran, J.**, **Syvitski, J.P.M.**, **Parker, G.**, **Puig, P.**, **Buttles, J.L.** and **Garca, M.H.** (2007) The Mechanics of Marine Sediment Gravity Flows. *Cont. Margin Sediment.*, 275–337.

Parsons, J.D. and **García, M.H.** (1998) Similarity of gravity current fronts. *Phys. Fluids*, **10**, 3209–3213.

Patacci, M. (2016) A high-precision Jacob's staff with improved spatial accuracy and laser sighting capability. *Sediment. Geol.*, **335**, 66–69.

Patacci, M., **Haughton, P.D.W.** and **McCaffrey, W.D.** (2014) Rheological complexity in sediment gravity flows forced to decelerate against a confining slope, Braux, SE France. *J. Sediment. Res.*, **84**, 270–277.

Patacci, M., **Haughton, P.D.W.** and **McCaffrey, W.D.** (2015) Flow behavior of ponded turbidity currents. *J. Sediment. Res.*, **85**, 903–936.

Patacci, M., **Marini, M.**, **Felletti, F.**, **Di Giulio, A.**, **Setti, M.** and **McCaffrey, W.** (2020a) Origin of mud in turbidites and hybrid event beds: Insight from ponded mudstone caps of the Castagnola turbidite system (north-west Italy). *Sedimentology*, **67**, 2625–2644.

Patacci, M., **Marini, M.**, **Felletti, F.**, **Di Giulio, A.**, **Setti, M.** and **McCaffrey, W.** (2020b) Origin of mud in turbidites and hybrid event beds: Insight from ponded mudstone caps of the Castagnola turbidite system (north-west Italy). *Sedimentology*, **67**, 2625–2644.

Payros, A. and **Martínez-Braceras, N.** (2014) Orbital forcing in turbidite accumulation during the Eocene greenhouse interval. *Sedimentology*, **61**, 1411–1432.

Peakall, J., **McCaffrey, B.** and **Kneller, B.** (2000) A process model for the evolution, morphology, and architecture of sinuous submarine channels. *J. Sediment. Res.*, **70**, 434–448.

Peakall, J. and **Sumner, E.J.** (2015) Submarine channel flow processes and deposits: A process-product perspective. *Geomorphology*, **244**, 95–120.

Petit, C., **Migeon, S.** and **Coste, M.** (2015) Numerical models of continental and submarine erosion: Application to the northern Ligurian Margin (Southern Alps, France/Italy). *Earth Surf. Process. Landforms*, **40**, 681–695.

Petter, A.L. and **Steel, R.J.** (2006) Hyperpycnal flow variability and slope organization on an Eocene shelf margin, Central Basin, Spitsbergen. *Am. Assoc. Pet. Geol. Bull.*, **90**, 1451–1472.

Pettingill, H.S. and **Weimer, P.** (2002) World-Wide Deepwater Exploration and Production: Past, Present and Future. *Proc. Annu. Offshore Technol. Conf.*, **21**, 371–376.

Piana, F., **Barale, L.**, **Bertok, C.**, **D'atri, A.**, **Irace, A.** and **Mosca, P.** (2021) The alps-apennines interference zone: A perspective from the maritime and wester ligurian alps. Geosci. doi: 10.3390/geosciences11050185

Piazza, A. and **Tinterri, R.** (2020) Cyclic stacking pattern, architecture and facies of the turbidite lobes in the Macigno Sandstones Formation (Chattian-Aquitanian, northern Apennines, Italy). Mar Pet Geol. doi: 10.1016/j.marpetgeo.2020.104704

Pickering, K., **Stow, D.**, **Watson, M.** and **Hiscott, R.** (1986) Deep-water facies, processes and models: a review and classification scheme for modern and ancient sediments. *Earth Sci. Rev.*, **23**, 75–174.

Pickering, K.T. and **Cantalejo, B.** (2015) Deep-marine environments of the middle Eocene upper Hecho Group, Spanish Pyrenees: Introduction. *Earth-Science Rev.*, **144**, 1–9.

Pickering, K.T. and **Hiscott, R.N.** (1985) Contained (reflected) turbidity currents from the Middle Ordovician Cloridorme Formation, Quebec, Canada: an alternative to the antidune hypothesis. *Sedimentology*, **32**, 373–394.

Pickering, K.T., **Hiscott, R.N.** and **Hein, F.J.** (1989) Deep-marine environments: clastic sedimentation and tectonics. In: *Deep-marine environments: clastic sedimentation and tectonics* (Ed. L.U. Hyman), *Allen & Unwin Australia*, 416.

Piper, D.J.W. (1978) Turbidite muds and silts on deepsea fans and abyssal plains.

Piper, D.J.W., **Hiscott, R.N.** and **Normark, W.R.** (1999a) Outcrop-scale acoustic facies analysis and latest Quaternary development of Hueneme and Dume submarine fans, offshore California. *Sedimentology*, **46**, 47–78.

Piper, D.J.W., **Hiscott, R.N.** and **Normark, W.R.** (1999b) Outcrop-scale acoustic facies analysis and latest Quaternary development of Hueneme and Dume submarine fans, offshore California. *Sedimentology*, **46**, 47–78.

Piper, D.J.W. and **Normark, W.R.** (2009) Processes that initiate turbidity currents and their influence

on turbidites: A marine geology perspective. *J. Sediment. Res.*, **79**, 347–362.

Pirmez, C., **Beaubouef, R.T.**, **Friedmann, S.J.**, **Mohrig, D.C.**, **Weimer, P.**, **Slatt, R.M.**, **Coleman, J.**, **Rosen, N.C.**, **Nelson, H.** and **Bouma, A.H.** (2000) Equilibrium profile and baselevel in submarine channels: examples from Late Pleistocene systems and implications for the architecture of deepwater reservoirs. In: *Global deep-water reservoirs: Gulf Coast Section SEPM Foundation 20th Annual Bob F. Perkins Research Conference*, 782–805.

Plink-Björlrklund, P. and **Steel, R.J.** (2004) Initiation of turbidity currents: Outcrop evidence for Eocene hyperpycnal flow turbidites. *Sediment. Geol.*, **165**, 29–52.

Ponce, J.J. and **Carmona, N.B.** (2011) Miocene deep-marine hyperpycnal channel levee complexes, Tierra del Fuego, Argentina: Facies associations and architectural elements. In: *AAPG Studies in Geology* (Ed. R.M. Slatt and C. Zavala), *AAPG Special Volumes*, 61, 75–93.

Ponce, J.J., **Olivero, E.B.** and **Martinioni, D.R.** (2008) Deep-marine hyperpycnal channel-levee complexes in the Miocene of Tierra del Fuego, Argentina: Architectural elements and facies associations. *AAPG Hedb. Conf. Sediment Transf. from Shelf to Deep. Deliv. Mech.*, 1–6.

Posamentier, H.W. and **Allen, G.P.** (1999) Siliciclastic sequence stratigraphy. *Concepts Appl. SEPM, Concepts Sedimentol. Paleontol.*, **7**, 210.

Posamentier, H.W. and **Kolla, V.** (2003) Seismic geomorphology and stratigraphy of depositional elements in deep-water settings. *J. Sediment. Res.*, **73**, 367–388.

Posamentier, H.W. and **Vail, P.R.** (1988) Eustatic controls on clastic deposition II - Sequence and systems tract models. *Wilgus, C. K., Posamentier, H. W., Ross, C. K., Kendall, C. G. St. C., eds., Sea-level Chang. An Integr. approach Soc. Econ. Paleontol. Mineral. - Spec. Publ.*, **42**, 125–154.

Prather, B.E. (2003) Controls on reservoir distribution, architecture and stratigraphic trapping in slope settings. *Mar. Pet. Geol.*, **20**, 529–545.

Prather, B.E., **Keller, F.B.** and **Chapin, M.A.** (2000) Hierarchy of Deep-Water Architectural Elements With Reference to Seismic Resolution: Implications for Reservoir Prediction and Modeling. *Deep. Reserv. World 20th Annu.*, 817–835.

Pratt, J.R., **Barbeau Jr, D.L.**, **Izykowski, T.M.**, **Garver, J.I.** and **Emran, A.** (2016) Sedimentary provenance of the Taza-Guercif Basin, South Rifean Corridor, Morocco: Implications for basin emergence. *Geosphere*, **12**, 221–236.

Prélat, A. and **Hodgson, D.M.** (2013) The full range of turbidite bed thickness patterns in submarine lobes: Controls and implications. *J. Geol. Soc. London.*, **170**, 209–214.

Prélat, A., **Hodgson, D.M.** and **Flint, S.S.** (2009) Evolution, architecture and hierarchy of distributary deep-water deposits: a high-resolution outcrop investigation from the Permian Karoo Basin, South Africa. *Sedimentology*, **56**, 2132–2154.

Pricope, N.G. (2013) Variable-source flood pulsing in a semi-arid transboundary watershed: The Chobe River, Botswana and Namibia. *Environ. Monit. Assess.*, **185**, 1883–1906.

Pyles, D.R., **Tomasso, M.** and **Jennette, D.C.** (2012) Flow processes and sedimentation associated with erosion and filling of sinuous submarine channels. *Geology*, **40**, 143–146.

Qin, Y. (2017) Geological controls on the evolution of submarine channels in the Espírito Santo Basin , SE Brazil. Cardiff University

Reading, H.G. (2009) Sedimentary environments: processes, facies and stratigraphy. *John Wiley & Sons*.

Reading, H.G. and **Richards, M.** (1994) Turbidite systems in deep-water basin margins classified by grain size and feeder system. *Am. Assoc. Pet. Geol. Bull.*, **78**, 792–822.

Reijmer, J.J.G., **Sprenger, A.**, **Ten Kate, W.**, **Schlager, W.** and **Krystyn, L.** (1994) Periodicities in the composition of Late Triassic calciturbidites (eastern Alps, Austria). *Orbital forcing Cycl. Seq.*, **19**, 323–343.

Reimchen, A.P., **Hubbard, S.M.**, **Stright, L.** and **Romans, B.W.** (2016a) Using sea-floor morphometrics to constrain stratigraphic models of sinuous submarine channel systems. *Mar. Pet. Geol.*, **77**, 92–115.

Reimchen, A.P., **Hubbard, S.M.**, **Stright, L.** and **Romans, B.W.** (2016b) Using sea-floor morphometrics to constrain stratigraphic models of sinuous submarine channel systems. *Mar. Pet. Geol.*, **77**, 92–115.

Richards, M., **Bowman, M.** and **Reading, H.** (1998) Submarine-fan systems I: characterization and stratigraphic prediction. *Mar. Pet. Geol.*, **15**, 689–717.

Rollet, N., **Déverchère, J.**, **Beslier, M.-O.**, **Guennoc, P.**, **Réhault, J.-P.**, **Sosson, M.** and **Truffert, C.** (2002) Back arc extension, tectonic inheritance, and volcanism in the Ligurian Sea, Western Mediterranean. *Tectonics*, **21**, 6-1-6–23.

Rosen, T. and **Xu, Y.J.** (2014) A hydrograph-based sediment availability assessment: Implications for Mississippi River sediment diversion. *Water (Switzerland)*, **6**, 564–583.

Rossi, M. and **Craig, J.** (2016) A new perspective on sequence stratigraphy of syn-orogenic basins: insights from the Tertiary Piedmont Basin (Italy) and implications for play concepts and reservoir heterogeneity. *Geol. Soc. London, Spec. Publ.*, **436**, 93–133.

Rossi, M., **Minervini, M.** and **Ghielmi, M.** (2018) Drowning unconformities on hinged clastic shelves. *Geology*, **46**, 439–442.

Rossi, M., **Mosca, P.**, **Polino, R.**, **Rogledi, S.** and **Biffi, U.** (2009) New outcrop and subsurface data in the Tertiary Piedmont Basin (NW-Italy): unconformity-bounded stratigraphic units and their relationships with basin-modification phases. *Riv. Ital. di Paleontol. e Stratigr.*, **115**, 305–335.

Samuel, A., **Kneller, B.**, **Raslan, S.**, **Sharp, A.** and **Parsons, C.** (2003a) Prolific deep-marine slope channels of the Nile Delta, Egypt. *Am. Assoc. Pet. Geol. Bull.*, **87**, 541–560.

Samuel, A., **Kneller, B.**, **Raslan, S.**, **Sharp, A.** and **Parsons, C.** (2003b) Prolific deep-marine slope channels of the Nile Delta, Egypt. *Am. Assoc. Pet. Geol. Bull.*, **87**, 541–560.

Sanders, J.E. (1965) Primary sedimentary structures formed by turbidity currents and related resedimentation mechanisms. *SEPM Spec. Publ.*, **12**, 192–219.

Sani, F., **Zizi, M.** and **Bally, A.W.** (2000) The Neogene–Quaternary evolution of the Guercif Basin (Morocco) reconstructed from seismic line interpretation. *Mar. Pet. Geol.*, **17**, 343–357.

Schneider, J.L., **Le Ruyet, A.**, **Chanier, F.**, **Buret, C.**, **Ferrière, J.**, **Proust, J.N.** and **Rosseel, J.B.** (2001) Primary or secondary distal volcaniclastic turbidities: How to make the distinction? An example from the Miocene of New Zealand (Mahia Peninsula, North Island). *Sediment. Geol.*, **145**, 1–22.

Scholle, P.A. (1971) Sedimentology of fine-grained deep-water carbonate turbidites, Monte Antola Flysch (Upper Cretaceous), northern Apennines, Italy. *Geol. Soc. Am. Bull.*, **82**, 629–658.

Shanmugam, G. (2000) 50 years of the turbidite paradigm (1950s-1990s): deep-water processes and facies models -- a critical perspective. *Mar. Pet. Geol.*, **17**, 285–342.

Shanmugam, G. (2019) Climatic and tectonic controls of lacustrine hyperpycnite origination in the Late Triassic Ordos Basin, central China: Implications for unconventional petroleum development: Discussion. *Am. Assoc. Pet. Geol. Bull.*, **103**, 505–510.

Shanmugam, G. and **Moiola, R.J.** (1985) Submarine fan models: problems and solutions. In:

Submarine fans and related turbidite systems, *Springer*, 29–35.

Shanmugam, G. and **Moiola, R.J.** (1988) Submarine fans: characteristics, models, classification, and reservoir potential. *Earth-Science Rev.*, **24**, 383–428.

Shanmugam, G., **Moiola, R.J.** and **Wagner, J.B.** (1997) Turbidite paradigm and sequence stratigraphy: a critical perspective. In: *Official Program-1997 AAPG Annual Convention, Dallas, Texas*, 106,

Simmons, S.M., **Azpiroz-Zabala, M.**, **Cartigny, M.J.B.**, **Clare, M.A.**, **Cooper, C.**, **Parsons, D.R.**, **Pope, E.L.**, **Sumner, E.J.** and **Talling, P.J.** (2020) Novel Acoustic Method Provides First Detailed Measurements of Sediment Concentration Structure Within Submarine Turbidity Currents. *J. Geophys. Res. Ocean.*, **125**, 1–24.

Simons, D.B., **RIchardson, E. V** and **Nordin Jr, C.F.** (1965) Sedimentary structures generated by flow in alluvial channels. *SEPM Spec. Publ.*, **12**, 34–52.

Simpson, J.E. and **Britter, R.E.** (1979) The dynamics of the head of a gravity current advancing over a horizontal surface. *J. Fluid Mech.*, **94**, 477–495.

Sinclair, H.D. (1994) The influence of lateral basinal slopes on turbidite sedimentation in the Annot sandstones of SE France. *J. Sediment. Res.*, **64**, 42–54.

Sinclair, H.D. and **Tomasso, M.** (2002) Depositional evolution of confined turbidite basins. *J. Sediment. Res.*, **72**, 451–456.

Sohn, Y.K. (1997) On Traction-Carpet Sedimentation. SEPM J Sediment Res. doi: 10.1306/D42685AE-2B26-11D7-8648000102C1865D

Sohn, Y.K., **Choe, M.Y.** and **Jo, H.R.** (2002) Transition from debris flow to hyperconcentrated flow in a submarine channel (the Cretaceous cerro toro formation, southern Chile). *Terra Nov.*, **14**, 405–415.

Soyinka, O.A. and **Slatt, R.M.** (2008) Identification and micro-stratigraphy of hyperpycnites and turbidites in Cretaceous Lewis Shale, Wyoming. *Sedimentology*, **55**, 1117–1133.

Sparks, R.S.J., **Bonnecaze, R.T.**, **Huppert, H.E.**, **Lister, J.R.**, **Hallworth, M.A.**, **Mader, H.** and **Phillips, J.** (1993) Sediment-laden gravity currents with reversing buoyancy. *Earth Planet. Sci. Lett.*, **114**, 243–257.

Sprague, A., **Box, D.**, **Hodgson, D.** and **Flint, S.** (2008) A physical stratigraphic hierarchy for deep-water slope system reservoirs 2: complexes to storeys. In: *American Association of Petroleum Geologists International Conference and Exhibition, Cape Town, South Africa, Abstracts*,

Sprague, A.R.G., **Garfield, T.R.**, **Goulding, F.J.**, **Beaubouef, R.T.**, **Sullivan, M.D.**, **Rossen, C.**, **Campion, K.M.**, **Sickafoose, D.K.**, **Abreu, V.**, **Schellpeper, M.E.**, **Jensen, G.N.**, **Jennette, D.C.**, **Pirmez, C.**, **Dixon, B.T.**, **Ying, D.**, **Ardill, J.**, **Mohrig, D.C.**, **Porter, M.L.**, **Farrell, M.E.** and **Mellere, D.** (2005) Integrated slope channel depositional models: the key to successful prediction of reservoir presence and quality in offshore West Africa.

Steel, E., **Simms, A.R.**, **Steel, R.** and **Olariu, C.** (2018) Hyperpycnal delivery of sand to the continental shelf: Insights from the Jurassic Lajas Formation, Neuquén Basin, Argentina. *Sedimentology*, **65**, 2149–2170.

Stocchi, S., **Cavalli, C.** and **Baruffini, L.** (1992) I depositi torbiditici di Guaso (Pirenei centro meridionali), Gremiasco e Castagnola (settore orientale del BTP): geometria e correlazioni di dettaglio. *Atti Ticinensi di Sci. della Terra*, **35**, 153–177.

Stow, D. and **Smillie, Z.** (2020) Distinguishing between deep-water sediment facies: Turbidites, contourites and hemipelagites. Geosci. doi: 10.3390/geosciences10020068

Stow, D.A.V. and **Mayall, M.** (2000) Deepwater Sedimentary Systems - New Models for 21st Century. *Mar. Pet. Geol.*, **17**, 125–135.

Stow, D.A. V, **Alam, M.** and **Piper, D.J.W.** (1984) Sedimentology of the Halifax Formation, Nova Scotia: Lower Palaeozoic fine-grained turbidites. *Geol. Soc. London, Spec. Publ.*, **15**, 127–144.

Stow, D.A. V, **Amano, K.**, **Batson, B.S.**, **Brass, G.W.**, **Corrigan, J.**, **Raman, C. V**, **Tiercelin, J.-J.**, **Townsend, M.**, **Wijayananda, N.P.** and **Cochran, J.R.** (1990) Sediment facies and processes on the distal Bengal Fan, Leg 116. *Cochran, JR, Stow, DAV, al. Proc. Ocean Drill. Proj. Leg*, **116**, 377–396.

Stow, D.A. V and **Shanmugam, G.** (1980) Sequence of structures in fine-grained turbidites: comparison of recent deep-sea and ancient flysch sediments. *Sediment. Geol.*, **25**, 23–42.

Stow, D.A. V and **Tabrez, A.R.** (1998) Hemipelagites: processes, facies and model. *Geol. Soc. London, Spec. Publ.*, **129**, 317–337.

Studer, B. (1847) Lehrbuch der physikalischen Geographie und Geologie. *Dalp*.

Sulli, A., **Agate, M.**, **Zizzo, E.**, **Gasparo Morticelli, M.** and **Lo Iacono, C.** (2021) Geo-hazards of the San Vito peninsula offshore (southwestern Tyrrhenian Sea). *J. Maps*, **17**, 185–196.

Sullivan, M.D., **Foreman, J.L.**, **Jennette, D.C.**, **Stern, D.**, **Jensen, G.N.** and **Goulding, F.J.** (2005) An integrated approach to characterization and modeling of deep-water reservoirs, Diana field, western Gulf of Mexico. *AAPG Mem.*, 215–234.

Sumner, E.J., **Amy, L.A.** and **Talling, P.J.** (2008) Deposit Structure and Processes of Sand Deposition from Decelerating Sediment Suspensions. *J. Sediment. Res.*, **78**, 529–547.

Sumner, E.J., **Talling, P.J.**, **Amy, L.A.**, **Wynn, R.B.**, **Stevenson, C.J.** and **Frenz, M.** (2012) Facies architecture of individual basin-plain turbidites: Comparison with existing models and implications for flow processes: *Basin-plain turbidites*. *Sedimentology*, **59**, 1850–1887.

Sylvester, Z., **Pirmez, C.** and **Cantelli, A.** (2011) A model of submarine channel-levee evolution based on channel trajectories: Implications for stratigraphic architecture. *Mar. Pet. Geol.*, **28**, 716–727.

Talling, P.J., **Allin, J.**, **Armitage, D.A.**, **Arnott, R.W.C.**, **Cartigny, M.J.B.**, **Clare, M.A.**, **Felletti, F.**, **Covault, J.A.**, **Girardclos, S.**, **Hansen, E.**, **Hill, P.R.**, **Hiscott, R.N.**, **Hogg, A.J.**, **Clarke, J.H.**, **Jobe, Z.R.**, **Malgesini, G.**, **Mozzato, A.**, **Naruse, H.**, **Parkinson, S.**, **Peel, F.J.**, **Piper, D.J.W.**, **Pope, E.D.**, **Postma, G.**, **Rowley, P.**, **Sguazzini, A.**, **Stevenson, C.J.**, **Sumner, E.J.**, **Sylvester, Z.**, **Watts, C.** and **Xu, J.** (2015) Key future directions for research on turbidity currents and their deposits. *J. Sediment. Res.*, **85**, 153–169.

Talling, P.J., **Wynn, R.B.**, **Schmmidt, D.N.**, **Rixon, R.**, **Sumner, E.** and **Amy, L.** (2010) How did thin submarine debris flows carry boulder-sized intraclasts for remarkable distances across low gradients to the far reaches of the Mississippi fan? *J. Sediment. Res.*, **80**, 829–851.

Tauxe, L., **Bertram, H.N.** and **Seberino, C.** (2002) Physical interpretation of hysteresis loops: Micromagnetic modeling of fine particle magnetite. doi: 10.1029/2001GC000241

Tauxe, L., **Mullender, T.A.T.** and **Pick, T.** (1996) Potbellies, wasp-waists, and superparamagnetism in magnetic hysteresis. *J. Geophys. Res. Solid Earth*, **101**, 571–583.

Tek, D.E., **McArthur, A.D.**, **Poyatos-Moré, M.**, **Colombera, L.**, **Patacci, M.**, **Craven, B.** and **McCaffrey, W.D.** (2021) Relating seafloor geomorphology to subsurface architecture: How mass-transport deposits and knickpoint-zones build the stratigraphy of the deep-water Hikurangi Channel. *Sedimentology*, **68**, 3141–3190.

Tek, D.E., **Poyatos-Moré, M.**, **Patacci, M.**, **McArthur, A.D.**, **Colombera, L.**, **Cullen, T.M.** and **McCaffrey, W.D.** (2020) Syndepositional Tectonics and mass-transport deposits control

channelized, bathymetrically complex deep-water systems (AíNSA depocenter, Spain). 729–762 pp.

Ten Kate, W.G.H.Z. and **Sprenger, A.** (1993) Orbital cyclicities above and below the Cretaceous/Paleogene boundary at Zumaya (N Spain), Agost and Relleu (SE Spain). *Sediment. Geol.*, **87**, 69–101.

Terlaky, V. and **Arnott, R.W.C.** (2014) Matrix-rich and associated matrix-poor sandstones: Avulsion splays in slope and basin-floor strata. *Sedimentology*, **61**, 1175–1197.

Tinterri, R. and **Muzzi Magalhaes, P.** (2011) Synsedimentary structural control on foredeep turbidites: An example from Miocene Marnoso-arenacea Formation, Northern Apennines, Italy. *Mar. Pet. Geol.*, **28**, 629–657.

Tinterri, R. and **Piazza, A.** (2019) Turbidites facies response to the morphological confinement of a foredeep (Cervarola Sandstones Formation, Miocene, northern Apennines, Italy). *Sedimentology*, **66**, 636–674.

Tinterri, R. and **Tagliaferri, A.** (2015) The syntectonic evolution of foredeep turbidites related to basin segmentation: Facies response to the increase in tectonic confinement (Marnoso-arenacea Formation, Miocene, Northern Apennines, Italy). *Mar. Pet. Geol.*, **67**, 81–110.

Toniolo, H., **Lamb, M.** and **Parker, G.** (2006) Depositional turbidity currents in diapiric minibasins on the continental slope: Formulation and theory. *J. Sediment. Res.*, **76**, 783–797.

Torres Carbonell, P.J. and **Olivero, E.B.** (2019) Tectonic control on the evolution of depositional systems in a fossil, marine foreland basin: Example from the SE Austral Basin, Tierra del Fuego, Argentina. *Mar. Pet. Geol.*, **104**, 40–60.

Tripsanas, E.K., **Bryant, W.R.** and **Phaneuf, B.A.** (2004) Slope-instability processes caused by salt movements in a complex deep-water environment, Bryant Canyon area, northwest Gulf of Mexico. *Am. Assoc. Pet. Geol. Bull.*, **88**, 801–823.

Trümpy, R. (1960) Paleotectonic evolution of the central and western Alps. *Bull. Geol. Soc. Am.*, **71**, 843–908.

Van Andel, T.H. and **Komar, P.D.** (1969) Ponded sediments of the Mid-Atlantic Ridge between 22 and 23 north latitude. *GSA Bull.*, **80**, 1163–1190.

Van Den Berg, J.H., **Van Gelder, A.** and **Mastbergen, D.R.** (2002) The importance of breaching as a mechanism of subaqueous slope failure in fine sand. *Sedimentology*, **49**, 81–95.

Van der Knaap, W. and **Eijpe, R.** (1968) Some experiments on the genesis of turbidity currents. *Sedimentology*, **11**, 115–124.

Vanossi, M. (ed) (1986) Atti del convegno sule tema, ‘geologia delle Alpi liguri’: Pavia, Alpi liguri, Genova, 11-16 giugno 1984.

Wade, B.S., **Pearson, P.N.**, **Berggren, W.A.** and **Pälike, H.** (2011) Review and revision of Cenozoic tropical planktonic foraminiferal biostratigraphy and calibration to the geomagnetic polarity and astronomical time scale. *Earth-Science Rev.*, **104**, 111–142.

Walker, R.G. (1967) Turbidite sedimentary structures and their relationship to proximal and distal depositional environments. *J. Sediment. Res.*, **37**, 25–43.

Wan, L., **Bianchi, V.**, **Hurter, S.** and **Salles, T.** (2020) Evolution of a delta-canyon-fan system on a typical passive margin using stratigraphic forward modelling. Mar Geol. doi: 10.1016/j.margeo.2020.106310

Warrick, J.A. and **Milliman, J.D.** (2003) Hyperpycnal sediment discharge from semiarid southern California rivers: Implications for coastal sediment budgets. *Geology*, **31**, 781–784.

Warrick, J.A., **Simms, A.R.**, **Ritchie, A.**, **Steel, E.**, **Dartnell, P.**, **Conrad, J.E.** and **Finlayson, D.P.** (2013) Hyperpycnal plume-derived fans in the Santa Barbara Channel, California. *Geophys. Res. Lett.*, **40**, 2081–2086.

Warrick, J.A., **Xu, J.**, **Noble, M.A.** and **Lee, H.J.** (2008) Rapid formation of hyperpycnal sediment gravity currents offshore of a semi-arid California river. *Cont. Shelf Res.*, **28**, 991–1009.

Watson, S.J., **Mountjoy, J.J.** and **Crutchley, G.J.** (2020) Tectonic and geomorphic controls on the distribution of submarine landslides across active and passive margins, eastern New Zealand. *Geol. Soc. London, Spec. Publ.*, **500**, 477–494.

Weaver, P.P.E., **Rothwell, R.G.**, **Ebbing, J.**, **Gunn, D.** and **Hunter, P.M.** (1992) Correlation, frequency of emplacement and source directions of megaturbidites on the Madeira Abyssal Plain. *Mar. Geol.*, **109**, 1–20.

Weimer, P. (2000) Deep-Water Reservoirs of the World: 20th Annual. *Society of Economic Paleontologists and Mineralogists*.

Weimer, P. and **Pettingill, H.S.** (2007) Deep-water exploration and production: A global overview. *T. Nilsen, R. D. Shew, G. S. Steffens, J. Studlick, eds., Atlas Deep. outcrops world AAPG Stud. Geol.*, **56**, 29.

Weirich, F.H. (1988) Field evidence for hydraulic jumps in subaqueous sediment gravity flows. *Nature*, **332**, 626–629.

Wentworth, C.K. (1922) A scale of grade and class terms for clastic sediments. *J. Geol.*, **30**, 377–392.

Wilson, P.A. and **Roberts, H.H.** (1995) Density cascading; off-shelf sediment transport, evidence and implications, Bahama Banks. *J. Sediment. Res.*, **65**, 45–56.

Winker, C.D. (1996) High-resolution seismic stratigraphy of a late Pleistocene submarine fan ponded by salt-withdrawal mini-basins on the Gulf of Mexico continental slope. In: *Offshore Technology Conference*, *OnePetro*,

Wolski, P. and **Murray-Hudson, M.** (2006) Flooding dynamics in a large low-gradient alluvial fan, the Okavango Delta, Botswana, from analysis …. *Hydrol. Earth Syst. Sci.*, **10**, 127–137.

Wright, L.D., **Wiseman Jr, W.J.**, **Yang, Z.-S.**, **Bornhold, B.D.**, **Keller, G.H.**, **Prior, D.B.** and **Suhayda, J.N.** (1990) Processes of marine dispersal and deposition of suspended silts off the modern mouth of the Huanghe (Yellow River). *Cont. Shelf Res.*, **10**, 1–40.

Wynn, R.B., **Cronin, B.T.** and **Peakall, J.** (2007) Sinuous deep-water channels: Genesis, geometry and architecture. *Mar. Pet. Geol.*, **24**, 341–387.

Yoshida, M., **Yoshiuchi, Y.** and **Hoyanagi, K.** (2009) Occurrence conditions of hyperpycnal flows, and their significance for organic-matter sedimentation in a Holocene estuary, Niigata Plain, Central Japan. *Isl. Arc*, **18**, 320–332.

Zavala, C. (2008) The Origin of Lofting Rhythmites - Lessons from Thin Sections. In: *JJ Ponce and EB Olivero, conveners, Sediment transfer from shelf to deepwater—Revisiting the delivery mechanisms: Conference Proceedings, AAPG Search and Discovery Article 50077*, 3–7.

Zavala, C., **Arcuri, M.** and **Blanco Valiente, L.** (2012) The importance of plant remains as diagnostic criteria for the recognition of ancient hyperpycnites. *Rev. Paleobiol.*, **31**, 457–469.

Zavala, C., **Arcuri, M.** and **Gamero, H.** (2006a) Towards a genetic model for the analysis of hyperpycnal systems. In: *Geological Society of America Abstracts with Programs*, 38, 541.

Zavala, C., **Arcuri, M.**, **Meglio, M. Di**, **Diaz, H.G.** and **Contreras, C.** (2011a) A Genetic Facies Tract for the Analysis of Sustained Hyperpycnal Flow Deposits. *Sediment Transf. from Shelf to Deep*

Water—Revisiting Deliv. Syst., **61**, 31–51.

Zavala, C., **Marcano, J.**, **Carvajal, J.** and **Delgado, M.** (2011b) Genetic Indices in Hyperpycnal Systems: A Case Study in the Late Oligocene–Early Miocene Merecure Formation, Maturin Subbasin, Venezuela. *Sediment Transf. from Shelf to Deep Water—Revisiting Deliv. Syst.*, **61**, 53–73.

Zavala, C. and **Pan, S.** (2018) Hyperpycnal flows and hyperpycnites: Origin and distinctive characteristics. *Lithol. Reserv.*, **30**, 1–27.

Zavala, C., **Ponce, J.J.**, **Arcuri, M.**, **Drittanti, D.**, **Freije, H.** and **Asensio, M.** (2006b) Ancient lacustrine hyperpycnites: A depositional model from a case study in the Rayoso Formation (Cretaceous) of west-central Argentina. *J. Sediment. Res.*, **76**, 41–59.

Zhang, L. and **Li, Y.** (2020) Architecture of deepwater turbidite lobes: A case study of Carboniferous turbidite outcrop in the Clare Basin, Ireland. *Pet. Explor. Dev.*, **47**, 990–1000.

Zijderveld, J.D.A. (1967) AC demagnetization of rocks: Analysis of results, Methods in Paleomagnetism DW Collinson, KM Creer, SK Runcorn, 254–286. *Elsevier, New York. Košler, J., Sláma, J., Belousova, E., Corfu, F., Gehrels, GE, Gerdes, A.,... Whitehouse, MJ (2013). U-Pb detrital zircon Anal. an inter-laboratory Comp. Geostand. Geoanalytical Res.*, **37**, 243–259.

Intentioanlly blank page

Appendix I

Appendix I provides the biostratigraphic review of planktonic foraminifera specimens of Gelati (1977) complete of Synonymzzzs and Geological range for each taxa. The review is based on Mikrotax database classifications (Huber *et al.*, 2016). At the end of the section is reported a summary table of taxa pointing out the original classification, reviewed classification, reviewed stratigraphic ranges, and associated references.

GLOBOROTALIA CERR. POMEROLI (in Gelati, 1977) -----> TURBOROTALIA POMEROLI (Current classification: Turborotalia pomeroli; Toumarkine & Bolli, 1970)

Reference:

http://www.mikrotax.org/pforams/index.php?dir=pf_cenozoic/Globanomalidae/Turborotalia/Turborotalia%20pomeroli

Synonyms:

- *Globorotalia centralis* Cushman and Bermúdez.—Howe, 1939:84, pl. 12: figs. 4-6 [Eocene, Cook Mountain Fm., Louisiana]. —Samanta, 1969:333, pl. 2: fig. 2a-c. [upper Eocene, Kapili Fm., Assam, India]. —Samanta, 1970 (partim), pl. 1: fig. 18 [middle Eocene *Orbulinoides beckmanni* Zone, Lakhpat Cutch, India]. [Not Cushman and Bermúdez, 1937.]
- *Globorotalia* (*Turborotalia*) *centralis* Cushman and Bermúdez.—Blow and Banner, 1962:117, pl. 12: figs. K-M [middle Eocene, Zone P15, Sample FCRM 1645, Lindi, Tanzania].—Blow, 1969:346, pl. 36: figs. 1-2. [middle Eocene, Zone P15, Sample FCRM. 1645, Lindi, Tanzania].—Blow, 1979:1052-1054, pl. 36: figs. 1-2 (re-illustration from Blow, 1969); pl. 173: fig. 9 [middle Eocene, Zone P11, Sample RS. 24, Kilwa, Tanzania]; pl. 190: figs. 1-5 [middle Eocene Zone P13, Sample RS. 311, Kilwa, Tanzania]; pl. 261, figs. 7-9 [middle Eocene Zone P13, Sample RS. 311, Kilwa, Tanzania, detail of organic pore linings]. [Not Cushman and Bermúdez, 1937.]
- *Turborotalia centralis* (Cushman and Bermúdez).—Nishi and Chaproniere, 1994:260, pl. 3: figs. 16-18 [upper Eocene Zone P15-P16, ODP Hole 841B, Tonga Trench, South Pacific Ocean]. [Not Cushman and Bermúdez, 1937.]
- ?*Globorotalia inflata* Hussey, 1943: pl. 29: figs. 4-5 [Eocene, Cane River Fm., La Salle Parish, Louisiana].
- ?*Globigerina subcorpulenta* Khalilov, 1956:248, pl. 4: figs. 5a-c [upper Eocene, Sovitabad, northern Azerbaijan]. ?*Globorotalia pseudomayeri* Bolli, 1957c:167, pl.37: figs. 17a,b [middle Eocene *Hantkenina aragonensis* Zone, Navet Fm., Trinidad].
- *Globorotalia cerroazulensis pomeroli* Toumarkine and Bolli, 1970:140, pl. 1: figs. 10-18 [middle Eocene, Possagno area, northern Italy].— Toumarkine, 1975:744, pl. 2: figs. 4-5 [middle Eocene *Globorotalia lehneri* Zone, DSDP Site 305, north-west Pacific Ocean].—Poore and Brabb, 1977:260, pl. 2: figs. 3-4 [middle Eocene Zone P14, San Lorenzo Fm., Santa Cruz Mountains, California].— Snyder and Waters, 1985:460, pl. 3: fig. 9-11 [middle Eocene Zones P13-P14, DSDP Site 549, Goban Spur, North Atlantic Ocean].
- *Globorotalia pomeroli* Toumarkine and Bolli.—Pujol 1983:652, pl. 662: fig. 3 [middle Eocene Zone P14, DSDP Hole 516F, Rio Grande Rise, Southwest Atlantic].
- *Turborotalia cerroazulensis pomeroli* (Toumarkine and Bolli).—Toumarkine and Luterbacher, 1985:137, figs. 34.9, 35.4-9 (re-illustrations from the literature).

- *Turborotalia pomeroli* (Toumarkine and Bolli).—Poore and Bybell, 1988:21, pl.1: fig. 9, pl. 2: figs. 8-9 [middle Eocene, Core ACGS#4, New Jersey]. —Coccioni and others, 1988, pl. 1: figs. 1-3 [upper Eocene Zone P15, Massignano, Italy].—Poag and Commeau, 1995, pl. 5: fig. 16-17, pl. 6: figs. 2-3 [Eocene, Salisbury Embayment, Virginia].
- *Globorotalia possagnoensis* Toumarkine and Bolli.— Pujol, 1983:652, pl. 662: fig. 3 [middle Eocene Zone P14, DSDP Sample 516F-52-4, 61-63 cm, Rio Grande Rise, Southwest Atlantic Ocean]. [Not Toumarkine and Bolli, 1970.]
- *Turborotalia possagnoensis* (Toumarkine and Bolli).—Poore and Bybell, 1988:21, pl. 2: figs. 4-7 [middle Eocene, Core ACGS#4, New Jersey]. [Not Toumarkine and Bolli, 1970.]
- Not *Globorotalia cerroazulensis pomeroli* Toumarkine and Bolli.—Toumarkine, 1978:710, pl. 6: figs. 6-9 [middle and upper Eocene, DSDP Site 363, Walvis Ridge, South Atlantic Ocean]. [=*Turborotalia* increbescens.]

- **Geological Range:**
  Notes: *Globigerinatheka mexicana* appears in the lower middle Eocene and its first occurrence was used to identify the base of Zone P11 (=E9) sensu Stainforth and others, 1975; Blow, 1979; Toumarkine, 1983. Although the appearance of *G. mexicana* is poorly calibrated it seems it occurs very close to that of *G. kugleri*. It ranges up to the topmost part of E14. [Premoli Silva et al. 2006]
  Last occurrence (top): within **E14** zone (35.89-37.99Ma, top in Priabonian stage). Data source: Premoli Silva et al. 2006 f7.1
  First occurrence (base): within **E9** zone (43.23-43.85Ma, base in Lutetian stage). Data source: Premoli Silva et al. 2006 f7.1

GLOBIGERINATHEKA MEX. MEXICANA (in Gelati, 1977) -----> GLOBIGERINATHEKA MEX. MEXICANA (Current classification: Cushman, 1925)

Reference:

http://www.mikrotax.org/pforams/index.php?dir=pf_cenozoic/Globigerinidae/Globigerinatheka/Globigerinatheka%20mexicana

Synonyms:

- *Globigerina mexicana* Cushman, 1925:61, pl. 1: figs. 8a-b [upper Eocene, *Tantoyuca* Fm., State of Vera Cruz, Mexico].
- *Globigerapsis mexicana* (Cushman).—Saito, 1962:219, pl. 34 (partim): figs. 6a-b (not 7a-c = *G. euganea*) [Eocene,
- *Hahajima*, Hillsborough Island, Japan].—Blow and Saito, 1968a:357-360, text-figs. 1-4 (refigured holotype). *Globigerinatheka mexicana mexicana* (Cushman).—Bolli, 1972:129, text-figs. 1-11 (1-2, refigured holotype; 3-6, holotype redrawn by Blow and Saito, 1968a) pl. 2 (partim): figs. 1-2, 4 (not pl. 2: fig. 3 = *G. kugleri*) [middle Eocene *O. beckmanni* Zone, Navet Fm., Pointe-à-Pierre, Trinidad].—McKeel and Lipps, 1975: pl. 2: ?figs. 2a-c [middle Eocene, Tyee Fm., Oregon Coast Range].— Toumarkine, 1975: pl. 4: figs. 3, 4 [middle Eocene *Globorotalia lehneri* to *Truncorotaloides* rohri Zone, DSDP Site 305, Shatsky Rise, north-west Pacific Ocean].—Poore and Brabb, 1977: pl. 4: figs. 1-2 [middle Eocene Zones P13-P14, San Lorenzo Fm., *California*].— Toumarkine, 1983: pl. 20 (partim): fig. 34 (from Bolli, 1972); pl. 20: fig. 39 (from Toumarkine, 1975); (not fig. 33 = *G. kugleri*; not figs. 35-38 = *G. subconglobata*). ?*Globigerinatheka mexicana mexicana* (Cushman).— Fleisher, 1974: pl. 8: fig. 5 [middle Eocene Zone P14, DSDP Site 219, Arabian Sea].

- *Globigerinatheka mexicana* (Cushman).—Stainforth and others, 1975: figs. 67.1-3, 5 (from Bolli, 1972); figs. 4a-d (refigured holotype from Blow and Saito, 1968a); (not fig. 67.6, from Bolli, 1972 = *G. kugleri*).
- *Porticulasphaera mexicana mexicana* (Cushman).—Blow, 1979: pl. 27: figs. 5-6 (new name for *G. tropicalis* of Blow, 1969); pl. 198 (partim): figs. 1, 3 (not figs. 2, 4-5 = *G. kugleri*) [middle Eocene Zone P13, Kilwa area, Tanzania].
- ?*Globigerinatheka mexicana* (Cushman).—Pujol, 1983: pl. 7: fig. 1 [middle Eocene Zone P11-13, DSDP Site 516, Rio Grande Rise, South Atlantic Ocean].
- *Globigerinatheka kutchensis* Singh and *Tewari*, 1967:425-426, fig. 1 [fide Blow, 1979:789, 872].
- ?*Globigerinatheka* ? sp. (cf. *Globigerinatheka barri* Brönnimann).—Samuel and Salaj, 1968: pl. 21: figs. 4a-b [middle Eocene ?*Truncorotaloides* rohri Zone, central Carpathians, *Slovakia*]. [Not Brönnimann, 1952.]
- *Globigerinatheka barri* Brönnimann. —*Samanta*, 1970: pl. 2: figs. 20-21 [middle Eocene *Orbulinoides beckmanni* Zone, Lakhpat, Cutch, India].—Toumarkine, 1971: pl. 3: figs., 1-4 [fig. 1, upper Eocene *Globigerapsis semiinvoluta* Zone; figs. 2-3, middle Eocene *Truncorotaloides* rohri Zone, *Halimba* borehole, Bakony, Hungary]. [Not Brönnimann, 1952.]
- *Globigerapsis tropicalis* Blow and Banner.—Blow, 1969: pl. 27: figs. 5-6 [middle Eocene Zone P13, Kilwa area, Tanzania]. [Not Blow and Banner, 1962.] *Globigerinoides kugleri* (Bolli, Loeblich and Tappan).— Mohan and Soodan, 1970: pl. 1: figs. 10a-b [middle Eocene *Globigerinoides kugleri* -*Globigerina frontosa* Zone, Kutch, India]. [Not Bolli, Loeblich and Tappan, 1957.]
- ?*Globigerinatheka index* (Finlay).—Berggren, 1992: pl. 3: fig. 7 [middle Eocene, ODP Hole 748B, Kerguelen Plateau, Indian Ocean]. [Not Finlay, 1939.]
- Not *Globigerina mexicana* Cushman.—Cushman, 1927: pl. 26: figs. 16, 17 [Mexico] (= *G. euganea*).
- Not *Globigerinoides mexicana* (Cushman).—Beckmann, 1953:395, pl. 25: figs. 15,16 (= *G. euganea*); figs. 17-19 (= *O. beckmanni*) [middle Eocene, Oceanic Fm., Barbados].
- Not *Porticulasphaera mexicana* (Cushman).—Bolli, Loeblich and Tappan, 1957:34-35, pl. 6: figs. 8-9b [middle Eocene *Orbulinoides beckmanni* Zone, Navet Fm., Trinidad].— Bolli, 1957:165, pl.37: figs. 1a-b [middle Eocene, *Orbulinoides beckmanni* Zone, Navet Fm., Trinidad] (= *O. beckmanni*).
- Not *Globigerinatheka mexicana mexicana* (Cushman).— Toumarkine, 1978: pl. 4: fig. 5 (= *G. subconglobata*), 6 and 7 (= *G. barri*) [middle Eocene *Hantkenina aragonensis* to *Globorotalia lehneri* Zone, DSDP Site 363, South Atlantic Ocean].—Nishi and Chaproniere, 1994: pl. 2: figs. 14-15, ?fig. 13 [upper Eocene Zones P15-16, DSDP Hole 841B, south-west Pacific Ocean] (= *G. index*).
- Not *Globigerapsis mexicana* (Cushman).—Blow, 1979:330, pl. 27: figs. 3-4 [upper Eocene Zone P15, Lindi area, Tanzania] (= *G. semiinvoluta*).—Baumann, 1970: pl. 3: fig. 4a-c [middle Eocene *Globigerapsis mexicana* Zone, Scalette Section, *Umbria*, central Italy] (= *G. tropicalis*).— Toumarkine, 1971: pl. 3: figs. 8-10 [upper Eocene *Globigerapsis semiinvoluta* Zone, *Halimba* borehole, Bakony, Hungary] (= *G. barri*). —*Postuma*, 1971:140, figs. on p. 141 [Trinidad] (= *G. semiinvoluta*).—Raju, 1971: pl. 11: figs. 1-6 [upper Eocene, Cauvery basin, India] (= *G. semiinvoluta*).

- **Geological Range:**
  Notes: *Globigerinatheka mexicana* appears in the lower middle Eocene and its first occurrence was used to identify the base of Zone P11 (=E9) sensu Stainforth and others, 1975; Blow, 1979; Toumarkine, 1983. Although the appearance of *G. mexicana* is poorly calibrated it seems it occurs very close to that of *G. kugleri*. It ranges up to the topmost part of E14. [Premoli Silva et al. 2006]
  Last occurrence (top): within **E14** zone (35.89-37.99Ma, top in Priabonian stage). Data source: Premoli Silva et al. 2006 f7.1
  First occurrence (base): within **E9** zone (43.23-43.85Ma, base in Lutetian stage). Data source: Premoli Silva et al. 2006 f7.1

GLOBIGERINATHEKA INDEX (in GELATI, 1977) ----> GLOBIGERINATHEKA INDEX (Current classification: Finlay, 1939)

Reference:

http://www.mikrotax.org/pforams/index.php?dir=pf_cenozoic/Globigerinidae/Globigerinatheka/Globigerinatheka%20index

Synonyms:

- *Globigerinoides index* Finlay, 1939:125 (partim), pl. 14: figs. 85-88 [middle Eocene, Bortonian stage, Hampden Section, New Zealand].—Hornibrook, 1958: pl. 1: figs. 11-13 (redrawn holotype), fig. 14 (redrawn paratype).
- *Globigerapsis index* (Finlay).—Blow and Banner, 1962: pl. 15 (partim): fig. G [middle Eocene, Kilwa district, Tanganyika] (not fig. H = *G. kugleri*).—Quilty, 1969, text-fig. 7, no. 42-48 [fide Bolli, 1972]. —Soldaini, 1970:67, pl. 5: figs. 1, 5 [upper Eocene *Globigerapsis semiinvoluta* Zone, Mor 1Well, Hungary].—Baumann, 1970: pl. 1: figs. 12a-c [middle Eocene *Globigerapsis subconglobata* Zone, Bottaccione Section, Gubbio, central Italy]. —Samanta, 1970: pl. 2: fig. 17, not fig. 16 [middle Eocene
- *Orbulinoides beckmanni* Zone, Lakhpat, Cutch. India].— Postuma, 1971:136, figs. on p. 137 [Eocene, Hampden Section, New Zealand].—Toumarkine, 1971: pl. 3: ?figs. 11, 12 [middle Eocene *Globorotalia lehneri* /*Hantkenina dumblei* Zone, *Halimba* borehole, Bakony Mountain, Hungary].—Blow, 1979: pl. 27: figs. 1, 2; pl. 192: fig. 1 [middle Eocene Zone P13, Kilwa Area, Tanzania]; pl. 174: ?fig. 1, figs. 2, 3, 4, 6, 8 [middle Eocene Zone P11, Kilwa Area, Tanzania]; pl. 181: fig. 1; pl. 183: ?figs. 1, 2 ; pl. 186: figs. 2, 3 [middle Eocene Zone P11, DSDP Site 19, Rio Grande Rise, South Atlantic Ocean].— Krasheninnikov and Basov, 1983: pl. 7: figs. 2-3, [upper Eocene, DSDP Site 512, Maurice Ewing Bank, South Atlantic Ocean]; pl. 7: figs. 4-5 [upper Eocene, DSDP Site 511, Falkland Plateau, South Atlantic Ocean].
- ?*Globigerapsis index* (Finlay).—Samuel and Salaj, 1968, text-fig. 38 [upper Eocene ?*Globigerina officinalis* Zone, *Magura* Flusch, *Bystrica* Unit, Kochanovce borehole, Slovakia].
- *Globigerinatheka* (*Globigerapsis*) *index index* (Finlay).— Jenkins, 1971:187-188, pl. 22: figs. 641-643 (redrawn holotype), fig. 644 (redrawn paratype), fig. 645 [middle Eocene *Globigerinatheka* (*Globigerapsis*) *index index* Zone, Bortonian stage, Hampden Section, New Zealand].
- *Globigerinatheka index index* (Finlay).—Bolli, 1972:124 (partim), text-figs. 51-57 (redrawn Finlay's type specimens), not text-figs. 63-64; pl. 1: ?fig. 1, figs. 3-4, not figs. 6-7 = *G. subconglobata* [middle Eocene *Globigerinatheka subconglobata subconglobata* Zone, Possagno Section, northern Italy].—Fleisher, 1974: pl. 8: fig. 6 [middle Eocene Zone P11, DSDP Site 220, Arabian Sea].—McKeel and Lipps, 1975: pl. 3: figs. 5a-c; pl. 5: figs. 1a-c [upper Eocene, Bastendorff Fm., Oregon Coast Range].—Toumarkine, 1975: pl. 4: figs. 6, 7 [upper Eocene *Globigerinatheka semiinvoluta* Zone, DSDP Site 305, Shatsky Rise, northwest Pacific Ocean].— Toumarkine, 1978: pl. 5:, figs. 3-5, 7-9, ?figs. 1, 6 [fig. 3, middle Eocene *Orbulinoides beckmanni* Zone; figs. 2-9, middle Eocene *Truncorotaloides rohri* Zone, DSDP Site 363, South Atlantic Ocean].—Toumarkine, 1983: pl. 19: figs. 20-21 [upper Eocene *Globigerinatheka semiinvoluta* Zone, DSDP Site 305, Shatsky Rise, northwest Pacific Ocean]; figs. 22-24 [middle Eocene *Truncorotaloides rohri* Zone, DSDP Site 363, South Atlantic Ocean].—Poag and Commeau, 1995: pl. 5: fig. 27 [upper Eocene Zone P15, Exmore core, Salisbury Embayment, Virginia-Maryland].
- *Globigerinatheka index* (Finlay).—Stainforth and others, 1975: figs. 56.1, 3, ?fig. 56.2 (from Bolli, 1972); fig. 56.6 (from Blow and Banner, 1962).—Snyder and Waters, 1985: pl. 5: fig. 3 [DSDP Hole 548A, Goban Spur, eastern North Atlantic Ocean]; ?fig. 4 [DSDP Hole 548A, Goban Spur, eastern North Atlantic Ocean]. —Coccioni and others, 1988: pl. 1: figs. 11, 12 [upper Eocene Zone P16, Massignano Section, Marche, central Italy]. —Nocchi and others, 1988: pl. VI: figs. 8a,b [upper Eocene Zone P16, Section PMI, Umbria, central Italy]. —Premoli

Silva and Spezzaferri, 1990: pl.1: figs. 8b,c [upper Eocene Zones P15/P17, ODP Hole 709C, Indian Ocean].—Huber, 1991:440, pl. 7: fig. 17, ?fig. 22 [middle Eocene, ODP Hole 738B, Kerguelen Plateau, Indian Ocean]. —Nocchi and others, 1991: pl. 4: ?figs. 17-19 [middle Eocene Zone P11, ODP Hole 702B, South Atlantic Ocean]; figs. 20-22 [middle Eocene Zone P12, ODP Hole 702B, South Atlantic Ocean].—Van Eijden and Smit, 1992: pl. 3: fig. 8, ?fig. 7 [middle Eocene Zones P13-P14, ODP Hole 752A, Broken Ridge, Indian Ocean].—Berggren, 1992: pl. 3 (partim): figs. 10-11 (not fig. 9 = *G. luterbacheri*) [middle Eocene, ODP Hole 748B, (figs. 9-11, 16H-5, 40-44 cm), Kerguelen Plateau, Indian Ocean].

- *Globigerina index* (Finlay).—Stott and Kennett, 1990:559, pl. 7: fig. 8 [middle Eocene Zone AP6, ODP Hole 690B, Maud Rise, Antarctic Ocean].
- *Globigerinatheka* sp. cf. *G. index* (Finlay).—Van Eijden and Smit, 1992: pl. 3 (partim): fig. 4, ?fig. 5 [fig. 4, lower middle Eocene Zones P10-P12, ODP Hole 752A; fig. 5, middle Eocene Zones P13-P14, ODP Hole 752A, Broken Ridge, Indian Ocean] (not fig. 9).
- ?*Globigerinatheka index* (Finlay).—V an Eijden and Smit, 1991: pl. 3: fig. 6 [middle Eocene Zones P13-P14, ODP Hole 752A, Broken Ridge, Indian Ocean].
- *Globigerinoides macrostoma* Hagn, 1956:173, pl. 16: fig. 11a-b [upper Eocene, Varignano, Lake Garda, northern Italy]. *Globigerinoides conglobatus* (Brady). —Shutskaya, 1958: pl. 2: fig. 1 [upper Eocene, fig. 1, Khieu River, Nalchik region], fig. 2 [Belaya River, Maikop district, Caucasus]. [Not Brady, 1879.]
- *Globigerapsis* aff. *semiinvoluta* (Keijzer). —Soldaini, 1970:67, pl. 5: figs. 4a,c [upper Eocene *Globigerapsis semiinvoluta* Zone, Mo_r 1Well, Hungary]. [Not Keijzer, 1945.]
- *Globigerinatheka mexicana mexicana* (Cushman).—Nishi and Chaproniere, 1994: pl. 2: figs. 14-15, ?fig. 13 [upper Eocene Zones 15-16, DSDP Hole 841B, south-west Pacific Ocean]. [Not Cushman, 1925.]
- Not *Globigerinoides index* Finlay.—Beckmann, 1953: pl. 25: fig. 14 [upper Eocene, Oceanic Fm., Barbados] (= *G. semiinvoluta*).—Hagn, 1956:172, pl. 16: figs. 6-8 (= *G. tropicalis*).
- Not *Globigerapsis index* (Finlay).—Bolli, 1957:165, pl. 36: figs. 14a,b-18b (= *G. subconglobata*).—Todd, 1966: pl. 2: figs. 1a-1c (= *G. curryi*).—Samuel and Salaj, 1968: pl. 21: figs. 2a-c (= *G. tropicalis*).—Blow, 1969: pl. 27: figs. 1-2 (= *G. korotkovi*). —Samanta, 1970: pl. 2: fig. 16 (= *G. barri*).—Blow, 1979: pl. 174: figs. 5, 7.—Krasheninnikov and Basov, 1983: pl. 7: fig. 1.
- Not *Globigerinatheka index* (Finlay).—Stainforth and others, 1975: fig. 56.4 [from Blow and Banner, 1962]; figs. 56.5,7,9 [from Bolli, 1972]; figs. 56.8a-b [from Blow, 1969].
- Not *Globigerinatheka index index* (Finlay).—Berggren, 1992: pl. 3: figs. 5-6 (= *G. tropicalis*); ?fig. 8 (= *G. korotkovi*) [middle Eocene, ODP Hole 748B, Kerguelen Plateau, Indian Ocean].—Nishi and Chaproniere, 1994: pl. 2: figs. 4-6 (= *G. tropicalis*), figs. 22-24 (= *G. luterbacheri*) [upper Eocene Zones P15-16, DSDP Hole 841B, south-west Pacific Ocean].

- **Geological Range:**
  Notes: Described from the middle Eocene of New Zealand, the extinction of *G. index* has been used for approximating the upper boundary of the Eocene at the high southern latitudes (Jenkins, 1971). It appears in upper E9. At middle latitudes *G. index* decreases in abundance in mid Zone E15 and disappears at the E15/E16 boundary (Berggren and Pearson, Chapter 2, this volume). [Premoli Silva et al. 2006]
  The LAD of *Globigerinatheka index* marks the base of zone E16 / top of E15 (Wade et al. 2011)
  Last occurrence (top): at top of **E15** zone (100% up, 34.7Ma, in Priabonian stage). Data source: zonal marker (Wade et al. 2011)
  First occurrence (base): in upper part of **E9** zone (80% up, 43.4Ma, in Lutetian stage). Data source: Premoli Silva et al. 2006 f7.1

GLOBIGERINATHEKA SEMIINVOLUTA (in GELATI, 1977) -----> GLOBIGERINATHEKA SEMIINVOLUTA (Current classificiation: Keijzer, 1935)

Reference:

http://www.mikrotax.org/system/index.php?dir=pf_cenozoic/Globigerinidae/Globigerinatheka/Globigerinatheka%20semiinvoluta

Synonyms:

- *Globigerinoides* semi-involutus Keijzer, 1945:206, pl. 4: figs. 58a-e (holotype) [upper Eocene, San Luis Fm., Guantanamo Basin, Cuba].
- *Globigerapsis semiinvoluta* (Keijzer).—Bolli, Loeblich and Tappan, 1957:34, pl. 6: figs. 7a-c [upper Eocene, Navet Fm., Trinidad].—Bolli, 1957:165, pl. 36: figs. 19-20 (hypotypes) [upper Eocene *Globigerapsis semiinvoluta* Zone, Navet Fm., Trinidad].
- *Globigerapsis semi-involuta* (Kejizer).—Blow and Banner, 1962:125, pl. 15: figs., J-K, ?L [upper Eocene *Globigerapsis semi-involuta* Zone, Lindi area, Tanzania].
- *Globigerapsis semiinvoluta* (Keijzer).—Samuel and Salaj, 1968: pl. 21: figs. 3a-c [upper Eocene *Globigerapsis index* Zone, Kravany, Carpathians, *Slovakia*].
- *Globigerinatheka semiinvoluta* (Keijzer).—Bolli, 1972:131, pl. 5: figs. 1-27, pl. 6: figs. 1-17 [upper Eocene *Globigerinatheka semiinvoluta* Zone type locality, Navet Fm., Trinidad]; text-figs. 72-76 (redrawn holotype), text-figs. 77-78 (from Bolli and others, 1957); text-fig. 79 (from Blow and Banner, 1962).—Stainforth and others, 1975:223-225, figs. 83-1-2, 6 [upper Eocene, Navet Fm., Trinidad]; figs. 83.3-4 (from Bolli, 1972); figs. 83.5,7 (refigured from Blow and Banner, 1962).—Toumarkine, 1975, pl. 4: ?figs. 17, 18 [upper Eocene *Globigerinatheka semiinvoluta* Zone, DSDP Site 305, Shatsky Rise, north-west Pacific Ocean].—Toumarkine and Bolli, 1975: pl. 6: figs. 15-24 [upper Eocene *Globigerinatheka semiinvoluta* Zone, Possagno Section, northern Italy].— Toumarkine, 1978: pl. 5: figs. 1-14 [upper Eocene *Globigerinatheka semiinvoluta* Zone, DSDP Site 363, South Atlantic Ocean]; pl. 5: figs. 15-21 [upper Eocene *Globorotalia cerroazulensis* s.l. to *Globigerinatheka semiinvoluta* Zone, DSDP Site 360, South Atlantic Ocean].—Salaj, 1980: pl. 27: ?fig.11 [middle Eocene ?Zone P15, Bartonian, Dj. Fkirine, *Tunisia*].— Toumarkine, 1983: pl. 20: figs. 1 [upper Eocene, Menton, Southern France]; fig. 2 [upper Eocene *G. semiinvoluta* Zone, Contes Section, Southern France]; figs. 3-4 [upper Eocene *G. semiinvoluta* Zone, Possagno Section, northern Italy]; fig. 7 [upper Eocene *G. semiinvoluta* Zone, DSDP Site 522, South Atlantic Ocean]; figs. 8-11 (from Bolli, 1972); figs. 12-14 [upper Eocene *G. semiinvoluta* Zone, DSDP Site 363, South Atlantic Ocean]. —*Coccioni* and others, 1988: pl. 1: fig. 10 [upper Eocene Zone P15, Massignano Section, Marche, Italy]. —Premoli Silva and Spezzaferri, 1990: pl.2: figs. 4a,c [upper Eocene Zones P15/P17, ODP Hole 709C, Indian Ocean]. —Nocchi and others, 1991: pl. VI: fig. 11 [upper Eocene Zone P15, *Umbria*, central Italy].—Poag and Commeau, 1995: pl. 5: fig. 14 [upper Eocene Zone P15, Exmore core, Salisbury Embayment, Virginia-Maryland].
- *Porticulasphaera semiinvoluta* (Keijzer).—Blow, 1979: pl. 27: figs. 3-4 (new name for *Globigerapsis mexicana* of Blow, 1969); pl. 240: figs. 9-10 [upper Eocene Zone P15, Lindi area, Tanzania]. —*Molina* and others, 1986: pl. 1: figs. 6a-b [upper Eocene *Porticulasphaera semiinvoluta* Zone, Fuente *Caldera* Section, south-east Spain].
- ?*Globigerinatheka semiinvoluta* (Keijzer).—Pujol, 1983: pl. 8: fig. 7, ?fig. 8 [upper Eocene Zone P15-16, DSDP Hole 516F, Rio Grande Rise, South Atlantic Ocean].
- *Globigerinatheka* cf. *semiinvoluta* (Keijzer).—Nishi and Chaproniere, 1994: pl. 2: figs. 19-21 [upper Eocene Zones P15-P16, ODP Hole 841B, south-west Pacific Ocean].
- *Globigerinoides index* Finlay.—Beckmann, 1953: pl. 25: fig. 14 [upper Eocene, Oceanic Fm., Barbados]. [Not Finlay, 1939.]
- *Globigerapsis mexicana* (Cushman).—Blow, 1969:330, pl. 27: figs. 3-4 [upper Eocene Zone P15, Lindi area, Tanzania]. —*Postuma*, 1971, figs. at p. 141 [Trinidad].— Raju, 1971: pl. 11: figs. 1-6 [upper Eocene, Cauvery basin, *S. India*]. [Not Cushman, 1925.]

- Not *Globigerapsis semiinvoluta* (Keijzer).—Eckert, 1963:1063, pl. 7: figs. 1a-3c [upper Eocene, Schimberg Section, Swiss Alps] (= *G. luterbacheri*).
- Not *Globigerinatheka* (*Globigerapsis*) *semiinvoluta* (Kejizer).—Jenkins, 1971:188, pl. 21: figs. 633-634 [upper Eocene, upper type Runangan, Port Elisabeth Section, New Zealand] (= *G. tropicalis*).
- Not *Globigerinatheka* cf. *semiinvoluta* (Keijzer).—Miller and others, 1991:35, Appendix 1: figs. 1-8 [upper Eocene Zone P15, DSDP Site 612, western North Atlantic] (= *G. tropicalis*).
- **Geological Range:**
  Notes: *Globigerinatheka semiinvoluta* evolved in the latest middle Eocene. The first forms occur just below the top of Zone E13 and its extinction marks the base of Zone E15. [Premoli Silva et al. 2006]
  Last occurrence (top): at top of **E14** zone (100% up, 35.9Ma, in Priabonian stage). Data source: zonal marker (Wade et al. 2011)
  First occurrence (base): within **E13** zone (37.99-39.97Ma, base in Bartonian stage). Data source: Premoli Silva et al. 2006 f7.1

PSEUDOHASTIGERINA BARBADOENSIS (in GELATI, 1977) -----> PSEUDOHASTIGERINA NAGUEWICHIENSIS (Current classification: Myatliuk, 1950)

Reference:

http://www.mikrotax.org/pforams/index.php?id=100265

Synonyms:

- *Globigerinella naguewichiensis* Myatliuk, 1950:281, pl. 4, figs. 4 a, b [Oligocene, Chechva River, Lopanetskie layer, western Ukraine].—Subbotina, 1953:124, pl.13, fig. 18a, b [re-illustration of holotype].
- *Pseudohastigerina naguewichiensis* (Myatliuk).—Blow, 1969:377, pl. 53, figs. 2, 3 [Oligocene Zone P18, Red Bluff Clay type locality, Mississippi (originally stated as Alabama)].
- *Pseudohastigerina naguewichiensis* (Myatliuk).—Blow, 1969:377, pl. 53: figs. 2, 3 [Oligocene Zone P18, Red Bluff Clay type locality, Mississippi (originally stated as Alabama)].—Blow, 1979:1189, pl. 53: figs. 2, 3 (reproduction of Blow, 1969, pl. 53: figs. 2, 3).— Toumarkine and Luterbacher, 1985:119, fig. 21: 10a, b (reillustration of holotype), fig. 21: 11, 12 [lower Oligocene Marnes a_ Foraminife_res, Vacherie, Haute-Savoie, France]; fig. 21: 13-16 (13, 16 reillustration of Toumarkine, 1975; pl 3: figs. 13, 14 identified as *Pseudohastigerina barbadoensis* Blow) [Oligocene Zone P18, DSDP Site 313, Central Pacific Ocean]. —Spezzaferri and Premoli Silva, 1991:257, pl. 14: figs. 1a-2c, 5a-c [Oligocene Zone P19, DSDP Hole 538A, Gulf of Mexico]. —Olsson and Hemleben, 2006:424-426, pl. 14.3, figs. 1, 2 [holotype of *P. barbadoensis* Blow [Oligocene Zone P19, Cipero Fm., Trinidad], figs. 3, 4, 6-8 [Zone E15/16, Shubuta Clay Member, Yazoo Fm., Chicksawhay River, Wayne County, Mississippi], figs. 5, 9 [Zone O1, TDP Site 11, Stakishari, Tanzania], fig. 10 [upper Eocene, Atlantic City borehole, New Jersey, ODP 150X, 1338.0-.1 feet].—Wade and Olsson, 2009, pl. 1, figs. a, b [lower Oligocene Zone O1, St. Stephen's Quarry, Alabama], fig. c [upper Eocene Zone E16, St. Stephen's Quarry, Alabama], figs. d, e [lower Oligocene Zone O1, TDP Site 11].—Pearson and Wade, 2015:23, fig. 26.8 [lower Oligocene Zone O1, TDP Site 12, Stakishari, Tanzania], fig. 26.9, 26.11 (reproduced from Olsson and Hemleben, 2006, pl. 14.3, figs. 9, 5), 26.10 [lower Oligocene Zone O1, TDP Site 17, Stakishari, Tanzania].
- *Pseudohastigerina* cf. *P. naguewichiensis* (Myatliuk).—Leckie and others, 1993:125, pl. 6, figs. 18, 19 [lower Oligocene Zone P18, ODP Hole 628A, western North Atlantic Ocean, and Hole 803D, western equatorial Pacific Ocean].

- *Pseudohastigerina naguewichiensis naguewichiensis* (Myatliuk).—Blow, 1979:1189, pl. 246: fig. 1 [Oligocene Zone P18, DSDP Site 14, South Atlantic Ocean], figs. 3, 4 [Oligocene Zone P18, base of Red Bluff Clay, type locality, Mississippi].
- *Pseudohastigerina barbadoensis* Blow, 1969:409, pl. 53: figs. 7-9 (figs. 7, 8 holotype; fig. 9 paratype) [Oligocene Zone P19, Cipero Fm., southern Trinidad]; pl. 54: figs. 1-3, paratypes [Oligocene Zone P19, Cipero Fm., southern Trinidad].—Toumarkine, 1975:746, pl. 3: figs. 13, 14 [Oligocene Zone P18, DSDP Site 313, Central Pacific Ocean]. —Spezzaferri and Premoli Silva, 1991:257, pl. 13: fig. 3a-b [Oligocene Zone P19, DSDP Hole 538A, Gulf of Mexico].—Nishi and Chaproniere, 1994:259, pl. 1: figs. 28, 29 [upper Eocene, ODP Hole 841B, Tonga Trench, South Pacific Ocean].
- *Pseudohastigerina naguewichiensis barbadoensis* Blow, 1979:1190, pl. 53: figs. 7-9; pl. 54: figs. 1-3 (reproduction of Blow, 1969, pl. 53: figs. 7-9; pl. 54: figs. 1-3), pl. 246: figs. 2, 6 [Oligocene Zone P18, DSDP, Site 14, South Atlantic Ocean]; pl. 246: fig. 7 [Oligocene Zone P18, base of Red Bluff Clay type locality, Mississippi]. [NB the synonymies from the Olig and Eocene Atlases have been merged here]
- **Geological Range:**
  Notes: Zone E14 (Cotton and others, 2017) to O1 (Bolli, 1957; Leckie and others, 1993; Pearson and Chaisson, 1997; Berggren and Pearson, 2005; see also comments under Genus *Pseudohastigerina*, above). [Pearson et al. 2018] The LAD of *Pseudohastigerina naguewichiensis* marks the base of zone O2 / top of O1 (Wade et al. 2011)
  Last occurrence (top): at top of **O1** zone (100% up, 32.1Ma, in Rupelian stage). Data source: zonal marker (Wade et al. 2011)
  First occurrence (base): at base of **E15** zone (0% up, 35.9Ma, in Priabonian stage). Data source: Olsson & Hemleben (2006) fig 14.1

HANTKENINA ALABAMENSIS (in GELATI, 1977) -----> HANTKENINA ALABAMENSIS (Current classification: Cushman, 1924)

http://www.mikrotax.org/pforams/index.php?dir=pf_cat/H/Hantkenina/Hantkenina%20alabamensis

Synonyms:

- *Hantkenina alabamensis* Cushman, 1924:3, pl. 1: figs. 1-6; pl. 2: fig. 5 [Eocene, Zeuglodon bed, Cocoa Post Office, Alabama].—Rey, 1939:325, pl. XXII: fig. 17 [upper Eocene and lower Oligocene, Nummulitique du Rharb, Morocco].
- *Hantkenina* (*Hantkenina*) *alabamensis* Cushman.— Thalmann, 1942:811, pl. 1: figs. 3a-e [refigured type material, Eocene, Zeuglodon bed, Cocoa Post Office, Alabama].—Ramsay, 1962:84, pl. 16: figs. 16, 17 [upper Eocene, Kitunda bluffs, Lindi, Tanzania].
- *Hantkenina* (*Hantkenina*) *thalmanni* Brönnimann, 1950:415, pl. 55: figs. 19-24; pl. 56: figs. 3, 11 [upper Eocene, San Fernando Group, Trinidad].
- *Hantkenina* (*Hantkenina*) *suprasuturalis* Brönnimann, 1950:416, pl. 56: figs. 12-13 [upper Eocene, Oceanic Fm., Barbados].
- *Hantkenina suprasuturalis* Brönnimann. —Samanta, 1969, pl. 3: fig. 2a [*Globorotalia cerroazulensis* Zone, Kopili Fm., Assam, India].— Coccioni, 1988:86, pl. 1: figs. 12-13; pl. 2: figs. 1-8 [upper Eocene, Massignano stratotype section, Italy].
- *Hantkenina* (*Hantkenina*) *australis* Finlay.—Brönnimann, 1950: 413, pl. 56: fig. 20, 21 [upper Eocene, Oceanic Fm., Barbados]. [Not Finlay, 1939.]
- *Hantkenina australis* Finlay.—Ramsay, 1962:83, pl. 16: fig. 10 [middle Eocene, Kilwa Masoko area, Tanganyika]. [Not Finlay, 1939.]

- Not *Hantkenina alabamensis* Cushman. —Coccioni, 1988:85, pl. 1: figs. 1-9 [upper Eocene, Massignano stratotype section, Italy] [=*Hantkenina primitiva*].
- **Geological Range:**
  Notes: Lower Zone E13 to the Eocene/Oligocene boundary. [Coxall & Pearson 2006]
  The LAD of *Hantkenina alabamensis* marks the base of zone O1/ top of E16 (Wade et al. 2011)
  Last occurrence (top): at top of **E16** zone (100% up, 33.9Ma, in Priabonian stage). Data source: zonal marker (Wade et al. 2011)
  First occurrence (base): near base of **E13** zone (10% up, 39.8Ma, in Bartonian stage). Data source: Coxall & Pearson (2006), fig. 8.1

GLOBOROTALIA CERR. CERROAZULENSIS (in GELATI, 1977) -----> TURBOROTALIA CERROAZULENSIS (Current classification: Cole, 1928)

Reference:

http://www.mikrotax.org/pforams/index.php?dir=pf_cenozoic/Globanomalidae/Turborotalia/Turborotalia%20cerroazulensis

Synonyms:

- *Globigerina* cerroazulensis Cole, 1928:217, pl. 32: figs. 11-13 [upper Eocene, Chapapote Fm., Mexico].
- *Globorotalia cerroazulensis* cerroazulensis (Cole).— Toumarkine and Bolli, 1970:144, pl. 1: figs. 19-24 [upper Eocene, Possagno area, Italy].—Toumarkine, 1975:744, pl. 2: fig. 6 [upper Eocene *Globigerinatheka semiinvoluta* Zone, DSDP Site 305, northwest Pacific Ocean].—Poore and Brabb, 1977:260, pl. 2: figs. 3-4 [middle Eocene Zone P14, San Lorenzo Fm., Santa Cruz Mountains, California].—Toumarkine, 1978:710, pl. 6: figs. 10-12 [middle Eocene *Truncorotaloides rohri* Zone, DSDP Site 363, Walvis Ridge, South Atlantic Ocean].—Snyder and Waters, 1985:460, pl. 3: figs. 6-8 [upper Eocene Zones P16-P17, DSDP Hole 549A, Goban Spur, North Atlantic Ocean.]
- *Globorotalia* (*Turborotalia*) *cerroazulensis* (Cole).—Blow, 1979:1054-1058 (partim), pl. 242: figs. 1-7 [upper Eocene Zone P15, Sample FCRM. 1644, Lindi, Tanzania].
- *Globorotalia cerroazulensis* (Cole).—Pujol, 1983:651, pl. 10: fig. 1 [upper Eocene Zone P15-P16, DSDP Hole 516F, Rio Grande Rise, southwest Atlantic Ocean].
- *Turborotalia cerroazulensis* cerroazulensis (Cole).— Toumarkine and Luterbacher, 1985:137, figs. 34.3-4, 36.16-18 (re-illustrations from the literature).— Nishi and Chaproniere, 1994:260 (partim), pl. 3: fig. 19-21 [upper Eocene Zone P15-P16, ODP Hole 841B, Tonga Trench, South Pacific Ocean].
- *Turborotalia cerroazulensis* (Cole).—Poore and Bybell, 1988:21, pl. 2: figs. 10-12 [upper Eocene, Core ACGS#4, New Jersey].—Poag and Commeau, 1995:pl. 7: figs. 1-2 [Eocene, Salisbury Embayment, Virginia].
- *Globorotalia cocoaensis* Cushman.—Cushman, 1946:38, pl. 7: figs. 14-16 [upper Eocene, Cocoa Sand member, Jackson Fm., Clarke County, Alabama]. [Not Cushman, 1928.]
- *Turborotalia cocoaensis* (Cushman).—Poore and Bybell, 1988:20, pl. 1: figs. 10-12 [upper Eocene, Core ACGS#4, New Jersey]. [Not Cushman, 1928.]
- *Globorotalia centralis* Cushman and Bermúdez, 1937:26, pl. 2: figs. 62-65 [Eocene, Santa Clara Province, Cuba].— Hamilton, 1953:229, pl. 32: fig. 8 [Eocene, Mid-Pacfic Ocean].—Colom, 1954:186-187, pl. 11: figs. 18-23 [upper Eocene, Alicante, Spain].—Bolli and others, 1957:41-42, pl. 10: fig. 4a-c [Eocene, Santa Clara Province, Cuba; re-illustration of holotype, in three views].—Bolli, 1957c:169, pl. 39: figs. 1-4 [Eocene Navet and San Fernando Fms, Trinidad].—Todd, 1957, pl. 71: figs. 1a-c [upper Eocene Hagman and Densinyama Fms,

Saipan, Mariana Islands].—Sourdillon, 1960, pl. 2: figs. 29-31 [upper Eocene, Landes, France].—Asano, 1962:57, pl. 19: figs. 3a-c [Eocene, Kyoragi Fm., Amakusa Islands, Kyushu, Japan].—Saito, 1962:213-214, pl. 33: figs. 1a-3 [middle Eocene, Haha-Jima, Bonin Islands, Western Pacific Ocean].—Aubert, 1962:59, pl. 3: fig 2a-c [Upper Lutetian-Bartonian, Morocco]. —Samanta, 1970:203 (partim), pl. 1: fig. 19 [middle Eocene *Orbulinoides beckmanni* Zone, Lakhpat Cutch, India].

- *Globorotalia* (*Turborotalia*) *centralis* Cushman and Bermúdez.—Cushman and Bermúdez, 1949:44-45, pl. 8: figs. 19-21 [lower upper Eocene, Jabaco Fm, Havana Province, Cuba].—Eckert, 1963:1062-1063, pl. 6: figs. 1a-3c [upper Eocene *Globigerapsis semiinvoluta* Zone, Mount Pilatus, central Switzerland].
- *Acarinina centralis* (Cushman and Bermúdez). — Subbotina, 1953:237-239 (partim), pl. 25: figs. 24a-25c [upper Eocene, Northern Caucasus and Mangyshlak Peninsula, USSR]. —Liszka, 1957:183, pl.9: fig. 11 [upper Eocene, Grabno, Poland]
- *Turborotalia centralis* (Cushman and Bermúdez).—Hagn, 1956:396, pl. 15: figs. 8a-b [upper Eocene, Northern Italy].—Bermúdez, 1961:1317-1319, pl. 17: figs. 5-7 [upper Eocene Jacabo Fm., Cuba].—Hofker, 1962:106, figs. 38a-41c [upper Eocene, Rohrdorf, Bavaria, Germany].—Gohrbandt, 1963:109-110, pl. 7: figs. 10a-c [upper Eocene, Reingruber series, lower Austria].

- **Geological Range:**
  Notes: Middle Eocene, lower Zone E11 (Toumarkine and Bolli, 1970) to just below the Eocene/Oligocene boundary (within Zone E16) (Coccioni and others, 1988). [Pearson et al. 2006]
  Last occurrence (top): in upper part of **E16** zone (80% up, 34.1Ma, in Priabonian stage). Data source: Pearson et al. (2006), fig. 15.1
  First occurrence (base): in lower part of **E11** zone (30% up, 41.4Ma, in Lutetian stage). Data source: Pearson et al. (2006), fig. 15.1

GLOBOROTALIA CERR. COCOAENSIS (in GELATI, 1977) -----> TURBOROTALIA COCOAENSIS (Current classification: Cushman, 1928)

Reference:

http://www.mikrotax.org/pforams/index.php?dir=pf_cenozoic/Globanomalidae/Turborotalia/Turborotalia%20cocoaensis

Synonyms:

- *Globorotalia cocoaensis* Cushman, 1928:75, pl. 10: figs. 3a-c [upper Eocene, Cocoa Sand, Choctaw County, Alabama].—Howe and Wallace, 1932:75-76, pl. 14: fig. 4 [upper Eocene, Jackson Fm., Danville Landing, *Lousiana*].—Cushman, 1935:50, pl. 21: figs. 1a-3c [upper Eocene, south-eastern USA].—Bandy, 1949:79-80, pl. 12: fig. 1a-c [upper Eocene, Jackson Fm., Little Stave Creek, Clarke County, Alabama].—Bolli, 1957c:169, pl. 39: figs. 5a-7b [upper Eocene, Navet and San Fernando Fms., Trinidad].—Aubert, 1962:59-60, pl. 3: fig. 3a-c [Bartonian, Morocco].—Eckert, 1963:1063, pl. 6: figs. 4a-5d [upper Eocene *Globigerapsis semiinvoluta* Zone, Mount Pilatus, Switzerland].—Pujol, 1983:651, pl. 10: fig. 1 [upper Eocene Zone P15-P16, DSDP Hole 516F, Rio Grande Rise, Southwest Atlantic].
- *Globorotalia cerroazulensis* cocoaensis Cushman.— Toumarkine and Bolli, 1970:144, pl. 1: figs. 28-33 [upper Eocene, Possagno area, Italy].—Toumarkine, 1975:744, pl. 2: fig. 7 [upper Eocene *Globigerinatheka semiinvoluta* Zone, DSDP Site 305, north-west Pacific Ocean].—Poore and Brabb, 1977:259, pl. 2: figs. 8-9 [upper Eocene Zone P16, San Lorenzo Fm., Santa Cruz Mountains, California].—Toumarkine, 1978:710, pl. 6: figs. 13-15 [upper Eocene *Globigerinatheka semiinvoluta* Zone, DSDP Site 363, Walvis Ridge, South Atlantic Ocean].—Snyder and Waters, 1985:460, pl. 3: figs. 3-5 [upper Eocene Zone P17, DSDP Hole 549A,

Goban Spur, North Atlantic Ocean].—Nishi and Chaproniere 1994:260 (partim), pl. 3: fig. 25-30 [upper Eocene Zone P15-P16, ODP Hole 841B, Tonga Trench, South Pacific Ocean].

- *Turborotalia cerroazulensis* cocoaensis (Cushman).— Toumarkine and Luterbacher, 1985:138, figs. 34.2, 36.7-12 [re-illustrations from the literature].
- ?*Globorotalia bonairensis* Pijpers, 1933:73, figs. 107-110 [upper Eocene, Columbia Plantation, Bonaire Island, West Indies].
- *Globorotalia armenica* Saakyan-Gesalyan, 1957 (fide Luterbacher, 1964).
- *Globorotalia* (*Turborotalia*) *cerroazulensis* (Cole).—Blow and Banner, 1962:135-136, pl. 12: figs. D-F [upper Eocene Zone P16, Sample FCRM 1923, Lindi, Tanzania].—Blow 1969:347, pl. 36: figs. 3-4 [upper Eocene Zone P16, Sample FCRM 1923, Lindi, Tanzania].—Blow, 1979:1054-1058 (partim), pl. 36: figs. 3-4 (re-illustration from Blow 1969). [Not Cole, 1928.]
- *Globorotalia cerroazulensis* (Cole). —Samanta, 1969:333-334, pl. 2: fig. 1a-c [upper Eocene, Kapili Fm., Assam, India]. [Not Cole, 1928.]
- *Globorotalia cerroazulensis* cerroazulensis (Cole).—Nishi and Chaproniere, 1994:260 (partim), pl. 3: figs. 22-24 [Upper Eocene Zone P15-P16, ODP Hole 841B, Tonga Trench, South Pacific Ocean]. [Not Cole, 1928.]
- **Geological Range:**
  Notes: Middle Eocene, upper Zone E13 to just below the Eocene/Oligocene boundary (Zone E16) (Toumarkine and Bolli, 1970; Coccioni and others, 1988). [Pearson et al. 2006]
  Last occurrence (top): in upper part of **E16** zone (80% up, 34.1Ma, in Priabonian stage). Data source: Pearson et al. (2006), fig. 15.1
  First occurrence (base): in upper part of **E13** zone (70% up, 38.6Ma, in Bartonian stage). Data source: Pearson et al. (2006), fig. 15.1

GLOBOROTALIA CERR. CUNIALENSIS (in GELATI, 1977) -----> TURBOROTALIA CUNIALENSIS (Current classification: Toumarkine & Bolli, 1970)

Reference:

http://www.mikrotax.org/pforams/index.php?dir=pf_cenozoic/Globanomalidae/Turborotalia/Turborotalia%20cunialensis

Synonyms:

- *Globorotalia cerroazulensis* cunialensis Toumarkine and Bolli, 1970:144-145, pl. 1: fig. 37-39 [upper Eocene, Possagno area, Italy].—Toumarkine, 1978:712, pl. 7: figs. 1-12 [upper Eocene *Globigerinatheka semiinvoluta* Zone, DSDP Site 363, Walvis Ridge, South Atlantic Ocean].—Snyder and Waters, 1985:460, pl. 3: fig. 1-2 [upper Eocene Zone P17, DSDP Hole 549A, Goban Spur, North Atlantic Ocean].
- *Turborotalia cerroazulensis* cunialensis (Toumarkine and Bolli).—Toumarkine and Luterbacher, 1985:138, figs. 34.1 (re-illustration of holotype), 36.1-6 (re-illustrations from the literature).
- *Turborotalia cunialensis* (Toumarkine and Bolli). —Coccioni and others, 1988, pl. 1:figs. 7-9 [upper Eocene Zone P16, Massignano, Italy].
- **Geological Range:**
  Notes: Upper Eocene, Zone E16, disappearing just below the Eocene/Oligocene boundary (Toumarkine and Bolli 1970; Coccioni and others, 1988). The apparent diachroneity of the first occurrence of this species is probably related to inconsistencies in recognizing it. [Pearson et al. 2006]
  Last occurrence (top): in upper part of **E16** zone (80% up, 34.1Ma, in Priabonian stage). Data source: Pearson et al. (2006), fig. 15.1

First occurrence (base): in lower part of **E16** zone (30% up, 34.4Ma, in Priabonian stage). Data source: Pearson et al. (2006), fig. 15.1

PSEUDOHASTIGERINA MICRA (in GELATI, 1977) -----> PSEUDOHASTIGERINA MICRA (Current classification: Cole, 1927)

Reference:

http://www.mikrotax.org/system/index.php?dir=pf_cenozoic/Globanomalidae/Pseudohastigerina/Pseudohastigerina%20micra

Synonyms:

- *Globigerinella micra* (Cole). —Subbotina, 1953:122 (partim; not fig. 18a-b =*Pseudohastigerina naguewichiensis*.), pl. 13: figs. 16a-b, 17 [fig. 16, upper Eocene zone of thin- walled pelagic foraminifera, northern Caucasus; fig. 17, upper Eocene Lagenid zone, Kiev stage, Stalingrad region].
- *Hastigerina micra* (Cole).—Bolli, 1957:161 (partim; not pl. 35: fig. 1a-b.), pl. 35: fig. 2a-b [middle Eocene *Porticulasphaera mexicana* Zone, Navet Fm., Trinidad].
- *Pseudohastigerina micra* (Cole).—Berggren and others, 1967:275, text-fig. 9 [middle Eocene Zone P12, type locality, Guayabal Fm., Mexico].—Toumarkine and Bolli, 1975:82, pl. 1: figs. 1, 2 [upper Eocene *Turborotalia cerroazulensis* s.l. Zone, Possagno, Italy].—Blow, 1979:1185 (partim; not pl. 198: figs. 1-6 = aff. *Pseudohastigerina wilcoxensis*), pl. 166: fig. 11 [middle Eocene Zone P11, Kilwa Area, Tanzania, East Africa]; pl. 198: figs. 8,9 [middle Eocene Zone P13, Kilwa Area, Tanzania, sample RS. 311]; pl. 253: figs. 7-9 [middle Eocene Zone P12, type locality, Guayabal Fm., Mexico].—Krasheninnikov and Basov, 1983:841, pl. 9: figs. 8-10 [middle Eocene, DSDP Site 512, Maurice Ewing Bank, South Atlantic Ocean].—Toumarkine and Luterbacher, 1985:118 (partim; not fig. 21:7, 8.), fig. 21:1 (holotype reillustrated), fig. 21: 2a-b (reillustration of Bolli, 1957, pl. 35: fig. 1a-b), fig. 21: 3, 4 (reillustration of Toumarkine and Bolli, 1975, pl.1: figs. 1, 2), fig. 21: 5, 6 (reillustration from literature) [middle Eocene, El Midawarah Fm., Fayoum Area, Egypt].—Nishi and Chaproniere, 1994:259, pl. 1: figs. 24-27 [upper Eocene ODP Hole 841B, Tonga Trench, South Pacific Ocean]._Warraich and Ogasawara, 2001:51, fig. 16: 16, 17 [Zone E10-12, Kirthar Fm., Sulaiman Range, Pakistan]._Pearson and others, 2004:36, pl. 1, fig. 11 [middle Eocene Zone E9, Tanzania].
- *Pseudohastigerina* cf. *P. micra* (Cole)._McKeel and Lipps, 1972:83, pl.1: fig. 6a, b [middle Eocene, Tyee Fm., Coast Range, Oregon]._ McKeel and Lipps, 1975:261, pl.2: fig. 7a, b [middle Eocene, Tyee Fm., Coast Range, Oregon].
- *Globanomalina micra* (Cole).—Jenkins, 1971:78, pl. 2: figs. 50-54 (figs. 50, 51, reillustration of holotype of Nonion iota Finlay; figs. 52-54, illustration of paratype of Nonion iota Finlay).
- *Nonion danvillensis* Howe and Wallace, 1932:51, pl. 9: fig. 3a-b [upper Eocene Zone P16, Jackson Fm., Danville Landing, Ouachita River, *Lousiana*].
- *Nonion iota* Finlay, 1940:456, pl. 65: figs. 108-110 [middle Eocene Bortonian Stage, McKay's marly clay, South Island, New Zealand].
- *Pseudohastigerina acutimarginata* Abdel-Kireem, 1980:66, pl. 1: fig. 1a-c [middle Eocene, Mokattam Fm., Gebel Mokattam area, El Darasah, Cairo, Egypt].
- *Pseudohastigerina pellucida* Abdel-Kireem, 1980:67, pl. 1: fig. 2a-c [middle Eocene, El *Mishigeiga* limestone Member, Wadi Rayan Fm., Fayoum Province, Egypt].
- *Pseudohastigerina quadrata* Abdel-Kireem, 1980:68, pl. 1: fig. 3a, b [middle Eocene, Mokattam Fm., Gebel Mokattam area, El Darasah, Cairo, Egypt].
- *Pseudohastigerina sharkriverensis* Berggren and Olsson._Warraich and Ogasawara, 2001:51, fig. 16: 18, 19 [Zone E10-12, Kirthar Fm., Sulaiman Range, Pakistan]. [Not Berggren and Olsson, 1967.]

- **Geological Range:**
  Notes: Zone E7 (Olsson and Hemleben, 2006) to Zone O1 (Keller, 1985; Nocchi and others, 1986; Leckie and others, 1993; Pearson and Chaisson, 1997; Wade and Pearson, 2008). The species is typically rare in Zone O1 and it is unclear how far through the zone the range extends. The highest occurrence we have confirmed is from the middle of Zone O1 (Leckie and others, 1993, pl. 6, fig. 20; recorded as *Pseudohastigerina aff. P. micra*).
  Last occurrence (top): within **O1** zone (32.10-33.90Ma, top in Rupelian stage). Data source: Olsson & Hemleben (2006) fig 14.1
  First occurrence (base): in mid part of **E7a** subzone (50% up, 49.3Ma, in Ypresian stage). Data source: Olsson & Hemleben (2006) fig 14.130,74

GLOBIGERINA CIPEROENSIS ANGUSTIUMBILICATA (in GELATI, 1977) -----> TENUITELLA ANGUSTIUMBILICATA (Current classification: BOLLI, 1957)

Reference:

https://www.mikrotax.org/pforams/index.php?id=104378

Synonyms:

- *Globigerina ciperoensis angustiumbilicata* Bolli, 1957:109 (partim), pl. 22, fig. 12 [Oligocene *Globorotalia opima opima* Zone, Cipero Fm., Trinidad].—Bolli and Saunders, 1985:182, pl. 13, fig. 8a-c (reproduction of holotype illustration).
- *Globigerina angustiumbilicata* Bolli.—Jenkins and Orr, 1972:1085 (partim), pl. 4, fig. 6 [lower Miocene *Globorotalia kugleri* Zone, DSDP Hole 77B, eastern equatorial Pacific Ocean], pl. 5, figs. 6-8 [lower Oligocene *Globigerina ampliapertura* Zone, DSDP Hole 77B, eastern equatorial Pacific Ocean].—Stainforth and others, 1975:253 (partim), fig. 105, no. 3 [Oligocene *Globigerina ciperoensis* Zone, Cipero Fm., Trinidad], no. 5 (reproduction of holotype illustration).—Quilty, 1976:637, pl. 1, figs. 12, 13 [lower Oligocene Zone P19, DSDP Site 321, Nazca Plate, southeastern Pacific Ocean], pl. 1, figs. 14, 15 [level uncertain, DSDP Hole 320A, Nazca Plate, southeastern Pacific Ocean].—Poore, 1984:444, pl. 3, figs. 5-7 [lower Oligocene Zone OL2, DSDP Site 522, Walvis Ridge, South Atlantic Ocean].—Keller, 1985, fig. 3 [lower Oligocene Zone P18-19, Shubuta Member, Red Bluff Fm., Wayne County, Mississippi].—van Eijden and Smit, 1991:110, pl. 2, fig. 9 [upper Oligocene Zone P22, ODP Hole 758A, Ninetyeast Ridge, equatorial Indian Ocean].
- ?*Globigerina* (*Globigerina*) *angustiumbilicata* (Bolli).—Kennett and Srinivasan, 1983:31, pl. 4, figs. 3-5 [middle Miocene Zone N11, DSDP Site 289, Ontong Java Plateau, equatorial western Pacific Ocean] (possibly reworked).
- *Tenuitellinata angustiumbilicata* (Bolli).—Li, 1987:311, pl. 2, figs. 15, 17-19 [*G. ciperoensis* Zone, Cipero Fm., Trinidad].—Spezzaferri and Premoli Silva, 1991:257, pl. 18, figs. 2a-d, 5a-d [lower Oligocene Zone P20, DSDP Hole 538A, Gulf of Mexico].—Leckie and others, 1993:125, pl. 6, figs. 4, 5 [upper Oligocene Zone P22, ODP Hole 628A, western North Atlantic Ocean].—Chaisson and Leckie, 1993:166, pl. 1, fig. 9 [lower Miocene Subzone N4b, ODP Hole 806B, Ontong Java Plateau, western equatorial Pacific Ocean].—Spezzaferri, 1994:61, pl. 32, fig. 6 [lower Oligocene Zone P20, DSDP Hole 538A, Gulf of Mexico], fig.7a-c [lower Miocene Zone N8, DSDP Site 94, Gulf of Mexico].—Pearson, 1995:53, pl. 1, fig. 17 [upper Oligocene to lower Miocene, ODP Hole 872C, Lo-En Guyot, Marshall Islands, equatorial western North Pacific Ocean].—Li and others, 2003b:16, pl. 2, fig. 8 [lower Oligocene Zone P18/P19, ODP Hole 1134A, Great Australian Bight].—Hernitz Kučenjak and others, 2006, pl. 4, figs. 2, 3 [lower Oligocene Zone O3, Jihar-1 well, Syria].
- *Tenuitella angustiumbilicata* (Bolli).—Pearson and Wade, 2009:213, pl. 8, figs. 4a-d [upper Oligocene Zone O6 (= O7), Cipero Fm., Trinidad].

- *Globigerinita stainforthi praestainforthi* Blow, 1969:383, pl. 25, figs. 3-5 [upper Oligocene part of *Globorotalia kugleri* Zone = Zone O7, Cipero Fm., Trinidad].
- *Globigerinita praestainforthi* Blow.—Li and others, 1992:581, pl. 3, fig. 1 [lower Miocene ODP Hole 747A, Kerguelen Plateau, southern Indian Ocean].
- *Tenuitellinata praestainforthi* (Blow).—Spezzaferri, 1994:61, pl. 32, figs. 1a-c [lower Miocene Zone N5, ODP Hole 709C, equatorial Indian Ocean], figs. 3a-c [lower Miocene Subzone N4a, ODP Hole 667A, equatorial Atlantic Ocean].
- *Tenuitella praestainforthi* (Blow).—Pearson and Wade, 2009:213, pl. 8, figs. 5a-e [upper Oligocene Zone O6 (=O7), Cipero Fm., Trinidad].
- *Tenuitellinata* cf. *T. pseudoedita* (Subbotina).—Li, 1987:312, pl. 3, figs. 1-5 [lower Miocene *Catapsydrax dissimilis* Zone, Cipero Fm., Trinidad], pl. 4, figs. 11-13, pl. 5, figs. 1, 4, 7, 11 [upper Oligocene *G. ciperoensis* Zone, Cipero Fm., Trinidad] (not Subbotina, 1953 = Problematica).
- *Tenuitella* cf. *T. pseudoedita* (Subbotina).—Li and others, 2003b:16, pl. 2, fig. 9 [lower Oligocene Zone P18/P19, ODP Hole 1134A, Great Australian Bight]. [Not Subbotina, 1953 = Problematica.]
- *Tenuitella gemma* (Jenkins).—Li and others, 1992:579, pl. 1, fig. 5 [upper Oligocene ODP Hole 747A, Kerguelen Plateau, southern Indian Ocean]. [Not Jenkins, 1965.]
- *Tenuitellinata* sp. 1 Spezzaferri, 1994, pl. 32, figs. 2a-c [upper Oligocene Subzone P21b, DSDP Hole 526A, western South Atlantic Ocean], fig. 4a-c [upper Oligocene Zone P22, DSDP Site 151, Beata Ridge, Caribbean Sea], fig. 5a-c [lower Miocene Subzone N4b, ODP Hole 709B, equatorial Indian Ocean].
- *Tenuitella postcretacea* (Myatliuk).—BouDagher-Fadel, 2012a [Oligocene Zone P21, Cipero Fm., Trinidad]. [Not Myatliuk, 1950.]
- *Tenuitella praepseudoedita* BouDagher-Fadel, 2012a:396, pl. 5.3, fig. 3 (reproduced without attribution from Li, 1987, pl. 3, fig. 1), fig. 4 (reproduced without attribution from Li, 1987, pl. 3, fig. 40) (invalid taxon, see discussion below).
- Not *Globigerina ciperoensis angustiumbilicata* Bolli, 1957:109, pl. 22, fig. 13 [Oligocene *Globorotalia opima opima* Zone, Cipero Fm., Trinidad] (paratype, of uncertain affinity).
- Not *Globigerina angustiumbilicata* Bolli.—Blow and Banner, 1962:85, pl. 9, figs. x-z [lower Oligocene *Globigerina oligocaenica* Zone, Lindi area, Tanzania] (= *Ciperoella ciperoensis* group).—Jenkins and Orr, 1972:1085, pl. 4, fig. 5 [lower Oligocene *Globigerina ampliapertura* Zone, DSDP Hole 77B, eastern equatorial Pacific Ocean] (= probable juvenile *Ciperoella*).—Stainforth and others, 1975:253, fig. 105, figs. 1, 2, 4 [Oligocene *Globigerina ciperoensis* Zone, Cipero Fm., Trinidad] (= *Ciperoella ciperoensis*).—Poore and Brabb, 1977:255, pl. 8, fig. 6 [Oligocene Rices Mudstone member, San Lorenzo Fm., California] (= *Ciperoella ciperoensis* group).

- **Geological Range:**
  Notes: The earliest confirmed occurrences are in the lower Oligocene. Premoli Silva and Spezzaferri (1990) record a clear lowest occurrence along with *Cassigerinella chipolensis* in the lower part of Zone P18 (= Zone O1) in ODP Site 709. According to van Eijden and Smit (1991) and Li and others (1992) it is very rare in the lower Oligocene, becoming abundant only in the upper Oligocene: this pattern seems to be true globally. The highest reliable occurrences are in the lower Miocene (*Tenuitella minutissima* Zone of ODP Hole 747A, Kerguelen Plateau; Li and others, 1992:585: probably equivalent to (sub)tropical Zone M2). Reported occurrences throughout the Neogene by various authors are considered doubtful in view of the homeomorphy within this group but this question is reserved for future study. [Pearson et al. 2018]
  Last occurrence (top): within **M2** zone (19.30-21.12Ma, top in Burdigalian stage). Data source: Pearson et al. 2018 f16.1
  First occurrence (base): within **O1** zone (32.10-33.90Ma, base in Priabonian stage). Data source: Pearson et al. 2018 f16.1

GLOBIGERINA AMPLIAPERTURA (in GELATI, 1977) -----> TURBOROTALIA AMPLIAPERTURA (Current classification: BOLLI, 1957)

Reference:

http://www.mikrotax.org/pforams/index.php?id=100311

Synonyms:

- *Globigerina ampliapertura* Bolli, 1957b:108, pl. 22: figs. 4a-6c [lower Oligocene *Globigerina ampliapertura* Zone, Cipero Fm., Trinidad].—Bolli, 1957c:164, pl. 36, figs. 8a-c [upper Eocene *Globorotalia cocoaensis* Zone, San Fernando Fm., Trinidad].—Asano 1962:54-55, pl. 21: fig. 4a-b [Eocene, *Sakasagawa* Fm., *Amakusa* Islands, Japan].—Brönnimann and *Rigassi*, 1963, pl. 21: fig. 1a-c [Oligocene, Havana Province, Cuba].—Saito and Be_, 1964: pl. 2 [Oligocene, Vicksburg Group, USA].— Jenkins, 1965: pl. 2: fig. 11a-c [upper Eocene – Oligocene, New Zealand].—Poore and Brabb, 1977:255, pl. 1: figs. 7-9 [lower Oligocene Zone P19-20, San Lorenzo Fm., California].—Pujol, 1983:650, pl. 10: figs. 4, 8, 10 [Oligocene Zone P17-P19, DSDP Hole 516F, Rio Grande Rise, Southwest Atlantic].—Poore and Bybell, 1988:17, pl. 4: figs. 3-5 [middle Eocene, Core ACGS#4, New Jersey].
- *Globigerina ampliapertura ampliapertura* Bolli.—Blow and Banner, 1962:83-84, pl. 11: figs. A-D; pl. 17: fig. C [lower Oligocene *Globigerina ampliapertura ampliapertura* Zone, Cipero Fm., Trinidad].—Blow, 1969:315, pl. 12: figs. 6, 9-10 [lower Oligocene *Globigerina ampliapertura ampliapertura* Zone, Cipero Fm., Trinidad].
- *Globigerina* sp. cf. *G. ampliapertura* Bolli. —Samanta, 1969:330, pl. 1: figs. 12a-c [upper Eocene Kopili Fm., Assam, India].
- "*Turborotalia*" *ampliapertura* (Bolli).— Leckie and others, 1993:125-126, pl. 4: figs. 3-8 [lower Oligocene Zone P18, ODP Hole 628A, West Atlantic Ocean].
- "*Globigerina*" *ampliapertura* Bolli.—Nishi and Chaproniere, 1994:259, pl. 4: fig. 1-6 [lower Oligocene Zone P18, ODP Hole 841B, Tonga Trench, South Pacific Ocean].
- *Turborotalia ampliapertura* (Bolli).—Pearson and others, 2006b:441-442, pl. 15.2, figs. 1-3 [SEMs of holotype], figs. 4-6, 8 [lower Oligocene *Globigerina ampliapertura* Zone, Cipero Fm., Trinidad], figs. 7, 17-20 [Zone E15/16, Shubuta Clay, Wayne County, Mississippi], figs. 9-11 [SEM of holotype of *Globigerina pseudoampliapertura* Blow and Banner, Zone E16, Sample FCRM 1923, Madingura (= Namadingura) River, Lindi, Tanzania], figs. 12-16 [topotypes of *Globigerina pseudoampliapertura* Blow, Zone E16, Sample FCRM 1923, Madingura (= Namadingura) River, Lindi, Tanzania].—Pearson and Wade, 2015, fig. 27.1-27.6 [lower Oligocene Zone O1, TDP Site 17, Stakishari, Tanzania].
- *Globigerina pseudoampliapertura* Blow and Banner, 1962:95, pl. 12, figs. a-c, pl. 17, figs. a, e [upper Eocene, Sample FCRM 1923, Madingura (= Namadingura) River, Lindi, Tanzania].
- *Globigerina kondoi* Todd, 1970:A16, pl. 7, fig. 2a-c [upper Eocene, southeastern Eua Island, Tonga].
- ?*Turborotalia pseudoampliapertura nukhulensis* Haggag and Luterbacher, 1995, pl. 2, figs. 5-9 [uppermost part of middle Eocene *Morozovella lehneri* Zone, Wadi Nukhul, Egypt].
- *Turborotalia pseudoampliapertura sinaiensis* Haggag and Luterbacher, 1995, pl. 3, figs. 1-4 [upper part of middle Eocene *Truncorotaloides rohri* Zone, Wadi Nukhul, Egypt].
- **Geological Range:**
  Notes: This form ranges from around the base of middle Eocene Zone E12 (Haggag and Luterbacher, 1995, fig. 2) to lower Oligocene Zone O2 (used as a zone marker by Bolli, 1957; calibrated to Chron C11r by Leckie and others, 1993; zone denoted O2 by Berggren and Pearson, 2005). [Pearson et al. 2018]
  Last occurrence (top): at top of **O2** zone (100% up, 30.3Ma, in Rupelian stage). Data source: zonal marker (Wade et al. 2011)

First occurrence (base): in mid part of **E15** zone (50% up, 35.3Ma, in Priabonian stage). Data source: Pearson et al. (2006), fig. 15.1

GLOBOROTALIA OPIMA OPIMA (in GELATI, 1977) -----> PARAGLOBOROTALIA OPIMA (Current classification: BOLLI, 1957)

Reference:

http://www.mikrotax.org/pforams/index.php?id=104345

Synonyms:

- *Globorotalia opima opima* Bolli, 1957:117-118, pl. 28, figs. 1a-c (holotype), fig. 2 (paratype) [Oligocene *Globorotalia opima opima* Zone, Cipero Fm., Trinidad; max. diameter = 0.45 mm (re-measured herein)].—Berggren and Amdurer, 1973, pl. 27, fig. 7 [upper Oligocene Zone P21, DSDP Hole 17B, South Atlantic Ocean].—Stainforth and others, 1975:300, fig. 132.1-7 [Oligocene *Globorotalia opima opima* Zone, Cipero Fm., Trinidad; max. diameters = 0.40 mm, 0.39 mm. 0.39 mm, 0.35 mm, 0.41 mm, 0.33 mm, and 0.35 mm], 8 (holotype drawing reproduced).—Toumarkine, 1978:714, pl. 8, figs. 7, 8 [mid Oligocene *Globorotalia opima opima* Zone, DSDP Site 360, southeast Atlantic Ocean; max. diameters = 0.34 mm and 0.34 mm].—Stainforth and Lamb, 1981:25, pl. 4, fig. 2a-c [Oligocene *Globorotalia opima opima* Zone, Atlantic Slope Project corehole 5B, western North Atlantic Ocean; max. diameter = 0.55 mm].—Bolli and Saunders, 1985:202, fig. 26.30a-c (holotype re-illustrated), figs. 26.24-29 (given as “paratypes”, actually topotypes) [Oligocene *Globorotalia opima opima* Zone, Cipero Fm., Trinidad; max. diameters = 0.43 mm, 0.47 mm, 0.48 mm, 0.53 mm, 0.50 mm, and 0.53 mm].—Martinotti, 1986, pl. 1, fig. 1 [Oligocene *Globorotalia opima opima* Zone, Ashqelon 4 Borehole, Israel; max. diameter = 0.41 mm], pl. 1, fig. 2 [Oligocene *Globorotalia opima opima* Zone, Shiqma 1 Borehole, Israel; max. diameter = 0.36 mm], pl. 1, fig. 3 [Oligocene *Globorotalia opima opima* Zone, Ashdod 1 Borehole, Israel; max. diameter = 0.36 mm], pl. 1, fig. 4 [Oligocene *Globorotalia opima opima* Zone, Beeri structure Hole 4, Israel; max. diameter = 0.45 mm].
- *Globorotalia* (*Turborotalia*) *opima opima* Bolli.—Blow, 1969:353, pl. 39, fig. 3 [lower Oligocene Zone N1 (=P20), Cipero Fm., Trinidad; max. diameter = 0.60 mm].—Jenkins, 1971:128, pl. 13, figs. 354-357 [Oligocene, Duntroonian-Whaingaroan Stage, South Island, New Zealand; max. diameter = 0.49 mm and 0.40 mm]. —Quilty, 1976:646, pl. 13, figs. 12, 13 [Oligocene Zone N2/N3, DSDP Hole 320B, southeastern Pacific Ocean; max. diameters = 0.34 mm and 0.37 mm].
- *Globorotalia opima* Bolli.—Postuma, 1971:344, pl. on p. 345 [Oligocene, Cipero Fm., Trinidad; max. diameter = 0.50 mm].
- *Turborotalia (Turborotalia) opima opima* (Bolli).—Fleisher, 1974:1036, pl. 19, fig. 12 [lower Oligocene Zone P20/P21, DSDP Site 223, Arabian Sea; max. diameter = 0.45 mm].
- *Paragloborotalia opima* (Bolli).—Cifelli and Scott, 1986, figs. 1c and 1g [?Trinidad].—Leckie and others, 1993:125, pl. 7, figs. 3 [upper Oligocene Subzone P21b, ODP Hole 803D, Ontong Java Plateau, western equatorial Pacific Ocean; max. diameter = 0.54 mm], 4 [upper Oligocene Zone P22, ODP Hole 628A, Little Bahama Bank, western North Atlantic Ocean; max. diameter = 0.42 mm (?specimen reworked)], 9 [lower Oligocene Zone P20, ODP Hole 803D, Ontong Java Plateau, western equatorial Pacific Ocean; max. diameter = 0.44 mm].—Olsson and others, 2006, pl. 5.8, figs. 13-15 (holotype re-illustrated by SEM).—Rincón and others, 2007:305, pl. 2, fig. 5a-c [upper Oligocene *Paragloborotalia opima* Zone, Carmen Fm., Colombia; max. diameter = 0.41 mm].—Wade and others, 2007:pl. I, figs. n-o [upper Oligocene Zone O5, ODP Hole 1218B, equatorial Pacific Ocean; max. diameters = 0.40 mm, 0.46 mm].—Wade and others, 2016:440-441, pl. 1, fig. 2 (holotype SEM re-illustrated), pl. 1,

fig. 3 (new SEM of paratype of *Globorotalia opima opima* Bolli), pl. 3, figs. 1a-1d, 4a-4d, pl. 4, fig. 5 [lower Oligocene Zone O3/O4, IODP Hole U1334A, equatorial Pacific Ocean; max. diameters = 0.35 mm, 0.37 mm, 0.48 mm], pl. 3, figs. 2a-2d, pl. 4, figs. 1a-4, pl. 5, figs. 1a-5d [upper Oligocene Zone O5, IODP Hole U1334A, equatorial Pacific Ocean; max. diameters = 0.35 mm, 0.38 mm, 0.40 mm, 0.46 mm, 0.49 mm, 0.50 mm, 0.51 mm, 0.54 mm], pl. 3, figs. 3a-3b [lower Oligocene Zone O1/O2, IODP Hole U1334A, equatorial Pacific Ocean; max. diameter = 0.36 mm].

- *Paragloborotalia opima opima* (Bolli).—Spezzaferri and Premoli Silva, 1991:248, pl. XI, figs. 5a-6b [lower Oligocene Subzone P21a, DSDP Hole 538A, Gulf of Mexico; max. diameter = 0.40 mm and 0.38 mm].—Spezzaferri, 1994:53-54, pl. 20, figs. 5a-c (reproduced from Spezzaferri and Premoli Silva, 1991).
- Specimen ex interc. *Globorotalia* (*Turborotalia*) *opima nana/G.* (*T.*) *opima opima* (Bolli).—Blow, 1969, pl. 39, fig. 2 [lower Oligocene Zone N1 (=P20), Cipero Fm., Trinidad; max. diameter = 0.37 mm].
- *Globorotalia nana* Bolli.—Postuma, 1971:340, pl. on p. 341 [Oligocene, Trinidad; max. diameter = 0.33 mm]. [Not Bolli, 1957.]
- *Globorotalia opima nana–opima opima* Bolli transition.—Bolli and Saunders, 1985, fig. 26.21-23 [Oligocene *Globorotalia opima opima* Zone, Cipero Fm., Trinidad; max. diameters = 0.42 mm, 0.38 mm, and 0.40 mm].
- *Paragloborotalia opima–nana* (Bolli) transition.—Wade and others, 2007:pl. I, figs. h-m [upper Oligocene Zone O5, ODP Hole 1218B, equatorial Pacific Ocean; max. diameters = 0.35, 0.35 mm, 0.36 mm, and 0.37 mm].
- *Paragloborotalia pseudocontinuosa* (Jenkins).—Wade and others, 2007, pl. II, figs. l, m [upper Oligocene Zone O5, ODP Hole 1218B, equatorial Pacific Ocean; max. diameters = 0.47 mm and 0.40 mm (scales corrected)]. [Not Jenkins, 1967.]
- Not *Globorotalia opima* subsp. *opima* Bolli.—Jenkins, 1960:366, pl. 5, fig. 3a-c [upper Oligocene pre-*Globoquadrina dehiscens dehiscens* Zone, Lakes Entrance Oil Shaft, Victoria, Australia] (= *Ciperoella ciperoensis*).
- Not *Turborotalia siakensis opima* (Bolli).—Chaproniere, 1981:124, figs. 11.Ca-c [Oligocene Zone N3/N4, Ashmore Reef No. 1 well, eastern Indian Ocean; max. diameter = 0.31 mm] (= *P. nana*).
- Not *Paragloborotalia opima opima* (Bolli).—Cifelli, 1982 (partim), pl. 2, fig. 1 [upper Oligocene *Globorotalia opima* Zone, Cipero Fm., Trinidad (given in plate caption as *Globorotalia opima*); max. diameter 0.25 mm] (?= *Globorotaloides*), fig. 2 [upper Oligocene *Globorotalia opima* Zone, Cipero Fm., Trinidad (given in plate caption as *Globorotalia opima*); max. diameter 0.22 mm] (= *P. nana*).
- Not *Paragloborotalia opima* (Bolli).—Li and others, 2005:19, pl. 2, figs. 25, 26 [upper Oligocene Zone P22, ODP Site 1148, South China Sea; max. diameter of specimens = P. nana).
- Not *Paragloborotalia opima* (Bolli) transitional form to *P. nana* (Bolli).—Rincón and others, 2007:305, pl. 10, fig. 6 a-c [lower Oligocene *Turborotalia ampliapertura* Zone, San Jacinto Fm., Colombia; max. diameter = 0.29 mm] (= *P. nana*).

- **Geological Range:**
  Notes: *Paragloborotalia opima* has a restricted stratigraphic range relative to *P. nana* and *P. siakensis*, a feature that has been utilized in biostratigraphic schemes (e.g., Bolli, 1957; Bolli and Saunders, 1985; Berggren and others, 1995; Berggren and Pearson, 2005; Wade and others, 2011). Its base occurrence has been calibrated to 30.6 Ma (Berggren and others, 1995). The highest occurrence of *P. opima* defines the O5/O6 zonal boundary at 27.5 Ma within Chron C9n (Wade and others, 2007, 2011, 2016). [Leckie et al. 2018]
  Last occurrence (top): at top of **O5** zone (100% up, 26.9Ma, in Chattian stage). Data source: Leckie et al. 2018
  First occurrence (base): in upper part of **O2** zone (80% up, 30.6Ma, in Rupelian stage). Data source: Leckie et al. 2018 f5.1

GLOBOROTALIA SIAKENSIS (in GELATI, 1977) -----> PARAGLOBOROTALIA SIAKENSIS (Current classification: LEROY, 1939)

Reference:

http://www.mikrotax.org/system/index.php?id=104349

Synonyms:

- *Globorotalia siakensis* LeRoy, 1939:262, pl. 4, figs. 20-22 [Miocene?, Rokan-Tapanoeli region, central Sumatra].—Berggren and Amdurer, 1973, pl. 28, figs. 6, 7 [lower Miocene Zone N4, DSDP Site 14, South Atlantic Ocean], fig. 8 [upper Oligocene Subzone P21b, DSDP Site 17B, South Atlantic Ocean].—Kennett, 1973, pl. 14, figs. 1, 2 [middle Miocene *G. mayeri* Zone, DSDP Site 206, New Caledonia Basin, western South Pacific Ocean].—Stainforth and others, 1975:317, 320, fig. 143.1, 2 [lower Miocene *Catapsydrax dissimilis* Zone, Cipero Fm., Trinidad]; fig. 143.3 (holotype drawing reproduced); fig. 143.4, 5 [middle Miocene *Globorotalia fohsi fohsi* Zone, corehole, Gulf of Mexico].—Iaccarino and Salvatorini, 1979, pl. 3, figs. 10, 14 [middle Miocene Zone N12, DSDP Site 398, Vigo Seamount, eastern North Atlantic Ocean].—Berggren and others, 1983, pl. 3, figs. 8-10 [lower Miocene Zone N5, DSDP Site 516, Rio Grande Rise, western South Atlantic Ocean].
- *Globorotalia* (*Turborotalia*) *siakensis* LeRoy.—Quilty, 1976:647, pl. 14, figs. 5, 6 [mid Miocene Zone N10/N11, DSDP Site 319, southeastern Pacific Ocean].—Molina, 1979:239-241, pl. 28, figs. 1A-C [lower Miocene *G. primordius* Zone, Levigado NA-4, Spain].
- *Globorotalia* (*Jenkinsella*) *siakensis* LeRoy.—Kennett and Srinivasan, 1983:172, pl. 42, figs. 1, 6-8 [middle Miocene Zone N9, DSDP Site 289, Ontong Java Plateau, western equatorial Pacific Ocean].
- *Paragloborotalia siakensis* (LeRoy).—Spezzaferri and Premoli Silva, 1991:253, pl. XI, figs. 2a-c [upper Oligocene Zone P22, DSDP Hole 538A, Catoche Knoll, Gulf of Mexico].—Spezzaferri, 1994:55, pl. 21, figs. 1a-c [reproduced from Premoli Silva and Spezzaferri, 1991, pl. 11, figs. 2a-c], figs. 2a-c [upper Oligocene Zone P22, DSDP Hole 667A, Sierra Leone Rise, equatorial Atlantic Ocean].—Fox and Wade, 2013:401, fig. 15.1-5, fig. 21 [middle Miocene Zone M6, IODP Hole U1338C, eastern equatorial Pacific Ocean].—Sanchez and others, 2014:116-117, pl. 11, figs. 1-8 [lower Miocene *Catapsydrax dissimilis* Zone, Cipero Fm., Trinidad], pl. 11, figs. 9-16 [lower Miocene *Globorotalia fohsi peripheroronda* Zone, Carapita Fm., eastern Venezuela Basin].
- *Globorotalia* cf. *mayeri* Cushman and Ellisor.—Keller, 1981:125-127, pl. 2, 7 figures [upper Oligocene Zone P22, DSDP Site 292, Benham Rise, western North Pacific Ocean].
- *Globorotalia mayeri* Cushman and Ellisor.—Bolli and Saunders, 1982a, pl. 1, figs. 25, 26, 30, 36, 38; pl. 2, figs. 1-6, 8, 9, 14-17, 21-31, 36, 38, 43-45; pl. 3, 1-6, 13-18, 22-29, 32-43 [upper Oligocene to middle Miocene, *Globigerina ciperoensis ciperoensis* Zone to *Globorotalia mayeri* Zone, Cipero Fm., Trinidad].
- *Paragloborotalia semivera* (Hornibrook)*/Paragloborotalia mayeri* (Cushman and Ellisor) group.—Leckie and others, 1993:125, pl. 7, figs. 5-8, 10-14 [upper Oligocene Zone P22, ODP Hole 803D, Ontong Java Plateau, western equatorial Pacific Ocean; upper Oligocene Zone P22, ODP Hole 628A, Little Bahama Bank, western North Atlantic Ocean].
- Not *Globorotalia siakensis* LeRoy.—Jenkins, 1960:366, 368, pl. 5, figs. 7a-c [lower Miocene *Globigerinoides trilobus trilobus* Zone, Lakes Entrance Oil Shaft, Victoria, Australia] (= *Globorotalia bella*).—Postuma, 1971:358, pl. on p. 359 [Trinidad] (= *P. mayeri*).

- **Geological Range:**
  Notes: Lower Oligocene Zone O3 to upper Miocene Zone M11 (Spezzaferri and Premoli Silva, 1991; Spezzaferri, 1994; Wade and others, 2011). [Leckie et al. 2018]
  Last occurrence (top): within **M11** zone (10.46-11.63Ma, top in Tortonian stage). Data source: Leckie et al. 2018

First occurrence (base): within **O3** zone (29.18-30.28Ma, base in Rupelian stage). Data source: Leckie et al. 2018

GLOBOQUADRINA GLOBULARIS (in GELATI, 1977) -----> DENTOGLOBIGERINA GLOBULARIS (Current classification: BERMÙDEZ, 1961)

Reference:

http://www.mikrotax.org/pforams/index.php?id=104374

Synonyms:

- *Globoquadrina globularis* Bermúdez, 1961:1311, pl. 13, figs. 4-6 [‘middle’ Oligocene, Tinguaro Fm., Matazanzas Province, Cuba].—Poore 1984:444, pl. 3, figs. 8-10 [upper Oligocene Zone OL4, DSDP Site 522, South Angola Basin, South Atlantic Ocean].
- *Globoquadrina altispira globularis* Bermúdez.—Quilty, 1976:644, pl. 10, figs. 11, 12 [lower Miocene Zone N4, DSDP Site 320, Nazca Plate, southeastern Pacific Ocean].
- *Dentoglobigerina globularis* (Bermúdez).—Spezzaferri and Premoli Silva, 1991:237, pl. 2, figs. 5, 7 [lower Oligocene Subzone P21a, DSDP Hole 538A, Gulf of Mexico], pl. 3, fig. 1 [upper Oligocene Zone P22, DSDP Hole 538A, Gulf of Mexico].—Spezzaferri, 1994:40, pl. 40, figs. 2a-c (reproduced from Spezzaferri and Premoli Silva, 1991).—Hernitz Kučenjak and others, 2006, pl. 3, fig. 4 [lower Oligocene Zone O1, Jihar-5 well, Syria].—Wade and others, 2007:172, pl. 2, figs. f-h [upper Oligocene Zone O5, ODP Hole 1218B, equatorial Pacific Ocean].
- *Dentoglobigerina globularis / D. altispira globosa* transition.—Spezzaferri and Premoli Silva, 1991:237, pl. 3, figs. 3, 6, 7 [upper Oligocene Zone P22, DSDP Hole 538A, Gulf of Mexico].
- *Subbotina*? *eocaena* (Gümbel).—Leckie and others, 1993:125, pl. 2, fig. 10 [uppermost Eocene Zone P17, ODP Hole 628A, Little Bahama Bank, western North Atlantic Ocean], pl. 2, fig. 11 [lower Oligocene Zone P18, ODP Hole 628A, Little Bahama Bank, western North Atlantic Ocean]. [Not Gümbel, 1868.]
- *Subbotina*? *yeguaensis* (Weinzierl and Applin).—Leckie and others, 1993:125, pl. 3, fig. 3 [uppermost Eocene Zone P17, ODP Hole 628A, Little Bahama Bank, western North Atlantic Ocean], pl. 3, fig. 4 [lower Oligocene Zone P18, ODP Hole 628A, Little Bahama Bank, western North Atlantic Ocean], pl. 3, fig. 5 [upper Oligocene Subzone P21b, ODP Hole 803D, Ontong Java Plateau, western equatorial Pacific Ocean]. [Not Weinzierl and Applin, 1929.]
- *Dentoglobigerina larmeui* (Akers).—Pearson and Wade, 2009:203, pl. 3, figs. 2a-d [upper Oligocene Zone O6 (= O7 of this study), Cipero Fm., Trinidad]. [Not Akers, 1955.]
- Not *Globoquadrina altispira globularis* Bermúdez.—Blow, 1969:340, pl. 28, figs. 1, 2 (fig. 1 = ?*Dentoglobigerina globosa*, fig. 2 = uncertain).
- Not *Dentoglobigerina altispira globularis* Bermúdez.—Blow, 1979:311, pl. 28, figs. 1, 2 (reproduced from Blow, 1969, pl. 28, figs. 1, 2).
- Not *Dentoglobigerina globularis* (Bermúdez).—Li and others, 2003, pl. 3, fig. 5 (=*Ciperoella ciperoensis*, same specimen as pl. 3, fig. 1).

- **Geological Range:**
  Notes: This species ranges through the entire Oligocene. Although not included in the *Atlas of Eocene Planktonic Foraminifera*, we now consider the first occurrence to have been in the uppermost Eocene (Zone E16 equivalent), as illustrated by Leckie and others (1993) from the western North Atlantic Ocean. The uppermost confirmed occurrence is from lower Miocene Zone M1 (Quilty, 1976). [Wade et al. 2018]
  Last occurrence (top): within **M1a** subzone (22.44-22.96Ma, top in Aquitanian stage). Data source: Wade et al. 2018 f11.1

First occurrence (base): within **E16** zone (33.90-34.68Ma, base in Priabonian stage). Data source: Wade et al. 2018

GLOBOQUADRINA PRAEDEHISCENS (in GELATI, 1977) -----> DENTOGLOBIGERINA TRIPARTITA (Current classification: KOCH, 1926)

Reference:

http://www.mikrotax.org/pforams/index.php?id=100084

Synonyms:

- *Globigerina bulloides* var. *tripartita* Koch, 1926:742, fig. 21a, b [middle Tertiary, lower Globigerina marl, Sadjau-Njak, southeast Bulongan, East Borneo].
- *Globigerina tripartita* Koch.—Blow and Banner, 1962:96 (partim), pl. 10, figs. A-C (re-illustration of holotype).—Brönnimann and Resig, 1971:1302, pl. 8, fig. 6 [upper Oligocene to lower Miocene Zone N4, DSDP Hole 64.1, Ontong Java Plateau, western equatorial Pacific Ocean].—Postuma, 1971:276, pl. on p. 277: 7 un-numbered figs. [Trinidad, unknown level].—Stainforth and others, 1975:325-328 (partim), fig. 148, nos. 2, 4 [lower to upper Oligocene *Globorotalia opima opima* Zone, Panama], fig. 148, no. 3 (reproduction of holotype illustration of *Globigerina tripartita* Koch from Koch, 1926, figs. 21a, b), fig. 148, nos. 7, 8 (reproduction of paratype and holotype illustrations of *Globigerina rohri* Bolli from Bolli, 1957, pl. 23, figs. 1a, 2b) (not fig. 148, nos. 1, 6 = *Dentoglobigerina eotripartita* n. sp.).—Quilty, 1976:639, pl. 4, figs. 9, 10 [upper Oligocene to lower Miocene Zone N4, DSDP Site 320, Nazca Plate, southeastern Pacific Ocean].—Bolli and Saunders, 1985:181, pl. 14, fig. 13 (reproduction of holotype from Blow and Banner, 1962, pl. 10, figs. A-C).—Leckie and others, 1993:124, pl. 5, figs. 6-8 [upper Oligocene Zone P22, ODP Hole 628A, western North Atlantic Ocean], pl. 5, fig. 9 [upper Oligocene Subzone P21b, ODP Hole 803D, Ontong Java Plateau, western equatorial Pacific Ocean], pl. 5, fig. 10 [lower Oligocene Zone P19, ODP Hole 803D, Ontong Java Plateau, western equatorial Pacific Ocean].
- Globigerina tripartita tripartita Koch.—Raju, 1971:27, pl. 3, fig. 3 [lower Oligocene Globigerina sastrii Zone, Well No. KKL-4, Cauvery Basin, southern India].
- *Globoquadrina tripartita* (Koch).—Fleisher, 1975, pl. 1, fig. 4 [lower Oligocene “Turborotalia” ampliapertura Zone, DSDP Site 313, central North Pacific Ocean].—Spezzaferri and Premoli Silva, 1991 (partim):248, pl. 9, fig. 2a-c [upper Oligocene Zone P22, DSDP Hole 528A, Gulf of Mexico].
- *Dentoglobigerina tripartita* (Koch).—Fox and Wade, 2013:399, figs. 8.1-3 [middle Miocene Zone M7 (note this specimen is from Sample U1338B-38H-2, 40-42 cm, not Core 36H as it says in the caption), IODP Hole U1338B, equatorial Pacific Ocean].
- *Globigerina rohri* Bolli, 1957:109, pl. 23, figs. 1a-4b [lower to upper Oligocene Globorotalia opima opima Zone, Cipero Fm., Trinidad].
- *Globoquadrina rohri* (Bolli).—Blow, 1959:185, pl. 11, fig. 57a-c [lower Miocene Catapsydrax stainforthi Zone, San Lorenzo Fm., Venezuela].—Spezzaferri and Premoli Silva, 1991:248, pl. 9, figs. 5a-c [lower Oligocene Subzone P21a, DSDP Hole 528A, Gulf of Mexico].—Spezzaferri, 1994:43-44, pl. 42, figs. 1a-c (reproduced from Spezzaferri and Premoli Silva, 1991, pl. 9, figs. 5a-c).
- *Globigerina tripartita rohri* Bolli.—Raju, 1971:27, pl. 3, figs. 2, 4a-b [lower Oligocene Globigerina sastrii Zone, Well No. KKL-4, Cauvery Basin, southern India].
- *“Dentoglobigerina” rohri* (Bolli).—Pearson and Wade, 2009:203, pl. 3, figs. 1a-c [upper Oligocene Zone O6 (= O7 of this study), Cipero Fm., Trinidad].
- *Globoquadrina dehiscens praedehiscens* Blow and Banner, 1962:116, pl. 15, figs. Q-S. [upper Oligocene Globorotalia kugleri Zone, Cipero Fm., Trinidad].—Blow, 1969:341, pl. 29, figs. 3-5

[upper Oligocene *Globorotalia kugleri* Zone, Cipero Fm., Trinidad].—Quilty, 1976:644, pl. 10, figs. 20-21 [lower Miocene Zone N8, DSDP Site 320, Nazca Plate, southeastern Pacific Ocean].—Iaccarino, 1985:304, fig. 5.11, no. 4 (reproduction of holotype from Blow and Banner, 1962, pl. 15, figs. Q-S).

- *Globoquadrina praedehiscens* Blow and Banner.—Poore, 1979:470, pl. 18, figs. 4-6 [lower Miocene Zone N5, DSDP Site 407, North Atlantic Ocean], fig. 7 [upper Oligocene Zone P22, DSDP Site 407, North Atlantic Ocean].—Kennett and Srinivasan, 1983:182, pl. 45, figs. 4-6 [lower Miocene *Catapsydrax dissimilis* Zone, DSDP Site 208, Lord Howe Rose, Tasman Sea].—Berggren and others, 1983, pl. 1, fig. 1 [lower Miocene Zone N5, DSDP Site 516, Rio Grande Rise, South Atlantic Ocean].
- *Globigerina sakitoensis* Asano, 1962:60, pl. 22, fig. 1a-c [Oligocene, 126 m in drill hole, Nakado, Kyushu, Japan].
- Globigerina sastrii Raju, 1971:26, pl. 4, figs. 1a-c (holotype) [lower Oligocene Globigerina sastrii Zone, Well No. KKL-4, Cauvery Basin, southern India], figs. 2a-c (paratype) [lower Oligocene *Globigerina sastrii* Zone, Well No. TPD-1, Cauvery Basin, southern India].
- *Globigerina sellii* (Borsetti).—Postuma, 1971:272, pl. on p. 273, 7 images (= form intermediate between *Dentoglobigerina eotripartita* and *D. tripartita*) [lower Oligocene *Globigerina oligocaenica* Zone, Lindi area, Tanzania]. [Not Borsetti, 1959.]
- *Globoquadrina sellii* Borsetti.—Li and others, 2005:19, pl. 2, figs. 8-10 [upper Oligocene Zone P22, ODP Hole 1148A, South China Sea]. [Not Borsetti, 1959.]
- *Globoquadrina tapuriensis* (Blow and Banner).—Li and others, 2005:19, pl. 2, fig. 7 [lower Oligocene Subzone P21a, ODP Hole 1148A, South China Sea]. [Not Blow and Banner, 1962.]
- *Globoquadrina dehiscens* (Chapman, Parr, and Collins) sensu lato.—Li and others, 2005:19, pl. 2, figs. 11, 12 [upper Oligocene Zone P22, ODP Hole 1148A, South China Sea]. [Not Chapman, Parr, and Collins, 1934.]
- Not *Globigerina tripartita* Koch.—Blow and Banner, 1962:96, pl. 10, figs. D-F.—Blow, 1969:322, pl. 16, fig. 6 (= *Dentoglobigerina eotripartita* n. sp.).
- Not *Dentoglobigerina tripartita* (Koch).—Blow, 1979:1310, pl. 244, figs. 3, 4.—Olsson and others, 2006:408-410 (partim), pl. 13.3, figs. 4-11, 13-15 (= Dentoglobigerina eotripartita n. sp.).—Li and others, 2005:19, pl. 2, fig. 6 (= *Dentoglobigerina venezuelana*).—Olsson and others, 2006:408-410 (partim), pl. 13.3, figs. 12, 16 (= *Dentoglobigerina galavisi*).
- Not *Globoquadrina tripartita* (Koch).—Spezzaferri and Premoli Silva, 1991:248, pl. 3, figs. 2a-c.—Spezzaferri, 1994:42, pl. 42, figs. 2a-c (reproduced from Spezzaferri and Premoli Silva, 1991:248, pl. 3, fig. 2a-c) (= *Dentoglobigerina tapuriensis*).
- Not *Globoquadrina dehiscens praedehiscens* Spezzaferri and Premoli Silva, 1991:248, pl. 9, figs. 1a-c.—Spezzaferri, 1994:43, pl. 43, figs. 1a-c (reproduced from Spezzaferri and Premoli Silva, 1991, pl. 9, figs. 1a-c) (= *Dentoglobigerina sellii*).

- **Geological Range:**
  Notes: This species has a distinct acme in the upper Oligocene. The oldest figured specimen we assign to this species is from lower Oligocene Zone O2 of DSDP Site 313, where the range is reported to extend intermittently down into the upper part of Zone O1 (Fleisher, 1975). We have observed *tripartita* sensu stricto appearing in the middle part of Zone O1 at IODP Site U1334 (B.S. Wade, unpublished data). The reported highest occurrence is variable, possibly because of varying species concepts. At IODP Sites U1337 and U1338 in the equatorial Pacific Ocean it is common to the top of Subzone M5b, and then infrequent until middle Miocene Zone M10/M11 (Pälike and others, 2010). The youngest figured specimen is from Zone M7 (Fox and Wade, 2013). [Wade et al. 2018]
  Last occurrence (top): within **M7** zone (13.77-14.24Ma, top in Serravallian stage). Data source: Wade et al. 2018 (tentative)
  First occurrence (base): within **O1** zone (32.10-33.90Ma, base in Priabonian stage). Data source: Wade et al. 2018

GLOBIGERINA BAROEMOENENSIS (in GELATI, 1977) -----> DENTOGLOBIGERINA BAROEMOENENSIS (Current classification: LEROY, 1939)

Reference:

http://www.mikrotax.org/pforams/index.php?id=104371

Synonyms:

- *Globigerina baroemoenensis* LeRoy, 1939:263, pl. 6, figs. 1, 2 [holotype, Miocene, Rokan, Tapanoeli area, Sumatra, Indonesia].
- *Globoquadrina baroemoenensis* (LeRoy).—Blow, 1969:340-341, pl. 28, fig. 8 [upper Oligocene Zone N3 = P22, Cipero Fm., Trinidad], pl. 28, fig. 4 [lower Miocene Zone N8, Cipero Fm., Trinidad].—Poore, 1979:470, pl. 18, figs. 8, 9 [lower Miocene Zone N7, DSDP Site 408, North Atlantic Ocean], figs. 10-12 [middle Miocene Zone N9-N11, DSDP Site 408, North Atlantic Ocean].—Blow, 1979, pl. 28, fig. 4 (reproduced from Blow, 1969, pl. 28, fig. 4).—Kennett and Srinivasan, 1983:186, pl. 46, figs. 1-3 [upper Miocene Zone N16, DSDP Site 289, western equatorial Pacific Ocean].—Berggren and others, 1983, pl. 1, fig. 12 [lower Miocene Zone N5, DSDP Site 516, Rio Grande Rise, southwest Atlantic Ocean].—Chaisson and Leckie, 1993:159 (partim), pl. 9, fig. 7 [lower Pliocene, ODP Hole 806B, Ontong Java Plateau, western equatorial Pacific Ocean].
- *Dentoglobigerina baroemoenensis* (LeRoy).—Blow, 1979:763, 1300, pl. 28, fig. 8 (reproduced from Blow, 1969, pl. 28, fig. 8).—Spezzaferri and Premoli Silva, 1991:237, pl. 2, fig. 4a-c [lower Oligocene Subzone P21a, DSDP Hole 538A, Gulf of Mexico].—Spezzaferri, 1994:40, pl. 40, fig. 1a-c (reproduced from Spezzaferri and Premoli Silva, 1991, pl. 2, fig. 4a-c).—Fox and Wade, 2013:379, figs. 5.1, 5.2 [lower Miocene Zone Subzone M5a, IODP Hole U1338B, equatorial Pacific Ocean].
- *Globigerina baroemoenensis* var. *quadrata* LeRoy, 1944:39, pl. 3, figs. 34-35; pl. 7, figs. 37-39 [lower and middle Miocene Telisa Fm., Sumatra, Indonesia].
- *Dentoglobigerina galavisi* Bermúdez / *Globoquadrina baroemoenensis* (LeRoy) transition.—Spezzaferri and Premoli Silva, 1991:237, pl. 2, fig. 3a-c [lower Oligocene Subzone P21a, DSDP Hole 538A, Gulf of Mexico].
- *Globoquadrina langhiana* Cita & Gelati - according to Kennett & Srinivasan 1983
- **Geological Range:**
  Notes: The oldest illustrated specimen of this species is from Zone O4 of the Caribbean (Spezzaferri and Premoli Silva, 1991) although the same authors recorded it as low as Zone P20 (=Zone O2), as also recorded by Blow (1969). Rögl (1985) restricted its occurrence to the lower Miocene of the Central Paratethys. According to Kennett and Srinivasan (1983) and various authors following their taxonomy, it persists to the end of the Miocene or basal Pliocene (Chaisson and Leckie, 1993), although its highest occurrence has not been studied as part of this investigation. [Wade et al. 2018]
  Last occurrence (top): within **N18** zone (5.20-5.72Ma, top in Zanclean stage). Data source: Wade et al. 2018
  First occurrence (base): within **O2** zone (30.28-32.10Ma, base in Rupelian stage). Data source: Kennett and Srinivasan (1983)

GLOBOROTALIA SEMIVERA (in GELATI, 1977) -----> PARAGLOBOROTALIA SEMIVERA (Current classification: HORNIBROOK, 1961)

Reference:

http://www.mikrotax.org/pforams/index.php?dir=pf_cenozoic/Globigerinidae/Paragloborotalia/Paragloborotalia%20semivera

Synonyms:

- *Globigerina semivera* Hornibrook, 1961:149-150, pl. 23, figs. 455-457 [lower Miocene *G. trilobus trilobus* Zone, Rifle Butts Fm., Awamoan Stage, Campbells Beach, South Island, New Zealand].
- *Globorotalia* (*Turborotalia*) *nana semivera* (Hornibrook).—Jenkins, 1971:125-127, pl. 12, figs. 342-344 [holotype re-illustrated from Hornibrook, 1961, pl. 23, figs. 455-457].
- *Globorotalia semivera* (Hornibrook).—Berggren and Amdurer, 1973, pl. 27, figs. 16-19 [lower Miocene Zone N4 and Zone N5, DSDP Site 18, South Atlantic Ocean].—Jenkins, 1977:308, pl. 4, figs. 5-7 [lower Miocene *G. trilobus trilobus* Zone, English Channel].—Jenkins, 1978, pl. 1, figs. 23, 24 [lower Miocene *G. trilobus trilobus* Zone, DSDP Site 360, eastern South Atlantic Ocean].—Berggren and others, 1983, pl. 3, figs. 4, 5, pl. 4, fig. 1 [lower Miocene Zone N5 and Zone N6, DSDP Site 516, Rio Grande Rise, western South Atlantic Ocean].—Hoskins, 1984, figs. 7:1-6 [lower Miocene *G. trilobus trilobus* Zone, Awamoan Stage, New Zealand].
- *Globorotalia* (*Jenkinsella*) *semivera* (Hornibrook).—Kennett and Srinivasan, 1983:172, pl. 42, figs. 3-5 [lower Miocene *Globorotalia miozea* Zone, DSDP Site 206, New Caledonia Basin, western South Pacific Ocean].
- *Paragloborotalia semivera* (Hornibrook).—Premoli Silva and Spezzaferri, 1990:304, pl. 3, figs. 8a-c [lower Miocene Zone N4, ODP Hole 709B, Madingley Rise, western equatorial Indian Ocean].—Spezzaferri, 1994:55-56, pl. 20, figs. 6a-c [upper Oligocene Subzone P21b, ODP Hole 709B, Madingley Rise, western equatorial Indian Ocean], pl. 22, figs. 1a-c [lower Miocene Zone N5, DSDP Hole 526A, Walvis Ridge, eastern South Atlantic Ocean].—Morgans and others, 2002, fig. 14P [lower Miocene *P. incognita* Zone, Altonian Stage, North Island, New Zealand].—Li and others, 2003a:23, pl. 1, fig. 23 [lower Miocene Zone SAN2, ODP Hole 1134B, Great Australian Bight, Indian Ocean], pl. 1, fig. 24 [lower Miocene Zone SAN3, ODP Hole 1134A, Great Australian Bight, Indian Ocean].—Li and others, 2003b:16, pl. 2, fig. 24 [upper Oligocene Subzone P21b, ODP Hole 1134A, Great Australian Bight, Indian Ocean], pl. 2, fig. 25 [upper Oligocene Zone P22, ODP Hole 1134A, Great Australian Bight, Indian Ocean].
- *Paragloborotalia semivera* (Hornibrook) – *Paragloborotalia acrostoma* (Wezel).—Spezzaferri, 1994, pl. 22, figs. 2a-c [lower Miocene Zone N5, DSDP Hole 526A, Walvis Ridge, eastern South Atlantic Ocean].
- *Paragloborotalia mayeri* s.l. (Cushman and Ellisor).—Chaisson and Leckie, 1993:164-165, pl. 8 (partim), figs. 16, 17 [lower Miocene Subzone N4b, ODP Hole 806B, western equatorial Pacific Ocean]. [Not Cushman and Ellisor, 1939.]
- *Paragloborotalia pseudocontinuosa* (Jenkins).—Li and others, 2003b:16, pl. 2, fig. 26 [lower Oligocene Zone P18-P19, ODP Hole 1134A, Great Australian Bight, Indian Ocean], pl. 2, figs. 27, 28 [upper Oligocene Zone P22, ODP Hole 1134A, Great Australian Bight, Indian Ocean]. [Not Jenkins, 1967.]
- **Geological Range:**
  Notes: Lower Oligocene Zone O4 to lower Miocene Zone M5. In New Zealand, Hornibrook (1961) records a range from the upper Oligocene (lower Miocene?) Waitakian Stage to the lower middle Miocene Lillburnian Stage. Jenkins (1971) recorded the range from the upper Oligocene upper Whaingaroan Stage, *Globigerina* (*G.*) *euapertura* Zone, to the upper lower Miocene Clifdenian Stage, *Praeorbulina glomerosa* Zone (Zone N8/M5; Wade and others,

2011). In the southeast Atlantic Ocean, Jenkins (1978) reported a range of uppermost Oligocene *G. euapertura* Zone through the middle part of the lower Miocene *G. triloba triloba* Zone at DSDP Sites 360 and 362. In her detailed study of many DSDP sites from around the world ocean, Spezzaferri (1994) reported a lowest occurrence within lower Oligocene Subzone P21a (= O3/O4). [Leckie et al. 2018]
Last occurrence (top): within **M5** zone (15.10-16.38Ma, top in Langhian stage). Data source: Leckie et al. 2018
First occurrence (base): within **O4** zone (28.09-29.18Ma, base in Rupelian stage). Data source: Leckie et al. 2018

GLOBOROTALIA PSEUDOCONTINUOSA (in GELATI, 1977) -----> PARAGLOBOROTALIA PSEUDOCONTINUOSA (Current classification: JENKINS, 1967)

Reference:

http://www.mikrotax.org/pforams/index.php?dir=pf_cenozoic/Globigerinidae/Paragloborotalia/Paragloborotalia%20pseudocontinuosa

Synonyms:

- *Globorotalia opima* Bolli subsp. *continuosa* Blow.—Jenkins, 1960:366, pl. 5 (partim), figs. 4a-c [lower Miocene *Globigerinoides triloba triloba* Zone, Lakes Entrance Oil Shaft, Victoria, Australia]. [Not Blow, 1959.]
- *Globorotalia continuosa* Blow.—Jenkins, 1966:9-10, pl. 2, figs. 9a-c [lower Miocene, lower Aquitanian stage, southwest France]. [Not Blow, 1959.]
- *Globorotalia nana pseudocontinuosa* Jenkins, 1967:1074-1077, fig. 4.20-22 (holotype), fig. 4.23-25 (paratype) [lower Miocene, *G.* (*G.*) *woodi connecta* Zone, Otaian Stage, North Island, New Zealand].
- *Globorotalia* (*Turborotalia*) *nana pseudocontinuosa* Jenkins.—Jenkins, 1971:124-125, pl. 12, figs. 336-341 [re-illustrated from Jenkins, 1967, pl. 1074, figs. 4.20-25].
- *Globorotalia pseudocontinuosa* Jenkins.—Berggren and Amdurer, 1973, pl. 27, figs. 11-15 [lower Miocene Zone N4 and Zone N5, DSDP Site 18, South Atlantic Ocean].—Jenkins, 1977:307, pl. 4, figs. 1, 2 [lower Miocene *G. trilobus trilobus* Zone, Sealab Trial Borehole, English Channel].—Jenkins, 1978, pl. 1, figs. 14-16 [lower Miocene *G. woodi connecta* Zone, DSDP Site 360, southeast Atlantic Ocean].—Hoskins, 1984, figs. 7.7-12 [lower Miocene *G. trilobus trilobus* Zone, Awamoan Stage, New Zealand], figs. 8:5-6 [middle Miocene *P. glomerosa curva* Zone, Clifdenian Stage, New Zealand], figs. 8:7-9 [lower Miocene *G. woodi connecta* Zone, Otaian Stage, New Zealand].—Jenkins and Srinivasan, 1986:813, pl. 5, figs. 2-4 [lower Oligocene *G. angiporoides* Zone, DSDP Site 593, Challenger Plateau, southwest Pacific Ocean].
- *Paragloborotalia pseudocontinuosa* (Jenkins).—Cifelli and Scott, 1986, figs. 1d and 1h [lower Miocene, *G.* (*G.*) *woodi connecta* Zone, Otaian Stage, North Island, New Zealand].—Spezzaferri and Premoli Silva, 1991:248, pl. XI, figs. 1a-c [lower Oligocene Subzone P21a, DSDP Hole 538A, Catoche Knoll, Gulf of Mexico], pl. XII, figs. 1a-c, 2a [lower Oligocene Zone P20, DSDP Hole 538A, Gulf of Mexico].—Spezzaferri, 1994:54, pl. 20, figs. 1a-c [re-illustration of specimen from Spezzaferri and Premoli Silva, 1991, pl. XI, figs. 1a-c].—Morgans and others, 2002, figs. 14M-O [lower Miocene *G. incognita* Zone, Altonian Stage, North Island, New Zealand].
- Not *Paragloborotalia pseudocontinuosa* (Jenkins).—Li and others, 2003b:16, pl. 2, fig. 26 [lower Oligocene Zone P18-P19, ODP Hole 1134A, Great Australian Bight, Indian Ocean], pl. 2, figs. 27, 28 [upper Oligocene Zone P22, ODP Hole 1134A, Great Australian Bight, Indian

Ocean] (= *P. semivera*).—Wade and others, 2007:pl. II, figs. L, M [upper Oligocene Zone O5, ODP Hole 1218B, equatorial Pacific Ocean](= *P. opima*).

- **Geological Range:**
  Notes: Zone O2 to Zone M5. The species spans the Oligocene and ranges into the middle Miocene (Spezzaferri, 1994), however there are very few studies in which *P. pseudocontinuosa* is a common component of Miocene material. Jenkins (1967) states that *Globorotalia nana pseudocontinuosa* (= *P. pseudocontinuosa*) ranges from the mid-Oligocene (Whaingaroan Stage, *G. euapertura* Zone) to lower middle Miocene (lower Lillburnian Stage, *O. suturalis* Zone) and does not overlap with middle Miocene *G. mayeri continuosa* (= *P. continuosa*). In the southeast Atlantic Ocean, the last occurrence of *P. pseudocontinuosa* is in the lower Miocene *Globigerinoides trilobus trilobus* Zone of DSDP Sites 360 and 362, whereas *G. mayeri continuosa* is reported to occur from the middle Miocene *G. mayeri mayeri* through the upper Miocene *G. conomiozea* Zone (Jenkins, 1978). A similar stratigraphic range for *Globorotalia* (*Turborotalia*) *pseudocontinuosa* is reported for DSDP Sites 279, 281, and 282 in the southwest Pacific (Jenkins, 1975). Poore (1984) recorded a lowest occurrence of *pseudocontinuosa* within lower Oligocene Zone OL2 (= ~O2) at DSDP Site 522 in the southeast Atlantic Ocean, and a highest occurrence in the lowermost Miocene Subzone M1a. Spezzaferri (1994) reported a range from lower Oligocene Subzone P21a (= O3/4) to within the middle Miocene based on her detailed study of numerous deep sea sites. Jenkins and Srinivasan (1986) also report a first occurrence of *pseudocontinuosa* in lower Oligocene Subzone P21a from the southwest Pacific Ocean. In a review paper of southern mid- and high latitude planktonic foraminiferal biostratigraphy and chronostratigraphy, Jenkins (1993) reported a lowest occurrence in lower Oligocene Zone P19. [Leckie et al. 2018]
  Last occurrence (top): within **M5** zone (15.10-16.38Ma, top in Langhian stage). Data source: Leckie et al. 2018
  First occurrence (base): within **O2** zone (30.28-32.10Ma, base in Rupelian stage). Data source: Leckie et al. 2018

GLOBIGERINA CIP. CIPEROENSIS (in GELATI, 1977) -----> CIPEROELLA CIPEROENSIS (Current classification: BOLLI, 1954)

Reference:

http://www.mikrotax.org/pforams/index.php?id=104358

Synonyms:

- *Globigerina concinna* Reuss, 1850:373, pl. 47, fig. 8a, b [Tertiary, Grinzing, Austria].—Nuttall, 1932:29, pl. 6, figs. 9-11 [Alazan shales, Mexico].—Franklin, 1944:317, pl. 48, fig. 5 [Oligocene, Carapita Fm., Venezuela]. [Not Reuss, 1850.]
- *Globigerina* cf. *concinna* Reuss.—Cushman and Stainforth, 1945:67, pl. 13, fig. 1a, b [Cipero Fm., Trinidad]. [Not Reuss, 1850.]
- *Globigerina ciperoensis* Bolli, 1954:1, figs. 3-3a (holotype drawing of *Globigerina* cf. *concinna* Reuss from Cushman and Stainforth, 1945), figs. 4-4b [Oligocene, *Globigerina ciperoensis* Zone, Cipero Fm., Trinidad], figs. 5-5b (drawing of *Globigerina concinna* Reuss from Nuttall, 1932), fig. 6 (drawing of *Globigerina concinna* Reuss from Franklin, 1944).—Jenkins and Orr, 1972:1087, pl. 7, figs. 7, 8 [lower Miocene G. kugleri Zone, DSDP Hole 77B, eastern equatorial Pacific Ocean].—Stainforth and others, 1975:263, fig. 111.1-8 [Oligocene, Trinidad and Tanzania].—Krasheninnikov and Pflaumann, 1978:591, pl. 1, figs. 5-7 [Oligocene, DSDP Site 369, eastern North Atlantic Ocean].—Leckie and others, 1993:123, pl. 9, figs. 7-10 [upper Oligocene, Zone P22, ODP Hole 628A, Little Bahama Bank, western Atlantic Ocean].—Rögl, 1994:135, pl. 1, figs. 1, 2 [Oligocene Zone P21/P22, Cipero Fm., Trinidad], figs. 3, 4, [Zone NP

23, Ottenthal, Austria].—Cicha and others, 1998:99, pl. 31, figs. 27, 28 [lower Oligocene, Central Paratethys].—Pearson and Wade, 2009:206, pl. 5, figs. 1a-3c [upper Oligocene Zone O6 (= O7), Cipero Fm., Trinidad].—Baldassini and others, 2013:111, text-fig. 4.27 and 4.28 [upper Oligocene Zone P22, Sliema Point section, Malta].

- *Globigerina ciperoensis ciperoensis* Bolli.—Bolli, 1957:109, pl. 22, figs. 10a, b [Oligocene *Globorotalia opima opima* Zone, Cipero Fm., Trinidad].—Jenkins, 1977:303, pl. 1, fig. 6 [lower Miocene *G. trilobus trilobus* zone, Sealba Trial Borehole, eastern North Atlantic Ocean].—Toumarkine, 1978, pl. 8, figs. 10, 11 [upper Oligocene *Globigerina ciperoensis ciperoensis* Zone, DSDP Site 363, eastern South Atlantic Ocean].—Bolli and Saunders, 1985:182, fig. 13.1a-b [mid-Oligocene, Cipero Fm., Trinidad], fig. 13.2 and 13.3 [upper Oligocene *G. ciperoensis ciperoensis* Zone, DSDP Site 363, Walvis Ridge, eastern South Atlantic Ocean (reproduced from Toumarkine, 1978)].
- *Globigerina ouachitaensis ciperoensis* Bolli.—Blow and Banner, 1962:90, pl. IX, figs. e-g [lower Oligocene Zone O3, Lindi Area, Tanzania].—Hooyberghs and De Meuter, 1972:22, pl. 6, figs. 1a-c ['upper Oligocene', Houthalen Sands, Belgium].—Molina, 1979:151, pl. 11, figs. 1A-C [lower Miocene, *Globigerinoides primordius* Zone, Navazuelo section, Guadahortuna, Spain].—Chaproniere, 1981:109, figs. 4Ga-d, Ia-d [upper Oligocene, Ashmore Reef No. 1 Well, northwest Australia].
- *Globigerina* (*Globigerina*) *ciperoensis* Bolli.—Kennett and Srinivasan, 1983:29, pl. 4, figs. 6-8 [upper Oligocene Subzone N4a, DSDP Site 289, Ontong Java Plateau, equatorial Pacific Ocean].
- "*Globigerina*" *ciperoensis* Bolli.—Spezzaferri and Premoli Silva, 1991:237, pl. IV, figs. 7a-b; pl. V, figs. 3a-d, 4a-d [upper Oligocene Zone P22, DSDP Hole 538A, Gulf of Mexico].—Spezzaferri, 1994:28, pl. 3, figs. 2a-c [upper Oligocene Subzone P21b, DSDP Hole 516F, South Atlantic Ocean].
- "*Globigerina*" cf. *ciperoensis* Bolli.—Pearson, 1995:46, pl. 1, figs. 13, 14 [upper Oligocene Zone P21/P22, ODP Hole 872A, Lo-En Guyot, western Pacific Ocean].
- *Globoturborotalita ciperoensis* (Bolli).—Rincón and others, 2007:294 (partim), pl. 5, figs. 6, 7 [upper Oligocene *Globoturborotalita ciperoensis* zone, Carmen Fm., Colombia].
- *Globorotalia opima* subsp. *opima* (Bolli).—Jenkins, 1960:366, pl. 5, fig. 3a-c [upper Oligocene pre-*Globoquadrina dehiscens dehiscens* Zone, Lakes Entrance Oil Shaft, Victoria, Australia]. [Not Bolli, 1957.]
- *Globigerina angustiumbilicata* Bolli.—Stainforth and others, 1975:253, pl. 105, figs. 1, 2, 4 [upper Oligocene *Globigerina ciperoensis* Zone, Cipero Fm., Trinidad]. [Not Bolli, 1957.]
- *Globigerina ciperoensis angulisuturalis* (Blow).—Jenkins, 1977:302, pl. 1, fig. 4 [lower Miocene *G. trilobus trilobus* zone, Sealba Trial Borehole, eastern North Atlantic Ocean]. [Not Bolli, 1957.]
- Not 'Giant' *Globigerina ciperoensis* Bolli.—Ujetz and Wernli, 1994:200-201 (partim), pl. 1, figs. 2a-b [lower Oligocene Zone P20, Haute Savoie, France] (= *Globigerinella wagneri*).
- Not *Globoturborotalita ciperoensis* (Bolli).—Rincón and others, 2007:294, pl. 1, figs. 4a-c [upper Oligocene Zone O5, Bolívar, Colombia] (= *C. angulisuturalis*).

- **Geological Range:**
  Notes: Zone O3 to Subzone M1a. The lowest occurrence is not well constrained. Most records are from the upper Oligocene, but Blow and Banner (1962) record *C. ciperoensis* in Zone O3 in Tanzania. The top of *C. ciperoensis* is used as a secondary marker within Subzone M1a (23.68 Ma, Pearson and Chaisson, 1997; Wade and others, 2011). [Olsson et al. 2018]
  Last occurrence (top): within **M1a** subzone (22.44-22.96Ma, top in Aquitanian stage). Data source: Olsson et al. 2018
  First occurrence (base): within **O3** zone (29.18-30.28Ma, base in Rupelian stage). Data source: Olsson et al. 2018

GLOBOQUADRINA ALTISPIRA (in GELATI, 1977) -----> DENTOGLOBIGERINA ALTISPIRA (Current classification: CUSHMAN & JARVIS, 1936)

Reference:

http://www.mikrotax.org/pforams/index.php?dir=pf_cenozoic/Globigerinidae/Dentoglobigerina/Dentoglobigerina%20altispira

Synonyms:

- *Dentoglobigerina altispira altispira* (Cushman & Jarvis 1936) [e.g. Kennett & Srinivasan 1983]
- *Globoquadrina altispira conica* Brönnimann & Resig (1971) [according to Kennett & Srinivasan 1983]
- **Geological Range:**
  Last occurrence (top): at top of **PL4 [Atl.]** zone (100% up, 3.1Ma, in Piacenzian stage). Data source: Wade et al. (2011), zonal marker - but occurs earlier in the Pacific
  First occurrence (base): within **M1b** subzone (21.12-22.44Ma, base in Aquitanian stage). Data source: Kennett & Srinivasan 1983; Wade et al. 2018 f11.1

GLOBIGERINA ANGULISUTURALIS (in GELATI, 1977) -----> CIPEROELLA ANGULISUTURALIS (Current classification: BOLLI, 1957)

Reference:

http://www.mikrotax.org/pforams/index.php?dir=pf_cenozoic/Globigerinidae/Ciperoella/Ciperoella%20angulisuturalis

Synonyms:

- *Globigerina ciperoensis angulisuturalis* Bolli, 1957:109, pl. 22, figs. 11a-c, holotype [Oligocene *Globorotalia opima opima* Zone, Cipero Fm., Trinidad].—Toumarkine, 1978, pl. 8, figs. 12-16 [upper Oligocene *Globigerina ciperoensis ciperoensis* Zone, DSDP Site 363, eastern South Atlantic Ocean].—Bolli and Saunders, 1985:182, fig. 13 (4-7), holotype re-illustrated [Oligocene *Globorotalia opima opima* Zone, Cipero Fm., Trinidad].
- *Globigerina angulisuturalis* Bolli.—Blow, 1969:118, pl. 11, fig. 8 (topotype) [Oligocene Zone N2 = P21, Trinidad], pl. 11, fig. 9, pl. 12, figs. 1, 2 [upper Oligocene Zone “N3 = P22”, Lr. Ragusa Limestone Fm., Sicily].—Stainforth and others, 1975:250, fig. 104 (1-6) [Oligocene *Globorotalia opima opima* Zone, Cipero Fm., Trinidad].—Krasheninnikov and Pflaumann, 1978:591, pl. 1, figs. 1, 2 [Oligocene, DSDP Site 369, eastern North Atlantic Ocean].—Molina, 1979:146, pl. 10, figs. 1A-C [upper Oligocene Zone O5, Fuente Caldera Section, Cordilleras Béticas, Spain].—Leckie and others, 1993:123, pl. 9, figs. 1-6 [upper Oligocene, Zone P22, ODP Hole 628A, Little Bahama Bank, western Atlantic Ocean].—Rögl, 1994:136, pl. 1, figs. 5, 6 [Zone NP 23, Ottenthal, Austria].—Cicha and others, 1998:99, pl. 31, figs. 22, 23 [lower Oligocene, Central Paratethys].—Pearson and Wade, 2009:203, pl. 5, figs. 4a-c [Zone O6 (= O7), Cipero Fm., Trinidad].
- *Globigerina officinalis angulisuturalis* Bolli.—Chaproniere, 1981:109, figs. 4Ca-Dc [upper Oligocene, Ashmore Reef No. 1 Well, northwest Australia].
- *Paragloborotalia angulisuturalis* (Bolli).—Cifelli, 1982:109, pl. 1, figs. 5, 5a [Oligocene *Globorotalia opima opima* zone, Cipero Fm., Trinidad].
- “*Globigerina*” *angulisuturalis* Bolli.—Spezzaferri and Premoli Silva, 1991:237, pl. IV, figs. 1a, 2a-c, 4a-b [mid Oligocene Subzone P21a/b, DSDP Site 538A, Gulf of Mexico].—Spezzaferri,

1994:29, pl. 3, figs. 3a-c [upper Oligocene Subzone P21b, DSDP Site 516F, South Atlantic Ocean].—Pearson, 1995:46, pl. 1, figs. 13, 14 [mid-upper Oligocene Zone P21/P22, ODP Hole 872A, Lo-En Guyot, western Pacific Ocean].

- *Globoturborotalita angulisuturalis* (Bolli).—Baldassini and others, 2013:111, fig. 4, 29, 30 [upper Oligocene, Zone P22, Reqqa Point section and Dingli section, Malta].—Rincón and others, 2007:292, pl. 5, figs. 1, 3 [upper Oligocene *Globoturborotalita ciperoensis* zone, Carmen Fm., Colombia].
- *Globigerina ottnangiensis* Rögl.—Roetzel and others, 2006:394, pl. 5, figs. 1-3 [lower Miocene, Ottnangian stage (=M1b) Bohemian Massif, Parisdorf, Austria, Central Paratethys]. [Not Rögl, 1969.]
- *Globoturborotalita ciperoensis* (Bolli).—Rincón and others, 2007:294 (partim), pl. 1, figs. 4a-c [upper Oligocene Zone O5, Bolívar, Colombia]. [Not Bolli, 1954.]
- Not *Globigerina ciperoensis angulisuturalis* Blow.—Jenkins, 1977:302, pl. 1, fig. 4 [lower Miocene *G. trilobus trilobus* zone, Sealba Trial Borehole, eastern North Atlantic Ocean] (= *C. ciperoensis*).
- Not *Globigerina* (*Globigerina*) *angulisuturalis* Blow.—Kennett and Srinivasan, 1983:32, pl. 5, figs. 1-3 [upper Oligocene Zone P22, DSDP Site 209, Queensland Plateau, South Pacific Ocean] (= *C. angulioficinalis*).
- **Geological Range:**
  Notes: Zone O4 to M2. The FAD of *C. angulisuturalis* defines the base of Zone O4 (29.4 Ma), and the LAD is within Zone M2 (21.6 Ma) (Berggren and others, 1995; Wade and others, 2011). An earlier LAD in Subzone M1b is recorded in the Indian Ocean and Caribbean by Spezzaferri (1994). Pearson and Chaisson (1997:40) remarked that the datum is difficult to place in the equatorial Atlantic Ocean because of "a combination of abundance fluctuations of "*G*." *angulisuturalis* in the higher part of its range and its susceptibility to dissolution". [Olsson et al. 2018]
  Last occurrence (top): within **M2** zone (19.30-21.12Ma, top in Burdigalian stage). Data source: Olsson et al. 2018
  First occurrence (base): within **O4** zone (28.09-29.18Ma, base in Rupelian stage). Data source: Olsson et al. 2018

GLOBIGERINA GALAVISI (in GELATI, 1977) -----> DENTOGLOBIGERINA GALAVISI (Current classification: BERMÙDEZ, 1961)

Reference:

http://www.mikrotax.org/system/index.php?dir=pf_cenozoic/Globigerinidae/Dentoglobigerina/Dentoglobigerina%20galavisi

Synonyms:

- *Globigerina galavisi* Bermúdez, 1961:1183, pl. 4, fig. 3 [upper Eocene Jackson Fm., Mississippi].—Blow, 1969:319, pl. 5, figs. 1-3 (reillustration of holotype), pl. 16, fig. 4 [upper Eocene Zone P16, upper Jackson Fm., Mississippi], pl. 16, fig. 5 [upper Eocene Zone P16, Lindi area, Tanzania].—Brönnimann and Resig, 1971, pl. 8, figs. 2, 3 [upper Eocene Zone P16, DSDP Hole 64.1, Ontong Java Plateau, western equatorial Pacific Ocean].—Krasheninnikov and Hoskins, 1973:122, pl. 8, figs. 3-5 [middle Eocene *Orbulinoides beckmanni* Zone, DSDP Site 202, western North Pacific Ocean].
- *Globoquadrina galavisi* (Bermúdez).—Fleisher, 1975:758, pl. 1, figs. 1, 2 [lower Oligocene *Cassigerinella chipolensis-Pseudohastigerina barbadoensis* Zone, DSDP Site 305, central North Pacific Ocean].

- *Dentoglobigerina galavisi* (Bermúdez).—Blow, 1979:1301-1305 (partim), pl. 5, figs. 1-3 (holotype, reproduced from Blow, 1969), pl. 16, fig. 4 (reproduced from Blow, 1969, pl. 16, fig. 4), pl. 16, fig. 5 (reproduced from Blow, 1969, pl. 16, fig. 5) (not pl. 177, figs. 8, 9, ?= *Subbotina tecta*, pl. 186, figs. 8, 9, ?= *Subbotina projecta* n. sp., pl. 244, figs. 1, 2 = *Subbotina tecta*).—Poore and Bybell, 1988:16, pl. 4, figs. 6, 9 [upper Eocene Zone E16, ACGS Borehole, New Jersey].—Spezzaferri and Premoli Silva, 1991:243, pl. 2, figs. 1a-c [upper Oligocene Zone P22, DSDP Hole 538A, Gulf of Mexico].—Nishi and Chaproniere, 1994:259, pl. 5, figs. 10-12 [upper Eocene, ODP Hole 841B, Tonga Trench, South Pacific Ocean].—Poag and Commeau, 1995:149, pl. 6, fig. 8 [upper Eocene Zone E14, Chickahominy Fm., USGS Exmore Core, Virginia].—Olsson and others, 2006:403-405, pl. 13.1, figs. 1-3 (reillustration of holotype in SEM), figs. 4-7, 12-16 [Zone E15/16, Shubuta Clay, Wayne County, Mississippi], figs. 8, 11 [upper Eocene Zone E16, Nanggulan Fm, Java], figs. 9, 10 [Zone E15/16, Istra More-4 well, Adriatic Sea].—Pearson and Wade, 2015:17-18, fig. 15.1a-c (reillustration of holotype in SEM, from Olsson and others 2006), fig. 15.2-3, 5a-6, 8a-b [upper Eocene Zone E15/16, TDP Site 12, Tanzania], fig. 15.4 [upper Eocene Zone E15/16, TDP Site 17, Tanzania], fig. 15.7 [lower Oligocene Zone O1, TDP Site 12, Tanzania].
- ?*Dentoglobigerina galavisi* (Bermúdez).—Blow, 1979:1301-1305 (partim), pl. 191, figs. 8, 9 (unknown specimens, showing features transitional between *Subbotina* and *Dentoglobigerina*; considered here possible phylogenetically primitive *galavisi*).
- *Dentoglobigerina galavisi* (Bermúdez) / *D. baroemoenensis* (LeRoy) transition.—Spezzaferri and Premoli Silva, 1991:243, pl. 2, figs. 2a-c [upper Oligocene Zone O6, DSDP Hole 538A, Gulf of Mexico], pl. 2, figs. 3a-c [lower Oligocene Zone O4, DSDP Hole 538A, Gulf of Mexico].
- *Globoquadrina larmeui* Akers.—Jenkins, 1960:355 (partim), pl. 3, figs. 1a-1c [Oligocene Zone 2-3, overlapping with range of *Paragloborotalia opima*, Lakes Entrance Oil Shaft, Victoria, Australia]. [Not Akers, 1955.]
- *Globigerina yeguaensis yeguaensis* Weinzierl and Applin.—Blow and Banner, 1962:99, pl. 13, figs. k-m (partim, not figs. h, j) [lower Oligocene *Globigerina oligocaenica* Zone, Lindi area, Tanzania]. [Not Weinzierl and Applin, 1929.]
- *Globigerina winkleri* (Bermúdez).—Quilty, 1976:639, pl. 4, figs. 15, 16 [Zone N4, DSDP Site 320, Nazca Plate, southeastern Pacific Ocean]. [Not Bermúdez, 1961.]
- Not *Globigerina galavisi* Bermúdez.—van Eijden and Smit, 1991:110, pl. 2, fig. 17 (= *Turborotalia ampliapertura*).

- **Geological Range:**
  Notes: *Dentoglobigerina galavisi* first occurs in the middle Eocene, probably Zones E10/E11, though further work is required to constrain its evolutionary first occurrence. This species was illustrated from middle Eocene Zone E12 by Krasheninnikov and Hoskins (1973), who recorded its first appearance at that level. It was also questionably recorded from the same zone by Blow (1979, pl. 191, figs. 8, 9) (see discussion above). Miller and others (1991) calibrated the first occurrence to Chron C16n (upper Eocene) at DSDP Site 612, northwest Atlantic Ocean; and it is from the upper Eocene and Oligocene that most reliable occurrences have been recorded.
- The uppermost datum may be difficult to define precisely because of intergradation with *D. larmeui*, which has been regarded as a closely related species since the work of Bermúdez (1961) and Brönnimann and Resig (1971). Krasheninnikov and Hoskins (1973) suggested a highest occurrence in the ‘middle’ Oligocene *Paragloborotalia opima* Zone. Spezzaferri and Premoli Silva (1991) recorded a range extending to the upper part of Zone P22, overlapping with the range of *Paragloborotalia pseudokugleri* (= upper Oligocene Zone O7) (see also Spezzaferri, 1994). Pearson and Chaisson (1997) recorded a range into the lower Miocene at Ceara Rise, Atlantic Ocean, but no specimens were illustrated. Here we show a specimen (Pl. 11.5, Fig. 4) from lower Miocene Zone M1 from ODP Site 904, western North Atlantic Ocean.
- [Wade et al. 2018]
  Last occurrence (top): within **M1a** subzone (22.44-22.96Ma, top in Aquitanian stage). Data source: Wade et al. 2018 f1.1

First occurrence (base): within **E10** zone (41.89-43.23Ma, base in Lutetian stage). Data source: Wade et al. 2018

GLOBIGERINA LINAPERTA (in GELATI, 1977) -----> SUBBOTINA LINAPERTA (Current classification: FINLAY, 1939)

Reference:

http://www.mikrotax.org/pforams/index.php?id=100288

Synonyms:

- *Globigerina linaperta* Finlay, 1939:125, pl. 23: figs. 54-57 [middle Eocene, Bortonian Stage, Hampden section, South Island, New Zealand].—Hornibrook, 1958:33, pl. 1: figs. 19-21(reillustration of holotype).—Gohrbandt, 1962:104, pl. 7: fig. 4a-c [upper Eocene, Bruderndorf, Austria].— Saito, 1962:216, pl. 32: fig. 4a-c [middle Eocene Zone E12, Haha-Jima, Bonin Islands, western Pacific Ocean].— McTavish, 1966:24, pl. 2: figs. 29, 31-33 [upper Eocene, Priabonian, British Solomon Islands, western Pacific Ocean].—Stainforth and others, 1975:201 (partim; not fig. 63, 2-5), fig. 63, 1a-c (reillustration of holotype).—Toumarkine, 1975:742, pl. 1: figs. 1, 2 [middle Eocene Zone E10/11, DSDP Site 313, northeastern Mid-Pacific Mountains, western Pacific Ocean].— Krasheninnikov and Basov, 1983:838, pl. 2: figs. 8-11 [middle Eocene, DSDP Site 511, Falkland Plateau, South Atlantic Ocean]. —Snyder and Waters, 1985:463, pl. 2: figs. 1-3 [lower Eocene Zone E5, DSDP Hole 548A, Goban Spur, eastern North Atlantic Ocean].
- *Globigerina (Subbotina) linaperta* Finlay.—Jenkins, 1971:162, pl. 18: figs. 551-554 (551-553 reillustrations of holotype, 554 topotype).
- *Subbotina linaperta* Finlay.—Poore and Brabb, 1977:269, pl. 5: fig. 8 [upper Eocene Zone E14/15, Twobar Shale Member, San Lorenzo Fm., Santa Cruz Mountains, California], pl. 5: fig. 9 [middle Eocene Zone P13/14, Butano Sandstone, Santa Cruz Mountains, California].—Belford, 1984:14, pl. 23: figs. 9-15 [lower Eocene Zone E6/7, Papua, New Guinea].—Stott and Kennett, 1990:559, pl. 7: fig. 9 [middle Eocene Zone AE8, ODP Hole 689B, Maud Rise, Weddell Sea, Antarctic Ocean].—Huber, 1991:440, pl. 5: fig. 1 [middle Eocene Zone AE8, ODP Hole 738B, Kerguelen Plateau, southern Indian Ocean].— Berggren, 1992:583, pl. 3: figs. 1-4 [middle Eocene, ODP Hole 748B, southern Kerguelen Plateau, southern Indian Ocean].
- *?Subbotina linaperta* Finlay.—Blow, 1979:1276 (partim), pl. 124: fig. 9 [lower Eocene Zone E5, DSDP Hole 47.2, Shatsky Rise, northwest Pacific Ocean] [Not pl. 91: fig. 8; pl. 158: fig. 8; pl. 160, figs. 6-8; pl. 177: figs. 4-6; pl. 240: Figs. 5, 6.]
- *Globigerina posttriloculinoides* Khalilov, 1956:242, pl. 3: fig. 2a-c [middle Eocene, Maly Caucasus].
- *Globigerina posttriloculinoides* Khalilov var. *clinata* Khalilov, 1956: 243, pl. 3: fig. 3a-c [upper Eocene, Maly Caucasus].
- ?*Subbotina oregonensis* McKeel and Lipps, 1975:81, pl. 4: figs. 3a-c [middle to upper Eocene Coaledo Fm., Oregon].
- Not *Globigerina* (*Eoglobigerina*) *linaperta* Finlay._Hillebrandt, 1976:331, pl. 1: figs. 14, 15 [=
- *Subbotina eocaena* (Guembel)].
- **Geological Range:**
  Notes: Zone E5 to Zone E16. [Olsson et al. 2006]
  Last occurrence (top): within **E16** zone (33.90-34.68Ma, top in Priabonian stage). Data source: Eocene Atlas
  First occurrence (base): within **E5** zone (50.67-52.54Ma, base in Ypresian stage). Data source: Eocene Atlas

GLOBIGERINA ANGIPOROIDES (in GELATI, 1977) -----> SUBBOTINA ANGIPOROIDES (Current classification: HORNIBROOK, 1965)

Reference:

http://www.mikrotax.org/pforams/index.php?id=100279

Synonyms:

- *Globigerina angipora* Stache.—Finlay, 1939:125 [not illustrated]. [Not Stache, 1865 = *nomen dubium*.]
- *Globigerina angiporoides* Hornibrook, 1965:835-838, text-figs. 1a-i, 2 [uppermost Eocene, Campbells Beach, South Island, New Zealand].□Quilty, 1976:637, pl. 1, figs. 5, 6 [lower Oligocene Zone P19, DSDP Site 321, Nazca Plate, southeast Pacific Ocean].□Loubere, 1985, pl. 4, fig. 4 [lower Oligocene Zone P20, DSDP Hole 549A, northeast Atlantic Ocean].□Poore, 1984, pl. 2, figs. 5, 6 [lower Oligocene Zone OL2, DSDP Site 522, Angola Basin, South Atlantic Ocean].□van Eijden and Smit, 1991:109-110, pl. 2, fig. 8 [lower Oligocene Zone P20, ODP Hole 756C, eastern Indian Ocean].
- *Globigerina* (*Subbotina*) *angiporoides angiporoides* Hornibrook.□Jenkins, 1971:160-161, pl. 20, figs. 588-594 [upper Eocene-lower Oligocene, Earthquakes Marl, South Island, New Zealand].
- *Globigerina angiporoides angiporoides* Hornibrook.□Poore and Brabb, 1977:255, pl. 1, figs. 1-4 [lower Oligocene, San Lorenzo Fm., Santa Cruz Mountains, California].
- *Subbotina angiporoides angiporoides* (Hornibrook).□Blow, 1979:1250-1252, pl. 12, fig. 3 [metatype; uppermost Eocene, Campbells Beach, South Island, New Zealand], fig. 4 [lower Oligocene Zone P19, Lindi, Tanzania].
- *Subbotina angiporoides* (Hornibrook).—Huber, 1991:440, pl. 5, fig. 5 [lower Oligocene Zone AP13, ODP Hole 738B, Kerguelen Plateau, South Indian Ocean].—Spezzaferri and Premoli Silva, 1991:257, pl. XV, fig. 3 [Subzone P21a = Zone O3-O5, DSDP Hole 538A, Gulf of Mexico], fig. 4 [lower Oligocene Zone P20 = Zone O1, DSDP Hole 538A, Gulf of Mexico].—Gallagher and Holdgate, 2000, fig.14 [lower Oligocene Zone P18-P21a = Zone O1-O4, Otway Basin, Australia].—Li and others, 2003, pl. 2, fig. 15 [lower Oligocene, ODP Hole 1134A, Great Australian Bight].—Olsson and others, 2006:126-129, pl. 6.6 (partim), figs. 1-3 [SEMs of holotype of *Globigerina angiporoides*, upper Eocene, Campbells Beach, South Island, New Zealand], fig. 4 [upper Eocene, Atlantic City Borehole, ODP Hole 150X, New Jersey], figs. 6, 7, 13 [upper Eocene, ODP Hole 690B, Maud Rise, Weddell Sea], figs. 8, 12, SEMs of paratype of *Globigerina angiporoides minima* Jenkins [middle Eocene *Globigerinatheka* (*Globigerapsis*) *index index* Zone (not upper Eocene as stated by Olsson and others, 2006), Hampden Beach, South Island, New Zealand].
- *Subbotina angiporoides minima* (Jenkins).—Nocchi and others, 1991:270, pl. 6, figs. 13-15 [lower Oligocene Zone P18-P20 = Zone O1-O2, ODP Hole 703A, Subantarctic South Atlantic Ocean]. [Not Jenkins, 1965.]
- *Globigerina linaperta* Finlay subsp. *transdanubica* Samuel, 1972:181-182, pl. 37, fig. 4a-c, pl. 38, figs. 1, 2 [upper Eocene, Nagyveleg-1 borehole, Bakony Mountains, Hungary].
- *Globorotalia* sp. 2. Loubere, 1985:559, pl. 4, fig. 1 [lower Oligocene Zone P18, DSDP Hole 549A, northeastern Atlantic Ocean], figs. 2, 3 [upper Eocene Zone P17, DSDP Hole 549A, northeastern Atlantic Ocean].
- Not *Subbotina angiporoides* (Hornibrook).—Leckie and others, 1993:125, pl. 1, fig. 18 [lower Oligocene Zone P18, ODP Hole 628A, western North Atlantic Ocean], fig. 19 [lower Oligocene Zone P19, ODP Hole 803D, Ontong Java Plateau, western equatorial Pacific Ocean], fig. 20 [lower Oligocene Zone P19, ODP Hole 628A, western North Atlantic Ocean] (= *Subbotina utilisindex*).—Olsson and others, 2006:126-129, pl. 6.6 (partim), fig. 5, SEM of paratype of *Globigerina angiporoides* [middle (not upper, as stated) Eocene, Campbells Beach, South Island, New Zealand], figs. 9-11, SEMs of holotype of *Globigerina angiporoides*

minima Jenkins [middle (not upper, as stated) Eocene, Hampden Beach, South Island, New Zealand] (= *Subbotina minima*).

- **Geological Range:**
  Notes: The first appearance datum of *S. angiporoides* marks the base of middle Eocene Zone AE7 (Huber and Quillévéré, 2005). [Wade et al. 2018 NB base AE7 is equivalent to base E11] The extinction of *S. angiporoides* has been used as a primary biostratigraphic marker in the high latitude zonations of Jenkins (1965) and Stott and Kennett (1990) and is used to define the base of Zone OL4 in Poore (1984) and the base of Zone AO2 in Huber and Quillévéré (2005). *Subbotina angiporoides* is a secondary marker in the tropical zonations of Berggren and others (1995) and Wade and others (2011). The last appearance datum is within lower Oligocene Zone O3 and calibrated to Chron C11n in multiple sites (Berggren and others, 1995). [Wade et al. 2018]
  Last occurrence (top): within **O3** zone (29.18-30.28Ma, top in Rupelian stage). Data source: Wade et al. 2018
  First occurrence (base): within **E11** zone (40.40-41.89Ma, base in Lutetian stage). Data source: Eocene Atlas

CATAPSYDRAX MARTINI MARTINI (in GELATI, 1977) -----> GLOBOTURBOROTALITA MARTINI (Current classification: BLOW & BANNER, 1962)

Reference:

http://www.mikrotax.org/pforams/index.php?dir=pf_cenozoic/Globigerinidae/Globoturborotalita/Globoturborotalita%20martini

Synonyms:

- *Globigerinita martini martini* Blow and Banner, 1962:110, pl. 14, fig. O [upper Eocene *Cribrohantkenina danvillensis* Zone, Sample FCRM 1932, Lindi area, Tanzania].—Blow, 1979:1340, pl. 24, fig. 5; pl. 245, figs. 5, 6 [upper Eocene Zone E15/16, Red Bluff Clay, type locality, Alabama].
- *Catapsydrax martini* (Blow and Banner).—Warraich and Ogasawara, 2001:45, figs. 12, 15, 16 [Zone E10/11, Kirthar Fm., Sulaiman Range, Pakistan].—Spezzaferri and Premoli Silva, 1991, pl. 1, figs. 5a-c [upper Oligocene Subzone P21b, DSDP Hole 538A, Gulf of Mexico].
- *Globoturborotalita martini* (Blow and Banner).—Olsson and others, 2006:121, pl. 6.2, figs. 14-18 [upper Eocene, Zone E15/E16, Shubuta Clay, Yazoo Fm. Wayne County, Mississippi].—Sexton and others, 2006:6, pl. 1, fig. 3 [middle Eocene Zone E13, ODP Site 1052, Blake Nose, western North Atlantic Ocean].—Miller and others, 2008:fig. 6a [lower Oligocene Zone O1, St Stephens Quarry, Alabama].
- *Globigerinita martini scandretti* Blow and Banner, 1962:111, pl. 14, figs. V-X [lower Oligocene *Globigerina oligocaenica* Zone, Sample FCRM 1922, Lindi area, Tanzania].—Blow, 1979:1342, pl. 24, figs. 6, 7 [lower Oligocene Zone O2, Sample FCRM 1922, Lindi area, Tanzania]; pl. 245, fig. 7 [lower Oligocene Zone O1, DSDP Site 14, central South Atlantic Ocean].
- *Globigerinita hardingae* Blow, 1979:1338, pl. 178, figs. 1-5 (4 = holotype) [middle Eocene Zone E9, Sample RS. 24, Kilwa area, Tanzania].[Spezzaferri et al. 2018]

- **Geological Range:**
  Notes: The distribution of this species ranges from Zone E9 (Olsson and others, 2006) to Zone O5 (Spezzaferri and Premoli Silva, 1991). [Spezzaferri et al. 2018]
  Last occurrence (top): within **O5** zone (26.93-28.09Ma, top in Chattian stage). Data source: Spezzaferri et al. 2018

First occurrence (base): within **E9** zone (43 Globigerina ampliapertura.23-43.85Ma, base in Lutetian stage). Data source: Eocene Atlas

Original Classification (Gelati, 1977)	Reviewed classification (this work; based on Microtax database)	Reviewed stratigraphic ranges		Mediterranean foraminifera biozones (Wade et al., 2011 and Lirer et al., 2019)
		First Occurrence	*Last Occurrence*	
Globorotalia cerroazulensis pomeroli (Toumarkine & Bolli, 1970)	Turborotalia pomeroli (Toumarkine & Bolli, 1970)	42.70 Ma (Pearson et al., 2006)	35.00 Ma (Pearson et al., 2006)	E10-E15
Globigerinatheka mex. Mexicana (Cushman, 1925)	*Unvaried*	43.23-43.85 Ma (Premoli Silva et al., 2006)	35.89-37.99 Ma (Premoli Silva et al., 2006)	E9-E14
Globigerinatheka index (Finlay, 1939)	*Unvaried*	43.40 Ma (Premoli Silva et al., 2006)	34.70 Ma (Wade et al., 2011)	E9-E15
Globigerinatheka semiinvoluta (Keijzer, 1935)	*Unvaried*	37.99-39.97 Ma (Premoli Silva et al., 2006)	35.90 Ma (Wade et al., 2011)	E13-E14
Pseudohastigerina barbadoensis (Blow, 1969)	Pseudohastigerina naguewichiensis (Myatliuk, 1950)	35.90 Ma (Olsson & Hemleben, 2006)	32.10 Ma (Wade et al., 2011)	E15-O1
Hantkenina albamensis (Cushman, 1924)	*Unvaried*	39.80 Ma (Coxall & Pearson, 2006)	33.90 Ma (Wade et al., 2011)	E13-E16
Globorotalia cerroazulensis cerroazulensis (Tourmarkine & Bolli, 1970)	Turborotalia cerroazulensis (Cole, 1928)	41.40 Ma (Pearson et al., 2006)	34.10 Ma (Pearson et al., 2006)	E11-E16
	Turborotalia cocoaensis (Cushman, 1928)	38.60 Ma (Pearson et al., 2006)		E13-E16

Globorotalia cerroazulensis cocoaensis (Cushman, 1928)			34.10 Ma (Pearson et al., 2006)	
Globorotalia cerroazulensis cunialensis (Tourmarkine & Bolli, 1970)	Turborotalia cunialensis (Tourmarkine & Bolli, 1970)	34.40 Ma (Pearson et al., 2006)	34.10 Ma (Pearson et al., 2006)	E16-E16
Pseudohastigerina micra (Cole, 1927)	*Unvaried*	49.30 Ma (Olsson & Hemleben, 2006)	32.10-33.90 Ma (Olsson & Hemleben, 2006)	E7a-O1
Globigerina ciperoensis angustiumbilicata (Bolli, 1957)	Tenuitellinata angustiumbilicata (Bolli, 1957)	32.1-33.9 Ma (Pearson et al., 2018)	19.3-21.12 Ma (Pearson et al., 2018)	O1-M2
Globigerina ampliapertura (Bolli, 1957)	Turborotalia ampliapertura (Bolli, 1957)	35.30 Ma (Pearson et al., 2006)	30.30 Ma (Wade et al., 2011)	E15-O2
Globorotalia opima opima (Bolli, 1957)	Paragloborotalia opima (Bolli, 1957)	30.60 Ma (Leckie et al., 2018)	26.90 Ma (Leckie et al., 2018)	O2-O5
Globorotalia siakensis (LeRoy, 1939)	Paragloborotalia siakensis (LeRoy, 1939)	29.18-30.28 Ma (Leckie et al., 2018)	10.46-11.63 Ma (Leckie et al., 2018)	O3-M11
Globoquadrina globularis (Bermúdez, 1961)	Dentoglobigerina globularis (Bermúdez, 1961)	33.90-34.68 Ma (Wade et al., 2018)	22.44-22.96 Ma (Wade et al., 2018)	E16-M1a
Globoquadrina praedehiscens (Blow & Banner, 1962)	Dentoglobigerina tripartita (Koch, 1926)	32.10-33.90 Ma (Wade et al., 2018)	13.77-14.24 Ma (Wade et al., 2018)	O1-M7
Globoquadrina baroemoensis (LeRoy, 1939)	Dentoglobigerina baroemoenensis (LeRoy, 1939)		5.10-5.72 Ma (Wade et al., 2018)	O2-N18

		30.28-32.10 Ma (Kennett & Srinivasan, 1983)		
Globorotalia semivera (Hornibrook, 1961)	Paragloborotalia semivera (Hornibrook, 1961)	28.09-29.18 Ma (Leckie et al., 2018)	15.10-16.38 Ma (Leckie et al., 2018)	O4-M5
Globorotalia nana pseudocontinuosa (Jenkins, 1967)	Paragloborotalia pseudocontinuosa (Jenkins, 1967)	30.28-32.10 Ma (Leckie et al., 2018)	15.10-16.38 Ma (Leckie et al., 2018)	O2-M5
Globigerina ciperoensis ciperoensis (Bolli, 1954)	Ciperoella ciperoensis (Bolli, 1954)	29.18-30.28 Ma (Olsson et al., 2018)	22.44-22.96 Ma (Olsson et al., 2018)	O3-M1a
Globoquadrina altispira (Brönnimann & Resig, 1971)	Dentoglobigerina altispira (Cushman & Jarvis, 1936)	21.12-22.44 Ma (Wade et al., 2018)	3.1 Ma (Wade et al., 2011)	M1b-PL4
Globigerina angulisuturalis (Bolli, 1957)	Ciperoella angulisuturalis (Bolli, 1957)	28.09-29.18 Ma (Olsson et al., 2018)	19.30-21.12 Ma (Olsson et al., 2018)	O4-M2
Globigerina galavisi (Bermúdez, 1961)	Dentoglobigerina galavisi (Bermúdez, 1961)	41.89-43.23 Ma (Wade et al., 2018)	22.44-22.96 Ma (Wade et al., 2018)	E10-M1a
Globigerina linaperta (Finlay, 1939)	Subbotina linaperta (Finlay, 1939)	50.67-52.54 Ma (Wade et al., 2018)	33.90-34.68 Ma (Wade et al., 2018)	E5-E16

Globigerina angiporoides (Hornibrook, 1965)	Subbotina angiporoides (Hornibrook, 1965)	40.40-41.89 Ma (Wade et al., 2018)	29.18-30.28 Ma (Wade et al., 2018)	E11-O3
Catapsydrax martini martini (Blow & Banner, 1962)	Globoturborotalia martini (Blow & Banner, 1962)	43.23-43.85 Ma (Spezzaferri et al., 2018)	26.93-28.09 Ma (Spezzaferri et al., 2018)	E9-O5

Biostratigraphic review of planktonic foraminifera taxa classified by Gelati (1977). The review is based on the Microtax database (Huber *et al.*, 2016).

Intentioanlly blank page

Appendix II

Appendix II provides uninterpreted seismic lines of Section 4.4.3.

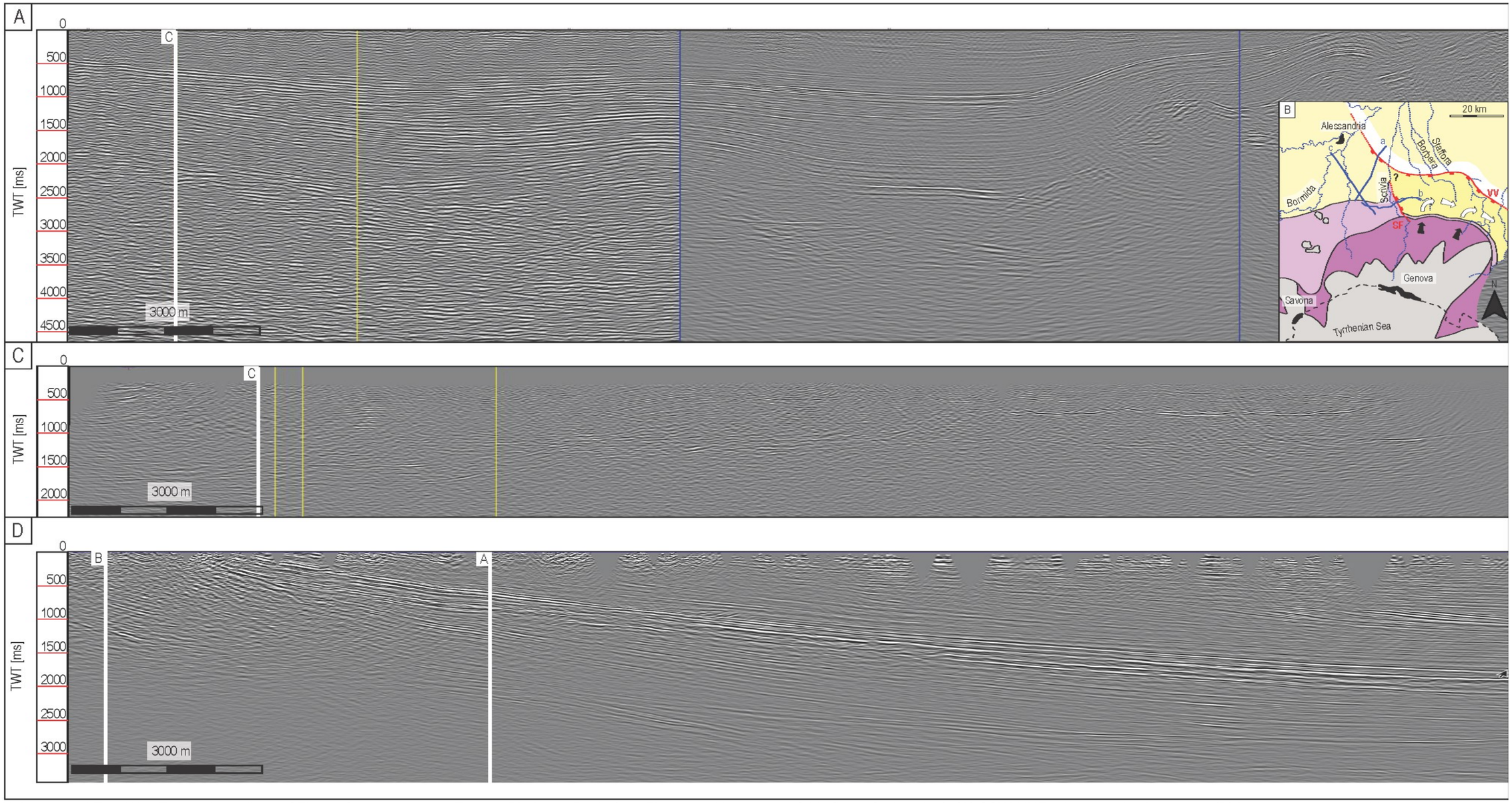

Uninterpreted Two-Way Time seismic lines of Fig. 61 from the eastern Tertiary Piedmont Basin (see Fig. 46 and inset map of this figure for location). (A) SSW-NNE oriented seismic section. (B) Inset palaeogeographic map showing the depositional setting at the time of the Monastero Fm. and location of sismic lines (see Fig. 64 for details). (C) E-W oriented seismic section. (D) NNW-SSE oriented seismic section.

Intentioanlly blank page

Appendix III

Appendix III provides the graphic representation of non-corrected hysteresis loops, which represents the thermal demagnetization path before the corrections for removing the minor contribution of the paramagnetic component.

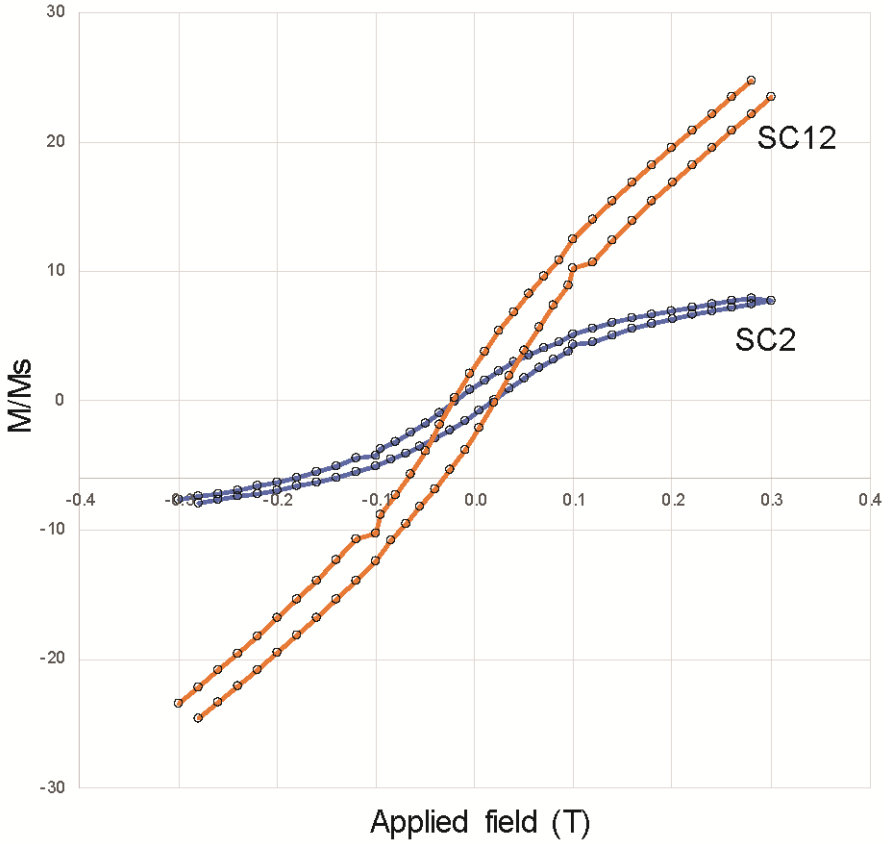

Thermal demagnetisation path of three-axes IRM on representative samples. The graph is not corrected for the paramagnetic component.